LIGAND DESIGN FOR DUAL PROPERTY SINGLE MOLECULE MAGNETS

TRINH (AMY) N.K. PHAM

A thesis submitted to the Department of Chemistry

in partial fulfillment of the requirements for the degree of Master of Science

Supervised by

Professor Melanie Pilkington

Brock University

St. Catharines Ontario, Canada

April 2016

Abstract

This thesis describes two different approaches for the preparation of polynuclear clusters with interesting structural, magnetic and optical properties. Firstly, exploiting *p-tert*-butylcalix[4]arene (TBC4) macrocycles together with selected Ln(III) ions for the assembly of emissive single molecule magnets, and secondly the preparation and coordination of a chiral mpmH ligand with selected 3*d* transition metal ions, working towards the discovery of chiral polynuclear clusters.

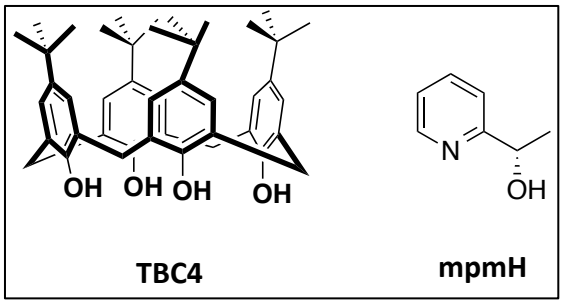

In **Project 1**, the coordination chemistry of the TBC4 macrocycle together with Dy(III) and Tb(III) afforded two $Ln_6[TBC4]_2$ complexes that have been structurally, magnetically and optically characterized. X-ray diffraction studies reveal that both complexes contain an octahedral core of Ln_6 ions capped by two fully deprotonated TBC4 macrocycles. Although the unit cells of the two complexes are very similar, the coordination geometries of their Ln(III) ions are subtly different. Variable temperature *ac* magnetic susceptibility studies reveal that both complexes display single molecule magnet (SMM) behaviour in zero *dc* field and the energy barriers and associated pre-exponential factors for each relaxation process have been determined. Low temperature solid state photoluminescence studies reveal that both complexes are emissive; however, the *f-f* transitions within the Dy_6

complex were masked by broad emissions from the TBC4 ligand. In contrast, the Tb(III) complex displayed green emission with the spectrum comprising four sharp bands corresponding to $^5D_4 \rightarrow {}^7F_J$ transitions (where J = 3, 4, 5 and 6), highlighting that energy transfer from the TBC4 macrocycle to the Tb(III) ion is more effective than to Dy. Examples of zero field Tb(III) SMMs are scarce in the chemical literature and the $Tb_6[TBC4]_2$ complex represents the first example of a Tb(III) dual property SMM assembled from a *p-tert*-butylcalix[4]arene macrocycle with two magnetically derived energy barriers, U_{eff} of 79 and 63 K.

In **Project 2**, the coordination of both enantiomers of the chiral ligand, α-methyl-2-pyridinemethanol (mpmH) to Ni(II) and Co(II) afforded three polynuclear clusters that have been structurally and magnetically characterized. The first complex, a Ni_4 cluster of stoichiometry $[Ni_4(O_2CCMe_3)_4(mpm)_4]\cdot H_2O$ crystallizes in a distorted cubane topology that is well known in Ni(II) cluster chemistry. The final two Co(II) complexes crystallize as a linear mixed valence trimer with stoichiometry $[Co_3(mpm)_6]\cdot(ClO_4)_2$, and a Co_4 mixed valence complex $[Co(II)_2Co(III)_2(NO_3)_2(\mu\text{-}mpm)_4(ONO_2)_2]$, whose structural topology resembles that of a defective double cubane. All three complexes crystallize in chiral space groups and circular dichroism experiments further confirm that the chirality of the ligand has been transferred to the respective coordination complex. Magnetic susceptibility studies reveal that for all three complexes, there are competing ferro- and antiferromagnetic exchange interactions. The $[Co(II)_2Co(III)_2(NO_3)_2(\mu\text{-}mpm)_4(ONO_2)_2]$ complex represents the first example of a chiral mixed valence Co_4 cluster with a defective double cubane topology.

Acknowledgments

The completion of this work would not have been possible without the participation and assistance of many people whose names may not all be specifically mentioned. Nevertheless, their contributions are sincerely appreciated and gratefully acknowledged. Firstly, I would like to express my deepest gratitude to my supervisor, Dr. Melanie Pilkington, for her support, patience, guidance, advice, valuable comments, and ongoing help. My appreciation also extends to Dr. Theocharis Stamatatos, for his enthusiasm and valuable co-mentoring which helped make this project successful. I would like to thank Dr. Jeremy Rawson (University of Windsor) for kindly teaching me the fundamentals of molecular magnetism. In addition, I extend a thank you to my former and current advisory committee members for their insightful suggestions. I would also like to acknowledge collaboration with Dr. F.S. Razavi at Brock University for magnetic susceptibility data and a collaboration with Dr. R.A.S. Ferreira, University of Aveiro, Portugal for solid state photoluminescence measurements. Thanks also to Dr. Emma Stares for help with magnetic measurements and for showing me how to model *ac* magnetic susceptibility data; also thanks to my laboratory colleagues, for sharing their experimental expertise and fun stories. From the Stamatatos group, I particularly wish to thank Angeliki Athanasopoulou and Dr. Dimitrios Alexandropoulos for their collaboration and support. A special shout out goes to all my friends, who have helped me survive all the stress over the years, and sustained a positive atmosphere in which to do chemistry. Above all, I am indebted to my family, whose precious love, unconditional support and value to me only grow more precious with age.

Table of Contents

List of Tables

List of Figures

List of Schemes

List of Abbreviations

0-D	zero-dimensional
1-D	one-dimensional
2-D	two-dimensional
3-D	three-dimensional
A	absorption
Å	Angstrom
ac	alternating current
B.M. (or β)	Bohr Magneton
B	magnetic induction
br	broad (NMR and IR peak descriptor)
bpy	bipyridine
calcd.	calculated
C	Curie constant
°C	degrees Celsius
CD	circular dichroism
$CDCl_3$	deuterated chloroform
CH_2Cl_2	Dichloromethane
CSMs	continuous shape measure
CPL	circularly polarized light
cm^{-1}	wavenumber
d	doublet
D	zero-field splitting parameter
dc	direct current
dd	doublet of doublets
DMF	dimethylformamide
DMSO	dimethylsulfoxide
D_2O	deuterium oxide
E	electric field ($kV \cdot cm^{-1}$)

E_C	coercive field
emu	electromagnetic unit
FAB	fast-atom bombardment
g	grams
g	Landé factor
G	Gauss
h	hour(s)
H	applied magnetic field
$\widehat{H}$	spin Hamiltonian
Hz	Hertz
i	inversion center
IR	infrared
J	magnetic exchange coupling constant (NMR); total angular momentum quantum number
k	Boltzmann constant (1.3806×10^{-23} J·K^{-1})
K	Kelvin
L	total orbital angular momentum quantum number
Ln(III)	lanthanide ion
m	multiplet
M	magnetization
M_S, M_J	microstates
MCD	magnetic circular dichroism
MChD	magnetochiral dichroism
min	minute
mol	moles
mL	milliliters
mmol	millimole
m.p.	melting point
mpmH	α-methyl-2-pyridinemethanol
MPMS	magnetic property measurement system

MS	mass spectrometry
m/z	mass/charge ratio
N	Avogradro's number (6.02×10^{23} mol^{-1})
Nadcb	sodium phenylphosphinate (3,5-dichlorobenzoate)
NCD	natural circular dichroism
nm	nanometer
NMR	nuclear magnetic resonance
ox	oxalate
P	polarization ($\mu c \cdot cm^{-2}$)
Pc	phthalocyanine
$+P_S$	spontaneous polarization
$+P_r$	remnant polarization
Ph	phenyl
pheHA	phenylalaninehydroxamic acid
PPMS	physical property measurement system
piv^-	pivalic acid
ppm	parts per million
py	pyridine
QTM	quantum tunneling mechanism
R	agreement factor
RT	room temperature
s	singlet
S	total spin angular momentum quantum number
$\hat{S}$	spin operator
S/C	substrate to catalyst molar ratio
SMM	single molecule magnet
$saoH_2$	salicylaldoxime
SOC	spin-orbit coupling
SQUID	superconducting quantum interference device
str	Stretch

Oe	Oersted
t	triplet
T	Tesla
T	temperature
T_B	blocking temperature
TBC4	*p-tert*-butylcalix[4]arene
TBC6	*p-tert*-butylcalix[6]arene
TBC8	*p-tert*-butylcalix[8]arene
TBDOC6	*p-tert*-butyltetrahomo-dioxacalix[6]arene
T_c	critical temperature
TLC	thin layer chromatography
TM	transition metal
TOF	time of flight mass spectrometry
U_{eff}	effective anisotropy barrier
UV-Vis	ultra violet-visible
VCD	vibrational circular dichroism
ZFS	zero-field splitting
χ	magnetic susceptibility
χ_M	molar magnetic susceptibility
λ	wavelength
μ_B	Bohr Magneton (9.274×10^{-24} J·T^{-1})
μ_{eff}	effective magnetic moment
μ_0	permeability
θ	Weiss constant
σ	mirror plane
τ	relaxation time
τ_0	pre-exponential factor
ω	angular frequency
18C6	18-crown-6

CHAPTER 1 - INTRODUCTION

1.1 From Classical to Molecule-Based Magnets

Traditional magnets are atomic-based materials, comprised of metals, alloys, or metal oxides such as Fe, $SmCo_5$, and Fe_2O_3, which are typically prepared via high temperature metallurgical routes.[1] They have contributed greatly to our everyday lives for centuries with applications that include data storage, switches, fridge magnets, medical magnetic resonance imaging (MRI) equipment, and the magnetic strips on our credit cards.[2] During the last three decades, chemists have focused efforts on developing new classes of magnetic materials from molecular precursors using low temperature solution-based methodologies. One advantage of this approach is that it is possible to rationally tune the physical properties of the resulting compounds by synthetically modifying their molecular precursors.[3] In addition, this synthetic flexibility also facilitates the preparation of dual property or multifunctional materials, where magnetism is combined together with two or more physical properties such as chirality, luminescence and/or conductivity.[4] Molecule-based or molecular magnets are typically divided into different families according to: (i) their magnetic behaviour; (ii) their molecular precursors or building blocks (organic molecules (radicals), coordination compounds, or a mixture of both) and (iii) their dimensionality (0-D, 1-D, 2-D, or 3-D).[5,6,7] My research focuses on the synthesis and study of two classes of single molecule magnets (SMMs) that are 0-D complexes of paramagnetic 4*f*-lanthanide or 3*d*-transition metal ions assembled

from a *p-tert*-butylcalix[4]arene [TBC4] macrocycle (**Project 1**- Chapter 2) and a chiral pyridyl alkoxide mpmH ligand (**Project 2** - Chapter 3). Since technology is getting smaller and faster, the need for smaller magnets has intensified research efforts in the field of single molecule magnets (SMMs). Below a certain operating or blocking temperature these SMMs are potentially capable of information storage at the molecular level. The first half of Chapter 1 contains a general introduction to the field of molecular magnetism followed by an overview of SMMs, highlighting dual property and chiral systems. The second half of Chapter 1 provides the reader with a brief overview of related studies concerning coordination complexes of calixarene macrocycles and pyridyl alkoxide ligands.

1.2 Magnetism

Magnetic fields are forces generated in materials via the circular motion of electrons. If an isotropic material is placed in a homogeneous magnetic field H (measured in Gauss, G), the magnetic induction B, or flux density varies from the free-space value and can be defined as:

$$\mathbf{B} = \mathbf{H} + \mathbf{4\pi M} \qquad \textbf{(Eqn 1.1)}$$

where H is the external magnetic field and *M* is the magnetization. Magnetization is the magnetic moment per unit volume.[6] In many materials M is proportional to H:

$$\mathbf{M} = \boldsymbol{\chi}\mathbf{H} \qquad \textbf{(Eqn 1.2)}$$

where χ is referred to as the magnetic susceptibility (where χ is a dimensionless quantity), which reflects the ease of alignment of spins within a sample that is placed into an external magnetic field. Magnetic susceptibility can thus be defined as magnetization *vs*. field:

$$\chi = \mu_0 \frac{\mathbf{M}}{\mathbf{B}} = \frac{\mathbf{M}}{\mathbf{H}} \qquad \textbf{(Eqn 1.3)}$$

where μ_0 is the permeability of the sample. A material is classified as 'paramagnetic' if $\chi > 0$ and 'diamagnetic' if $\chi < 0$ (see below).[6]

Macroscopically, in the presence of a magnetic field, each electron in an atom has a magnetic moment that originates from two sources. The first from the precession of the electron spin around its axis, and the second due to its orbital motion around the nucleus, giving rise to spin *S* and orbital angular momentum *L*, respectively, Figure 1.1.[8]

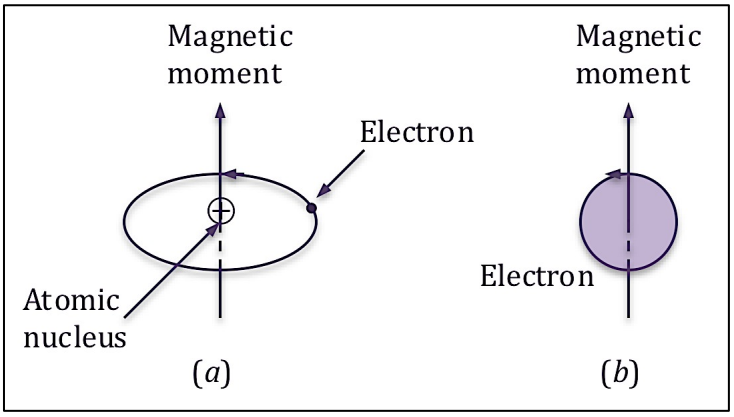

Figure 1.1 Illustration of the magnetic moment associated with (a) an orbiting electron and (b) a spinning electron. Reproduced with permission from Ref. 8.

S and *L* can be considered as vectors (having both magnitude and direction) and may couple to produce the total angular momentum *J* through a mechanism known as spin-orbit coupling.[9] Since molecules have multiple electrons, the net magnetic moment is the vector sum of magnetic moments from all of the electrons in the system.[10]

As presented above, there are two types of magnetic phenomena which may be exhibited by a particular molecule: diamagnetism and paramagnetism.

Diamagnetism exists due to the presence of electron pairs in a molecule such as core electrons, bonding pairs and lone pairs. The magnetic moments of electron pairs within a molecular orbital are arranged antiparallel and thus cancel each other out, resulting in no magnetic moment in zero-field. In the presence of a magnetic field, diamagnetic materials create a small-induced magnetization in such a direction as to oppose the applied magnetic field, Figure 1.2(a). Diamagnetism is found in all materials. Fortunately the diamagnetic response is typically small in paramagnetic materials and can be considered as a correction to the sample paramagnetism. [2,8]

Paramagnetism exists due to the presence of unpaired electrons and contributes to a net magnetic moment greater than zero. When exposed to a magnetic field, paramagnetic materials are attracted towards an applied magnetic field, Figure 1.2(b). The magnetic moments experience a torque created by the force of the field and orient themselves in the direction of the applied magnetic field, resulting in a positive magnetization and magnetic susceptibility, that is typically temperature dependent, Figure 1.2.[2]

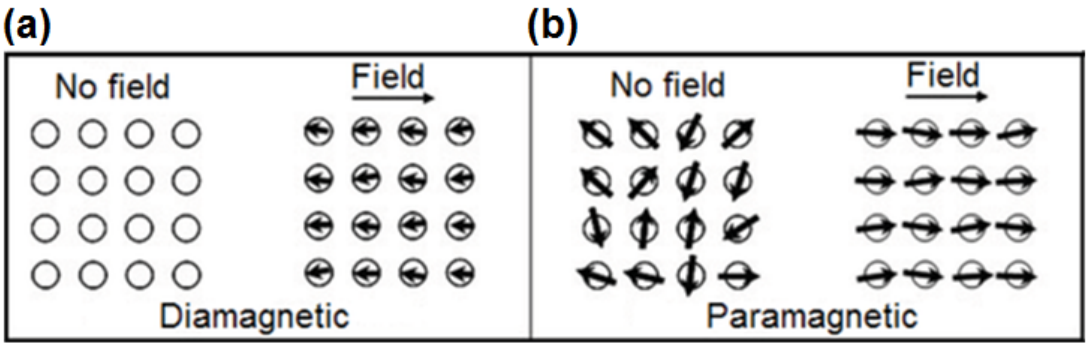

Figure 1.2 Schematic illustration of the atomic dipoles for a diamagnet (a) and a paramagnet (b), in the presence and absence of an external magnetic field.[11]

The temperature dependence of the magnetic susceptibility, χ for many materials can be described by the Curie law:

$$\boldsymbol{\chi_M = \frac{N_A g^2 \beta^2}{3kT} S(S+1)} \qquad \textbf{(Eqn 1.4)}$$

where N_A is Avogradro's number, g is the Landé g-factor, β is the Bohr magneton, k is the Boltzmann constant, T is the temperature (K), and *S* is the spin quantum number (equal to half the number of unpaired electrons). This is more simply represented by the inverse relationship between χ_M and T for a paramagnetic substance where C is the Curie constant ($cm^3 \cdot K \cdot mol^{-1}$), otherwise known as the Curie Law.[12,13,14]

$$\boldsymbol{\chi_M = \frac{C}{T}} \qquad \textbf{(Eqn 1.5)}$$

Susceptibility can be converted to mass susceptibility, χ_g ($cm^3 g^{-1}$), or molar susceptibility, χ_M ($cm^3 \cdot mol^{-1}$). Molar susceptibility is the measure of susceptibility most commonly used in the field of molecular magnetism. Throughout the chapters of this thesis we routinely refer to χ or χ_M as molar susceptibility.

As discussed above, a paramagnetic material typically shows a linear response in a χ^{-1} *vs.* T plot. However, the intercepts of some materials do not pass through the origin as shown in Figure 1.3, where $\theta < 0$ and $\theta > 0$. These deviations may be due to: (i) weak intermolecular interactions in which the spins interact with each other at low temperatures and/or (ii) to the presence of spin-orbit coupling.

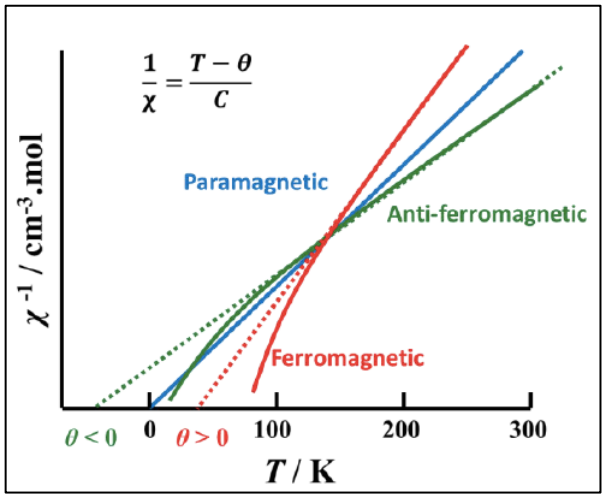

Figure 1.3 χ^{-1} vs. T plot showing Curie-Weiss behavior for an ideal paramagnet (blue line).[15]

With respect to the interactions between spins, these can either be ferromagnetic giving rise to a preferred co-parallel spin alignment Figure 1.4(b), or antiferromagnetic in which spins are aligned antiparallel to each other Figure 1.4(c). The antiferromagnetic alignment of spins of different magnitudes can also give rise to ferrimagnetic spin systems, Figure 1.4(d).[16]

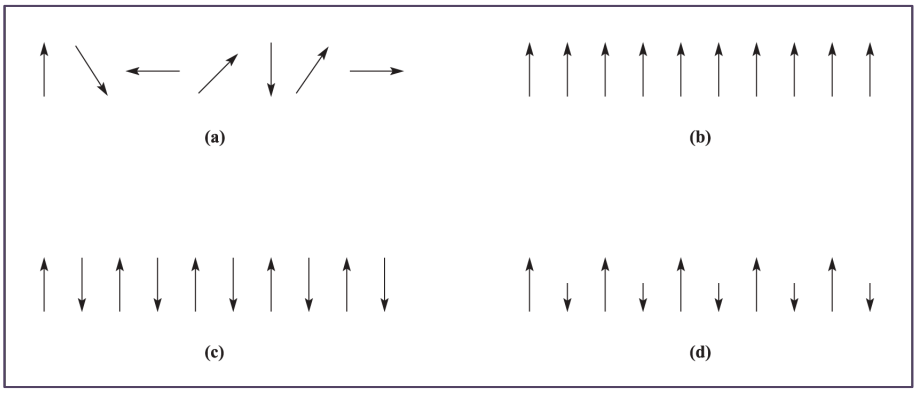

Figure 1.4 Representation of four common types of spin arrangements (a) paramagnetic, (b) ferromagnetic, (c) antiferromagnetic and (d) ferrimagnetic. Adapted from Figure 20.31 of Ref. 16.

To account for these deviations, a correction term or Weiss constant θ is included in the Curie law. The modified Curie law is known as the Curie-Weiss law and is described by equation 1.6.

$$\chi_M = \frac{C}{T-\theta} \qquad \textbf{(Eqn 1.6)}$$

The sign of the Weiss constant is dependent upon the nature of the intermolecular magnetic interactions. If ferromagnetic interactions occur in a compound, θ is positive (red line in Figure 1.3); whereas θ is negative when the interactions are antiferromagnetic as shown by the green line in Figure 1.3.

The magnetic moment of the metal ions can be determined from the number of unpaired electrons n, which is related to the spin quantum number *S*. Thus, the spin-only formula is described by:

$$\mu = 2\sqrt{S(S+1)} \qquad \textbf{(Eqn 1.7)}$$

which is often also written as:

$$\mu_{eff} = \sqrt{n(n+2)} \qquad \textbf{(Eqn 1.8)}$$

As previously mentioned, the different types of magnetic behavior are a direct result of exchange coupling interactions between spins. The exchange interaction between spins on two atoms A and B is described by *J*, using the Heisenberg spin Hamiltonian (where $\hat{S}$ is the spin operator).[4]

$$\hat{H} = -2J\hat{S}_A \cdot \hat{S}_B \qquad \textbf{(Eqn 1.9)}$$

The sign and magnitude of the *J* values can also be used to predict the type of magnetic behavior between two interacting spins. If $J > 0$, the two spins interact in a ferromagnetic manner, while an antiferromagnetic interaction is observed if $J < 0$.[14] In designing magnetic materials, it is important to enhance the spin-spin

interactions, either through bond or through space.[7] It should also be noted that if coupling is allowed to propagate in three dimensions then this can give rise to long range magnetic order or bulk magnetic properties which can be ferro-, antiferro- or ferrimagnetic in nature.

The four most common interactions observed in magnetic materials are often characterized by a change in the value of $\chi_M T$ as a function of temperature, Figure 1.5. A purely paramagnetic material displays no change in $\chi_M T$ as a function of temperature due to the random distribution of the spins within the material. The presence of ferromagnetic interactions within a material leads to an increase in $\chi_M T$. In contrast, the $\chi_M T$ value for a material exhibiting antiferromagnetic interactions decreases upon cooling. A material with antiferromagnetic interactions between spins of different magnitudes exhibits more complex behaviour reflected in an initial downward curvature on cooling due to the antiferromagnetic alignment of neighbouring spins and then an upward curvature due to longer range spin alignment as the temperature decreases, Figure 1.5.

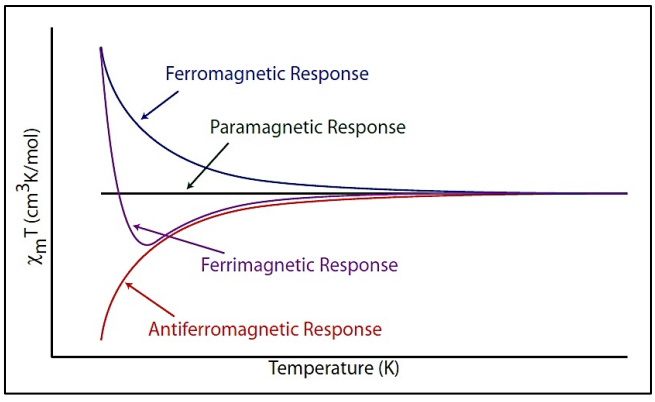

Figure 1.5 Plot of $\chi_M T$ *vs.* T for paramagnetic, ferromagnetic, antiferromagnetic, and ferrimagnetic interactions in the solid state. Reproduced with permission from Ref. 8.

1.3 Single Molecule Magnets

Single-molecule magnets (SMMs) are individual complexes that can be magnetized in the presence of an applied field and retain their magnetization for an appreciable amount of time below a certain blocking temperature T_B, most commonly defined as the temperature below which the time (τ) taken for the magnetization to relax is 100 s after the field is removed.[17] This magnetic memory, often referred to as slow relaxation of magnetization, is one of the most intellectually captivating aspects of SMMs. It is an intrinsic property of the molecule and not the bulk solid which is promising for information storage on the molecular level leading to potential applications of these compounds as ultra-high density memory devices and for quantum computing.[18] Unfortunately, their major drawback to-date are their operating temperatures which are very low due to: (i) the large amount of thermal energy available at higher temperatures which is sufficient for the electrons to overcome the energy barrier within the spin ground state and/or (ii) thermal population of low-lying excited states (which depend upon the exchange coupling, *J*). Hence one of the current challenges in this field is to work towards the discovery of SMMs with higher energy barriers in order render them more practical for future technologies. The aforementioned energy barrier is related to the magnetic anisotropy of the system, which is the directional dependence of the magnetization. In this respect, this energy should be large enough for the spins of an SMM to be aligned with an 'easy axis' or 'Ising' type anisotropy. An easy axis means that the magnetization is preferentially oriented along one direction, Figure 1.6.[19,20,21] As previously mentioned, an attractive feature concerning the slow

relaxation of magnetization in SMMs is that it does not stem from cooperative effects, but is due to the intrinsic properties of the molecule itself.[22] Two distinct strategies have been developed to prepare SMMs which are based on either transition metal (*d*-block metals) or lanthanides (*f*-block metals).

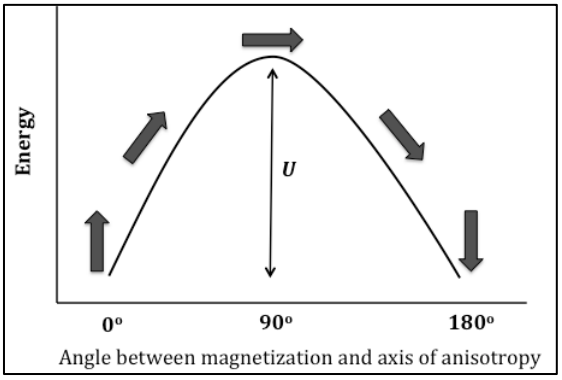

Figure 1.6 Schematic showing the preference for the magnetization of an SMM to be aligned parallel to the easy axis of anisotropy. Adapted from Ref. 21.

1.3.1 Transition Metal SMMs

For a molecule to exhibit SMM behaviour, it must have an appreciable spin ground state *S*, and a large negative spin anisotropy, which is represented by the axial zero-field splitting parameter *D*. Zero-field splitting (ZFS) refers to the loss of degeneracy of the M_S states for transition metals in the absence of an applied magnetic field, which is often caused by a number of factors that include spin-orbit coupling, the coordination geometry of the metal center(s), and the overall symmetry of the molecule. For example, when considering the coordination geometry of a transition metal center, *Jahn-Teller* distortions can enhance magnetic anisotropy by lowering the coordination geometry around the metal center from octahedral to D_{4h} symmetry. These properties can lead to a significant anisotropy

barrier, U (in cm^{-1}), whose maximum value is given by equations 1.10 and 1.11 for systems with integer and half-integer spins, respectively. [17,19]

$$\boldsymbol{U = |D|S^2} \qquad \textbf{(Eqn 1.10)}$$

$$\boldsymbol{U = |D|(S^2 - 0.25)} \qquad \textbf{(Eqn 1.11)}$$

For the majority of first row 3*d* transition metal ions, the magnetic moment of an SMM is produced solely from spin angular momentum because their orbital angular momentum is quenched. In this respect, ZFS results from the coordination environment and molecular symmetry and therefore the magnetic behaviour can be primarily described by the total spin quantum number *S,* where the spin multiplicity is defined as (2*S*+1). The spin multiplicity can be considered in terms of a series of M_S states ranging from +*S* to –*S* in integer steps. Thus for S = 1 the spin multiplicity is three (a spin 'triplet' since 2S +1 = 3) with three M_S values: 1, 0, and +1. If there is no ZFS, the M_S sublevels are degenerate in the absence of a magnetic field but split when an external field is applied. On the other hand, if ZFS is present ($D \neq 0$), the M_S sublevels are not degenerate, even in the absence of an applied field.[21] The ZFS parameter *D* can either be positive or negative and defines the type of magnetic anisotropy associated with the *S* multiplet. The energy of the M_S sub-levels is given by:

$$\mathbf{E(M_S) = g\beta HM_S + DM_S^2} \qquad \textbf{(Eqn 1.12)}$$

In the absence of zero-field splitting ($D = 0$), the M_S levels are degenerate in zero-applied-field. If $D > 0$, then the $M_S = 0$ state will be lowest in energy, which affords no SMM behavior since relaxation to the $M_S = 0$ ground state affords no magnetic response. To the contrary, if $D < 0$, then the $M_S = \pm S$ sublevels will be lowest in

energy affording SMM behaviour.[21,23] Since M_S values range from –S to +S then equation 1.12 reveals that in the presence of ZFS, large values of S will lead to greater energy barriers to the reversal of magnetization (U_{eff}) since the ground state $\pm M_S$ levels lie much lower than the highest-lying $M_S = 0$ level for integer spins, or $M_S = \pm 1/2$ for half-integer spins. This is traditionally described by a 'double-well' diagram, where the $\pm \mathbf{M_S}$ sublevels are located on either side of a 'double well' potential as shown in Figure 1.7.[22]

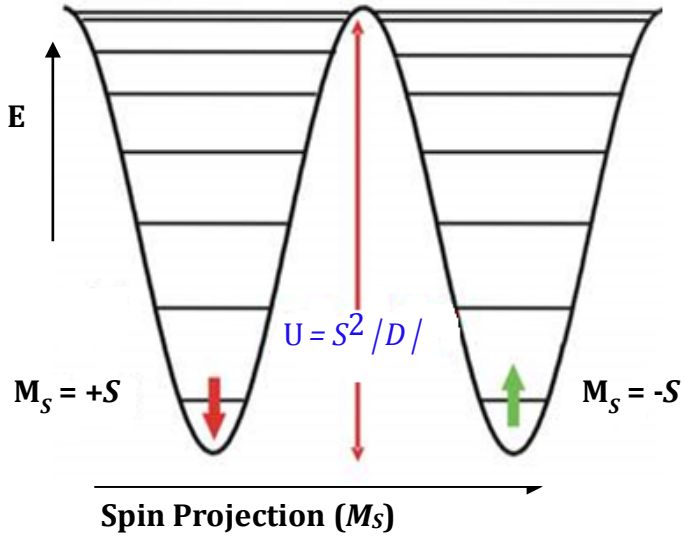

Figure 1.7 Schematic illustration of a transition metal based SMM system where the magnetization is aligned with the easy axis type of anisotropy. Modified from Ref. 19.

As previously mentioned, energy is required to reorient a spin from the "spin up" to the "spin down" state. Classically this occurs via molecules having sufficient thermal energy to cross over the energy barrier $|D|S^2$ *i.e.* for incremental realignment from $+M_S$ to $-M_S$ via the intermediate M_S states. If this energy barrier is too high then it is possible for the spin of an SMM to be magnetized in one

direction.[19] However, to date, very few SMMs possess desirable relaxation times due to the presence of fast relaxation processes in the low temperature region (*where* kT << $|D|S^2$) which occur via quantum tunneling mechanisms (QTMs) between M_S sublevels. Such QTMs occur when various $+M_S$ and $-M_S$ levels are degenerate and molecules relax via passing through, rather than over the energy barrier. The rate of tunneling depends on the M_S levels and the transverse ZFS term, E which defines the anisotropy in the *xy* plane. When a magnetic field is applied, $H = (nDg)/\beta$ (where n is an integer), different M_S sublevels become degenerate and the electrons cross between these degenerate M_S states by undercutting the energy barrier. In this respect, the height of energy barrier U is reduced from U to U_{eff}, known as the effective energy barrier.[21] Over the past twenty years hundreds of novel SMMs have been developed and studied with particular attention paid to the relationship between the size of the energy barrier (U_{eff}), the total spin (S), and the magnetic anisotropy (D). To a large extent, progress in this field has been fueled by the race to achieve a large energy barrier U_{eff} by maximizing the ground state spin S, focusing on the synthesis and characterization of large polynuclear transition metal clusters, many of which have nanoscale dimensions and are prepared from single molecules via a 'bottom-up' approach.[24,20]

In 1993, the SMM comprised of a ferromagnetic dodecanuclear Mn_{12}-acetate cluster $[Mn_{12}O_{12}(CH_3COO)_{16}(H_2O)_4]$ (**1.1**) was reported, Figure 1.8(a).[25]

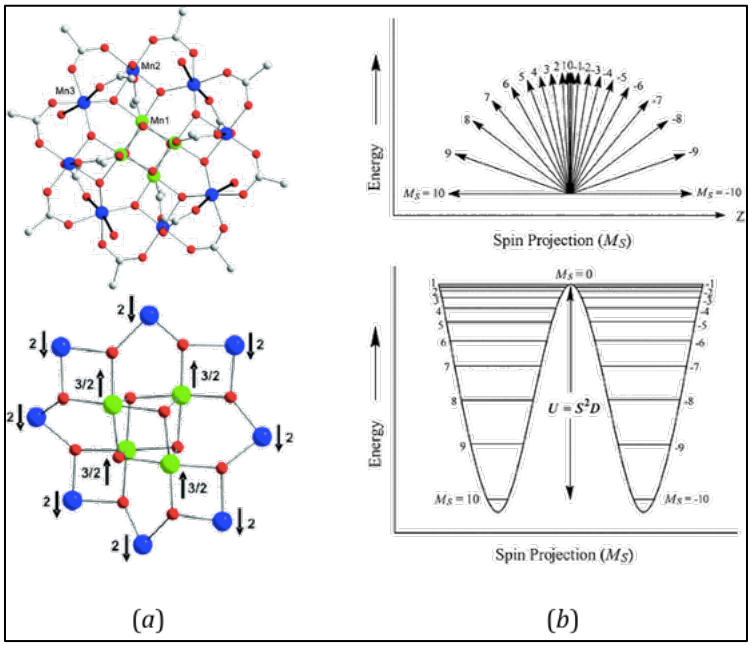

Figure 1.8 (a) (top) Core structure of $Mn_{12}Ac$ and (bottom) spin alignment in the ground state of $Mn_{12}Ac$ that gives S_T = 10. Color code: Mn(IV) green, Mn(III) blue, O red; (b) Two different views of the energy level diagram of the $Mn_{12}Ac$, illustrating the energy barrier S^2D for reversal of the magnetization. Reproduced with permission from Ref. 25.

For this complex, antiferromagnetic interactions between eight ferromagnetically coupled Mn(III) ions (S = 2, S_{local1} = 8 × 2 = 16) and four ferromagnetically coupled Mn(IV) ions (S = 3/2, S_{local2} = 4 × 3/2 = 6) result in a total ground state of S = 10, which is fully populated below 3 K. The *Jahn-Teller* distortion of eight Mn(III) ions, together with spin-orbit interactions contribute significantly to the magnetic anisotropy of this complex, giving rise to a negative ZFS parameter D of -0.50 cm^{-1} and an anisotropy barrier U_{eff} of 51 cm^{-1} below a blocking temperature T_B of 3 K. For this complex, the barrier is between the "spin up" M_S = -10 and "spin down" M_S = +10 orientations of the magnetic moment, Figure 1.8(b). Since the selection rule for the change in M_S states only allows for a change of ± 1 then

electrons have to move up each subsequent microstate in order to overcome the energy barrier towards reorientation of their magnetization.

The incredible success of $Mn_{12}Ac$ fueled the discovery of several families of manganese-based SMMs, all of which have been extensively studied.[26–35] As previously mentioned, the initial approach to synthesizing high energy barrier transition metal SMMs focused on maximizing the total spin S by targeting the synthesis of high nuclearity clusters comprised of many paramagnetic transition metals. However, this approach is not without its drawbacks for example, the mixed valence manganese cluster $[Mn^{III}_{12}Mn^{II}_{7}(\mu_4\text{-}O)_8(\mu_3,\eta_1N_3)_8(HL)_{12}(MeCN)_6]Cl_2\cdot 10MeOH\cdot MeCN$ (H_3L = 2,6-bis(hydroxymethyl)-4-methylphenol) (**1.2**), reported by Powell *et al*. has a very large S = 83/2 ground state arising from ferromagnetic interactions between 12 ferromagnetically coupled Mn(III) ions (S = 2, S_{local1} = 12 × 2 = 24) and 7 ferromagnetically coupled Mn(II) ions (S = 5/2, S_{local2} = 7 × 5/2 = 35/2 (Figure 1.9).[36]

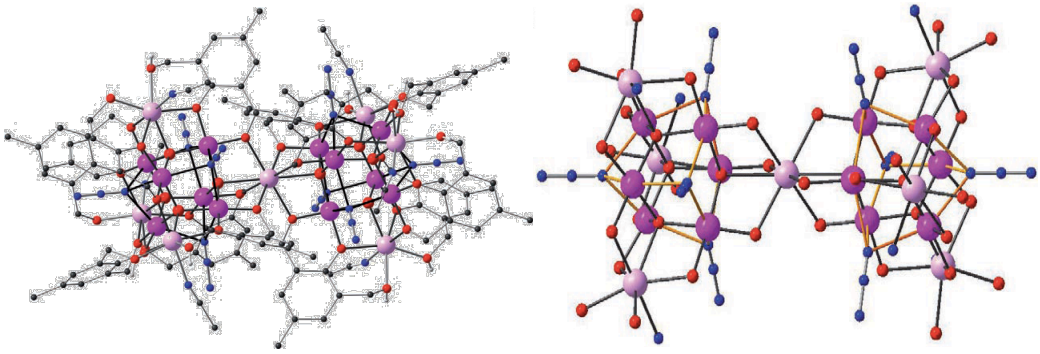

Figure 1.9 Molecular structure of Mn_{19} (left) and core structure (right). Colour scheme: Mn(III) purple, Mn(II) pink, O red, N blue, C black, H white. Reproduced with permission from Ref. 36.

Unfortunately, despite its large S value, the complex possesses only a very small energy barrier, U_{eff} = 4 cm^{-1} resulting in the observation of no SMM behaviour.[36]

Two factors have been proposed to account for the small U_{eff} of this complex. The first is due to the structural arrangement of the magnetic centers or more specifically, to the alignment of the local anisotropy axes. In other words, the magnetic anisotropy in transition metal clusters is very sensitive to the alignment of the *Jahn-Teller* axes, and it is more likely to decrease with increasing nuclearity if there is a misalignment of the local anisotropy axes. The second factor arises from the fundamental theoretical expression that is used to determine the energy barrier, $U_{eff} = |D|S^2$, suggesting that the height of the energy barrier is a function of S. However, this is not exactly as it appears since according to the exact eigenstates of the Born-Oppenheimer Hamiltonian, $|D|S^2$ is independent of S, implying that the discovery of an SMM with a large U should not be pursued solely by increasing S.[22] In order to overcome this issue, over the last decade researchers have started to focus more on developing design strategies that maximize the magnetic anisotropy term, D. This has afforded a second family of SMMs for which paramagnetic transition metals are often replaced by lanthanide ions affording a new families of mono- and polynuclear Ln-SMMs, several of which display very large energy barriers for the reversal of their magnetization.[22]

1.3.2 Lanthanide-based SMMs

Unlike most first row transition metals, lanthanide (Ln) ions possess a large unquenched orbital angular momentum L, which gives rise to large magnetic

anisotropy due to spin-orbit coupling (SOC), a process by which the magnetic fields generated from S and L interact.[37] The electronic states of Ln(III) ions are referred to as term symbols $^{2S+1}L_J$ according to Russell-Saunders coupling scheme, where S is the spin multiplicity ($2S$ +1), L is the orbital angular momentum, and J is the total angular momentum. Ligand field effects in Ln(III) complexes are small but perturb the energy levels which splits the $^{2S+1}L_J$ level into $2J$ +1 sublevels (or 'Stark' levels), each with a quantum number M_J whose maximum values do not necessarily lie lowest in energy, Figure 1.10. Moreover, the large ground states S of transition metal SMMs are due to the interaction between spins localized on different metal centers.

In contrast, the large ground state J of Ln-SMMs originate from the individual metal ions, since their *f*-orbitals are radically contracted and thus any exchange interactions between neighboring Ln-centers are extremely weak. Those Ln(III) ions most commonly used for the preparation of SMMs include Dy, Ho, Er, and Tb, Table 1.1. Of these four, Dy(III) and Er(III) are Kramers ions, which implies that they have an odd number of *f*-electrons leading to a bistable ground state, regardless of their ligand field symmetry.

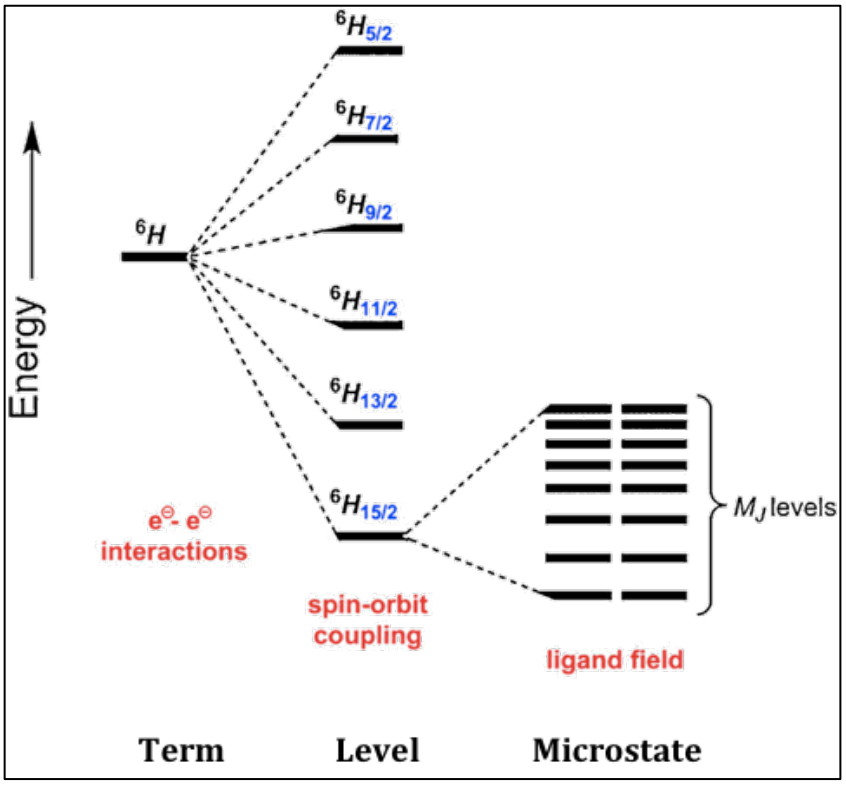

Figure 1.10 The splitting of the ^6H_J levels of a Dy(III) ion by spin orbit coupling and ligand field. Only the M_J microstates of the lowest energy $^6H_{15/2}$ level are shown.[21]

In contrast, Ho(III) and Tb(III) are non-Kramers ions and thus complexes prepared from these ions require the appropriate ligand field symmetry to exhibit bistable ground states since it is possible for the $M_J = 0$ level to be the ground state.[17]

Table 1.1 The four most common Ln(III) ions used for the synthesis of SMMs.[17]

	Non-Kramers ions		**Kramers ions**	
	Tb(III)	Ho(III)	Dy(III)	Er(III)
4*f*	$4f^8$	$4f^{10}$	$4f^9$	$4f^{11}$
Spin-orbit ground term	$^7F_6$	$^5I_8$	$^6H_{15/2}$	$^4I_{15/2}$
Free-ion *g*-value	3/2	4/3	5/4	6/5

Due to its odd number of electrons and its high intrinsic anisotropy, Dy(III) is currently the most well exploited lanthanide ion in the field of SMMs.

The approach currently adopted for the synthesis of Ln-SMMs is to employ appropriate ligand field symmetry in order to enhance their single-ion anisotropy. In this respect, Long *et al.* proposed that the type of ligand field that enhances this anisotropy is based on the shape of the 4*f* electron density of the Ln(III) metal ion in the ground state.[38] These shapes can either be oblate (*i.e.*, extended in the *xy* plane), prolate (*i.e.,* elongated along the *z*-axis), or isotropic (spherical), Figure 1.11. In order to obtain a highly anisotropic ground state with a large $\pm M_J$ for a prolate ion such as Er(III), the electron density should expand equatorially in the *xy* plane, while for the oblate ions such as Dy(III), Tb(III), and Ho(III), the ligand electron density should be placed above and below the *xy* plane. For this reason, double-decker or sandwich type structures with square antiprismatic geometries are often preferred for Dy(III) ions in order to maximize their axial anisotropy.[38]

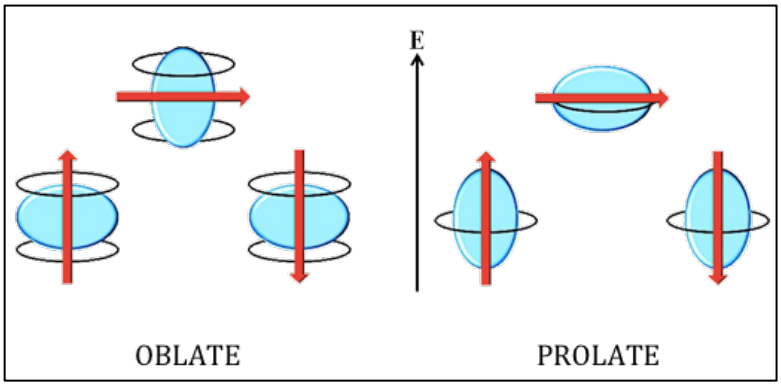

Figure 1.11 Schematic illustration of the low and high-energy configurations of a 4*f* ion of oblate (left) and prolate (right) electron density in a crystal field environment. The blue ovals represent electron density, the black circles represent ligand electron density, and the red arrow represents the orientation of the projection of the spin orbit coupled *J* state. Adapted from Reference 38.

In 2003, Ishikawa *et al*. reported the first mononuclear SMM, a $[Bu_4N][Pc_2Ln]$ complex (**1.3**) where Pc = phthalocyanine, comprising of a single Dy(III) or Tb(III) ion. The Ln(III) ions were sandwiched between two tetradentate $[Pc]^{2-}$ ligands, with four nitrogen atoms from each ligand coordinating to the metal, giving rise to an 8-coordinate square antiprismatic geometry with a double-decker structure, Figure 1.12.[39]

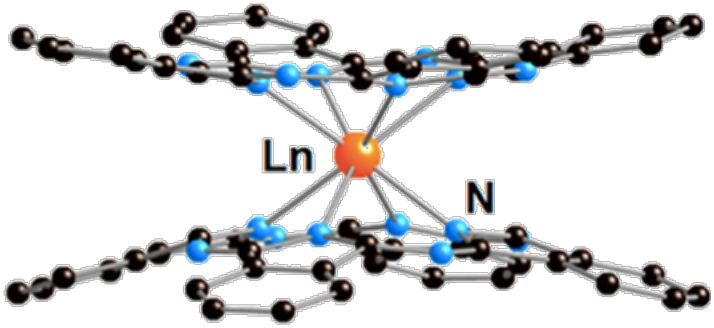

Figure 1.12 Molecular structure of the double decker $[Pc_2Ln]^-$ complex. Colour scheme: Ln(III) ion orange; N blue; C black. Hydrogen atoms are omitted for clarity. Reproduced with permission from Ref. 39.

The Tb(III) complex, has an extremely large energy barrier U_{eff} of 566 cm^{-1}, representing a significant improvement when compared to the energy barriers reported previously for polynuclear transition metal SMMs. This work initiated an insurgence in the preparation and study of Ln-SMMs, particularly with respect to the design of Ln-SMMs with sandwich type topologies.

Regarding design strategies for SMMs, three factors must be considered: (i) the type of metal ion employed (ii) the symmetry of the resulting complex and/or (iii) the class of ligand. The selection of the primary organic ligand is essential because this often governs not only the symmetry of the final complex, but also the

topology, the number of paramagnetic metal ions present and the nature of the intramolecular magnetic-exchange interactions, which as mentioned previously is particularly important for SMMs assembled from transition metal ions.[40]

1.3.3 Characterizing SMM Behaviour

The magnetic properties of SMMs are typically characterized by alternating-current (*ac*) measurements employing a conventional SQUID (superconducting quantum interference device) or a PPMS (physical property magnetic system) magnetometer. These *ac* measurements are often measured both in the absence of and/or in the presence of an applied static (*dc*) field. One of the most useful features of an *ac* susceptibility measurement is that both the in-phase (or real component) χ', and the out-of-phase (or imaginary component) χ'' can be measured. They can be written as:

$$\chi' = \chi\cos\varphi \qquad \textbf{(Eqn 1.13)}$$

$$\chi'' = \chi\sin\varphi \qquad \textbf{(Eqn 1.14)}$$

where χ' is a measure of energy dispersed by the sample from the applied *ac* field, χ'' is a measure of energy absorbed by the sample from the applied *ac* field, and φ is the phase shift, which is due to the lag of the magnetization caused by an energy barrier in an oscillating magnetic field. In low oscillating *ac* fields, the system has ample time to relax (via thermal or quantum tunneling mechanisms) and the magnetization follows the applied field; $\chi' = \chi$ and $\chi'' = 0$. However, at higher *ac* frequencies there is insufficient time for the magnetization to 'follow' the applied oscillating field and a clear out-of-phase component in the *ac* susceptibility is

observed and is a specific trait of the slow magnetization relaxation behaviour of an SMM, Figure 1.13.

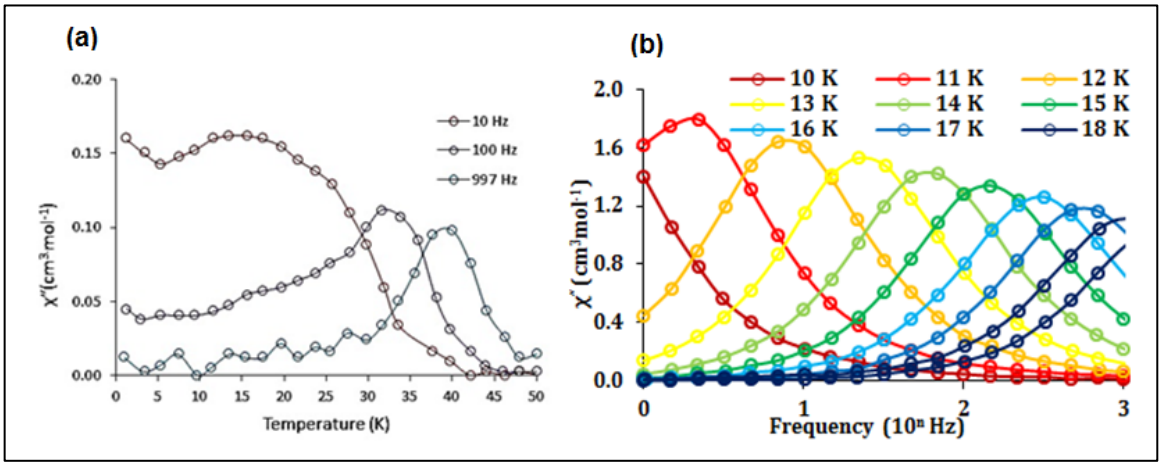

Figure 1.13 The temperature and frequency dependence of the out-of-phase (χ'') of the susceptibility of $[Bu_4N][Pc_2Dy]$ (a) and $[K(18\text{-crown-}6)][\{[(Me_3Si)_2N]_2Dy(III)(THF)^2\}(\mu\text{-}\eta^2\text{:}\eta^2\text{-}N_2)]$ (b) at the temperatures and frequencies indicated.[39,41]

From the plots of χ'' *vs.* T, SMM behaviour can be observed through the change in position of the maxima as a function of temperature at different frequencies (Fig. 1.13a), or as a function of frequency at different temperatures (Fig. 1.13b). Since the out-of-phase component of the susceptibility is associated with the relaxation rate of magnetization, the energy barrier to magnetization reversal U_{eff} can be quantified by an Arrhenius-type relationship for the thermally activated region defined as:

$$\tau = \tau_0 e^{(U_{eff}/kT)} \qquad \textbf{(Eqn 1.15)}$$

where τ is the relaxation time at a given temperature, τ_0 is the pre-exponential factor, and k is the Boltzmann constant. An Arrhenius plot can then be constructed by plotting $\ln(\tau)$ *vs.* $1/T$, yielding a straight line for which the slope gives the value of the effective energy barrier, U_{eff}.[17]

1.4 Multifunctional Materials

Following the discovery of diverse families of molecule-based magnets, the challenge to discover novel combinations of properties within one single material has intensified. These materials are prepared by combining unique magnetic properties together with at least one additional physical property such as conductivity,[42] chirality,[43] and luminescence,[40] which could ultimately lead to new materials. To date, there are several examples of multifunctional SMMs reported in the literature.[44] The introduction of chirality into magnets opens up new opportunities for their potential applications in the field of multiferroics, including memory and logic devices due to their capacity to encode information in both electric polarization and magnetization.[45,46,47] In order for materials to exhibit ferroelectric properties, they need to have molecular structures that crystallize in non-centrosymmetric, polar or 'chiral' point groups (1, 2, 3, 4, 6, *m*, *mm*2, 4*mm*, 3*m*, 6*mm*).[47] The co-existence of magnetism and chirality in molecular materials is also of great interest in the study of both circular dichroism (CD) and magnetochiral dichroism (MChD) (see below).[44]

1.4.1 Chirality

The term chirality is generally understood to mean that a molecule has a non-superimposable mirror image, leading to a pair of structural enantiomers. Most chiral molecules can be identified by their lack of a plane of symmetry (mirror plane, σ) and/or an inversion center, *i*.[48] In this case, the two enantiomers have the same connectivity, but differ in their spatial arrangement of atoms, which is also

often referred to as "structural chirality", Figure 1.14.[49] In coordination chemistry, structural chirality can be introduced as a consequence of the spatial arrangement of chelating ligands around a transition metal ion for example, the *tris*(bidentate) complex of an octahedral metal ion, gives rise to delta (Δ) and lambda (Λ) enantiomers, Figure 1.15.

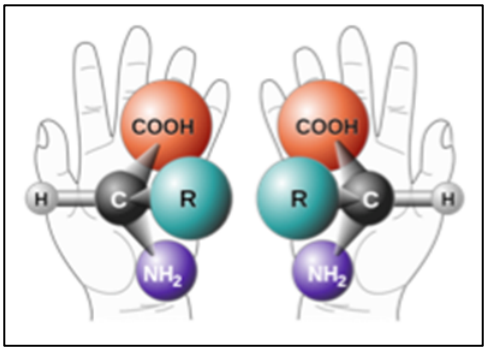

Figure 1.14 Depiction of chirality with hands and two enantiomers of a generic amino acid molecule. Reproduced with permission from Ref. 49.

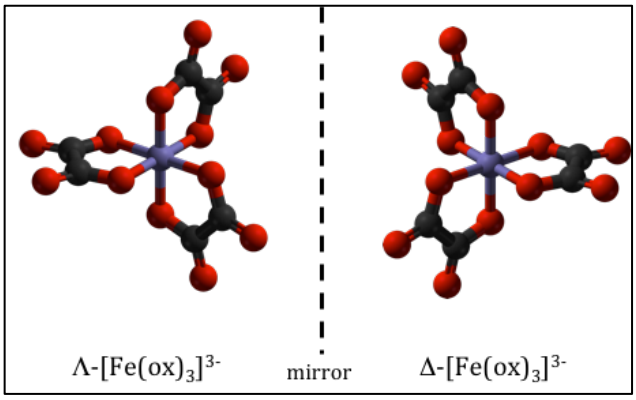

Figure 1.15 Two enantiomers of *tris*(oxalato)ferrate(III) complex exist as lambda (Λ, left-handed propeller twist) and delta (Δ, right-handed propeller twist).[50]

The beauty of a chiral molecule is that its two mirror images with two absolute configurations can exhibit interesting properties arising from their

differences with respect to the rotation of a plane of linearly polarized light, Figure 1.16.[16]

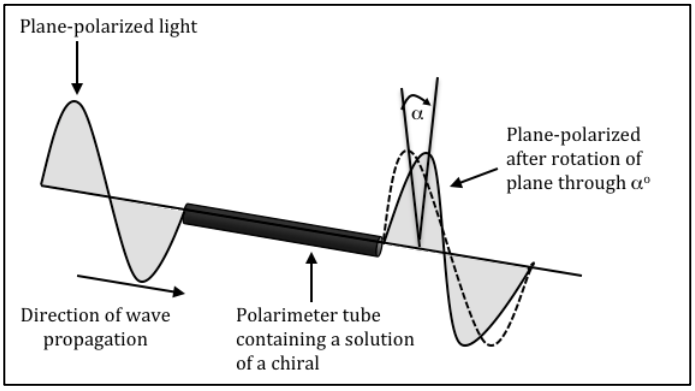

Figure 1.16 Schematic representation of one of the enantiomers of a chiral molecule that rotates the plane of linearly polarized light through an angle α^{o} (a positive α^{o} indicates clockwise direction and a negative sign indicates anticlockwise direction). Adapted from Ref. 16.

Optical activity is the interaction of chiral molecules with polarized light. In this context, enantiomers absorb and rotate right-and-left-handed circularly polarized light with opposite yet equal amplitudes. In fact, the extent and sign of the rotation depends on the wavelength of the incident light, the temperature at which the sample is measured, its solvent and concentration.[16]

"Magnetic chirality" is analogous to structural chirality but the considered property is a set of magnetic moments which are not superimposable on its mirror images, Figure 1.17.[3] Within a triangular topology, the magnetic moments are commonly arranged in a 120^{o} manner in order to best accommodate the frustration associated with a triangular antiferromagnetically coupled spin lattice, Figure 1.17(a). In the case of Figure 1.17(b), the spin rotates from one site to another by an angle $+\theta$, depending on the magnetic enantiomer.

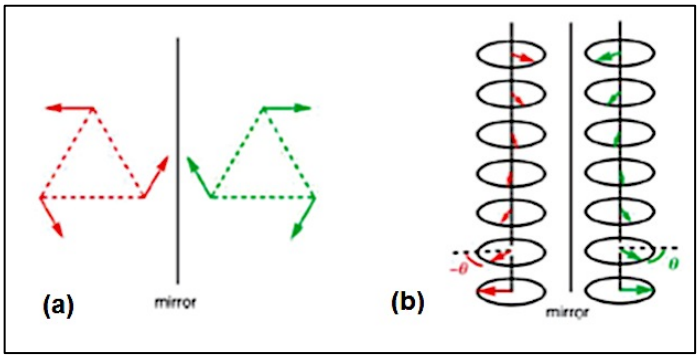

Figure 1.17 (a) Chirality of magnetic moments can be found in a frustrated antiferromagnetically coupled triangular lattice (a) and a helical arrangement (b). Reproduced with permission from Ref. 3.

With respect to studying the physicochemical properties of chiral magnets, the main goals are to investigate whether the enantiopurity of the chiral system has any influence on its magnetic properties. Depending on the class of magnetic compounds studied, several types of magnetic properties are exhibited that include long range magnetic ordering, single molecule magnetism, single chain magnetism, spin crossover properties as well as antiferromagnetic and paramagnetic behaviour.[45] Detailed studies on all of these systems are currently in progress in order to establish a link between their magnetic and chiral properties and identify the parameters that govern it. To-date such studies have afforded chiral magnets that possess ferroelectric properties[51,52] as well as compounds which display magneto-chiral dichroism.[53]

1.4.2 Molecule-based Multiferroics

Multiferroics were first proposed by Pierre Curie[54] and then practically discovered in the 1960s.[55] Very recently, numerous reports concerning magnetic

ferroelectrics have marked a renaissance of research interest in this field.[55] In multiferroic materials, the coupling between the magnetic and electrical order parameters can produce a magnetoelectric effect. This effect arises from the induction of magnetization in the presence of an electric field and/or the induction of polarization in the presence of a magnetic field. The magnetoelectric effect can be observed in single-phase materials, which exhibit two or more ferroic properties in the same phase, such as ferroelasticity (materials exhibit a spontaneous deformation by means of an applied stress), ferromagnetism, and ferroelectricity.[56] In order for material to be a ferroelectric, it must be polar, possess a permanent dipole moment, and be capable of having this moment reversed in the presence of an applied voltage.[51] Spontaneous polarization occurs if the material crystallizes in one of ten polar crystal classes (1, 2, 3, 4, 6, *m*, *mm*2, 3*m*, 4*mm*, or 6*mm*). Polarization reversal, or ferroelectric hysteresis may be measured through a Sawyer-Tower circuit.[51] Ferroelectric behaviour is typically observed via a polarization *vs.* applied voltage plot called a ferroelectric hysteresis loop, Figure 1.18.[51] There are several important features of the loop: (i) spontaneous polarization ($+P_S$) is the linear extrapolation of the curve back to the polarization axis; (ii) remnant ($+P_r$) polarization occurs when some dipole moments remain aligned as the applied voltage is decreased from its maximum positive value to zero. $-P_S$ and $-P_r$ are also observed when the applied voltage spans the range from its maximum positive to negative values; (iii) the electric coercive field (E_C) is the magnitude of an applied voltage required to remove all the polarization in the material and (iv) the shape of the loop: in this context, 'banana', non-linear, and linear-shaped loops indicate

ferroelectric, paraelectric and dielectric materials, respectively. Structurally, all of the dipole moments have switched from the positive (↑ arrow) to negative (↓ arrow).[51,52]

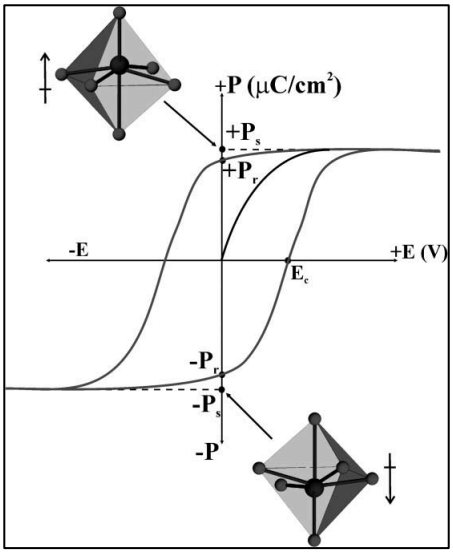

Figure 1.18 Ferroelectric hysteresis loop for a perovskite oxide (ABO_3) unit-cell structure, with A = Pb^{2+}, La^{3+}; B = Zr^{4+}, Ti^{4+} and O = O^{2-}. Reproduced with permission from Refs. 51 and 52.

In 1966, the first ferromagnetic ferroelectric material reported was nickel iodine boracite,[57] $Ni_3B_7O_{13}I$, with ferroelectricity that arises from its distorted iodine-oxygen octahedron, that was then followed by the first synthetic multiferroic material, a ferroelectric Perovskite containing Fe(III).[58] Since then, Perovskite oxides have been the most exploited family of multiferroic materials, which are simultaneously ferromagnetic and ferroelectric, with or without ferroelasticity.[58] Initial attempts to realize molecular multiferroics, afforded two compounds, $Rb(I)_{0.82}Mn(II)_{0.20}Mn(III)_{0.80}[Fe(II)(CN)_6]_{0.80}[Fe(III)(CN)_6]_{0.14}\cdot H_2O$ (**1.4**),[59] and $(C_2H_5NH_3)Cu(II)Cl_4$ (**1.5**)[60] that have been thoroughly investigated, Figure 1.19.

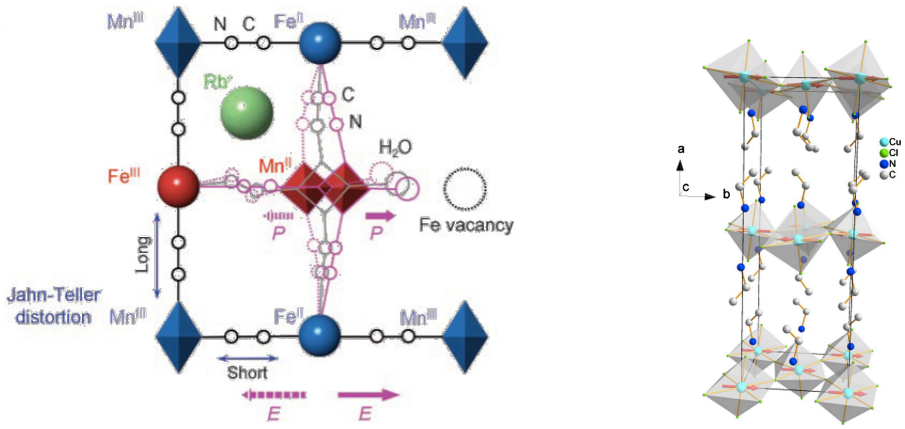

Figure 1.19 Schematic view of crystal structures of **1.4** (left), and **1.5** (right). Reproduced with permission from Ref. 59 and 60.

The parallel ordering of the magnetic spins of the Mn(III) centers in the rubidium manganese hexacyanoferrate complex (**1.4**) afforded ferromagnetic properties. The ferromagnetic behaviour was characterized by a M *vs.* T plot with a Curie temperature of 11 K, and the presence of a magnetic hysteresis loop with a coercive field of 800 Oe, Figure 1.20(a). Ferroelectricity was observed due to the presence of a ferroelectric hysteresis loop with P_r = 0.041 μCcm^{-2} and E_c = 17.5 kVcm^{-1}, Figure 1.20, right. In **1.4**, a local electric dipole moment is created due to an Fe vacancy as well as the difference in ionic radii among four metal ions and Mn(III) *Jahn-Teller* distortion which enhance the local structural distortion. Thus, a spontaneous polarization can be induced in such a distorted structure that is held by the structural flexibility of the cyano-bridged 3-D network. As a consequence, the ferroelectricity of the compound is related to a superposition of the mixing of Fe(II), Fe(III), Fe vacancy, Mn(II), and *Jahn-Teller* distorted Mn(III) ions in the compound, Figure 1.20(b).[59]

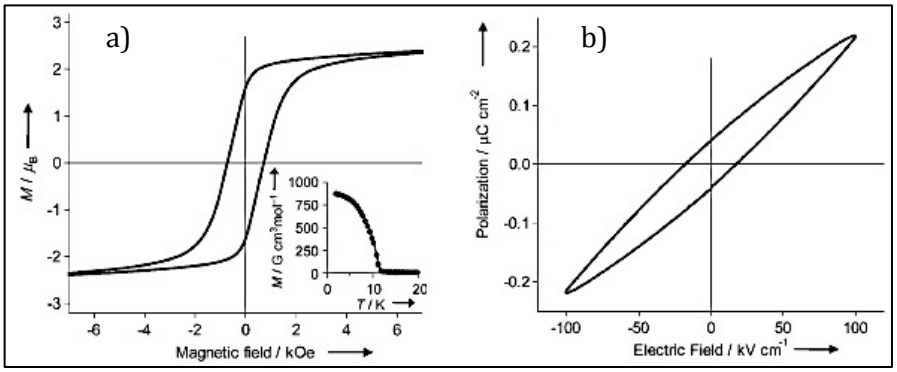

Figure 1.20 *M*-*H* hysteresis loop (inset: *M vs. T* plot) (a) and *P* vs. *E* plot (b) of **1.4**. Reproduced with permission from Ref. 59.

Compound **1.5** crystallizes in a layered Perovskite topology, in which adjacent layers of corner-sharing copper chloride octahedra are stacked directly over one another stabilized via *van der Waals* interactions between terminal alkylammonium cations. In the Perovskite structure, the choice of hydrogen-bonding pattern is essential for determining the orientation and conformation of the organic molecules, as well as the temperature of the structural phase transitions. In this complex, the ammonium heads (NH_3^+) of the organic cations form strong N-H···Cl hydrogen bonds to the chloride ions, giving rise to a reorientational disorder of the H-bonding pattern which is the origin of its ferroelectric properties.[60] The temperature dependence of the magnetization for this compound revealed that it behaves as an antiferromagnet due to weak interactions between the layers with T_c = 10.2 K, which was previously studied by de Jongh *et al.*[61] In 2010, this compound was reported to exhibit ferroelectric properties through the presence of a ferroelectric hysteresis loop at 77 K with P_s = 37 μCcm^{-2} and E_c = 10 kVcm^{-1}, Figure 1.21. The ferroelectricity was assigned to the spontaneous reorientation of the

hydrogen bonding patterns, as the cation motion gradually "freezes" when the crystal is cooled down.[60]

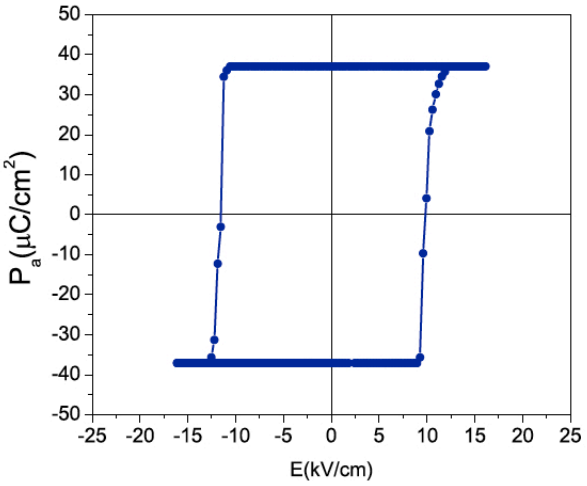

Figure 1.21 Ferroelectric hysteresis loop for $(C_2H_5NH_3)Cu(II)Cl_4$ (**1.5**). Reproduced with permission from Ref. 60.

An alternative strategy to prepare a ferroelectric material is to employ a chiral building block since chiral materials also crystallize in non-centrosymmetric space groups. In the last decade, the quest for new ferromagnetic and ferroelectric materials for novel devices has led to an increase in research activity in this area in particular with respect to the discovery and study of chiral SMMs with ferroelectric properties (see later in Section 1.5.1).

1.4.3 Magneto-Chiral Dichroism

The discovery of molecule-based materials with magnetic and optical properties is also important from the perspective of studying synergistic interactions between the two properties such as magneto-chiral effects. In this context, magneto-chiral dichroism (MChD) was first observed by Rikken and Raupach in 1997, after the discovery of MChD in a chiral paramagnet.[53] It was

predicted that if a light beam travels parallel or antiparallel with respect to an applied magnetic field, then for two enantiomers of a chiral molecule this light would be absorbed slightly differently.

This was later demonstrated to be the case for a chiral molecule-based oxalate system. The oxalate ligand, $C_2O_4^{2-}$ (or ox^{2-}) has been well known for decades due to its capacity to bridge two metal centers affording significant exchange interactions. When all of the metal ions are *tris*-chelated by oxalate ions, compounds of general formula $C^{n+}[MM'(ox)_3]^{n-}$ are obtained. The cationic counterpart C^{n+} (n = 1, 2) templates the formation of either 2- or a 3-D coordination networks.[45] In the 3-D networks, two metal sites adopt the same (Δ or Λ) configuration and the cationic counterpart fills the vacancies of the anionic network. In contrast, in the 2-D networks, the cationic counterpart is located between the anionic layers; within each layer, M' sites have the same chirality (Δ or Λ), while M sites adopt the opposite configuration.[62] The enantioselective self-assembly of 3-D networks by *tris*(oxalato)ruthenium(II) complexes[63] have been studied, in which the absorption of the templating cation dominates the compounds' optical properties, preventing the observation of the MChD arising from the anionic network. The 3-D oxalate networks reported to date are less interesting than the 2-D networks despite the fact that the enantioselective self-assembly of 2-D anionic networks are harder to rationalize and to carry out. The reason is because the adjacent metal centers within the 2-D anionic layers have alternate Δ- and Λ-configurations. The 2-D systems have a heterochiral arrangement, such as (ΔM, ΛM') or (ΔM, ΛM'), in which the chiral or achiral cation plays the role of a template.[64] In 2008, Train *et al*.

reported two enantiomers of a 2-D bimetallic oxalate-based material of stoichiometry, $[N(CH_3)(n\text{-}C_3H_7)_2((S)\text{-}s\text{-}C_4H_9)][\Lambda MnA Cr(ox)_3]$ (**1.6**) and $[N(CH_3)(n\text{-}C_3H_7)_2((R)\text{-}s\text{-}C_4H_9)][\Delta MnA Cr(ox)_3]$ (**1.7**), Figure 1.22. Both enantiomers are assembled from a chiral organic templating $[N(CH_3)(n\text{-}C_3H_7)_2(s\text{-}C_4H_9)]^+$ cation and a racemic *tris*(oxalato)chromate(III) $[Cr(ox)_3]^{3-}$ anion, and crystallize as a chiral ferromagnet with magnetic and optical properties that are designed to enhance large magnetochiral dichroism in the ferromagnetic phase, with equal and opposite signals for the two enantiomeric forms. In the paramagnetic phase, a weak dichroism is observed, Figure 1.23 (left). The MChD, increases gradually through the paramagnetic-to-ferromagnetic transition, when approaching the Curie temperature of 7 K, then increases by a factor of 17 between 11 K and 3 K, closely following the thermal variation of the magnetization, Figure 1.23 (right).[45]

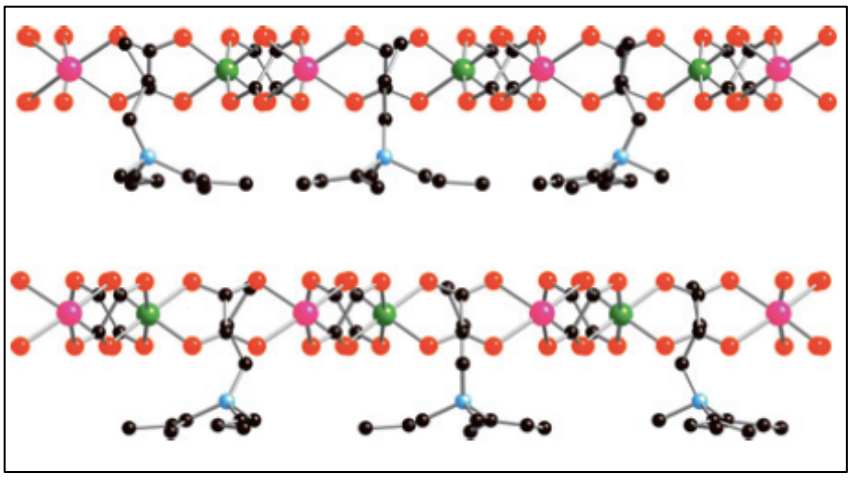

Figure 1.22 Projection of the crystal structure of **1.6** along the [010] direction. Reproduced with permission from Ref. 45.

This result suggests that the magneto-chiral effect is independent of the polarized light and thus has opposite signs for the two enantiomers. MChD arises

from the interplay of chiral and magnetic effects on the molecular optical properties. The magneto-chiral effect can be optimized if the chiral molecule itself is ferromagnetic.[65,66]

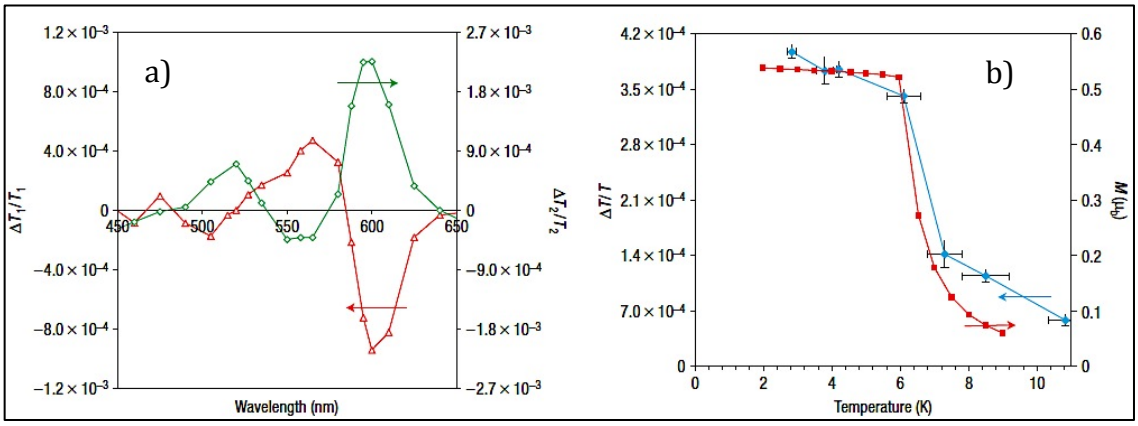

Figure 1.23 a) Inversion of the MChD with the enantiomer at 4 K for **1.6** (triangles) and **1.7** (diamonds). b) Enhancement of MChD at the Curie temperature of **1.6**, with temperature dependence of the MChD effect (diamonds) and field-cooled magnetization (squares). Reproduced with permission from Ref. 45.

Within the field of molecular magnetism examples of chiral complexes that display magneto-chiral dichroism are still very rare to date.

1.5 Synthetic Approaches to Chiral Magnets

The five strategies most commonly employed for the synthesis of chiral molecule-based magnets are the following:[3]

i. spontaneous resolution starting from achiral building blocks;

ii. employment of chiral ligands bearing unpaired electrons (chiral radicals);

iii. employment of chiral bridging ligands from a chiral pool;

iv. associate a chiral co-ligand with achiral connectors to build chiral extended networks; and

v. master the configurations of intrinsically chiral networks by enantioselective self-assembly.

The versatility of molecular chemistry, along with each of these strategies, has provided chemists with all of the appropriate tools necessary to work towards the challenging synthesis of chiral magnets. In this context, four classes of compounds have been investigated that include Prussian Blue derivatives,[67–69] oxalate-based chiral magnets,[63,70–74] spin crossover compounds[75,76] and single molecule magnets, with most of the studies focusing on the Prussian Blue and oxalate systems that are outside the scope of this thesis. In the next section I will therefore review only the literature concerning the synthesis and study of chiral SMMs.

1.5.1 Chiral SMMs

The strategy most commonly employed for the realization of chiral SMMs is that of rational design, *i.e.* by employing enantiomerically pure building blocks. Although a few chiral molecular magnets have been synthesized following this strategy,[77,78] the literature includes only two reports of chiral SMMs.[79,80] In both reports, simple chiral carboxylate ligands were substituted for the acetate ligands of the original SMM, Mn_{12}-acetate,[25] affording (*R*)- and (*S*)-$[Mn_{12}O_{12}(O_2CCHClMe)_{16}(H_2O)_4]\cdot CHClMeCO_2H$ (*R*-**1.8** and *S*-**1.8**),[79] (*S*)-$[Mn_{12}O_{12}(O_2CCHMeC_{10}H_6OMe)_{16}]$ (**1.9**), and (*S*)-$[Mn_{12}O_{12}(O_2CHEtC_6H_5)_{16}]$ (**1.10**).[80] The magnetic behaviour of these complexes is very similar to that of Mn_{12}-acetate, and no magnetochiral effects were reported. CD spectra confirmed the presence of single enantiomers. In this context, the *R*-**1.8** complex exhibits positive Cotton

effects at λ_{max} = 520 and 260 nm and a negative dichroic signal centered at λ_{max} = 345 nm, while as expected, the *S*-**1.8** enantiomer shows Cotton effects of the opposite sign at the same wavelengths, Figure 1.24 (left).[79] The CD spectrum for complex **1.9** in solution exhibited Cotton effects between 500 and 400 nm, while the spectrum of **1.10** is the mirror image of **1.9**, but with a shift of *ca.* 30 nm to the blue, Figure 1.24 (right).[80]

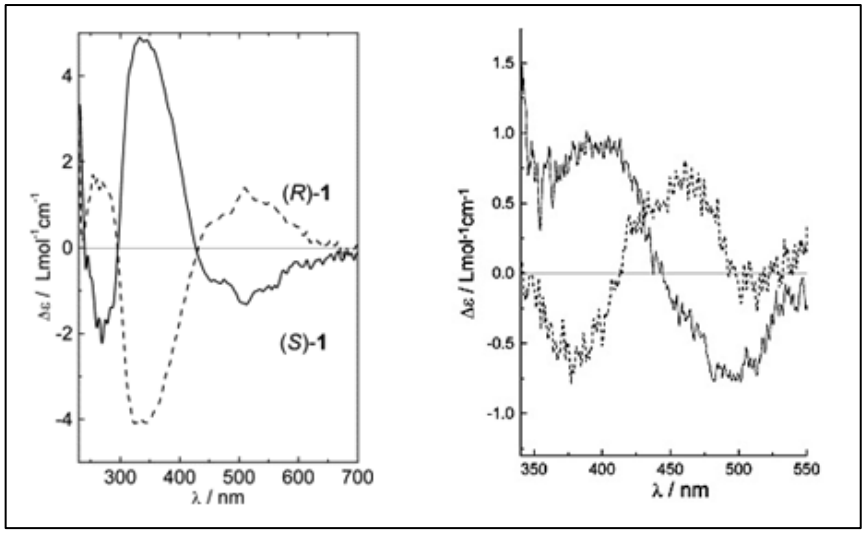

Figure 1.24 CD spectra of **1.8** (*R* and *S* isomers) (left) and **1.9** (solid line) and **1.10** (dotted line) in DCM (right). Reproduced with permission from Refs. 79 and 80.

In 2010, Zhu *et al.* reported reactions of 2-((*E*)-((*R*)-2,3-dihydroxypropyl-imino)methyl)-6-methoxyphenol (*R*-LH_3) and 2-((*E*)-((*S*)-2,3-dihydroxypropyl-imino)methyl)-6-methoxyphenol (*S*-LH_3) with $MnCl_2$ in the presence of NEt_3 which afforded the first nanoscale homochiral manganese clusters $\{[Mn(III)_3Mn(II)O(H_2O)_3(R\text{-}L)_3]_4[Mn(III)_6Cl_4O_4]\}[Mn(III)_3O(H_2O)_3(R\text{-}L)_3](OH)_4$ (*R*-**1.11a**) and $\{[Mn(III)_3Mn(II)O(H_2O)_3(S\text{-}L)_3]_4[Mn(III)_6Cl_4O_4]\}[Mn(III)_3O(H_2O)_3(S\text{-}L)_3](OH)_4$ (*S*-**1.11b**) displaying both ferroelectric and ferromagnetic properties.[81]

Single-crystal X-ray diffraction analyses showed that both enantiomers crystallize in the chiral space group *R*3 as C_3-symmetric structures comprised of a $\{Mn_{22}\}$ cation and a $\{Mn_3\}$ anion, Figure 1.25 (left). The $\{Mn_{22}\}$ cation comprises four $\{Mn(III)_3Mn(II)\}$ distorted cubane subunits that are linked around a $[Mn(III)_6Cl_4O_4]^{6+}$ core via oxo bridges, generating a $[Mn(III)_6Mn(II)_4O_4]^{18+}$ supertetrahedron. There are also 15 chiral stereogenic centers from the 15 chiral Schiff-base ligands. As expected, the *R*-**1.11a** exhibits a strong positive Cotton effect at λ = 300 nm and a positive dichroic signal centered at 394 nm, while the *S*-enantiomer **1.11b** showed Cotton effects of the opposite sign at the same wavelengths, Figure 1.25 (right).

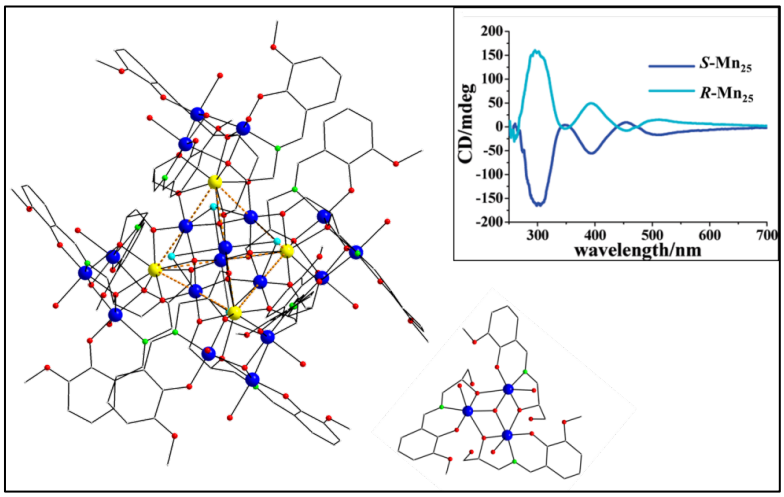

Figure 1.25 Crystal structure of cluster *R*-**1.11**. Color scheme: Mn(III) blue, Mn(II) yellow, N green, O red, C grey. H atoms are omitted for clarity. Inset: CD spectra of *R*- and *S*-**1.11** in MeOH at RT. Reproduced with permission from Ref. 81.

Magnetic and polarization studies were performed on the *R*-enantiomer **1.11a**. In this context, magnetic studies reveal a continuous increase of χT product, upon lowering the temperature indicative of predominantly ferromagnetic

interactions between the metal centers in the clusters and a large ground-state spin value, S_T, Figure 1.26a. Above 150 K, the χ^{-1} *vs.* T plot obeys the Curie-Weiss law with θ = 71.5 K and C = 71.4 emu·K·mol^{-1}. The ferroelectric behaviour of *R*-**1.11** was measured at room temperature affording an electric hysteresis loop, Figure 1.26b, with a remnant polarization (P_r) of 1.16 μCcm^{-2}, a spontaneous polarization (P_S) of 1.92 μCcm^{-2} and a coercive field (E_c) of 2.65 kVcm^{-2}.

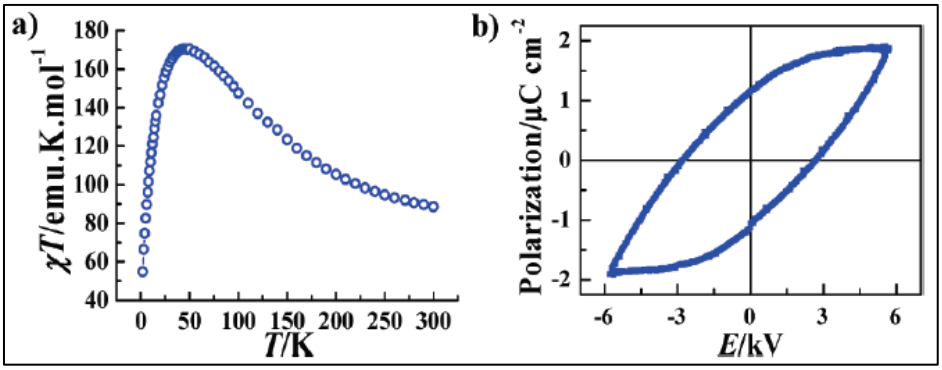

Figure 1.26 (a) Plot of χT *vs. T* for the *R*-**1.11** measured under a field of 1 kOe. (b) Electric hysteresis loop for a single-crystal of *R*-**1.11** at room temperature. Reproduced with permission from Ref. 81.

In 2011, Papaefstathiou and co-workers reported the first example of a chiral SMM of stoichiometry $[Mn_9O_4(OMe)_4(OAc)_3(Me\text{-}sao)_6(H_2O)_2]\cdot 1.5H_2O$ (**1.12**)[82] ($saoH_2$ = salicylaldoxime) assembled from achiral starting materials. The compound crystallizes in the cubic space group *I*23 and consists of a partial $\{Mn^{III}_9\}$ supertetrahedron, Figure 1.27.

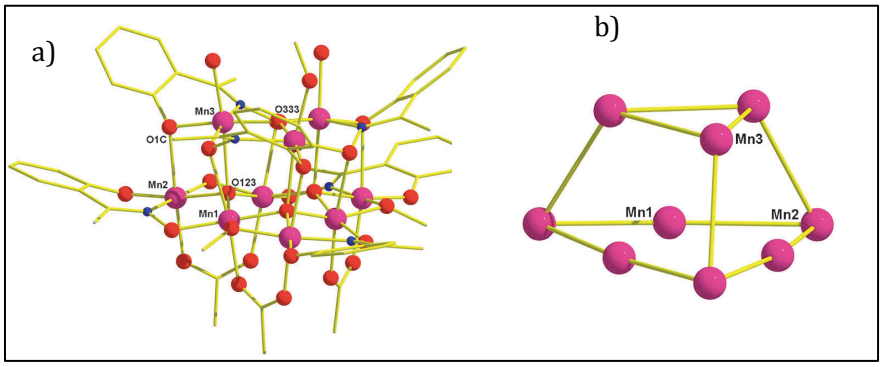

Figure 1.27 Molecular structure of **1.12** (left) and the core of the partial {Mn(III)$_9$} supertetrahedron (right). Colour code: Mn(III) purple, O red, N blue, and C gold. Reproduced with permission from Ref. 82.

Compound **1.12** exhibits frequency-dependent in phase (χ') and out-of-phase (χ") signals in the *ac* magnetic susceptibility below 3 K. A fit of the *ac* data to the Arrhenius equation gave an effective energy barrier U_{eff} of 30 K. The steps in the temperature-dependent and field sweep-rate-dependent hysteresis loops were indicative of QTM, further confirming its SMM properties, Figure 1.28.

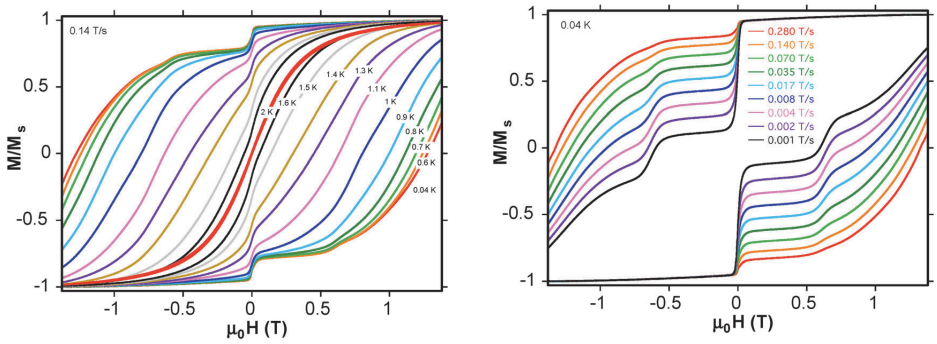

Figure 1.28 Plot of temperature-dependent magnetization *vs.* field hysteresis loops (left) and sweep-rate-dependent hysteresis loops (right) measured on single crystals of **1.12**. Reproduced with permission from Ref. 82.

In recent years, most of the research concerning chiral SMMs has focused on the development of lanthanide or mixed lanthanide-transition metal complexes for

applications as molecule-based multiferroic materials. In particular, a series of chiral clusters comprised of metallacrown (MC), and (*S*)- phenylalaninehydroxamic acid (or (*S*)-pheHA) ligands with stoichiometry {Ln(III)[15-MC$_{Cu}$(II)(N)(*S*)-pheHA-5]}$^{3+}$, where Ln(III) = Dy (**1.13**) and Ho (**1.14**), have been reported.[83] These complexes crystallize into two distinct polymorphs that have dimer and helix topologies respectively, Figure 1.29. The magnetic properties of the two complexes are very similar with both displaying a decrease in χT at low temperature due to the combined effects of strong spin-orbit coupling and ligand-field splitting of the ground state terms of the Ln(III) ions. Unfortunately, no magnetochiral effects were observed.

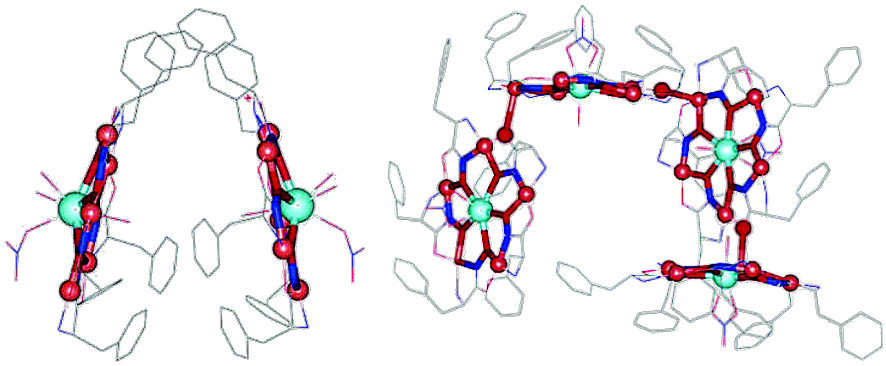

Figure 1.29 15-MC-5 complexes form a dimer (left) and a helix (right). Colour scheme: Ln(III) cyan, Cu(II) gold, C grey, O red, N blue. Reproduced with permission from Ref. 83.

As previously mentioned, when designing chiral SMMs, the choice of chiral ligand is an important consideration. With this in mind, Li and co-workers[47] chose to employ an enantiomeric pair of pyrazine ligands, (+)/(-)-2,5-bis(4,5-pinene-2-pyridyl)pyrazine (L_S/L_R, Figure 1.30 left), as linkers for the assembly of two clusters of stoichiometry [Dy(dbm)$_3$L$_{R/S}$]·2H$_2$O (*R*-/*S*-**1.15**, dbm = dibenzoylmethanato) and

$[Dy_2(dbm)_6L_{R/S}]\cdot 2H_2O$ (*R*-/*S*-**1.16**). Both enantiomers of *R*-/*S*-**1.15** and *R*-/*S*-**1.16** crystallize in the chiral space groups $P2_12_12_1$ and $P2_1$, respectively, confirming the transfer of chirality from the ligand to the resulting complexes, Figure 1.30 (right). The optical activity of these two pairs of complexes was confirmed by CD spectroscopy. In this context, the CD spectrum of *R*-**1.15** exhibited positive Cotton effects at λ = 250 and 330 nm and a negative dichroic signal at λ = 285 and 380 nm, while the *S*-enantiomer displays Cotton effects with opposite signs at the same wavelengths, Figure 1.31 (a).[47]

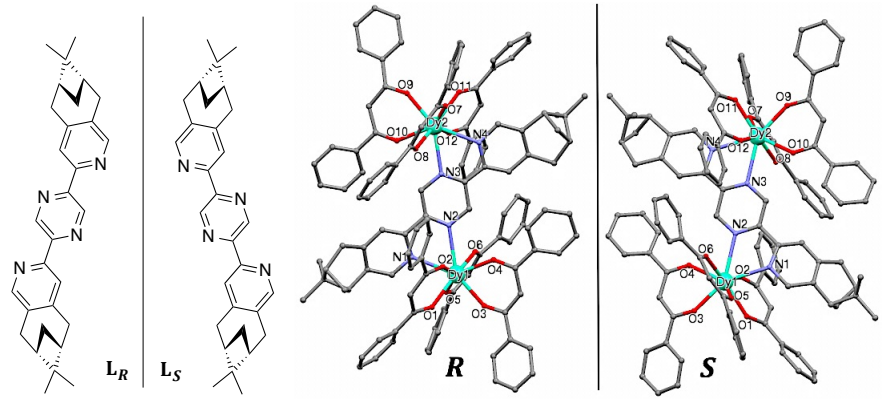

Figure 1.30 Left: Enantiomeric bridging ligands L_R and L_S. Right: Molecular structure of the enantiomeric pair of *R*-/*S*-complexes **1.16**. Colour code: Dy cyan; N blue; O red; and C grey.[47]

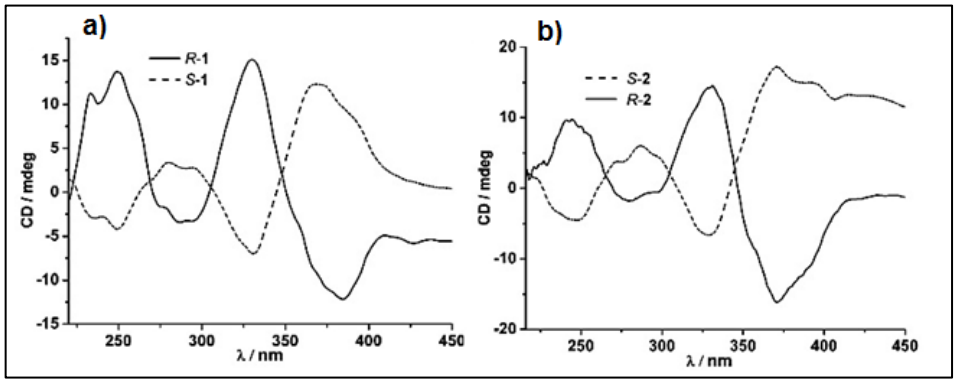

Figure 1.31 CD spectra of *R*-/*S*-**1.15** (a) and *R*-/*S*-**1.16** (b). Reproduced with permission from Ref. 47.

Magnetic susceptibility studies on both the *R*-**1.15** and *R*-**1.16** complexes reveal the presence of weak antiferromagnetic interactions between the Dy(III) ions, Figure 1.32(a).

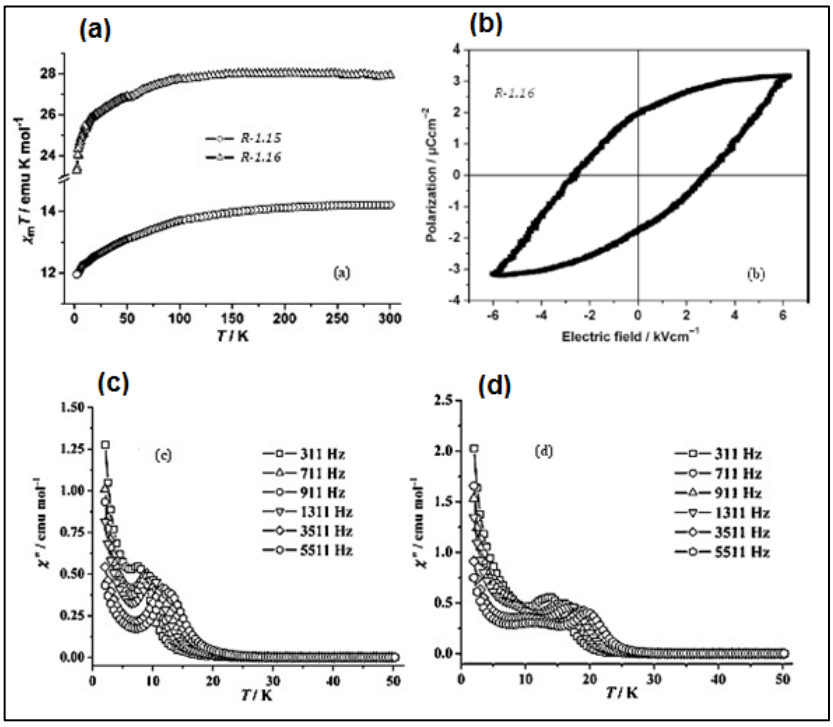

Figure 1.32 (a) Plot of $\chi_M T$ *vs.* T for the *R*-**1.15** and *R*-**1.16**, (b) electric hysteresis loop for *R*-**1.15** at room temperature, (c) temperature-dependence of the *ac* susceptibility for single crystals *R*-**1.15** and (d) *R*-**1.16**, at different frequencies under zero *dc* field. Reproduced with permission from Ref. 47.

The temperature dependence of the *ac* susceptibility for both compounds indicates slow relaxation of magnetization characteristic for an SMM, with the effective energy barriers U_{eff} of 46.91 and 89.16 K and $\tau_0 = 1.37 \times 10^{-7}$ and 5.9×10^{-8} s for *R*-**1.15** and *R*-**1.16**, respectively, Figure 1.32(c and d). *R*-**1.16** exhibits an electric hysteresis loop, Figure 1.32(b), indicative of its ferroelectric behaviour, with P_r of

1.8 μCcm^{-2}, P_S of 3.2 μCcm^{-2} and E_c of 2.9 kVcm^{-2}, whereas no such behaviour was observed for *R*-**1.15**.

SMM behaviour can be found in complexes comprising a single anisotropic lanthanide ion, which is often referred to as single-ion magnets (SIMs). These SIMs play a crucial role in elucidating the electronic structures of SMMs due to their accessible structure design and the simplification in the analysis of local anisotropy, when compared to the complexity of the polynuclear system. With this in mind, Lin and co-workers worked towards the design of chiral mononuclear macrocyclic lanthanide complexes by employing both enantiomers of the chiral macrocyclic ligand, $H_3L_{RRRRRR/SSSSSS}$, Figure 1.33(a) and studying the resulting magnetic properties of the complexes. Following this strategy, three pairs of enantiopure chiral macrocyclic complexes with stoichiometries $[LnH_4L_{RRRRRR/SSSSSS}(SCN)_2](SCN)_2{\cdot}xCH_3OH{\cdot}yH_2O$ (Ln = Dy, x = 5, y = 0 (*R*-**1.117**); Dy, x = 4, y = 1 (*S*-**1.17**); Ho, x = 5, y = 0 (*R/S*-**1.18**) and Er, x = 5, y = 0 (*R*-**1.19**); Er, x = 4, y = 1, (*S*-**1.19**)) were prepared and synthesized.[44]

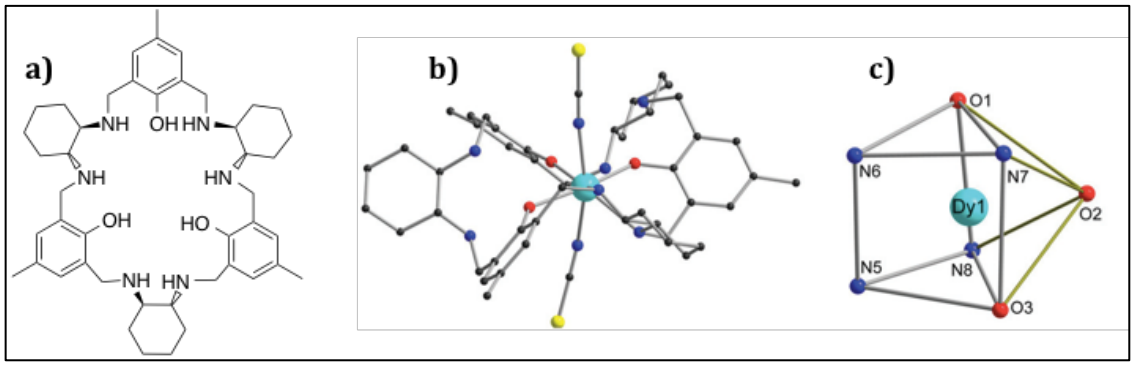

Figure 1.33 a) Structure of the H_3L_{RRRRRR} ligand, b) molecular structure of *R*-**1.17**, and c) the coordination polyhedron for the Dy1 ion in *R*-**1.17**. Reproduced with permission from Ref. 44.

Slow magnetic relaxation was observed for *R*-**1.117** under a 200 Oe *dc* field at 2 K with U_{eff} = 34.5 K and τ_0 = 1.1 × 10^{-6} s, Figure 1.34(a). The solid-state CD spectra confirmed the optical activity and enantiomeric nature of the three pairs of complexes. *R*-**1.17** exhibited negative Cotton effects at λ = 253 and 313 nm, whereas the *S*-enantiomer showed Cotton effects of the opposite signs at the same wavelengths, Figure 1.34(b). These results highlighted that the chirality of these compounds originates from ligands and demonstrates that oxophilic macrocycles can also be employed for the synthesis of chiral SMMs.

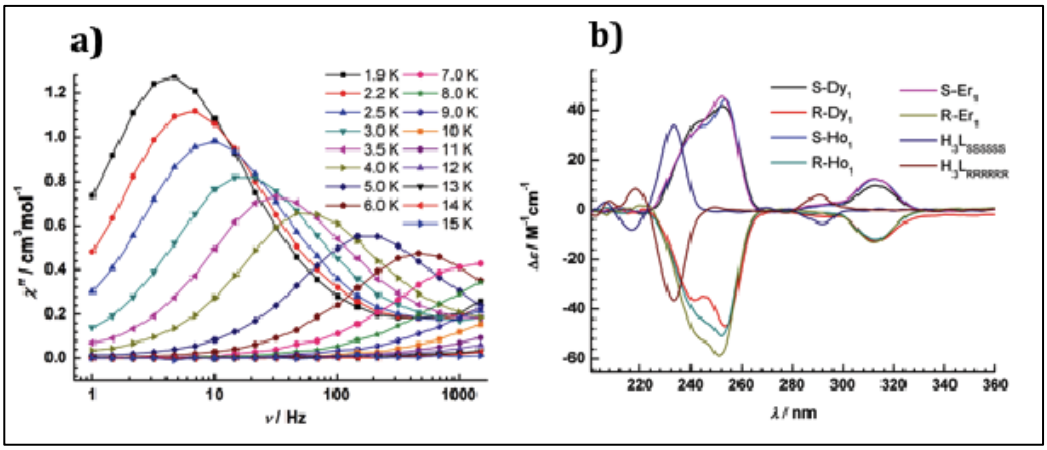

Figure 1.34 a) Frequency dependence of the *ac* susceptibility for *R*-**1.17** under a *dc* field of 200 Oe; b) CD spectra of *R/S*-**1.17**, *R/S*-**1.18**, and *R/S*-**1.19**, $H_3L_{RRRRRR/SSSSSS}$ in MeOH at RT. Reproduced with permission from Ref. 44.

In order to further study the effect of different ligands on the magnetic properties of chiral SMMs, a chiral hexadentate Schiff-base ligand was recently employed by Wen and co-workers, Figure 1.35. Following this strategy, a new family of 3*d*–4*f* heterometallic dinuclear complexes with stoichiometry [Ni(L)Ln$(NO_3)_3(H_2O)$] (Ln(III) = Ce (**1.20**), Nd (**1.21**)), and [Ni(L)Ln$(NO_3)_3$] (Ln(III)

= Sm (**1.22**), Eu (**1.23**), Gd (**1.24**), Tb (**1.25**), Dy (**1.26**) and Yb (**1.27**)) (H_2L = (*R*,*R*/*S*,*S*)-*N*,*N*'-bis(3-methoxysalicylidene)cyclohexane-1,2-diamine) were isolated.[84] Remarkably, the Ni(II)-Tb(III) (**1.25**) and Ni(II)-Dy(III) (**1.26**) complexes display field-induced slow relaxation of magnetisation.

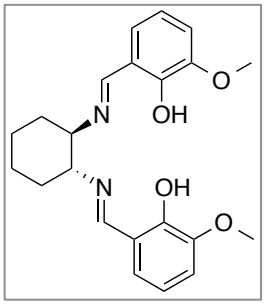

Figure 1.35 The chiral hexadentate Schiff-base ligand employed by Wen *et al*., for the preparation of chiral SMMs.[84]

These compounds exhibited both frequency and temperature dependent in (χ') and out-of-phase (χ") signals under H_{dc} = 0 kOe and H_{ac} = 2.5 Oe, Figure 1.36. A fit of the *ac* susceptibility data to the Arrhenius equation gave an energy barrier of 29.2 K for **1.25** and 18.4 K for **1.26**, with pre-exponential factors of 3.21 × 10^{-9} s and 7.39 × 10^{-6} s respectively, Figure 1.36 (inset).

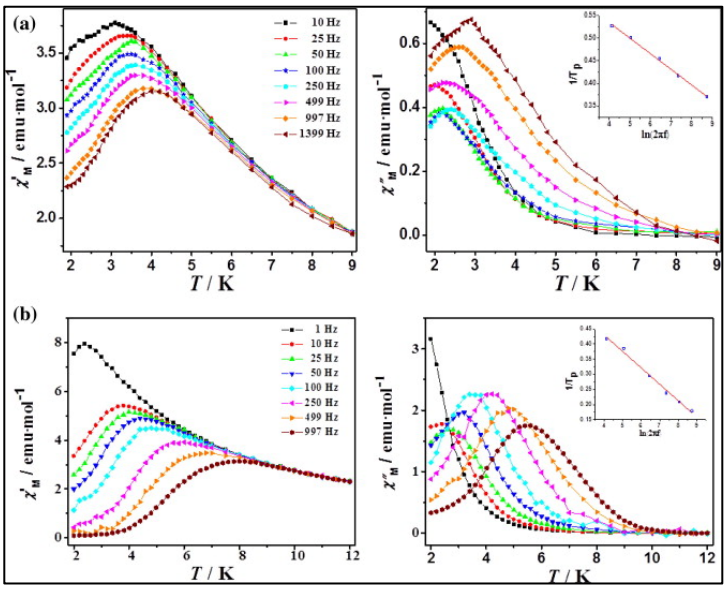

Figure 1.36 Temperature dependence of the out-of-phase *ac* signals at different frequencies under the external *dc* field of 2 kOe; the inset is the least-square fit of the data to the Arrhenius equation for (a) compound **1.25** and (b) compound **1.26**. Reproduced with permission from Ref. 84.

Complexes **1.20** – **1.27** are neutral diphenoxo-bridged Ni(II)-Ln(III) dinuclear clusters which crystallize in the triclinic space group *P*1. Their optical activity was confirmed by CD spectroscopy. For the *R* enantiomers, the CD spectra of **1.20** – **1.27** exhibit strong negative Cotton effects around λ = 280 and 400 nm, and a weak positive dichroic signal centered at 558 nm, whereas the *S* enantiomers show Cotton effects of the opposite signals at the same wavelengths, Figure 1.37.

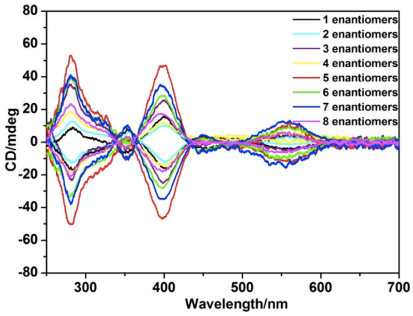

Figure 1.37 CD spectra of complexes **1.20** – **1.27**. Reproduced from Ref. 84.

In 2003 Tong *et al*. reported a chiral, multifunctional tetranuclear Dy(III) cluster that exhibits SMM behaviour with a large U_{eff} of 116 K, displaying both white light emission, and ferroelectric properties. This complex, Λ/Δ-[Dy_4(μ-bpt)$_4$(μ$_3$-OH)$_2$(μ-OMe)$_2$(NO_3)$_4$]($MeOH$)$_3$ (**1.28**) (where bpt$^-$ is the anion of Hbpt or 3,5-bis(pyridine-2-yl)-1,2,4-triazole), Figure 1.38,[85] was obtained from the solvothermal reaction of Dy(NO_3)$_3$, Hbpt, and Et_3N in MeOH at 120˚C.

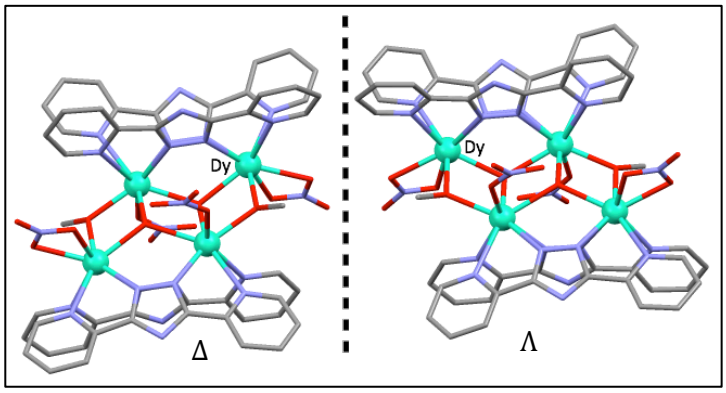

Figure 1.38 Molecular structures of the enantiomeric pair of clusters **1.28**. Colour code: Dy cyan, O red, N blue, and C grey.[85]

Both enantiomers of the cluster crystallize in the polar space group $P2_1$ as the ligand exhibits potential chirality due to the presence of torsion angles between its aromatic rings which is transferred to the coordination complex, Figure 1.39.

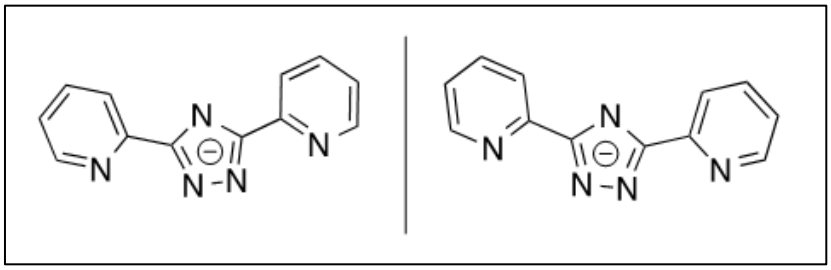

Figure 1.39 Two enantiomeric ligands, Δ-**1.28** (left) and Λ-**1.28** (right).[85]

For further confirmation of the optical activity, solid-state CD spectroscopy measurements were carried out on both enantiomers at room temperature. Complex Δ-**1.28** exhibited positive Cotton effects at λ = 288, 344, 413, and 527 nm and negative Cotton effects at λ = 302, 391, and 456 nm, while Λ-**1.28** showed the opposite Cotton effects at the same wavelengths, Figure 1.40.[85]

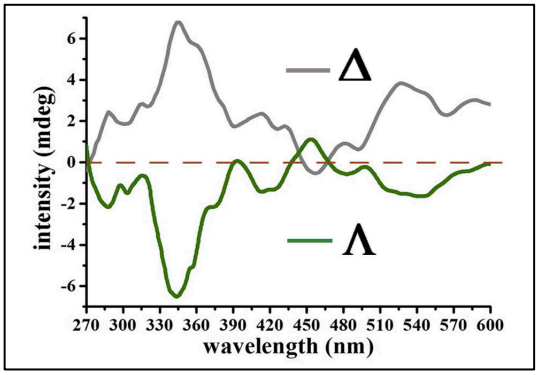

Figure 1.40 CD spectra of both enantiomers of **1.28**. Reproduced with permission from Ref. 85.

Polarization *vs.* electric field studies of the two enantiomers revealed that they display ferroelectric properties at room temperature with P_r = 0.10 μCcm^{-2}, P_S = 0.16 μCcm^{-2}, and E_C of 58.4 kVcm^{-1}, Figure 1.41.

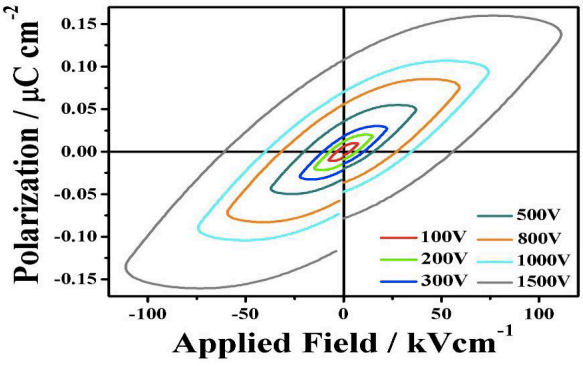

Figure 1.41 Ferroelectric hysteresis loop of Λ- and Δ-**1.28** measured at different voltages at room temperature. Reproduced with permission from Ref. 85.

The solid-state photoluminescence emission spectra of the two enantiomers were also observed at room temperature, Figure 1.42(a), revealing the expected transitions for Dy(III) ion at λ = 482, 575, and 636 nm corresponding to $^4F_{9/2} \rightarrow {}^6H_J$ transitions where J = 15/2, 13/2, and 11/2. When excited between 200 – 330 nm, complex **1.28** displays distinct white emission that arises due to a combination of ligand-centered excimer, as well as metal-centered *f-f* emission. The white emission remains nearly unchanged across a wide range of wavelengths and can be used as a stable white-light-emitting diode. When excited above 330 nm, the emission colour gradually changes to cold white, Figure 1.42(b).

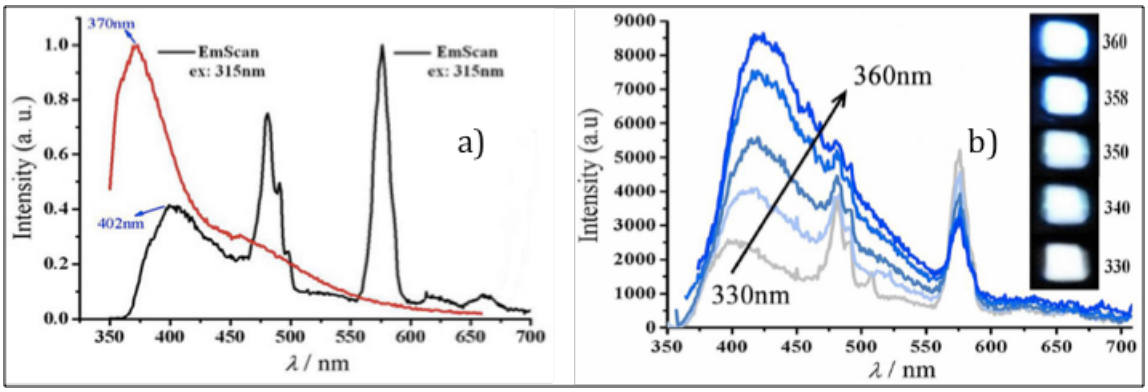

Figure 1.42 (a) Solid state emission spectra of Λ/Δ-**1.28** (black line) and Hbpt ligand (red line), and (b) excited at 330 – 360 nm. The inset indicated emission photos under a 450 W UV lamp when changed to cold white. Reproduced with permission from Ref. 85.

Both frequency-dependent in-phase (χ') and out-of-phase (χ") signals were observed for both enantiomers of **1.28** under zero *dc* field, Figure 1.43 revealing the presence of slow relaxation of magnetization. A fit of the *ac* magnetic susceptibility data to the Arrhenius equation gave an energy barrier of 116 K, and a pre-exponential factor or 2.89×10^{-7} s.

The combination of electrical bistability, luminescence, and magnetism in a single smart multifunctional molecule-based system is still uncommon,[86] despite attractive applications such as four-level density data storage or multifunctional sensors.[86] It is well-known that Dy(III) can exhibit luminescence with well-resolved emission bands and long lifetimes,[106] and that the presence of an antenna ligands can enhance the lanthanide luminescence.

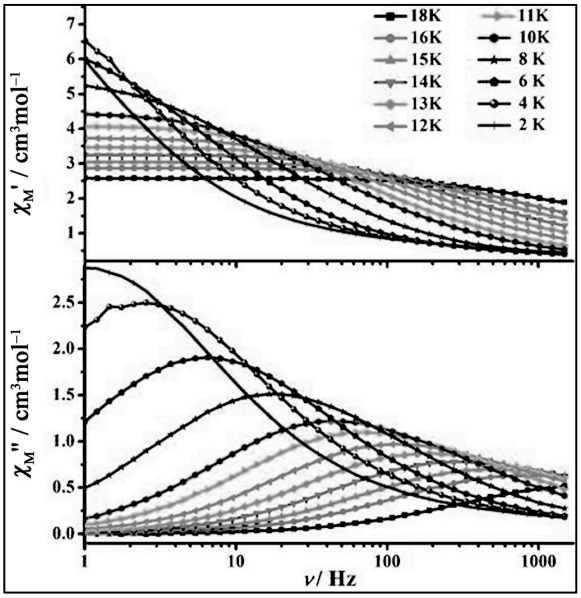

Figure 1.43 Frequency-dependent in-phase (χ'_M, top) and out-of-phase (χ''_M) *ac* susceptibility under zero *dc* field for **1.28**. Reproduced with permission from Ref. 85.

Furthermore, the chirality of the ligand employed in a reaction system may favor the crystallization of the molecule in a non-centrosymmetric space group compatible with ferroelectricity. Taking all of these factors into consideration, Long and co-workers synthesized a pair of chiral complexes [*R,R*-ZnLDy(μ-OAc)$(NO_3)_2$] (*R,R*-**1.29**) and [*S,S*-ZnLDy(μ-OAc)$(NO_3)_2$] (*S,S*-**1.29**) by reacting the enantiomers of the Schiff-base ligand *R,R*-H_2L or *S,S*-H_2L (where H_2L = phenol,2,2'[2,2-diphenyl-1,2-

ethanediyl]bis[(*E*)-nitrilomethylidyne]-bis(6-methoxy) together with $Zn(OAc)_2 \cdot 2H_2O$ and $Dy(NO_3)_3 \cdot 5H_2O$ in MeOH, Figure 1.44.[87]

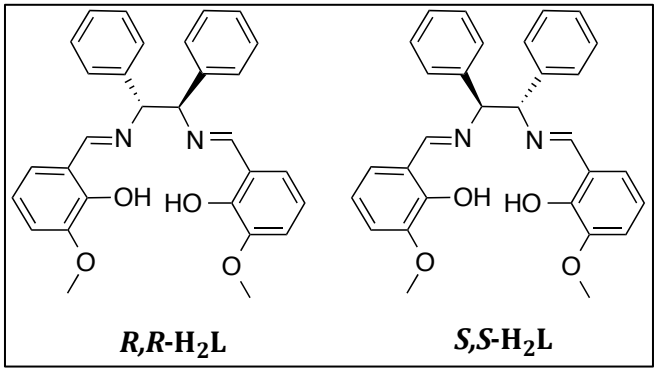

Figure 1.44 Molecular structure of two enantiomeric ligands, *R,R*-H_2L and *S,S*-H_2L.[87]

The two complexes, *R,R*-**1.29** and *S,S*-**1.29**, Figure 1.45 crystallize in the polar space group $P2_1$, confirming that the ligand chirality is transferred to their respective coordination complexes.

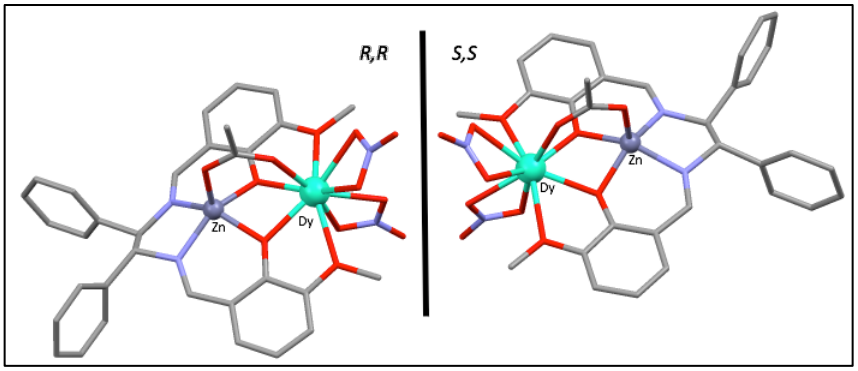

Figure 1.45 Molecular structure of the *R,R*- and *S,S*- enantiomers. Colour code: Dy(III) cyan, Zn(II) purple, O red, N blue, and C grey.[87]

The optical activity of the two enantiomers was verified by CD spectroscopy. The spectrum of the *R*-enantiomer exhibited a strong positive Cotton effect at λ = 230 nm and a positive dichroic signal centered at 350 nm, while the *S*-enantiomer showed Cotton effects of the opposite sign at the same wavelengths, Figure 1.46.

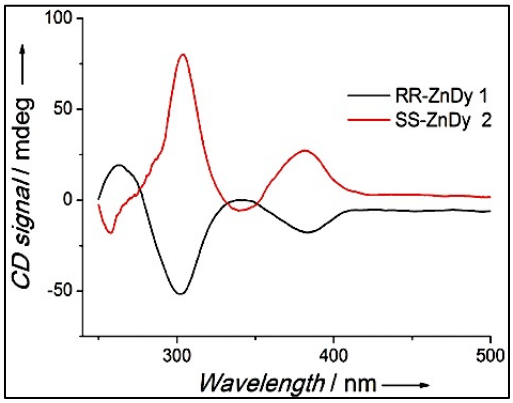

Figure 1.46 CD spectra of *R,R*- and *S,S*-clusters **1.29** at room temperature. Reproduced with permission from Ref. 87.

Magnetic studies reveal that both enantiomers behave as paramagnets at high temperatures and single ion magnets below 5 K, as confirmed by the presence of frequency dependent out-of-phase peaks in the *ac* susceptibility from 0.91 – 5 K, Figure 1.47. U_{eff} values for the *R,R*-enantiomer were reported to be 19.40 between 0.91 and 2.7 K, and 51.82 K in between 2.7 and 5 K. The corresponding effective energy barriers for the *S,S*-enantiomer were also determined to be 20.48 and 51.71 K, for the "low" and "high" temperature regions respectively.

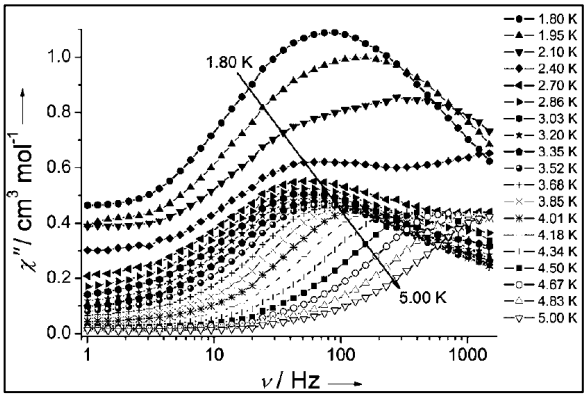

Figure 1.47 Frequency dependence of the out-of-phase susceptibility for the *R,R*-enantiomer of **1.29** at different temperatures under a 1500 Oe *dc* field. Reproduced with permission from Ref. 87.

The emissive properties of both *R,R*- and *S,S*-enantiomers of **1.29** were investigated by the solid state photoluminescence measurements at both room temperature and at 12 K, Figure 1.48. At room temperature, emission from both the ligand and Dy(III) intra-4f^9 transitions are observed owning to a partial energy transfer from the ligand to the lanthanide upon the excitation at 365 nm. In contrast at 12 K only the $^4F_{9/2} \rightarrow {}^6H_J$ (J = 15/2, 13/2, and 11/2) transitions were observed.[87]

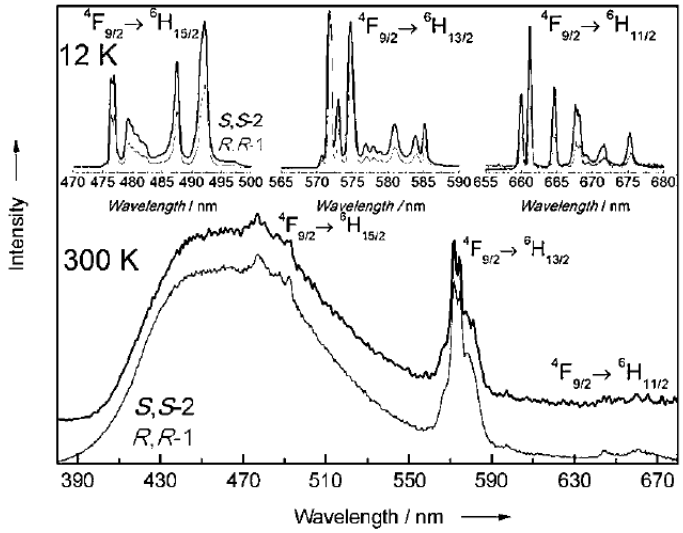

Figure 1.48 Emission spectrum at room temperature and 12 K for the *R,R*- and *S,S*-enantiomers of **1.29**. Reproduced with permission from Ref. 87.

Polarization *vs.* applied electric field measurements carried out on the *R,R*-enantiomer at 400 K gave a ferroelectric hysteresis loop with a large value of E_C = 17 kVcm^{-1} and P_S = 9.1 μCcm^{-2}, Figure 1.49. Clear hysteresis loops were observed at 10 and 563 K before the complex decomposed, while no hysteresis loop has been observed at room temperature. This is the highest temperature at which an electrical hysteresis loop has been observed for a molecule-based ferroelectric material to date, and is 170 K above the Curie temperature of the ferroelectric

$BaTiO_3$ Perovskite compound which shows real promise for the future applications of molecule-based compounds in the field of multiferroics.[87]

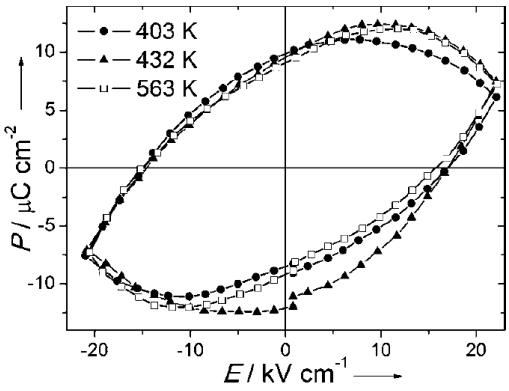

Figure 1.49 *P vs. E* plot for *R,R*-**1.29**. Reproduced with permission from Ref. 87.

1.6 Ligand Design for Molecule-Based Magnets

As previously mentioned, one of the most important factors for the construction of new 3*d*- or 4*f*-metal complexes with SMM properties with unprecedented topologies, and nuclearities is the selection of the primary organic bridging and/or chelating ligands.[40] Since two classes of organic ligands have been employed during the course of these studies, the following section will provide the reader with an overview of selected examples of *p*-*tert*-butylcalix[4]arene and pyridine-based alkoxide complexes that have been previously prepared and studied within the field of molecular magnetism.

1.6.1 Calix[4]arenes

Calixarenes are cyclic oligomeric phenolic compounds formed via the condensation of formaldehyde with *p*-alkylphenols under alkaline conditions. In a one-step synthetic reaction, the formation of various phenolic ring systems bridged

by methylene (-CH_2-) spacers can be controlled by changing the temperature or the amount of base used in the reaction. To date, up to 20 phenolic residues have been incorporated within a calixarene ring system; however yields are low for those macrocycles comprised of an odd number of phenolic units. The smaller members of the family, such as calix[4/6/8]arenes all have a cone-shaped structures. Gutsche coined the name 'calix[*n*]arene' in 1975 which is derived from the Greek *calix* meaning 'chalice' or 'vase', *arene* which indicates the presence of aryl units, and *n* that denotes the number of phenolic units within the macrocyclic array.[88] Such conformation gives rise to the hydrophobic characteristics and electron-rich cavities which are a significant advantage for the coordination of 3*d*, 4*d*, 5*d*, 4*f*, 5*f* metal ions.[89] For this reason, this class of macrocycles have found applications in many areas of chemistry including medical diagnostics, fluorescent probes, phase-transfer agents, separation chemistry, nanochemistry, and ion-channel blockers.[88] Both the phenolic lower rim and the non-phenolic upper rim can be chemically modified, which has afforded a large range of derivatives, many of which have been exploited for the self-assembly of larger supramolecular compounds. Since the mid-1980s, calix[4]arenes or C[4]s have been employed as ligands in the field of coordination chemistry largely due to their conformational flexibility, molecular cavities, and their ability to coordinate several metal centers in a multidentate fashion. In this context, *p*-*tert*-butylcalix[4]arenes, or TBC4s are of particular interest, since they are easily prepared, able to retain their cone conformation, and can bind at least one metal center.[88] Moreover, TBC4 has C_{4v} symmetry and a π-basic cavity in its upper rim, Figure 1.50.[90,91]

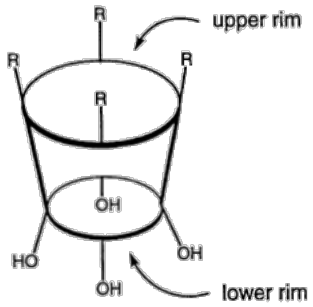

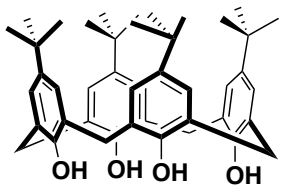

(L2.2) TBC4

Figure 1.50 Representation (left) of the designation of the faces of C4 (R = alkyl), and (right) the molecular structure of TBC4.[88]

Given their ability to bind metal ions, TBC4 macrocycles are also interesting ligands for the construction of polynuclear transition metal (TM),[89,92–96] lanthanide (Ln),[97,98] and 3*d*-4*f* clusters[99–101] with interesting magnetic properties. In this regard, a number of new cluster motifs have been discovered including $[Mn(III)_2Mn(II)_2(TBC4)_2]$ SMMs,[95] $[Mn(III)_4Ln(III)_4(C[4])_4]$ clusters that are either magnetic refrigerants or SMMs depending on the lanthanide employed,[100,101] as well as $[Cu(II)_9(TBC4)_3]$ clusters that act as versatile anion binding materials.[102] Thia-, sulfinyl- and sulfonyl-bridged C[4]s owing to their bridging atoms can also participate in the coordination of metal ions.[101,103] In recent years, Liao[104–106] and Hong[107,108] have employed thia-C[4] analogues in a series of studies, where polybenzoates have been used as ancillary ligands to afford a series of metal-organic nanocapsules. Since the focus of Project 1 of this thesis is concerned with exploiting TBC4 macrocycles for the synthesis of Ln(III)-SMMs, this next section focuses solely on the synthesis and magnetostructural studies of previously reported TBC4 complexes.

A notable example of the first manganese polynuclear cluster comprised of two TBC4 capping ligands is the mixed-valence complex $[Mn(III)_2Mn(II)_2(OH)_2(TBC4)_2(DMF)_6]\cdot 2MeOH$ (DMF = *N*,*N*-dimethylformamide) (**1.30**), Figure 1.51(a).[96] *Ac*-susceptibility studies reveal steps in the temperature and field sweep-rate-dependent hysteresis loops, indicative of QTM, confirming its SMM properties, Figure 1.51 (b and c).

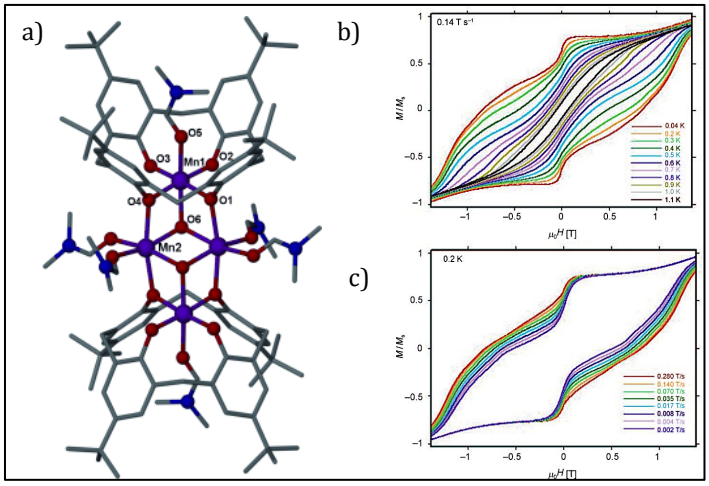

Figure 1.51 a) Molecular structure of **1.30**; b) hysteresis loops measured on single crystals of **1.30** over a range of temperatures; c) field sweep rates. Reproduced with permission from Ref. 96.

Based on addition of carboxylate co-ligands to the aforementioned $[Mn(III)_2Mn(II)_2(OH)_2(TBC4)_2]$ motif, Dalgarno and Brechin synthesized and characterized a number of TBC4-supported clusters **1.31** – **1.36** that possess similar structural features and magnetic properties to **1.30**.[95]

$[Mn(III)_2Mn(II)_2(OH)_2(TBC4)_2(DMF)_4(H_2O)_2]\cdot 4MeOH\cdot 2DMF$ (**1.31**),

$[Mn(III)_2Mn(II)_2(OH)_2(TBC4)_2(DMF)_6]\cdot 2.8MeOH$ (**1.32**),

$[Mn(III)_2Mn(II)_2(OH)_2(TBC4)_2(DMF)_4(EtOH)(H_2O)]$ (**1.33**),

$[Mn(III)_2Mn(II)_2(OH)_2(TBC4)_2(DMSO)_6]\cdot 2MeOH\cdot 2DMSO$ (**1.34**),

$[Mn(III)_2Mn(II)_2(OH)_2(TBC4)_2(DMSO)_6]$ (**1.35**),

$[Mn(III)_2Mn(II)_2(OH)_2(TBC4)_2(MeOH)_6]\cdot 4MeOH$ (**1.36**).

Despite the fact that carboxylate co-ligands were also used in the syntheses, they were not incorporated into the resulting assemblies. Magnetic studies revealed that all six compounds display SMM properties. Extending this approach employing a combination of TBC4 together with a complementary cluster ligand e.g. 2-hydroxymethyl)pyridine (hmpH), a $[Mn_5]$ complex of stoichiometry $[Mn(III)_3Mn(II)_2(OH)_2(TBC4)_2(hmp)_2(DMF)_6](TBC4\text{-}H)\cdot 2.6DMF\cdot 1.4H_2O$ (**1.37**),[92] was synthesized. The cluster that has been synthesized employing a combination of TBC4 and a complementary cluster ligand, such as 2-(hydroxymethyl)pyridine (hmpH), crystallized in the triclinic space group $P\bar{1}$, Figure 1.52 and exhibited SMM behaviour with a U_{eff} = 42 K and $\tau_0 = 1.125 \times 10^{-10}$ s, Figure 1.53.

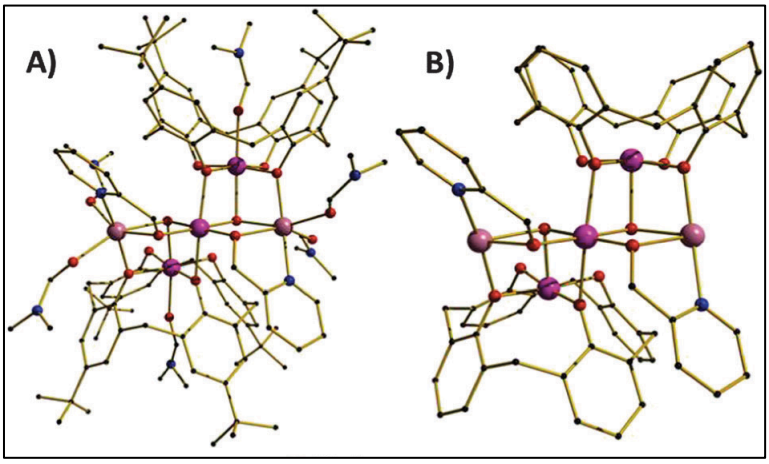

Figure 1.52 a) Molecular structure of the cation in **1.37** and b) with TBC4 and DMF molecules removed. Colour code: Mn(III) purple, Mn(II) pink, O red, N blue, C black. Reproduced with permission from Ref. 92.

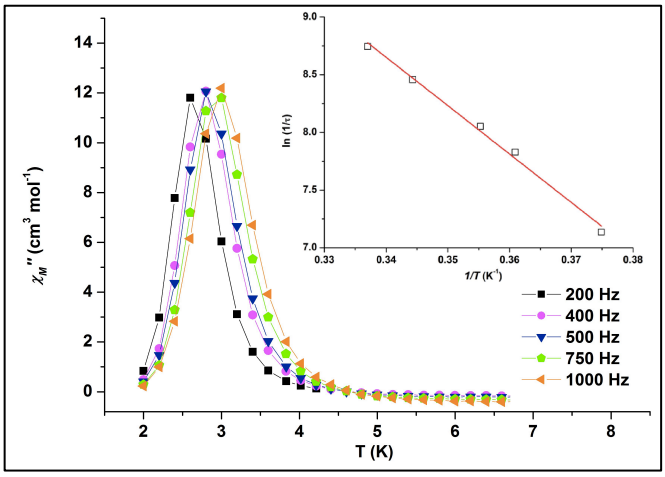

Figure 1.53 Plot of the out-of-phase *ac* susceptibility of **1.37**. Inset: Arrhenius plot. Reproduced with permission from Ref. 92.

Two new TBC4-supported Mn(III)/Mn(II) clusters were formed by the addition of sodium phenylphosphinate or 3,5-dichlorobenzoate (Nadcb) as ancillary ligands to a system already known to afford novel $Mn(III)_2Mn(II)_2$ clusters. In this respect two complexes $[Mn(III)Mn(II)(O_2P(H)Ph)(DMF)_2(MeOH)_2]_2$ (**1.38**)[103] and $[Mn(III)Mn(II)(TBC4)(dcb)(\mu\text{-}DMSO)(H_2O)]$ (**1.39**)[94] were isolated, Figure 1.54.

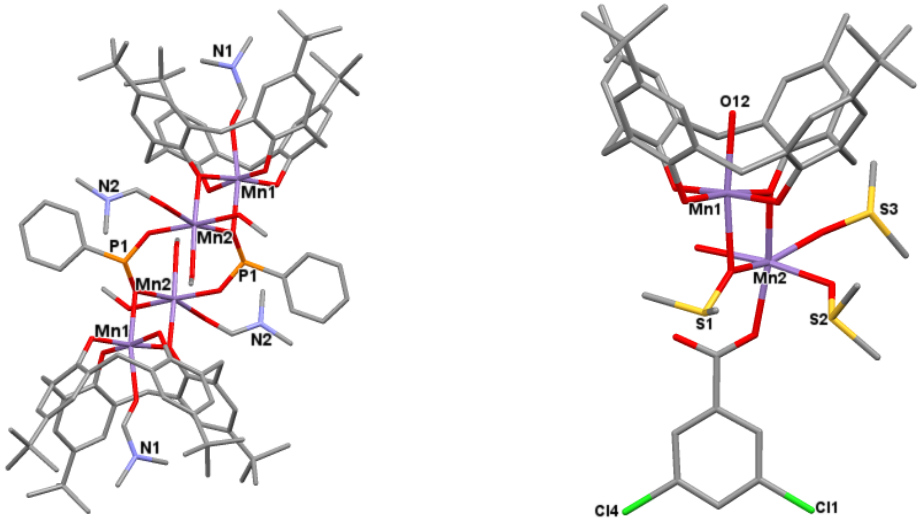

Figure 1.54 Molecular structures of **1.38** and **1.39**. Reproduced with permission from Refs. 94 and 103.

Cluster **1.38** comprises of a modulated TBC4-supported $Mn(III)_2Mn(II)_2$ cluster in which two Mn(III)Mn(II) dimers are linked via two bridging phenylphosphinates, while **1.39** has an unusual topology which is stabilized via halogen···halogen interactions affording a bi-layer arrangement of clusters that is reminiscent of the packing observed in TBC4 solvates, Figure 1.55.

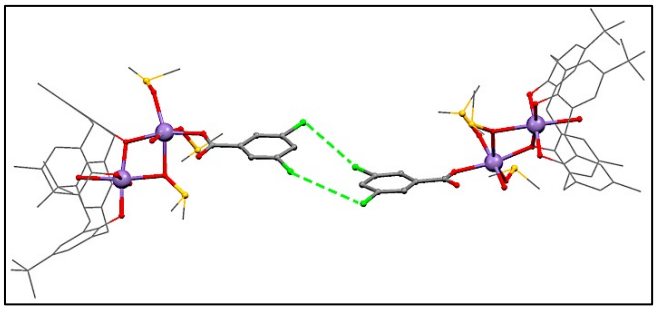

Figure 1.55 Representation of the coordination chain of **1.39** stabilized via halogen-halogen interactions.[94]

The magnetic behaviour of **1.38** is analogous to the butterfly structure of the parent cluster **1.30** in which the exchange between the Mn(III) and Mn(II) ions is weakly ferromagnetic, Figure 1.56(a). The interesting structural topology of **1.39** incorporates Nadcb ligands, which have been shown to promote weak ferromagnetic interactions at low temperature (T < 5 K), Figure 1.56(b). Cluster **1.39** displays frequency-dependent out-of-phase (χ") signals at both zero and 3.5 G applied *dc* field, consistent with it being an SMM, Figure 1.56(c).[94]

There are several reports of TBC4-supported cluster formation with Fe(II/III),[99] Mn(II/III),[109] and Ln(III) ions for the construction of 3*d*-4*f* systems, which highlight strategies for their syntheses as well as detailed magnetostructural

studies that further our understanding of exchange interactions between the paramagnetic metal ions in the systems.

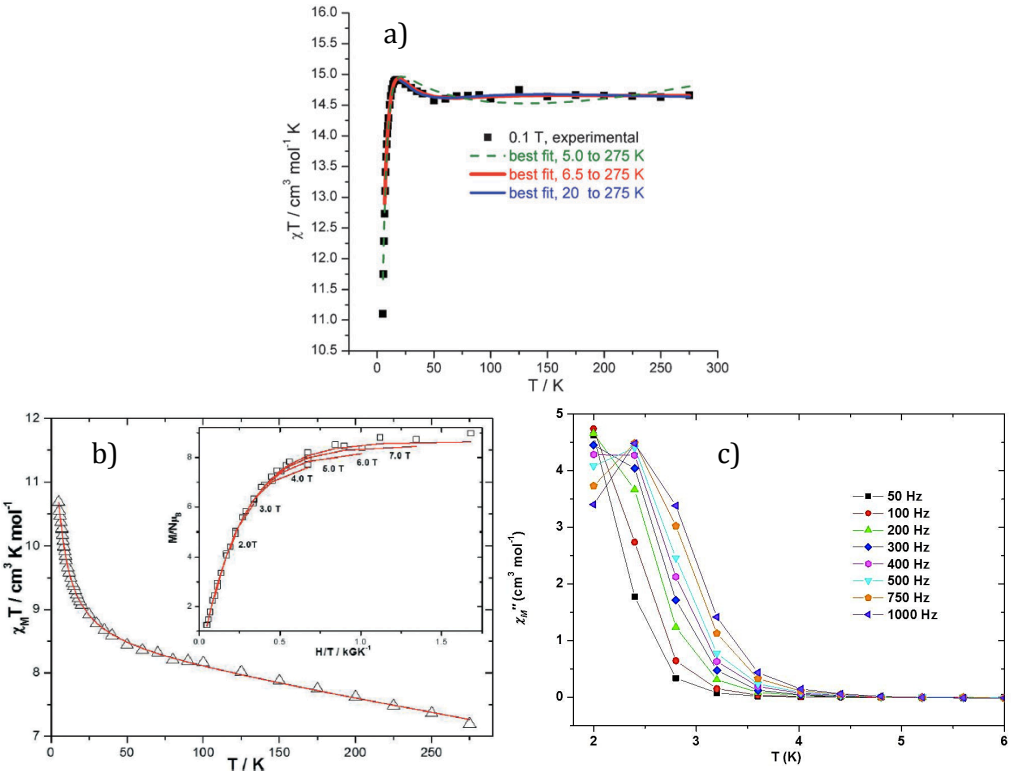

Figure 1.56 Plots of χ' *vs*. T for **1.38** (a) and **1.39** (b) in an applied field of 0.1 T. The red line represents the fit of the experimental data; (c) frequency-dependence of the *ac* susceptibility for **1.39** measured between 50 and 1000 Hz frequency range. Reproduced from Ref. 94.

In 2013, the first three novel lanthanide-based complexes were reported by by Zuo and co-workers assembled from a TBC4 derivative (C4) with the general formula [Ln(III)(C4)(L_{OEt})] (L(III) = Dy (**1.40**); Tb (**1.41**); and Ho (**1.42**)), where NaL_{OEt} = sodium (η^5-cyclopentadienyl)tris(diethylphosphito-*p*)cobaltate(III)), Figure 1.57.[110] Interestingly, X-ray diffraction studies revealed that for all three complexes, a single TBC4 derivative ligand coordinates the Ln(III) ion *via* all four of the phenoxide substituents on its lower rim.

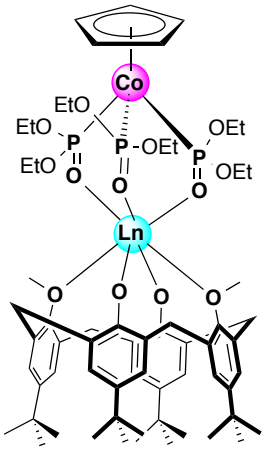

Figure 1.57 Molecular structure of complexes **1.40** – **1.42**.[110]

Ac susceptibility measurements carried out on the Dy(III) complex **1.40** confirmed that it exhibited both temperature and frequency dependent in-phase (χ') and out-of-phase (χ'') signals at low temperature (3 – 8 K) under both zero and 900 Oe *dc* field, consistent with SMM behaviour, Figure 1.58 (a and b).

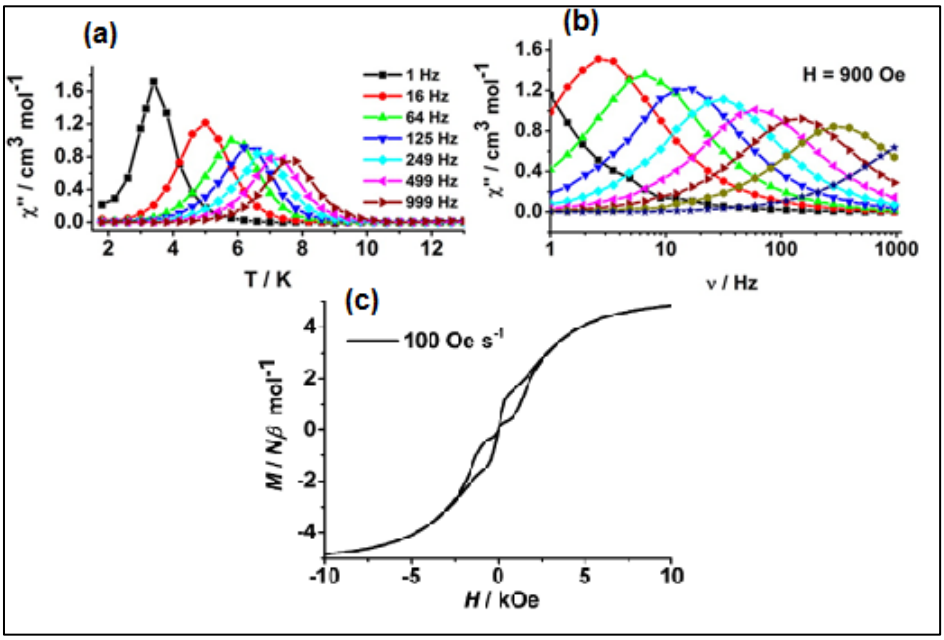

Figure 1.58 a) Temperature and b) frequency-dependent out-of-phase χ'' *ac* susceptibility signals for **1.40** under a 900 Oe *dc* field, and (c) hysteresis loop for **1.40** at 1.8 K with a sweeping rate of 100 Oe. Reproduced from Ref. 110.

A fit of the *ac* susceptibility data to the Arrhenius equation for **1.40** afforded an effective energy barrier U_{eff} = 73.7 K and $\tau_0 = 9.1 \times 10^{-8}$ s. A hysteresis loop for **1.40** was also observed at 1.8 K, which further confirms its SMM properties, Figure 1.58(c). In contrast, no obvious out-of-phase peaks were observed for **1.41** and **1.42** under both zero or applied *dc* field which is attributed to the fact that their non-Kramers ions possess non-degenerate ground states with larger energy gaps between their lowest first excited and ground states.

These results highlight that slight structural modifications due to employing a TBC4 derivative can have a significant influence on the local coordination environment of the metal ions and thus also on the nature of the 4*f* ion anisotropy, which may ultimately result in different SMM behaviour within a family of complexes. Given the aforementioned use of TBC4, Dalgarno and Brechin have also investigated the larger calixarene analogues, such as TBC6, *p-tert*-butyltetrahomo-dioxacalix[6]arene (TBDOC6), and TBC8, Figure 1.59. The formation of Co(II) complexes of TBC6,[111] a series of binuclear lanthanide TBC8 complexes[112] and a TBC8-supported ferromagnetic [Mn(IV)Mn(III)] dimer[113] have all been synthesized and characterized, employing different experimental conditions and metal salts, which illustrates that these macrocycles are in fact extremely versatile in terms of both conformations, varying levels of deprotonation, and their bridging capabilities. Recent studies suggest that a wide range of clusters may be formed from calixarene building blocks that could potentially afford new structural topologies with interesting magnetic properties in the future.

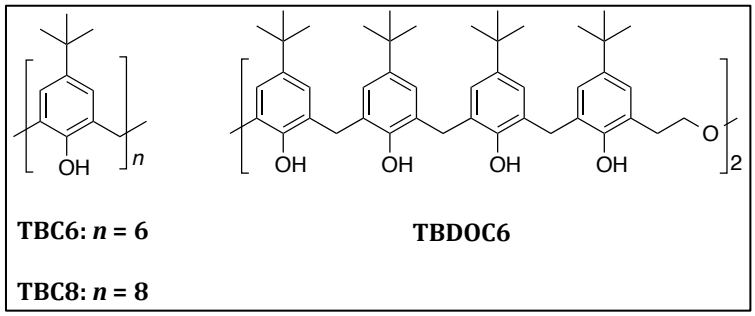

Figure 1.59 Schematic representation of the molecular structures of TBC6, TBC8, and TBDOC6 ligands.

1.6.2 Pyridine-based Alkoxide Ligands

The use of functional alkoxide ligands containing an additional N-donor group has been of considerable interest to coordination chemists over the past decade due to their potential applications in diverse areas of chemistry that include structural chemistry, homogeneous catalysis, and molecular magnetism. The efficiency of such ligands for the design and synthesis of high nuclearity metal clusters arises from their simultaneous N,O-chelating and O-bridging capabilities and their relatively high acidity.[114,115] Just considering pyridine as the N donor group, the vast library of pyridine-based alkoxide ligands has been well documented. Examples of such ligands include 2-(hydroxymethyl)pyridine (hmpH) (**L1.1**), 2-(2-hydroxyethyl)pyridine (hepH) (**L1.2**),[116] as well as 2,6-pyridinedimethanol ($pdmH_2$) (**L1.3**),[114] and its derivatives[116], Figure 1.60. Interestingly, the coordinating versatility of these simple ligands towards a wide range of TM ions has afforded several new families of compounds, many of which have intriguing structural topologies, as well as magnetic and optical properties.[117]

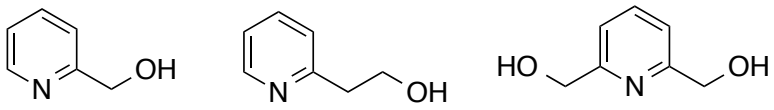

L1.1 **L1.2** **L1.3**

Figure 1.60 Three examples of commonly employed pyridyl alcohol ligands, hmpH (**L1.1**), HepH (**L1.2**) and pdmH2 (**L1.3**).

Within this context, the optically active α-methyl-2-pyridinemethanol (mpmH) ligand (**L3.1**) is of particular interest (Figure 1.61).

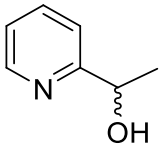

L3.1 mpmH

Figure 1.61 Molecular structure of the chiral ligand **L3.1**.

In this case, the deprotonated oxygen atom of ligand **L3.1** is not coordinately saturated by binding to one metal, and thus can act as a bridge, fostering the assembly of high nuclearity clusters with interesting physical properties. Moreover, the alkoxide arm often promotes strong ferromagnetic exchange interactions between the subsequent bridged metal ions.[118] Despite the simplicity and robustness of pyridine-derived alcohols, the chiral derivative **L3.1** has remained relatively unexplored as a class of ligand for the synthesis of transition metal and Ln-based SMMs. Nevertheless, the wide array of pyridyl alcoholate ligands suggests that new chiral derivatives may afford tuneable families of complexes, through which the effects of structural variation on magnetostructural and optical properties can be investigated.

In order to target the synthesis of such new high spin molecules, Stamatatos *et al*. exploited the coordination chemistry of hmp^- ligands together with $Mn(NO_3)_2{\cdot}H_2O$ and $Mn(ClO_4)_2{\cdot}6H_2O$ salts with a combination of azide (N_3^-) and alkoxide (hmp^-) ligands to afford the two decanuclear, mixed-valence complexes $[Mn(II)_4Mn(III)_6O_4(N_3)_4(hmp)_{12}](N_3)_2$ (**1.43**) and $[Mn(II)_4Mn(III)_6O_4(N_3)_4(hmp)_{12}](ClO_4)_2{\cdot}MeCN$ (**1.44**), displaying high (S = 22) ground state spin values.[119] The molecular structures of these complexes were characterized by X-ray diffraction which reveals that both complexes are isostructural with the Mn_{10} cation adopting a tetra-face-capped octahedral geometry, Figure 1.62.

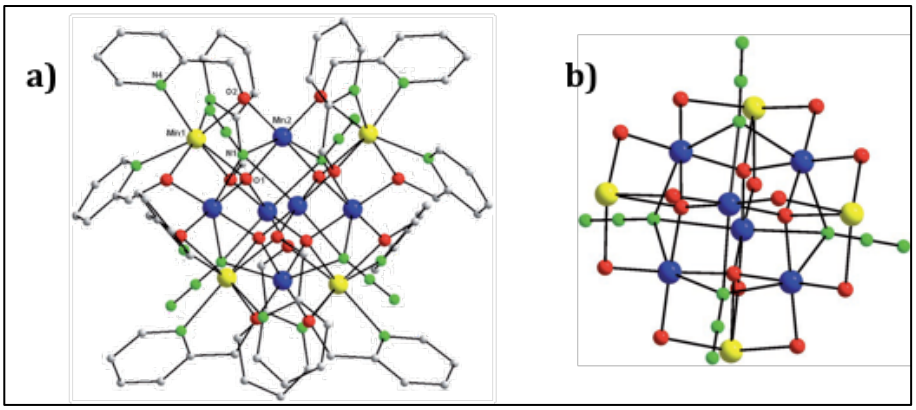

Figure 1.62 Representation of the cation (a) and core (b) of **1.43**. Color scheme: Mn(II) yellow, Mn(III) blue, O red, N green, C grey. Reproduced with permission from Ref. 119.

The magnetic properties of compounds **1.43** – **1.44** comprise ferromagnetic exchange interactions between the Mn_{10} units. *Ac* susceptibility measurements were performed on complex **1.44**, showing that the molecule exhibits temperature-dependent in phase (χ') signals from 15 K down to 8 K, Figure 1.63, but there are no

out-of-phase (χ'') signals down to 1.8 K. Additionally, no hysteresis was observed for **1.44**, which suggests that this complex is not an SMM.

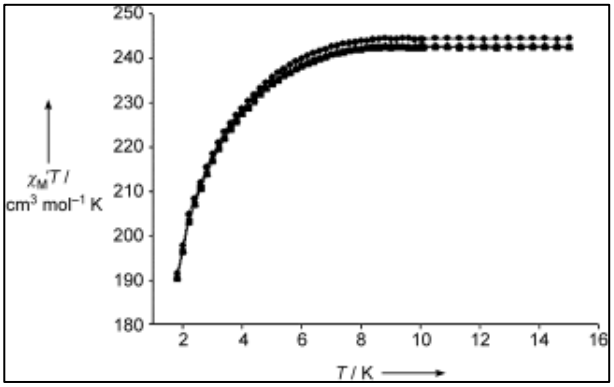

Figure 1.63 In-phase (χ_M'T) *ac* susceptibility signals for **1.44** below 15 K at different frequencies. Reproduced with permission from Ref. 119.

Motivated by the versatility of alkoxide-containing ligands such as hmpH (**L1.1**) for coordinating to transition metal ions, Braunstein *et al.* recently used NaH to deprotonate ligand **L1.1** and obtained a range of unusual Ni(II) polynuclear complexes that include $[Ni_7(hmp)_{12}]Cl_2$ **1.49**, Figure 1.64(a) and $[Ni_6Na(hmp)_{12}]Cl$ **1.50**, Figure 1.64(b).[120]

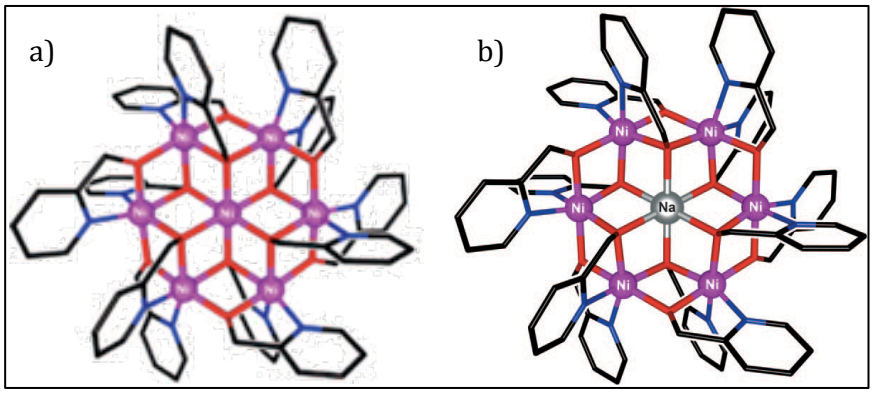

Figure 1.64 Molecular structures of the multicubane **1.49** (a) and **1.50** cations (b). Color scheme: Ni(II) pink, Na silver, O red, N blue, and C black. Reproduced with permission from Ref. 120.

In both complexes, the cations crystallize in Anderson-type structural topologies comprising of six-face-sharing incomplete cubane moieties arranged in a cyclic fashion, and the seven central metal ions are co-planar. Although Anderson-type structures are not unusual for TMs, this arrangement had not been reported for Ni(II) prior to this study.[120] The *dc* magnetic susceptibility data for **1.49** and **1.50** reveal that the room temperature χT value of 8.1 $cm^3mol^{-1}K$ for **1.49** increases continuously up to a maximum value of 13.1 $cm^3mol^{-1}K$ at 8 K upon decreasing the temperature, Figure 1.65.

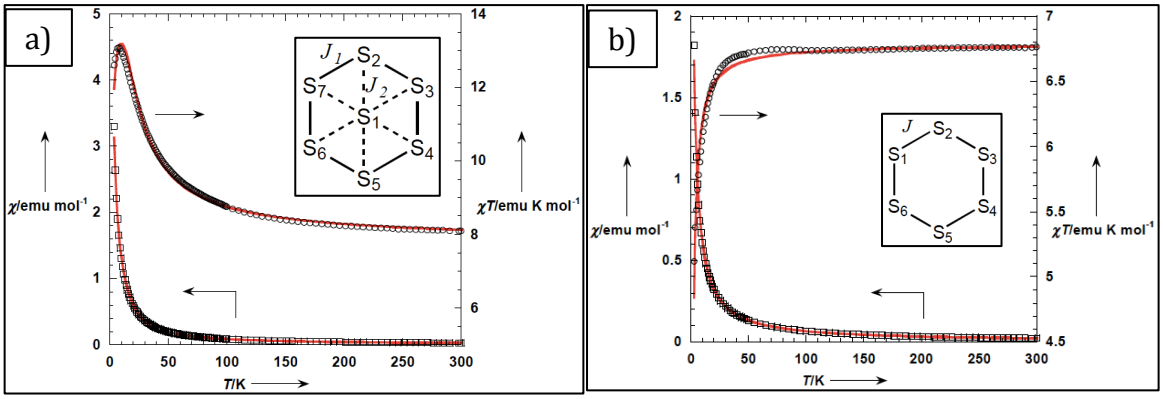

Figure 1.65 χ *vs.* T (squares) and χ_MT *vs.* T (circles) plots for complexes **1.49** (a) and **1.50** (b), with the considered spin topology (inset). Solid lines are the fit of χ_MT data. Reproduced with permission from Ref. 120.

This behaviour indicates the presence of ferromagnetic interactions between the seven Ni(II) ions. Below 8 K, the χT product decreases down to 11.3 $cm^3mol^{-1}K$ at 1.8 K, which is attributed to ZFS and inter- and/or intramolecular antiferromagnetic interactions. For the second cluster **1.50**, χT remains constant down to 6.8 $cm^3mol^{-1}K$ at 60 K, and then drops rapidly to 4.9 $cm^3mol^{-1}K$ at 1.8 K. This behaviour indicates the presence of antiferromagnetic intramolecular interactions, or may due

to the effect of ZFS. Even though hmpH is an excellent ligand for the synthesis of higher nuclearity 3*d* clusters, it was not until 2011, that it was employed for the preparation of homometallic 4*f* clusters. In this context, reaction of hydrated lanthanide nitrate salts with hmpH in the presence of an Et_3N base afforded a new family of nonanuclear Ln(III) clusters displaying both magnetic and optical properties. Three Ln(III) complexes were prepared with the structural formulae $[Ln(III)_9(OH)_{10}(hmp)_8(NO_3)_8(DMF)_8](OH)$, where Ln(III) = Dy (**1.51**), Gd (**1.52**), and Eu (**1.53**), all of which crystallize in a tetragonal space group *P*4/*n*.[121] The core structure of compound **1.51** contains eight Dy(III) atoms at the apexes and one Dy(III) atom at the center of a Dy_8 square antiprism, which adopts a sandglass-like topology, Figure 1.66. All three complexes are reported to be isostructural with all of their Ln(III) ions being eight coordinate.

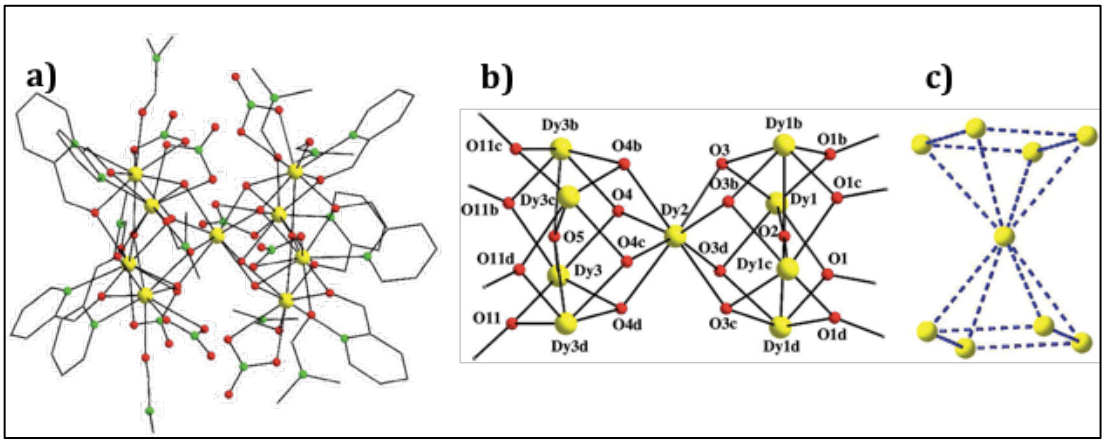

Figure 1.66 Structure of the cation (a), representation of the core (b), and sandglass topology of **1.51** (c). Reproduced with permission from Ref. 121.

Magnetic studies were carried out on compounds **1.51** and **1.52**. *Dc* studies reveal that the room temperature $\chi_M T$ product for **1.52** is 66 $cm^3mol^{-1}K$ and remains constant before gradually decreasing to a minimum value of 35.19 $cm^3mol^{-1}K$ at 5 K.

This behaviour indicates the presence of weak antiferromagnetic interactions between the nine Gd(III) ions. For **1.51**, the room temperature $\chi_M T$ value is 113 $cm^3mol^{-1}K$. Upon decreasing temperature $\chi_M T$ remains constant and then drops slowly down to a minimum value of 68.71 $cm^3mol^{-1}K$ at 5 K, Figure 1.67(a).

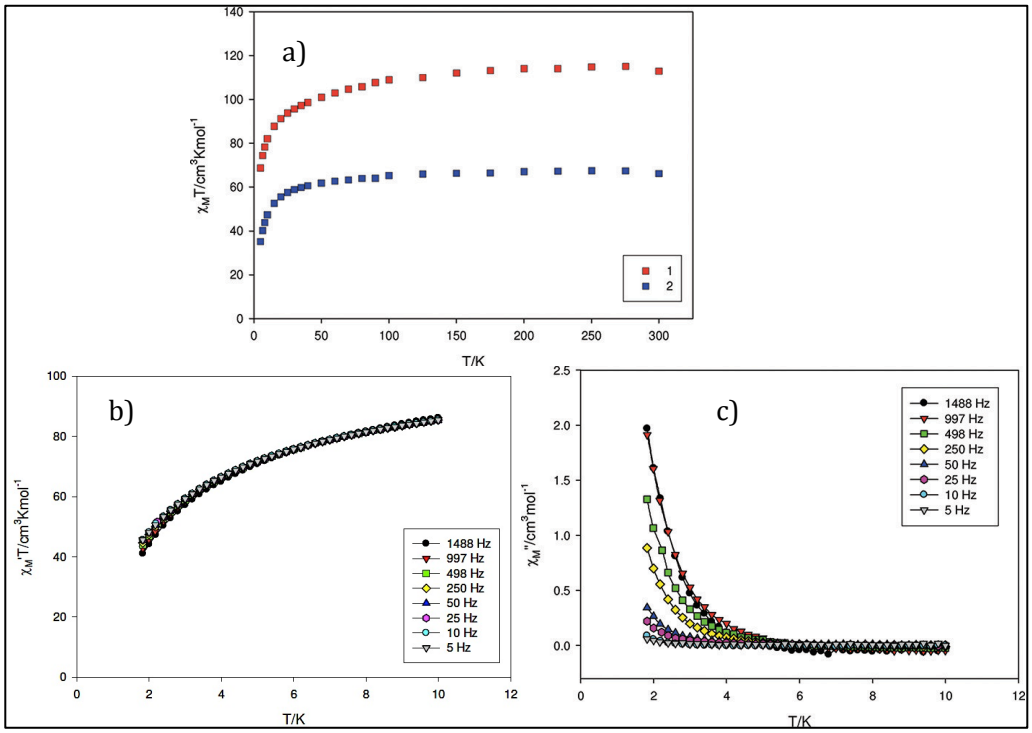

Figure 1.67 a) Plot of $\chi_M T$ *vs.* T for complexes **1.51** (red squares) and **1.52** (blue squares), b) in-phase (χ'), and c) out-of-phase (χ'') signals for **1.51** in a 3.5 G oscillating at various frequencies. Reproduced with permission from Ref. 121.

Ac susceptibility measurements show that the molecule exhibits temperature-dependent in phase (χ') signals at about 7.5 $cm^3mol^{-1}K$ from 4 down to 0 K, Figure 1.67(b), and out-of-phase (χ'') signals below 5 K, Figure 1.67(c). This behaviour is indicative of slow relaxation of magnetization, suggesting that **1.51** is an SMM.[121] Solid-state photoluminescence studies were carried out on **1.53** at room

temperature, Figure 1.68. At this temperature, no emission for the free organic ligand hmpH was observed, but some of the expected transitions, $^5D_0 \rightarrow {}^7F_J$ (J = 0 – 4) transitions were observed at λ = 593, 616, 652, and 697 nm. In addition emission peaks were observed below 590 nm most likely due to transitions from $^5D_1$ and $^5D_2$ excited states to the ^7F_J levels.

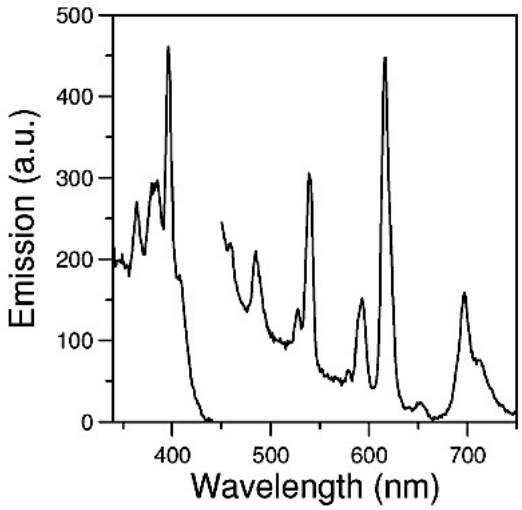

Figure 1.68 The solid-state emission spectra of **1.53** at 396 nm. Reproduced with permission from Ref. 121.

Over the past few decades, the search for new SMMs, which continues to be actively pursued, has led to interesting discoveries concerning the structural and magnetic properties of 3*d*- and 4*f*- metal complexes. Despite the successful use of pyridine-based alkoxide ligands for the preparation of coordination clusters, there has been limited progress in exploring the coordination chemistry of these ligands for the discovery of new multifunctional materials that includes chiral SMMs for potential applications in the field of multiferroics. Given that this is currently an area of intense scientific interest, it serves as a major goal for the research described in Chapter 3 of this thesis.

CHAPTER 2 – RESULTS AND DISCUSSION

PROJECT 2- Dy(III) and Tb(III) complexes of a p-tert-butylcalix[4]arene macrocycle: towards dual property polynuclear Ln-SMMs

2.1 Preface

In recent years the Pilkington group has been investigating the use of crown ether macrocycles e.g. **L2.1** for the preparation and study of dual property Ln(III)-SMMs.[122] Given that these ligands are neutral, *ac* magnetic susceptibility and photoluminescence studies reveal that the energy barriers for their resulting Dy(III) complexes are small, which is problematic for any practical applications.[122] We thus extended our approach to exploit a second family of tetra-anionic macrocycles which should facilitate stronger metal-ligand interactions giving rise to a larger crystal field splitting of the M_J states and thus higher energy barriers. The objectives of this project are therefore to study the coordination chemistry of a *p-tert*-butylcalix[4]arene (TBC4) macrocycle **L2.2**, together with Tb(III) and Dy(III) ions for the preparation of polynuclear SMMs with larger energy barriers, thereby moving one step closer towards the realization of Ln-SMMs suitable for technological applications.

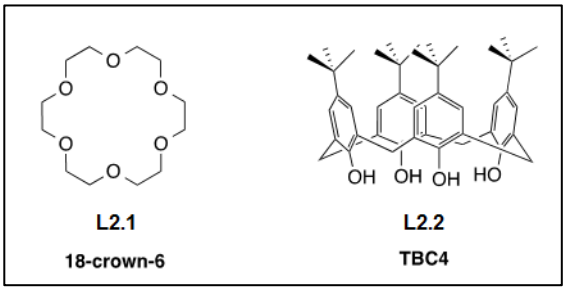

Figure 2.1 Molecular structures of 18-crown-6 (**L2.1**) and TBC4 (**L2.2**).

In addition, we were also interested in investigating the photoluminescene properties of these complexes to assess whether or not they are suitable candidates for the discovery of emissive SMMs. As previously mentioned, the polyphenolic substituents on the lower rim of TBC4 ligands renders them excellent candidates for coordination to hard Ln(III) centers such as Dy and Tb.[97,98] Furthermore, the bulky *tert*-butyl groups of TBC4 should also serve to isolate the magnetic centers in a polynuclear cluster, preventing significant intermolecular interactions between molecules which is a prerequisite for SMM properties.

With respect to utilizing TBC4 ligands for the preparation of polynuclear Ln(III)-SMMs, the first investigations were carried out by Dalgarno and Brechin in 2012.[97] In these studies, reaction of $LnCl_3{\cdot}6H_2O$, TBC4 and Et_3N in 10 mL of a 1:1 v/v ratio of DMF/ROH (R = Me and Et) afforded solutions from which crystals of polynuclear Ln(III)-complexes with stoichiometry $[Ln_6(TBC4)_2O_2(OH)_{3.32}Cl_{0.68}(HCO_2)_2(DMF)_8(H_2O)_{0.5}]$ (**2.1a-d**) (Ln = Gd(III), Tb(III), Dy(III), and Ho(III)) were isolated by slow evaporation of the reaction mixture.[97] Unfortunately, the quality of the single crystals were poor and only the partial X-ray crystal structure of the Tb(III) complex **2.1b** was elucidated from synchrotron data.[97] This complex is reported to crystallize in the monoclinic space group C2/m, comprising of a polymetallic core of six Tb(III) ions capped by two fully deprotonated TBC4 ligands, coordinating via their lower rim polyphenolic substituents. The structure contains three crystallographically independent Tb(III) ions in the asymmetric unit with the remaining three metal centers generated via symmetry. The polymetallic core is organized into an octahedral arrangement of six Tb(III) ions, Figure 2.2 (right).

Resolving the disorder between the chloride and hydroxide ligands in the core of the cluster proved to be problematic. The cavities of the two fully deprotonated TBC4 ligands house the apical Tb1 ions which have either 9-coordinate, tri-capped trigonal prismatic, or 8-coordinate square anti-prismatic geometries depending on the presence of aquo ligands with partial occupancy which could not be fully assigned. In contrast, the Tb2 and Tb3 ions which form the equatorial plane are 8-coordinate, with the remaining coordination sites filled by terminally bonded DMF molecules, giving rise to distorted square antiprismatic geometries, Figure 2.2.

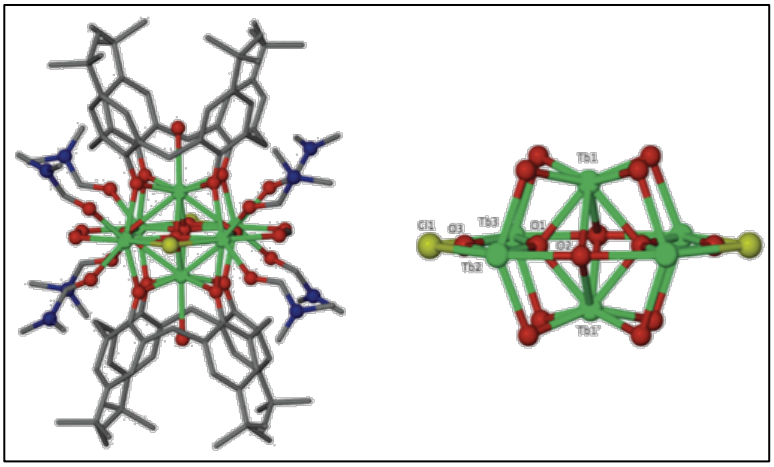

Figure 2.2 (left) Molecular structure and (right) the magnetic core of the Tb_6 $TBC4_2$ cluster (**2.1b**). Colour scheme: Tb^{III} dark green, O red, N dark blue, C grey, and Cl light green. Reproduced with permission from Ref. 96.

Although no full X-ray crystal structures of the other three Ln(III)-complexes were reported, the authors reported that the unit cell parameters are all consistent with them being isostructural with **2.1b**.[97] *Dc* magnetic susceptibility data for the isotropic Gd(III) complex, **2.1a** supports the presence of a spin only paramagnetic Gd_6 moiety until T = 75 K, where the value of χT drops rapidly to reach a value of 22.5 emu·K·mol^{-1} at 2 K, attributed to the presence of weak antiferromagnetic

exchange interactions.[97] Unfortunately, no *dc* data were reported for complexes (**2.1a, c** and **d**). Although no *ac* magnetic susceptibility data were provided for any of the complexes in either the paper or the supplementary information, the authors state that they do not display any frequency dependence in the out-of-phase component, which they describe as 'surprising' given that the Dy(III) analogue is structurally similar to the square based pyramidal complex $[Dy_5O(OtBu)_{13}]$ which is reported to have an extremely large energy barrier of 528 K.[123]

Following these studies, Wang *et al*. reported a second family of $Ln_6[TBC4]_2$ clusters prepared *via* hydrothermal methods.[98] In this case, reaction of $Ln(NO_3)_3{\cdot}6H_2O$ (0.15 mmol), TBC4 (0.1 mmol), and Et_3N (1 mL) in 10 mL of a 1:1 v/v ratio of DMF/MeOH at 130°C for 3 days, followed by cooling to 20°C at 4 °C/h afforded single crystals of three complexes with stoichiometry $[Ln_6(\mu_4\text{-}O)_2(TBC4)_2(NO_3)_2(HCOO)_2(CH_3O)_2(DMF)_4(CH_3OH)_4]$ (**2.2a-c**), where Ln_6 = Gd(III), Tb(III), and Dy(III) for **a-c** respectively, Figure 2.3.[98]

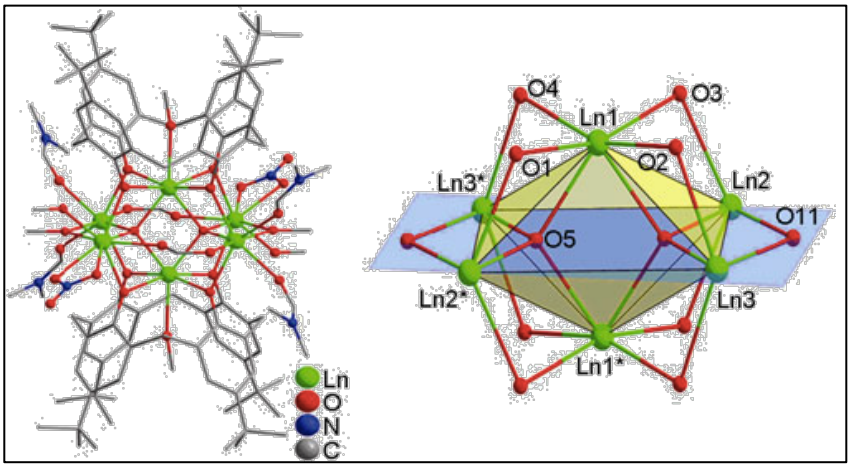

Figure 2.3 (left) Molecular structure of the $Ln_6[TBC4]_2$ clusters (**2.2a-c**) and their polymetallic core (right). Reproduced with permission from Ref. 98.

All three Ln(III) complexes were isostructural and crystallized in the triclinic space group $P\bar{1}$. Structural investigations reveal the clusters comprise of three crystallographically independent Ln(III) sites, (Ln1 to Ln3) that together with their symmetry equivalent ions crystallize in the same polymetallic Ln_6 core reported earlier by Brechin *et al.*, Figure 2.3 (right). In sharp contrast to the previous report however, the structures of **2.2a-c** were all fully refined and the coordination geometries of the three crystallographically independent Ln(III) ions were fully determined. In this respect the core of these clusters comprise of two apical Ln1 ions that are coordinated by four phenoxide oxygen atoms from a TBC4, two μ_4-O^{2-} units and a methanol oxygen giving rise to 7-coordinate geometry. The four peripheral Ln2 and Ln3 ions are coordinated by phenoxide oxygen atoms from two different TBC4's, one μ_4-O^{2-} moiety, one methanol and a formate oxygen, with the two remaining coordination sites of Ln2 occupied by oxygen atoms from DMF, completing 7-coordinate geometry, while two nitrate oxygen atoms and one methanol complete the 8-coordinate geometry for Ln3.[98]

Contrary to the first study, the out of phase component of the *ac* susceptibility data for the Dy_6 cluster (**2.2c**) exhibited a frequency dependence, that has not been reliably modeled.[98] The marked differences in the magnetic properties between these two previously reported $Dy_6(TBC4)_2$ clusters could in part be due to the different coordination geometries of their Ln(III) ions which are summarized in Table 2.4, (*vide infra*).

In order to shed more light on the discrepancy in the literature regarding the magnetic properties of *p-tert*-butylcalix[4]arene supported Ln(III) clusters we

turned our attention towards the development of a synthetic strategy for the growth of X-ray quality single crystals applying conventional coordination chemistry rather than hydrothermal synthesis. Our primary objectives were therefore to carry out comprehensive magnetostructural and optical studies on *p-tert*-butylcalix[4]arene-supported Dy(III) and Tb(III) complexes to determine whether or not they display SMM and/or photoluminescence properties.

2.2 Synthesis and Structural Studies

Following the reaction conditions reported by Dalgarno and Brechin[97] we observed that single crystals of the resulting coordination complexes grow very quickly and that also in our hands they do not diffract well enough for a full structure determination on our Apex II X-ray diffractometer.[124] Given these problems we thought that slowing down both the rate of formation of the complex and the subsequent growth of single crystals might help the isolation of better quality crystals for conventional single crystal X-ray diffraction experiments. In order to address this challenge we proposed to start from an 18-crown-6 (18C6) complex of the appropriate lanthanide salt. Our thinking was that substitution of the 18C6 macrocycle by the fully deprotonated TBC4 ligand may slow down the rate of cluster formation and subsequently afford better quality crystals. In addition, we were also interested to investigate whether or not the presence of the 18C6 macrocycle would alter the structural topology of the resulting coordination complexes in any way.

Following this methodology, one equivalent of commercially available 18C6 was heated with one equivalent of $Ln(ClO_4)_3 \cdot 6H_2O$ (Ln(III) = Dy and Tb) in a 1:3 ratio of MeCN/MeOH at 61˚C for 2.5 hrs, followed by the addition of a solution of TBC4 (0.21 g, 0.32 mmol) in 1:1 ratio of a mixture of DMF/MeOH (20 mL). After 5 min, Et_3N (1.2 mL) was added into the resulting mixture which was stirred under the same conditions for a further 5 hrs at 61˚C. After two days, slow evaporation of the reaction mixture at room temperature afforded colourless block shaped crystals of $[Dy_6(TBC_4)_2(DMF)_4(HCO_2)_2(HCO_3)_2(\mu_4\text{-}O)_2(OH)_2(H_2O)_4] \cdot 7MeCN \cdot 7MeOH$ for (**2.3**) and $[Tb_6(TBC4)_2(DMF)_4(HCO_2)_2(HCO_3)_2(\mu_4\text{-}O)_2(OH)_2(H_2O)_2] \cdot 10MeCN \cdot 8H_2O \cdot 3MeOH$ for (**2.4**) that were initially characterized by elemental analysis, IR, UV-vis spectroscopy, and mass spectrometry, Table 1.1. In this respect, the formate is formed *via* the *in situ* oxidation of the MeOH solvent ($OH^- + CO \rightarrow HCO_2^-$)[97] and the hydrogen carbonate is generated by the dissociation of the carbonic acid (H_2CO_3) which is formed *via* the hydration reaction of CO_2 with water ($CO_2 + H_2O \rightarrow H_2CO_3 \rightarrow HCO_3^- + H^+$). Both complexes display very similar IR spectra; an intense band at ν = 3520 cm^{-1} is assigned to the O-H stretch of the terminal hydroxyl ligands and several bands from ν = 1540 to 1300 cm^{-1} are consistent with the stretching vibrations of the aromatic rings of the TBC4 ligands. In addition to these bands, a C=O str for the DMF ligands is present at ν = 1656 cm^{-1}.[125] The UV-vis spectra of the uncoordinated TBC4 ligand and both Ln^{III}_6 complexes recorded in MeCN are compared in Figure 2.4. The free ligand shows three absorption bands at λ = 208, 279, and 287 nm, which based on literature are assigned to the singlet $\pi \rightarrow \pi^*$ transitions of the TBC4 ligand.[125] Both complexes possess three absorption bands

between λ = 209 and 305 nm, which are characteristic of the free ligand, and the shift of these bands to higher wavelengths is indicative of coordination to the lanthanide ions. The TOF mass spectrum of **2.3** displays a peak at *m/z* = 2341 assigned to $[M\text{-}TBC4+H_2O]^+$ (75%), while the ESI mass spectrum of **2.4** displays a peak at *m/z* = 2976 assigned to $[M\text{-}(OH)_2\text{-}H_2O+H]^+$ (25%). The CHN data for both complexes is within the acceptable $\pm$0.4% limits for (**2.3**) and (**2.4**), which was further corroborated by the determination of their molecular structures via single crystal X-ray diffraction.

Table 2.1 Summary of spectroscopic data for the $Ln_6[TBC4]_2$ complexes **2.3** and **2.4.**

Complex		%C	%H	%N	MS (*m/z*)	λ_{max} (nm) (ε / L·mol^{-1}·cm^{-1})
2.3	Found	44.42	5.13	4.44	2341	209 (318000)
$Dy_6[TBC4]_2$	Calcd	44.33	5.80	4.55	$[M\text{-}TBC4+H_2O]^+$ (75%)	279 (44600) 287 (41400)
2.4	Found	44.01	6.15	6.00	2976	212 (350400)
$Tb_6[TBC4]_2$	Calcd	43.98	5.81	5.65	$[M\text{-}(OH)_2\text{-}H_2O+H]^+$ (25%)	297 (39800) 305 (34800)

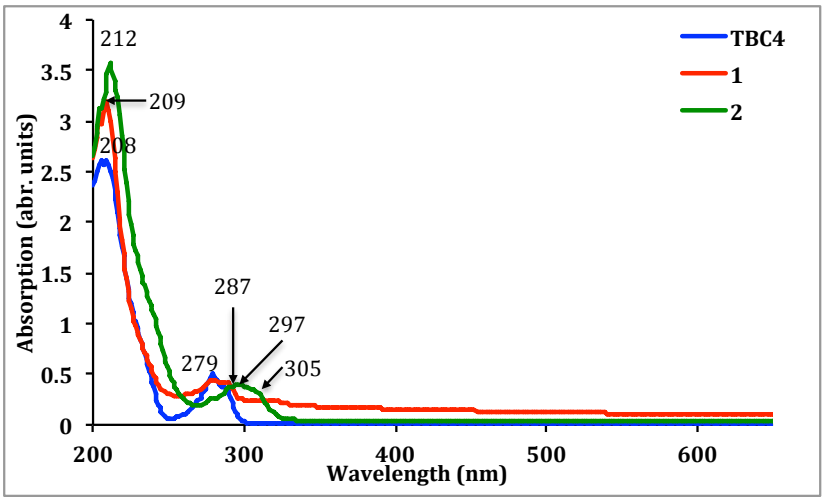

Figure 2.4 UV-Vis spectra of the TBC4 ligand **L2.2** (blue), and complexes **2.3** (red) and **2.4** (green), at room temperature in 10^{-5} M solution of MeCN.

For both complexes, single crystals were stored in their mother liquor and then suspended in paraffin oil and mounted on a nylon loop before being flash cooled to 150 K on the X-ray diffractometer to prevent any loss of solvent from the crystal lattice. The raw crystallographic data for **2.3** was integrated as a TWIN in the Bruker APEX II suite.[124] For both complexes, disordered solvent was removed from the crystallographic model using the SQUEEZE[126] command in PLATON.

The Dy(III) cluster **2.3** crystallizes in the monoclinic space group, *C*2/*m*. The asymmetric unit comprises three Dy(III) ions, half a TBC4 ligand together with a DMF, one hydroxide, two water ligands, an oxide linker, a formate and a hydrogen carbonate ligand, Figure 2.5. All three Dy(III) ions sit on crystallographic special positions, (point-group symmetry elements of the space group *C2/m)*.

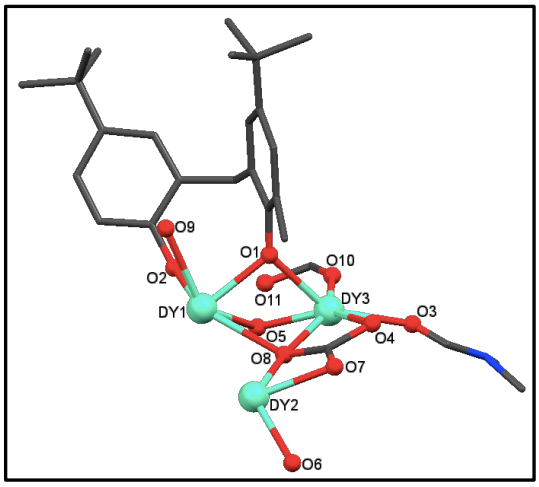

Figure 2.5 Molecular structure of the asymmetric unit of the $Dy_6[TBC4]_2$ cluster **2.3**. H-atoms are removed for clarity. Colour scheme: Dy cyan, O red, N blue, and C black.

For comparison, the unit cell parameters for the Brechin $Tb_6[TB4C]_2$ (**2.1b**), Wang $Dy_6[TB4C]_2$ (**2.2c**) and our $Dy_6[TB4C]_2$ and $Tb_6[TB4C]_2$ complexes (**2.3**) and (**2.4**) are summarized in Table 2.2.

Table 2.2 Unit cell parameters for **2.1b**[97], **2.2c**[98] and our complexes **2.3** and **2.4**.

Unit cell parameters	Brechin Tb_6 (**2.1b**)[97]	Wang Dy_6 (**2.2c**)[98]	Dy_6 (**2.3**) (this work)	Tb_6 (**2.4**) (this work)
Temperature (K)	100	185	150	150
a, b, c axes (Å)	23.0463(28), 27.6415(32), 15.0835 (26)	11.8708(4), 14.5023(4), 17.3226(5)	22.957(3) 28.023(5) 15.2098(18)	23.484(3) 28.178(4) 15.647(2)
α, β, γ (°)	90, 129.005(1), 90	101.8210(10), 93.7430(10), 98.9210(10)	90, 128.736(4), 90	90, 129.968, 90
Cell volume (Å)^3	7305.15	2863.01(4)	7632.6(19)	7935.3(18)
Crystal System	monoclinic	triclinic	monoclinic	monoclinic
Space Group	$C2/m$	$P\bar{1}$	$C2/m$	$C2/m$
$R[F^2 > 2\sigma(F^2)]$, $wR(F^2)$	0.0484, 0.1622	0.0344, 0.1005	0.090, 0.260	0.090, 0.260

X-ray diffraction studies of **2.3** reveal the magnetic core is comprised of an octahedral arrangement of Dy(III) ions, three of which are crystallographically unique (Dy1, Dy2 & Dy3), capped by two fully deprotonated TBC4 ligands, Figures 2.6 and 2.7.

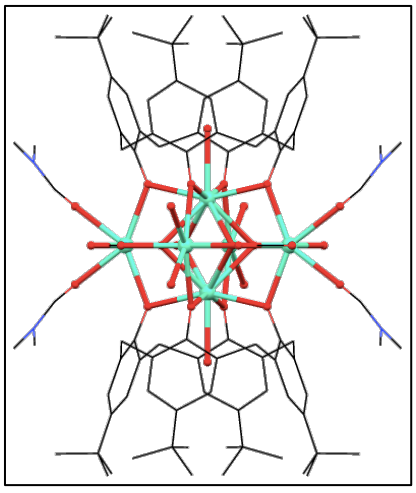

Figure 2.6 Molecular structure of $Dy_6[TBC4]_2$ (**2.3**). Solvent molecules and hydrogen atoms are omitted for clarity. Colour code: Dy cyan, O red, N blue, and C black.

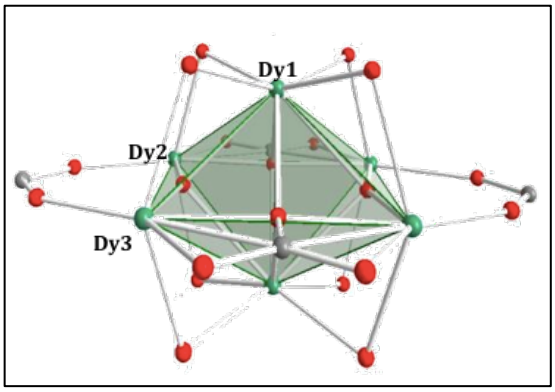

Figure 2.7 Structure of the Dy_6 core of **2.3** showing the crystallographically independent apical Dy1 and peripheral Dy2 and Dy3 ions. The disorder in the formate ligand is omitted for clarity.

Within the octahedron, all six metal ions are connected internally by μ_4-O^{2-} bridges and the edges of the equatorial plane formed by the Dy2 and Dy3 ions are linked further via a combination of disordered formate as well as hydrogen carbonate ligands, with the remaining coordination sites filled by terminally bound hydroxide, water and/or DMF ligands, Figure 2.6. The Dy···Dy distances within the core of the cluster are Dy1···Dy3 = 3.568 Å; Dy1···Dy2 = 3.577 Å and Dy2···Dy3 = 4.381 Å. The apical Dy1 ions are 9-coordinate, bound to four oxygen atoms (O1 and O2) of the same deprotonated TBC4 ligand in a μ_2-fashion, two μ_4-O^{2-} (O5) linkers, two oxygen atoms from a hydrogen carbonate (O8) and one oxygen atom (O9) from a water molecule residing within the cavity of the *p-tert*-butylcalix[4]arene, Figure 2.8.

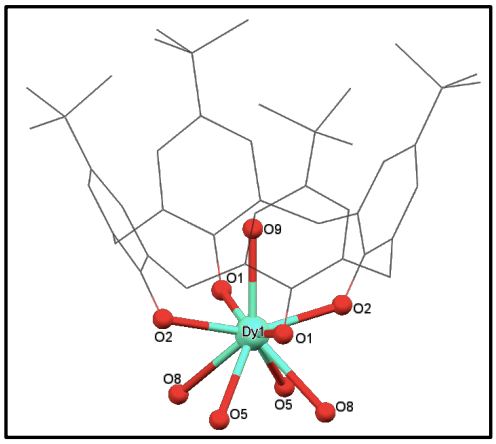

Figure 2.8 Coordination geometry of the apical Dy1 ion in $Dy_6[TBC4]_2$ (**2.3**). Colour code: Dy cyan, O red, N blue, and C grey.

The peripheral Dy2 ions are coordinated to two μ_2-oxygen atoms from two different TBC4 ligands, a μ_4-oxide (O5), one terminal hydroxide (O6), one terminal water (O6), one formate oxygen (O11), and two oxygen atoms (O7 and O8) from a hydrogen carbonate ligand to afford an 8-coordinate geometry, Figure 2.9 (left).

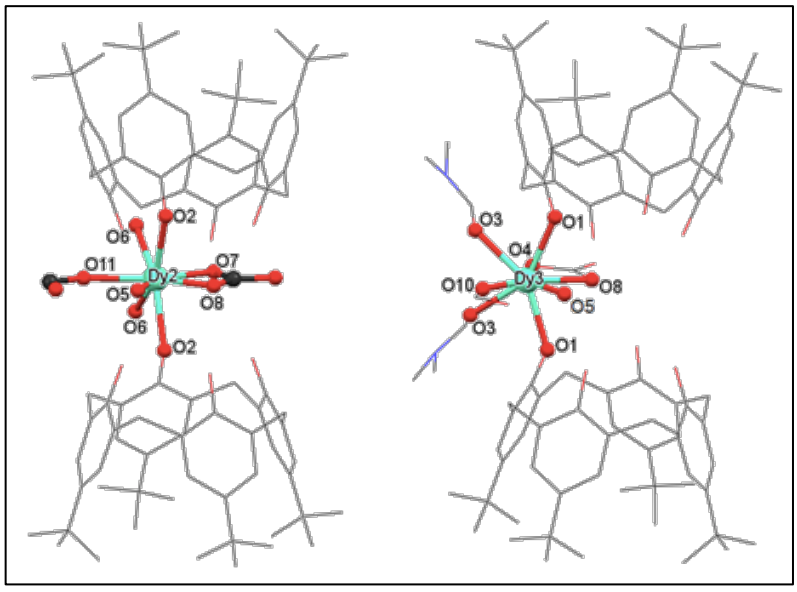

Figure 2.9 Coordination geometries of the peripheral Dy2 and Dy3 ions of **2.3**. Colour code: Dy cyan, O red, N blue, and C grey.

Lastly, the peripheral Dy3 ions are coordinated to two oxygen atoms from two TBC4 ligands, (O1), a μ_4-oxide (O5), two oxygen atoms from two DMF molecules (O3), two oxygen atoms from a hydrogen carbonate group (O8 and O4) and one formate oxygen atom (O10), also affording 8-coordinate geometry, Figure 2.9 (right). It should also be noted that the carbon atom of the formate ligand is disordered over two positions.

The coordination geometries of the three crystallographically independent Dy(III) ions were further studied by continuous shape measures (CSMs).[127] In this respect, the apical Dy1 ion was determined to be closest in geometry to a spherical capped square antiprism (**a**), whereas the peripheral Dy2 and Dy3 ions both adopt triangular dodecahedral geometries, (**b**) and (**c**) respectively, Figure 2.10. The deviations from ideal C_{4v} symmetry for Dy1, and D_{2d} symmetry for Dy2 and Dy3 are summarized in Table 2.3.

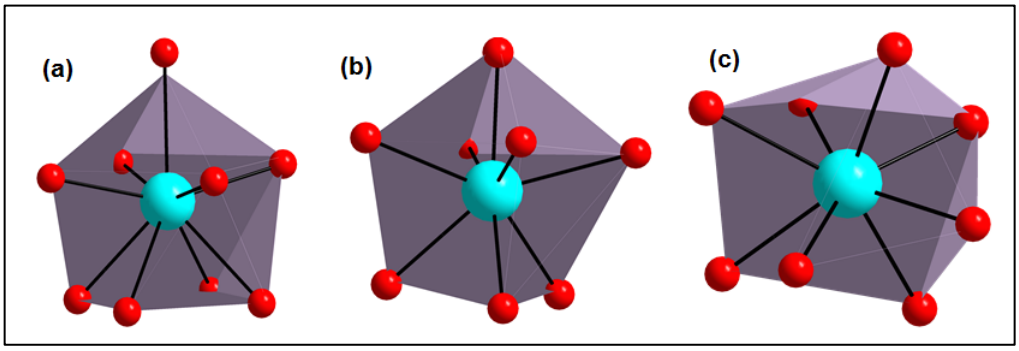

Figure 2.10 Coordination spheres of Dy1 (a), Dy2 (b), and Dy3 (c) in **2.3**, superimposed on their idealized polyhedra (purple) determined from CSMs. [127]

Table 2.3 Continuous shape measures (CSMs) for the apical Dy1 ion and the peripheral Dy2 and Dy3 ions in $Dy_6[TBC4]_2$ (**2.3**). The values in red indicate the closest polyhedron which best describes the geometry according to CSMs.[127]

Polyhedron	Dy1
EP-9	37.25
OPY-9	21.51
HBPY-9	21.89
JTC-9	17.00
JCCU-9	10.89
CCU-9	9.95
JCSAPR-9	1.34
CSAPR-9	0.52
JTCTPR-9	2.25

Polyhedron	Dy2	Dy3
OP-8	32.26	32.47
HPY-8	24.54	24.67
HBPY-8	15.74	15.86
CU-8	8.85	8.79
SAPR-8	3.03	3.00
TDD-8	0.20	0.18
JGBF-8	15.25	15.23
JETBPY-8	30.23	30.61
JBTPR-8	3.54	3.57
BTPR-8	2.72	2.80
JSD-8	3.13	3.15
TT-8	9.45	9.40
ETBPY-8	25.79	25.77

Interestingly, the coordination geometries of the three crystallographically independent Dy(III) ions are very similar to those reported for the Tb(III) ions in the Brechin structure, but differ significantly from the $Dy_6[TBC4]_2$ cluster prepared by hydrothermal methods as shown in Table 2.4.

Table 2.4 Summary of the coordination geometries observed for the Ln(III) ions in $[Ln]_6[TBC4]_2$ clusters.

Ln(III) ion	$Tb_6[TBC4]_2$ (2.1b) Brechin *et al.*[97]	$Dy_6[TBC4]_2$ (2.2c) Wang *et al.*[98]	$Dy_6[TBC4]_2$ (2.3) This work	$Tb_6[TBC4]_2$ (2.4) This work
Apical, Ln1	8/9	7	9	8
Peripheral, Ln2	8	7	8	8
Peripheral, Ln3	8	8	8	8

Selected bond lengths and angles for **2.3** are presented in Table 2.5. Although hydrogen atoms could not be located in the difference map, for charge balance considerations, two of the four peripheral O6 ligands were assigned to terminal hydroxyl and two to neutral water molecules.

Table 2.5 Selected bond lengths (Å) and bond angles (°) for **2.3**.

Bond Distance (Å)		**Bond Distance (Å)**	
Dy1–O1	2.324(8)	Dy2-O11$^{(b)}$	2.354(15)
Dy1-O2	2.307(10)	Dy2-O2$^{(a)}$	2.408(10)
Dy1–O5	2.505(17)	Dy2-O6	2.430(13)
Dy1–O8	2.597(18)	Dy2-Dy1$^{(b)}$	2.5767(12)
Dy1–O9	2.55(2)	Dy3-O5	2.21(3)
Dy1–Dy1$^{(b)}$	3.445(2)	Dy3-O8	2.24(2)
Dy1–Dy3	3.5680(9)	Dy3-O10	2.280(19)
Dy1–Dy3$^{(b)}$	5.5681(9)	Dy3-O4	2.330(18)
Dy2-O5$^{(b)}$	2.25(2)	Dy3-O3	2.393(1)
Dy2-O8	2.26(2)	Dy3-O1	2.394(9)
Dy2-O7	2.354(17)	Dy2-O11$^{(b)}$	2.354(15)
Bond Angle (°)		**Bond Angle (°)**	
O2—Dy1—O2$^{(a)}$	154.1 (5)	O1—Dy1—O5$^{(b)}$	131.3 (6)
O2—Dy1—O1$^{(a)}$	87.5 (3)	O5—Dy1—O5$^{(b)}$	93.1 (7)
O2i—Dy1—O1$^{(a)}$	86.9 (3)	O2—Dy1—O9	77.1 (3)
O2—Dy1—O1	86.9 (3)	O2i—Dy1—O9	77.1 (3)
O2i—Dy1—O1	87.5 (3)	O1i—Dy1—O9	77.3 (2)
O1i—Dy1—O1	154.5 (5)	O1—Dy1—O9	77.3 (2)
O2—Dy1—O5	70.0 (5)	O5—Dy1—O9	133.4 (4)
O2$^{(a)}$—Dy1—O5	130.5 (6)	O8—Dy3—O1	73.4 (3)
O1$^{(a)}$—Dy1—O5	131.3 (6)	O10—Dy3—O1	96.8 (3)
O1—Dy1—O5	69.1 (5)	O4—Dy3—O1	95.5 (3)
O2—Dy1—O5$^{(b)}$	130.5 (6)	O3—Dy3—O1	147.8 (4)
O2$^{(a)}$—Dy1—O5$^{(b)}$	70.0 (5)	O3$^{(c)}$—Dy3—O1	74.2 (4)
O1$^{(a)}$—Dy1—O5$^{(b)}$	69.1 (5)	O1$^{(c)}$—Dy3—O1	138.0 (4)
O2$^{(a)}$—Dy1—O8$^{(b)}$	131.5 (5)	O1$^{(a)}$—Dy1—O8	131.4 (5)
O1$^{(a)}$—Dy1—O8$^{(b)}$	68.3 (5)	O1—Dy1—O8	68.3 (5)
O1—Dy1—O8$^{(b)}$	131.4 (5)	O5—Dy1—O8	62.4 (7)
O5—Dy1—O8$^{(b)}$	63.3 (7)	O5$^{(b)}$—Dy1—O8	63.3 (7)

O5[b]—Dy1—O8[b]	62.4 (7)	O9—Dy1—O8	131.5 (4)
O9—Dy1—O8[b]	131.5 (4)	O8[b]—Dy1—O8	96.9 (7)
O2—Dy1—O8	131.5 (5)	O1[a]—Dy1—O8	131.4 (5)
Dy1—O1—Dy3	98.3 (3)	Dy1—O2—Dy2[b]	98.6 (4)
Dy3—O5—Dy1[b]	98.2 (8)	Dy2[b]—O5—Dy1[b]	97.4 (7)
Dy1—O5—Dy1[b]	86.9 (7)	Dy2—O8—Dy1	94.7 (7)
Dy3—O8—Dy1	94.7 (7)	O2[a]—Dy2—O2[b]	136.8 (5)
O5[b]—Dy2—O8	72.9 (9)	O5[b]—Dy2—O6[c]	132.0 (5)
O5[b]—Dy2—O7	140.2 (7)	O8—Dy2—O6[c]	129.0 (5)
O8—Dy2—O7	67.4 (8)	O7—Dy2—O6[c]	77.0 (5)
O5[b]—Dy2—O11[b]	74.7 (7)	O11[a]—Dy2—O6[c]	74.9 (5)
O8—Dy2—O11[b]	147.6 (8)	O2[a]—Dy2—O6[c]	75.4 (4)
O7—Dy2—O11[b]	145.0 (6)	O2[b]—Dy2—O6[c]	147.7 (4)
O5[b]—Dy2—O2[a]	72.7 (3)	O8—Dy2—O6	129.0 (5)
O8—Dy2—O2[a]	72.9 (3)	O2[a]—Dy2—O6	147.7 (4)
O7—Dy2—O2[a]	95.2 (3)	O6[c]—Dy2—O6	72.4 (7)
O11[b]—Dy2—O2[a]	97.5 (2)	Dy1[b]—Dy1—Dy3[b]	61.133 (16)
Dy1[b]—Dy1—Dy3	61.133 (16)	Dy3—Dy1—Dy3[b]	122.27 (3)
Dy1—Dy2—Dy1[b]	57.58 (3)		

Symmetry code(s): (a) $-x+2, y, -z+1$; (b) $-x+2, -y, -z+1$; (c) $x, -y, z$.

Since all four of these atoms are symmetry related it is not crystallographically possible to distinguish between them based on their Dy-O bond distances. However, evidence for a mixture of both water and hydroxide ions is supported by the structure of the Dy_6 cluster reported by Wang *et al.*, which requires two peripheral methanol and two peripheral methoxide ligands, also for charge/balance considerations. In the latter case, due to the lower crystallographic symmetry of the cluster, these ligands are not crystallographically equivalent and so could be assigned based on their respective Dy-O bond distances.[97, 98]

A view of the crystal packing of the cluster is shown in Figure 2.11. Examination of the extended structure reveals that the clusters pack in layers where

the *p-tert*-butyl groups of the calix[4]arenes are sandwiched between the aromatic regions of TBC4 ligands from clusters in adjacent layers.

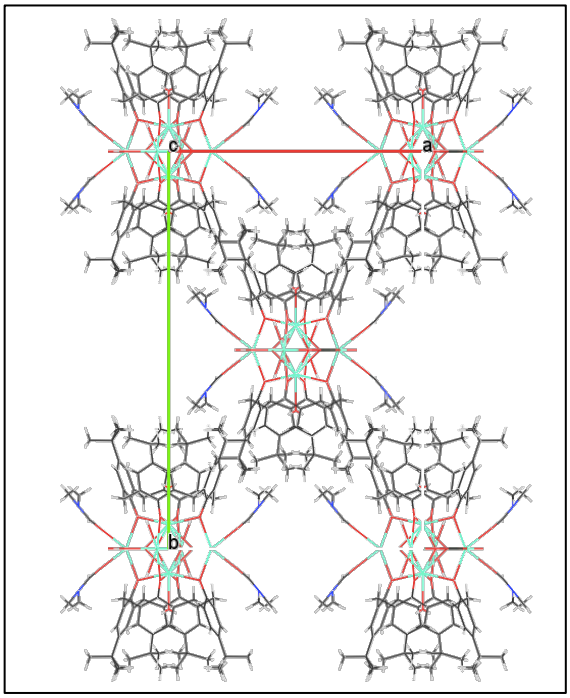

Figure 2.11 Crystal packing of the $Dy_6[TBC4]_2$ cluster **2.3**. View down the *c*-axis of the unit cell.

This in part serves to accommodate the DMF ligands coordinating to the peripheral Dy3 ions, affording voids in the crystal lattice which contain disordered solvent molecules. The shortest intermolecular Dy···Dy distances are 9.293 Å which demonstrates how well-isolated the Ln(III) ions are in the magnetic core by the bulky organic TBC4 macrocycles.

The Tb(III) analogue **2.4** also crystallizes in the monoclinic space group $C2/m$, Figure 2.12. Detailed analysis of its molecular structure shows it adopts the same hexanuclear structural topology, comprising three crystallographically unique Tb(III) ions (Tb1 to Tb3). The peripheral Tb2 and Tb3 ions form the corners of the

square of the octahedron and are linked by μ_4-O^{2-}, formate and hydrogen carbonate ligands, with DMF, water and hydroxide ligands completing their 8-coordinate geometries, Figure 2.12.

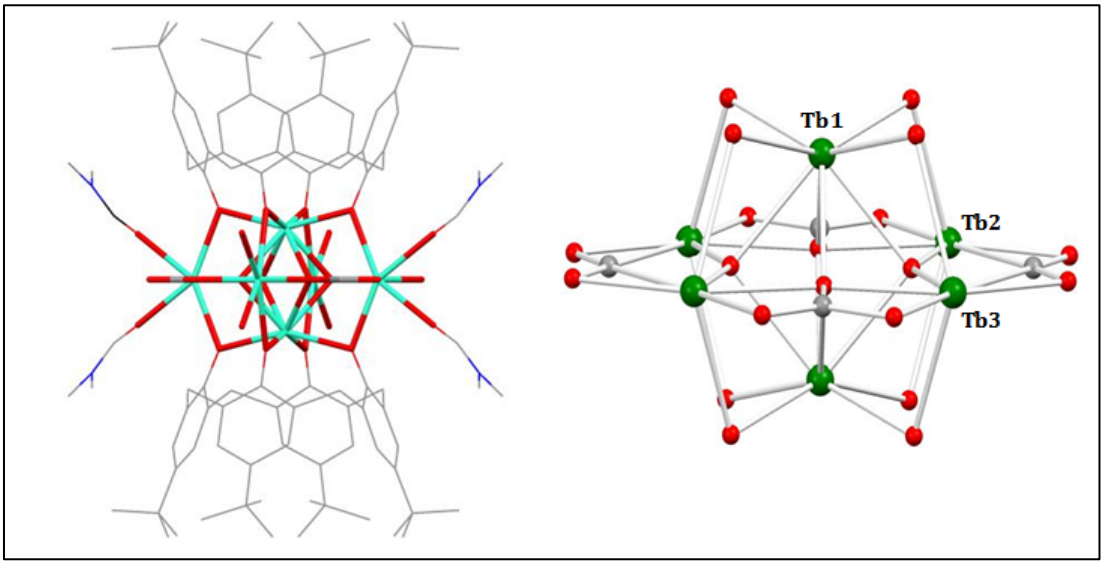

Figure 2.12 (Left) molecular structure of $Tb_6[TBC4]_2$ (**2.4**). Additional solvent molecules and hydrogen atoms are omitted for clarity. Colour scheme: Tb green, O red, N blue, and C grey; (right) structure of the Tb_6 magnetic core.

As observed previously for **2.3**, the Tb2 and Tb3 ions are coordinated by two hydroxide ions and two water molecules that are symmetry related satisfy the charge balance of the cluster. The Tb···Tb distances within the core of the cluster are Tb1···Tb2 = 3.594 Å; Tb1···Tb3 = 3.591 Å and Tb2···Tb3 = 4.493 Å. Interestingly, the coordination geometry of apical Tb1 ion is 8- rather than 9-coordinate since the coordinated water molecule present in the TBC4 cavity of the $Dy_6[TBC4]_2$ cluster is now absent from this complex. Selected bond lengths and angles for **2.4** are summarized in Table 2.6.

Table 2.6 Selected bond lengths (Å) and bond angles (°) for **2.4**.

Bond Distance (Å)		Bond Distance (Å)	
Tb1—O4	2.304 (12)	Tb2—O12	2.33 (2)
Tb1—O71	2.318 (16)	Tb2—O72	2.34 (3)
Tb1—O1	2.327 (11)	Tb2—O71	2.38 (2)
Tb1—O12	2.402 (16)	Tb2—O13	2.38 (3)
Tb2—O12	2.33 (2)	Tb2—O4$^{(a)}$	2.451 (12)
Tb2—O72	2.34 (3)	Tb2—O5	2.459 (16)
Tb2—O71	2.38 (2)	Tb3—O73$^{(b)}$	2.28 (3)
Tb1—Tb2$^{(b)}$	3.5941 (13)	Tb3—O12	2.29 (2)
Tb1—Tb1$^{(b)}$	3.411 (2)	Tb3—O3	2.409 (15)
Tb1—Tb3	3.5815 (14)	Tb3—O1	2.442 (12)
Bond Angle (°)		**Bond Angle (°)**	
O4—Tb1—O4$^{(a)}$	151.7 (6)	O12—Tb2—O5	131.8 (5)
O4—Tb1—O71	128.8 (6)	O72—Tb2—O5	76.2 (7)
O4^{i}—Tb1—O71	74.5 (6)	O71—Tb2—O5	133.4 (6)
O71—Tb1—O71$^{(b)}$	85.3 (9)	O13—Tb2—O5	77.5 (8)
O4—Tb1—O1	86.5 (4)	O4$^{(a)}$—Tb2—O5	73.8 (5)
O71—Tb1—O1	131.3 (5)	O4$^{(b)}$—Tb2—O5	150.8 (5)
O71$^{(b)}$—Tb1—O1	72.4 (5)	O4$^{(a)}$—Tb2—O4$^{(b)}$	135.4 (6)
O4—Tb1—O1^{i}	86.6 (4)	O12—Tb2—O5	131.8 (5)
O71$^{(b)}$—Tb1—O1$^{(a)}$	131.3 (5)	O72—Tb2—O5	76.2 (7)
O1—Tb1—O1$^{(a)}$	151.8 (6)	O72—Tb2—O5$^{(c)}$	76.2 (7)
O4—Tb1—O12	130.7 (6)	O13—Tb2—O5$^{(c)}$	77.5 (8)
O4$^{(a)}$—Tb1—O12	72.2 (5)	O71$^{(b)}$—Tb3—O73$^{(b)}$	79.5 (9)
O71$^{(b)}$—Tb1—O1$^{(a)}$	131.3 (5)	O71$^{(b)}$—Tb3—O12	59.5 (8)
O4—Tb1—O12	130.7 (6)	O73$^{(b)}$—Tb3—O12	139.0 (9)
O71—Tb1—O12	59.9 (6)	O71$^{(b)}$—Tb3—O3	134.4 (5)
O71$^{(b)}$—Tb1—O12	57.1 (7)	O73$^{(b)}$—Tb3—O3	77.0 (7)
O1—Tb1—O12	71.8 (5)	O12—Tb3—O3	131.6 (6)
O1$^{(a)}$—Tb1—O12	131.2 (6)	O71$^{(b)}$—Tb3—O3$^{(c)}$	134.4 (5)
O4$^{(a)}$—Tb1—O12$^{(b)}$	130.7 (6)	O3—Tb3—O3$^{(c)}$	76.3 (8)
O71—Tb1—O12$^{(b)}$	57.1 (7)	O71$^{(b)}$—Tb3—O1$^{(c)}$	71.3 (3)
O71$^{(b)}$—Tb1—O12$^{(b)}$	59.9 (6)	O73$^{(b)}$—Tb3—O1$^{(c)}$	96.6 (4)
O12—Tb1—O12$^{(b)}$	89.5 (7)	O12—Tb3—O1$^{(c)}$	71.7 (3)
O12—Tb2—O72	139.3 (9)	O3—Tb3—O1$^{(c)}$	149.6 (5)
O12—Tb2—O71	60.1 (8)	O3$^{(c)}$—Tb3—O1$^{(c)}$	73.3 (5)
O72—Tb2—O71	79.2 (9)	O71$^{(b)}$—Tb3—O12	59.5 (8)
O12—Tb2—O13	74.6 (10)	O73$^{(b)}$—Tb3—O12	139.0 (9)

O72—Tb2—O13	146.1 (11)	O1—Tb3—O11	96.6 (4)
O71—Tb2—O13	134.7 (10)	O3—Tb3—O11	74.5 (7)
O12—Tb2—O4$^{(a)}$	70.9 (3)	O12—Tb3—O11	77.6 (8)
O72—Tb2—O4$^{(a)}$	97.0 (4)	O73$^{(b)}$—Tb3—O11	143.4 (9)
O71—Tb2—O4$^{(a)}$	70.8 (3)	O71$^{(b)}$—Tb3—O11	137.1 (8)
O13—Tb2—O4$^{(a)}$	95.7 (4)	O3—Tb3—O1	73.3 (5)
O4$^{(a)}$—Tb2—O4$^{(b)}$	135.4 (6)	O12—Tb3—O3$^{(c)}$	131.6 (6)
Tb1—Tb2—Tb1$^{(b)}$	56.66 (4)	Tb1$^{(b)}$—Tb1—Tb2$^{(b)}$	61.669 (17)
Tb1$^{(b)}$—Tb1—Tb3$^{(b)}$	61.561 (18)	Tb3—Tb1—Tb2$^{(b)}$	76.34 (4)
Tb3—Tb1—Tb3$^{(b)}$	123.12 (4)	Tb3$^{(b)}$—Tb1—Tb2$^{(b)}$	77.53 (4)

Symmetry code(s): (a) $-x, y, -z$; (b) $-x, -y+1, -z$; (c) $x, -y+1, z$.

The coordination geometries of the three crystallographically unique Tb(III) ions were also further analyzed by continuous shape measures (CSMs), Figure 2.13.[127]

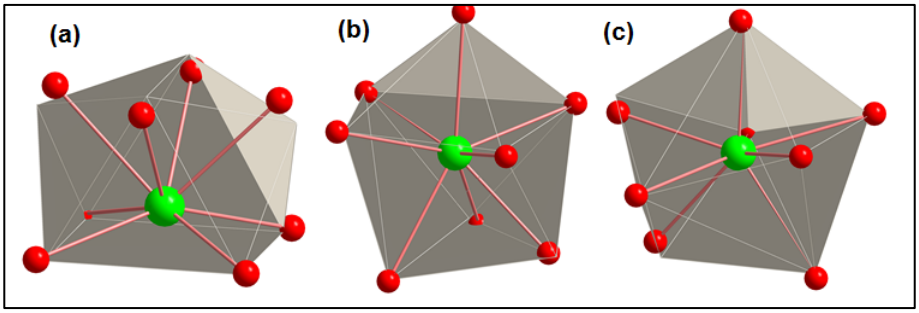

Figure 2.13 Coordination spheres (from the left to right) of Tb1 (a), Tb2 (b) and Tb3 (c) in **2.4**. Colour code: Tb green, red oxygen. Idealized polyhedra are shown in grey.

Although all three Dy(III) ions are 8-coordinate, the apical Tb1 is closest to trigonal prismatic geometry, while the peripheral Tb2 and Tb3 ions both have triangular dodecahedral geometries, Table 2.7.

Table 2.7 Continuous shape measures (CSMs) for the 8-coordinate Tb(III) ions in $Tb_6[TBC4]_2$ (**2.4**). The values in red indicate the closest polyhedron for each ion according to the CSMs.[127]

Polyhedron	Tb1	Tb2	Tb3
OP-8	27.46	31.38	31.41
HPY-8	25.22	22.52	22.48
HBPY-8	20.03	17.19	16.89
CU-8	12.82	9.98	10.03
SAPR-8	2.59	3.23	3.29
TDD-8	5.09	**0.43**	**0.46**
JGBF-8	18.51	14.66	15.13
JETBPY-8	29.22	29.59	29.86
JBTPR-8	3.53	3.48	3.62
BTPR-8	**1.60**	2.79	2.76
JSD-8	7.11	2.88	3.30
TT-8	13.48	10.58	10.37
ETBPY-8	25.03	25.44	25.35

The crystal packing of **2.4** is very similar to that discussed for the $Dy_6[TBC4]_2$ analogue **2.3**, however, the shortest intermolecular Tb···Tb distances in the crystal lattice are slightly longer at 9.735 Å, between symmetry related Tb2 ions, Figure 2.14.

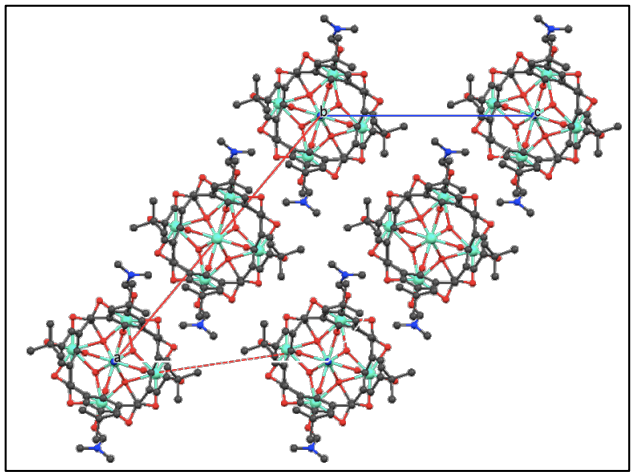

Figure 2.14 Crystal packing of $Tb_6[TBC4]_2$ (**2.4**). View down the *b*-axis of the unit cell. The shortest intermolecular Tb···Tb distance is shown as a red dashed line.

From Table 2.5 and 2.6, the average Ln-O bond lengths for the $Dy_6[TBC4]_2$ (2.370 Å) and $Tb_6[TBC4]_2$ (2.364 Å) clusters reveal that the difference in Ln-O bond lengths is in accordance with the lanthanide contraction.[128]

2.3 Magnetic Studies

The magnetic properties of both clusters were investigated by *dc* and *ac* susceptibility experiments. Variable temperature *dc* magnetic susceptibility data for $Dy_6[TBC4]_2$ (**2.3**) was collected in an applied field of 0.5 T between 5 and 300 K, Figure 2.15.

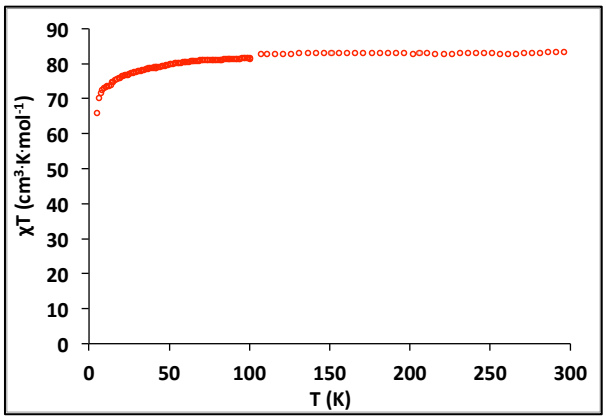

Figure 2.15 χT *vs* temperature for $Dy_6[TBC4]_2$ (**2.3**) in an applied field of 0.5 T from 5 – 300 K.

Above 100 K, the χT value of 83.40 $cm^3 \cdot K \cdot mol^{-1}$ is in good agreement with the expected value of 85.02 $cm^3 \cdot K \cdot mol^{-1}$ for six non-interacting Dy(III) ions ($^6H_{15/2}$, S = 5/2, L = 5, g = 4/3, J = 15/2), where $g_J = \frac{3}{2} + \frac{S(S+1)-L(L+1)}{2J(J+1)}$. Below 50 K the χT value gradually decreases, dropping to a minimum value of 65.90 $cm^3 \cdot K \cdot mol^{-1}$ at 5 K, most likely due to the depopulation of the M_J sublevels of the ground J multiplet. A plot of

1/χ vs. temperature was fit to the Curie-Weiss law, affording a Curie constant C of 83.80 $cm^3 \cdot K \cdot mol^{-1}$ and a Weiss constant θ of -2.2 K, Figure 2.16.

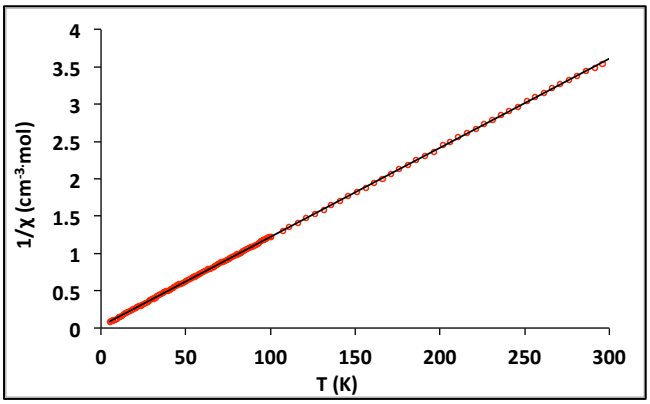

Figure 2.16 Plot of 1/χ *vs.* temperature for $Dy_6[TBC4]_2$ (**2.3**) in a field of 0.5 T from 5 – 300 K. The black line represents the best fit to the Curie-Weiss equation.

Ac susceptibility measurements were carried out for **2.3** below 70 K, in an oscillating field of 3.5 Oe, over a range of frequencies between 50 and 10,000 Hz, in various applied static fields ranging from 0 to 0.5 T. As mentioned in Chapter 1, the rationale behind carrying out such measurements is that for an SMM, the magnetization will lag behind the alternating current, resulting in a phase shift of the imaginary component of the *ac* susceptibility. Initially, *ac* measurements were carried out in a zero applied *dc* field. The resulting in-phase, χ' and out-of-phase, χ'' susceptibility *vs.* temperature plots are presented in Figure 2.17. Since the dynamic susceptibility, χ (ω), is a complex quantity with real (dispersion, χ' (ω)) and imaginary (absorption, χ" (ω)) components that are dependent on the angular frequency of the *ac* field.

$$\chi(\omega) = \chi'(\omega) - i\chi''(\omega) \qquad \textbf{(Eqn 2.1)}$$

As the *ac* frequency approaches the relaxation rate of the molecule, the observed in-phase susceptibility reduces and therefore, the out-of-phase component increases. A plot χ" *vs.* T will have a peak maximum at the temperature where $\omega = 1/\tau$. When the *ac* frequency increases, the peak maxima are shifted to higher temperatures and therefore the sign of an SMM is frequency dependence of the out-of-phase component in the *ac* magnetic susceptibility.

Although there are many examples of 'field-induced' SMMs in the chemical literature,[93,110] compounds which display slow relaxation of magnetization in the absence of a static *dc* are of greater interest. [94,110] We were very excited to observe frequency dependent magnetization in both the in and out of phase components of the *ac* magnetic susceptibility below 25 K. A clear separation between the susceptibility curves for each frequency is visible at low temperature, with a single maximum emerging around 10 K and a second maximum just visible below 8 K which is not quite resolved. The absence of this second maxima is likely due to the presence of fast relaxation processes such as quantum tunneling that are commonly observed in Ln-based SMMs.[129]

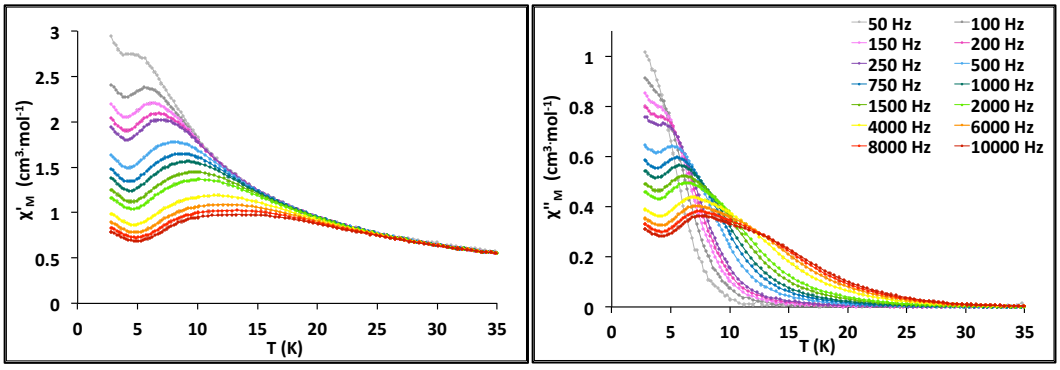

Figure 2.17 χ'(left) and χ''(right) *vs.* temperature for $Dy_6[TBC4]_2$ (**2.3**) from 3-35 K, in zero *dc* field.

In order to resolve the second maxima at low temperature, the *ac*-susceptibility experiments were repeated in several applied *dc* fields ranging from 0.03 to 0.5 T, Figure 2.18. The application of a small static *dc* field serves to quench, or partially quench the quantum tunneling processes by slightly perturbing the energies of the M_J states via the Zeeman effect, thus removing the degeneracy of the spin states between which the quantum tunneling occurs. The objective here is to apply as small a *dc* field as possible in order that any effective energy barrier is as close to the true energy barrier of the system in zero-field. In addition, the application of a small *dc* field ensures the magnetic response observed is not due to any additional magnetic phenomena such as long-range ordering. The χ' and χ" *vs*. temperature plots in 0.03, 0.1 and 0.5 T applied *dc* fields are presented in Figure 2.17. From this data it is apparent that in a field of 0.5 T the quantum tunneling is suppressed sufficiently that two maxima in both χ' and χ" are clearly resolved between 3-8 K ("low" temperature regime) and between 9-18 K ("high" temperature regime). In each temperature regime, the maximum in χ" shifts between adjacent temperature curves, confirming the frequency-dependent nature of the response.

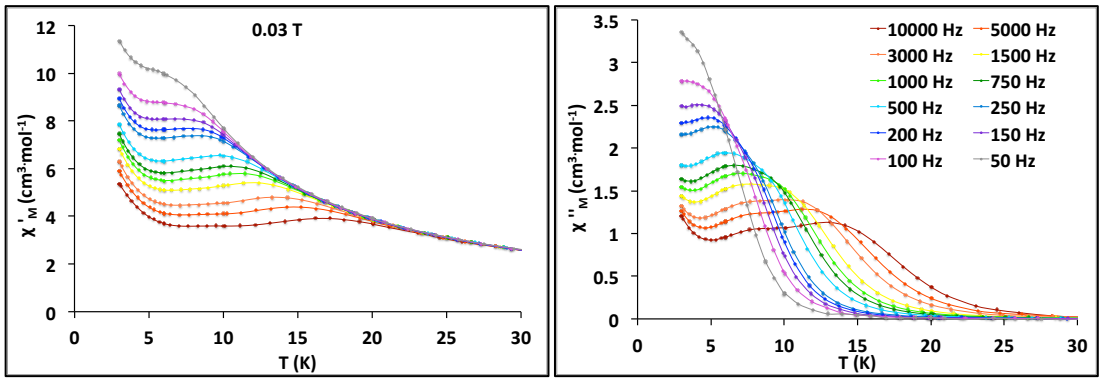

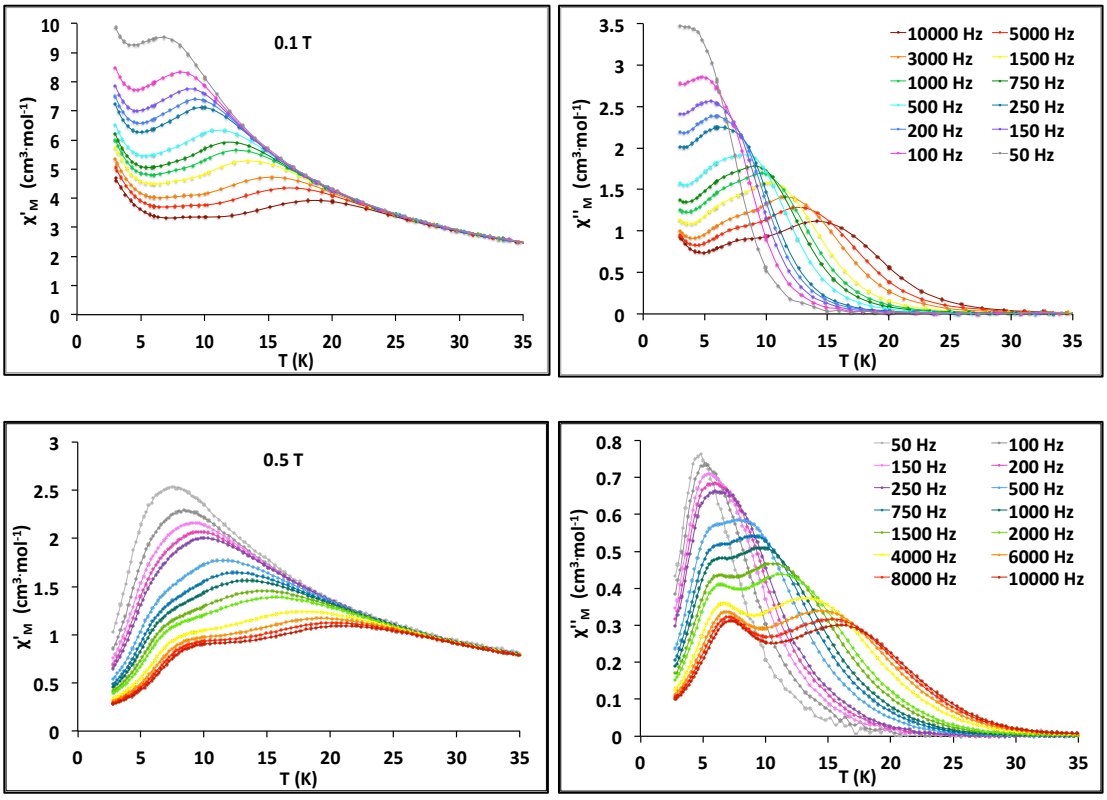

Figure 2.18 Temperature dependence of χ' (left) and χ" (right) for **2.3** in 0.03 (top), 0.1 (middle) and 0.5 T (bottom) *dc* field, from 3 – 35 K.

The frequency dependence of the out of phase susceptibility is further apparent when χ" is plotted as a function of frequency, Figure 2.19.

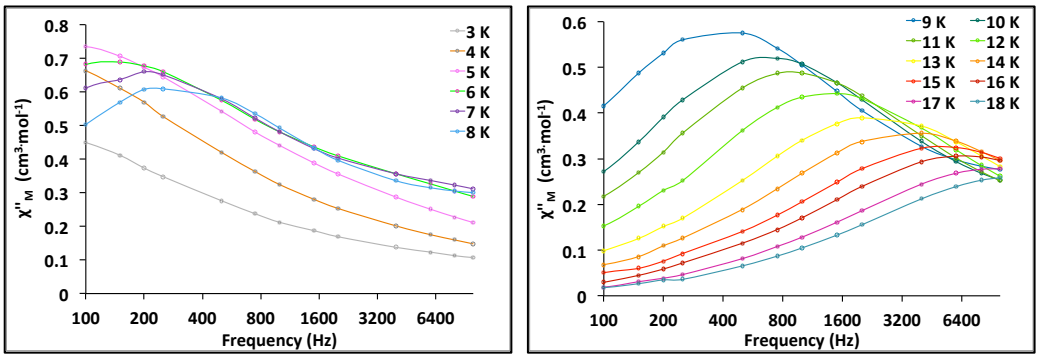

Figure 2.19 χ'' *vs.* frequency for $Dy_6[TBC4]_2$ (**2.3**) in 0.5 T applied field at "low" temperature (3-8 K, left) and "high" temperatures (9 to 18 K right).

In order to further probe the energy barriers and the relaxation processes for the Dy_6 cluster, the χ' and χ'' data in a 0.5 T static field were further examined in order to determine the parameters that describe the relaxation mechanism(s) through a fit to the Cole-Cole equation, describing the *ac* susceptibility as:

$$\chi(\omega) = \chi_S + \frac{\chi_T - \chi_S}{1+(i\omega\tau_C)^{1-\alpha}} \quad \textbf{(Eqn 2.2)}$$

where angular frequency $\omega = 2\pi\nu$, τ_C is the temperature-dependent relaxation time, or the time it takes for thermal equilibrium to be established, α is the dispersivity parameter of relaxation times with $\alpha = 0$, reflecting a single relaxation time, and $\alpha = 1$ reflecting an infinitely wide dispersion of the τ_C values; χ_T is the isothermal susceptibility, and χ_S is the adiabatic susceptibility. If the angular frequency ω of the *ac* field is low, $\omega\tau << 1$, for which the temperature equilibrium is obtained over the timescale of the experiment, the measured susceptibility is the isothermal susceptibility χ_T in the limit of the lowest field frequencies. In contrast, if the oscillations of the *ac* field are fast compared to the time constant τ, $\omega\tau >> 1$, the magnetic system remains isolated from its surroundings, and then the adiabatic susceptibility χ_S should be lower than χ_T. According to Eqn. 2.1 and 2.2, the real (χ') and imaginary (χ'') components can be separated into [15,130]

$$\chi'(\omega) = \chi_S + \frac{\chi_T - \chi_S}{1+(\omega\tau)^2} \quad \textbf{(Eqn 2.3)}$$

$$\chi''(\omega) = \frac{(\chi_T - \chi_S)\omega\tau}{1+(\omega\tau)^2} \quad \textbf{(Eqn 2.4)}$$

These two equations are related to the relaxation process with a single relaxation time τ where the maximum of χ" can be reached when ωτ = 1 and τ = 1/ω. However, for most magnetic samples, the relaxation process is not characterized by a single τ, but rather by a distribution of relaxation times. In this respect, this complex comprises two well-separated relaxation processes that are better described by the generalized two-component Debye function shown in Fig. 2.20 (right).

$$\chi(\omega) = \chi_{S1} + \frac{\chi_{T1}-\chi_{S1}}{1+(i\omega\tau_{C1})^{1-\alpha1}} + \chi_{S2} + \frac{\chi_{T2}-\chi_{S2}}{1+(i\omega\tau_{C2})^{1-\alpha2}} \qquad \textbf{(Eqn 2.5)}$$

In addition, the shape of the Cole-Cole (Argand) plots can dictate a single or multiple relaxation processes (Figure 2.20).

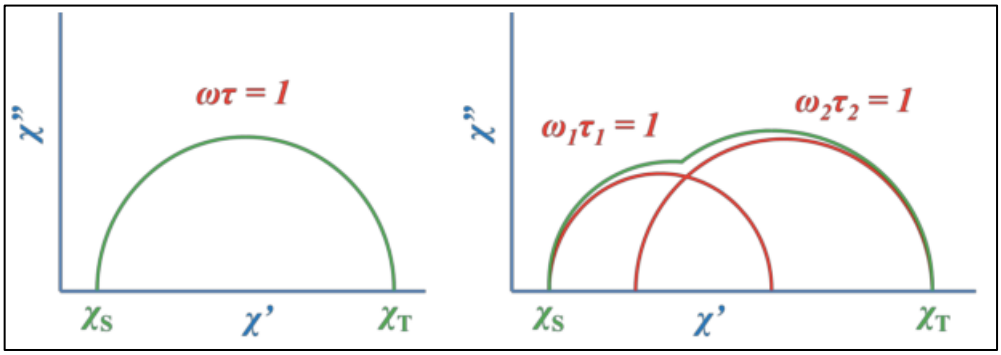

Figure 2.20 Cole-Cole plots of a system with a single relaxation process (left) where a perfect semi-circle is observed at a certain temperature/frequency and multiple relaxation processes (right), where the red fit lines yield two different relaxation times. Reproduced from Ref. 15.

Within each of the two temperature regimes, the χ' *vs.* χ" data were fitted to the Cole-Cole equation (Figure 2.21). Fitting the data with a generalized Debye model from 3 – 18 K, the α parameter is in the range of 0.29 – 0.45, indicating that several

overlapping relaxation pathways are most likely at play, an observation which is fairly common for Ln-SMMs.

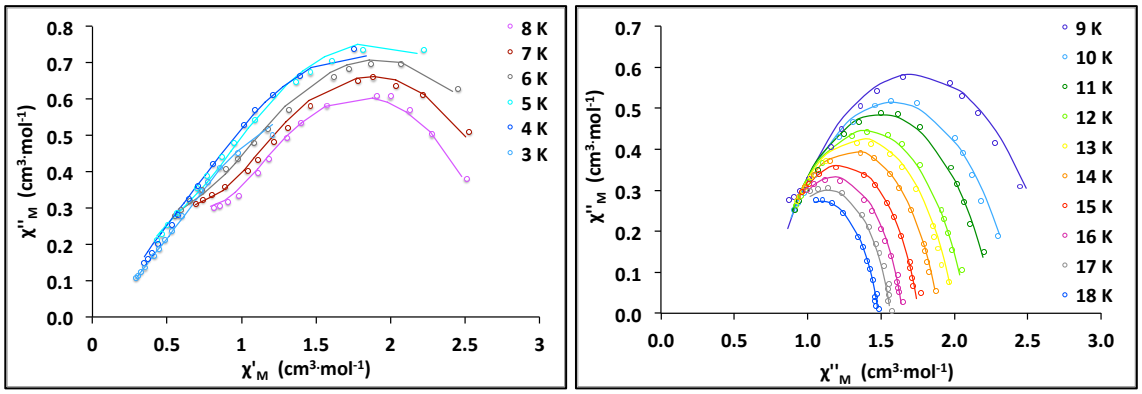

Figure 2.21 χ" *vs.* χ' plot for **2.3** in 0.5 T *dc* field over the frequency range 50 – 10,000 Hz. (left) "low" temperature range 3 – 8 K and (right) "high" temperature range 9 – 18 K; the circles correspond to the experimental data and the lines correspond to a best fit to the Cole-Cole equation.

For each modelled temperature regime, a fit of the temperature dependent relaxation time τ_c, to the Arrhenius expression allows the tunneling rate τ_0, and the effective energy barriers U_{eff} for the cluster to be determined. In this context, when the natural log of τ_c is plotted against the inverse of temperature ($\ln\tau_c$ *vs.* 1/T), the energy barrier U_{eff} (in Kelvin) is determined by the slope of the line, and the resulting tunneling rate τ_0 (in seconds), also referred to as the pre-exponential factor is described by exp(y-intercept), Figure 2.22. A noteworthy observation is that the Arrhenius plot between 3-8 K deviates (purple circles, Fig 2.22) from linearity, which is a common observation in *f*-element SMMs when multiple magnetic relaxation processes are operative.[131]

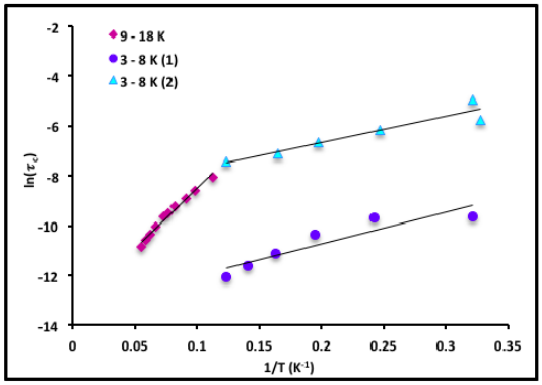

Figure 2.22 Arrhenius plot for **2.3**. The circles correspond to calculated values; the black lines are the best fit to the Arrhenius equation.

The resulting parameters determined for cluster **2.3** are U_{eff} = 48.2 K and τ_0 = 1.71 × 10^{-6} s in the high temperature regime (9 – 18 K), and U_{eff} = 10.2, 12.6 K and τ_0 = 1.62 × 10^{-4}, 1.81 × 10^{-6} s in the low temperature regime (3-8 K), confirming its SMM properties. These observations are clearly supported by the work of Wang and co-workers who also report slow relaxation of magnetization for the closely related $Dy_6[TBC4]_2$ cluster **2.2c,** but are in sharp contrast to the observations of Brechin *et al*., which were unfortunately not corroborated by experimental data.

Variable temperature *dc* magnetic susceptibility data for the $Tb_6[TBC4]_2$ cluster **2.4** were collected in a 0.5 T applied field between 5 and 300 K, Figure 2.23. Above 100 K, a χT value of 69.47 $cm^3 \cdot K \cdot mol^{-1}$ is close to the expected value of 70.89 $cm^3 \cdot K \cdot mol^{-1}$ for six non-interacting Tb(III) ions ($^7F_6$, S = 3, L= 3, g = 3/2, J = 6). Below 50 K, the χT value decreases to a minimum value of 47.59 $cm^3 \cdot K \cdot mol^{-1}$ at 7 K due to the depopulation of the M_J sublevels of the ground J multiplet and/or the presence of weak antiferromagnetic exchange interactions.

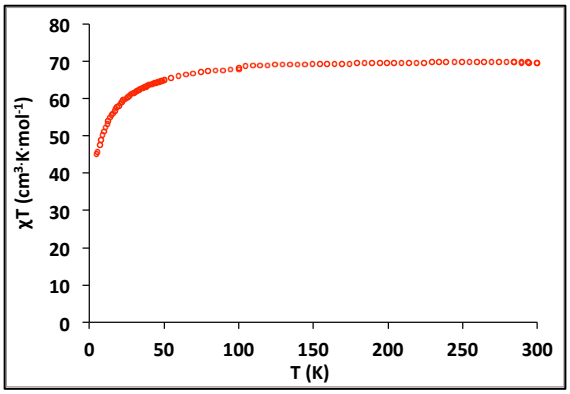

Figure 2.23 Plot of χT *vs.* temperature for **2.4** in an applied field of 0.5 T from 5-300 K.

A plot of $1/\chi$ *vs.* temperature was fit to the Curie-Weiss law, affording a Curie constant, C of 70.92 $cm^3 \cdot K \cdot mol^{-1}$ and a Weiss constant θ of -4.0 K, indicating the presence of weak antiferromagnetic interactions at low temperature. It is clear that the experimental data obeys the Curie-Weiss law across the whole temperature range as shown in Figure 2.24.

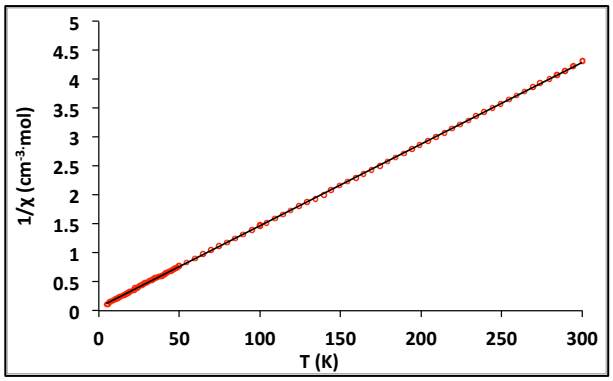

Figure 2.24 Plot of $1/\chi$ *vs.* temperature for **2.4** in a field of 0.5 T from 5 – 300 K. The black line represents the best fit to the Curie-Weiss equation.

Ac susceptibility experiments were carried out on **2.4** at five frequencies from 100 to 5000 Hz in zero *dc* field. To our delight, a frequency dependence in the

out of phase component of the *ac* susceptibility consistent with SMM behaviour is clearly visible in plot the χ'' *vs.* frequency data as shown in Figure 2.25.

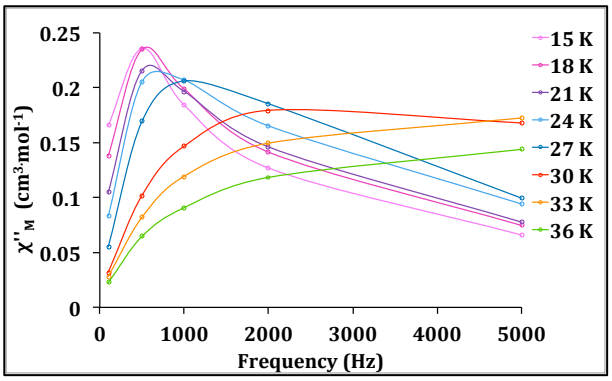

Figure 2.25 χ″ *vs.* frequency for **2.4** in zero *dc* field.

Between 15-35 K, analysis of the *ac* data using the generalized Debye model as previously described for the Dy(III) derivative afforded effective energy barriers U_{eff} of 79.49 and 63.24 K with corresponding pre-exponential factors τ_0 of 2.92 × 10^{-4} and 9.73 × 10^{-6} s, Figure 2.26 (right). The small α parameter quantified the distribution width which is in the range of 0.04 – 0.27, corresponding to more narrow distribution of relaxation times when compared to the Dy(III) analogue.

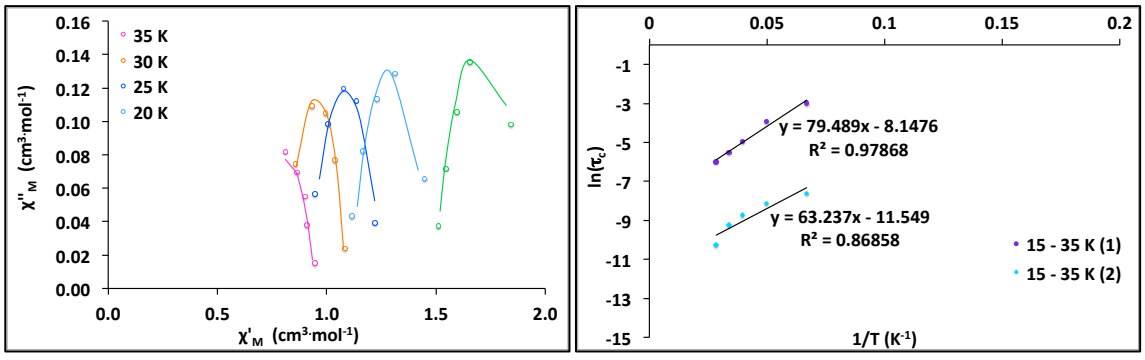

Figure 2.26 χ' *vs.* χ'' plot for **2.4** in zero *dc* field over the frequency range 100 – 5000 Hz. (left) between 15-35 K; the circles correspond to the experimental data and the lines correspond to the best fit to the Cole-Cole equation.

This result is extremely interesting since in contrast to Dy(III), Tb(III) is not a Kramers ion and as a consequence it does not inherently possess a degenerate ground state. In this case an appropriate crystal field splitting is required to afford a doubly degenerate ground state (rather than the possible M_J = 0) for the oblate Tb(III) ions in the complex, which has clearly been successfully achieved in this case. Reports of zero field multinuclear Tb(III)-based SMMs are quite rare in the chemical literature. Nevertheless, given that Tb-SMMs account for some of the highest energy barriers e.g. $[TbPc_2]^-$ U_{eff} = 652 cm^{-1},[132] and the highest blocking temperatures e.g. $\{[Me_3Si)_2N]_2(THF)Tb\}(\mu\text{-}N_2)$, T_B = 14 K,[41] magnetostrutural studies of these systems are of great importance for the design and construction of SMMs better suited for practical applications. Complex **3.4** is the first example of a $Tb_6[TBC4]_2$ cluster reported in the literature displaying SMM behaviour, in sharp contrast to the two previously reported Tb(III) analogues that display no such properties.[98,133] This study therefore serves to highlight how very subtle changes to the coordination geometries of the Ln(III)-ions in the magnetic core of a polynuclear cluster can have a dramatic effect on their magnetic properties.

2.4 Photoluminescence Studies

The photoluminescence properties of polynuclear 4*f*-metal complexes have been known to exhibiting sharp, intense emission bands, high photochemical stability, and long-lived emissions in the μs – ms range, which makes them particularly fascinating for various optical applications including display devices and luminescent sensors.[40,134,135,136] There are several electronic transitions possible

within lanthanide ions including intra-configurational 4*f* – 4*f*, inter-configurational 4*f* – 5*d*, or charge-transfer transitions between the metal and ligand. As for the optical properties, distinct features of lanthanide complexes, especially Dy(III)- and Tb(III)-based clusters are their long and sharp emission bands arising from the electronic transitions between the 4*f* orbitals, making them of particular interest.[137] However, lanthanide ions tend to emit in the visible range and have a poor absorption cross-section, leading to weak emission. This is due to the forbidden nature of the electronic transitions between the 4*f* orbitals. In this respect, since the *f-f* electronic transitions of the lanthanide ions are both spin- and parity-forbidden, they often require the use of organic chromophores that act as light harvesting 'antennae' to transfer energy to the Ln(III) excited state either through bonds (*Dexter mechanism*), or through space (*Foster mechanism*),[138] so that they can undergo quick internal conversion to the emitting state. Table 2.8 shows the typical luminescent transitions for each Ln(III) ion from Pr(III) through to Yb(III).[137,139]

Table 2.8 Luminescent *f-f* transitions of Ln(III) ions, where P = phosphorescence, F = fluorescence.[139,140]

Ln^{III}	Excited state	Final state	*J*	Type of lum.	Colour of emission
Pr^{III}	$^1G_4$	^3H_J	4-6	P	NIR
	$^1D_2$	^3F_J	2-4	P	NIR
	$^3P_0$	^3H_J	2-6	F	Orange
Nd^{III}	$^4F_{3/2}$	^4I_J	9/2-15/2	F	NIR
Sm^{III}	$^4G_{5/2}$	^6H_J	5/2-15/2	P	Orange
Eu^{III}	$^5D_0$	^7F_J	0-6	P	Red
Gd^{III}	$^6P_{7/2}$	$^8S_{7/2}$		P	UV
Tb^{III}	$^5D_4$	^7F_J	6-0	P	Green
Dy^{III}	$^4F_{9/2}$	^6H_J	15/2-5/2	P	Yellow/Orange

Ho^{III}	$^5F_5$	^5I_J	8-4	F	NIR
	$^5S_2$	^5I_J	8-4	F	Green
Er^{III}	$^4S_{3/2}$	^4I_J	15/2-9/2	F	
	$^4I_{13/2}$	$^4I_{15/2}$		F	NIR
Tm^{III}	$^1G_4$	^3H_J	6-4	P	
Yb^{III}	$^2F_{5/2}$	$^2F_{7/2}$		F	NIR

In addition to their interesting magnetic properties, the photoluminescence properties of lanthanide ions makes them attractive for the preparation of dual property SMMs. In this context, fitting the luminescence data for mononuclear Ln-SMMs has provided important information regarding the actual energy barriers for the magnetic relaxation of these complexes in zero field which can subsequently be used to corroborate the relaxation data obtained from magnetic susceptibility experiments, as well as *ab initio* calculations.[141] On the other hand, the potential luminescent properties of these systems can also be exploited to study these clusters when organized, or deposited onto a surface, which in the longer term may facilitate their processing into molecular devices.[139,142]

Working towards the discovery of dual property optically active SMMs, solid-state luminescence measurements were carried out on both clusters. At room temperature, the Dy_6 complex **2.3** showed no emission in the visible region, but at 12 K a broad band between 470 and 495 nm could be detected. This was assigned in part to ligand-based emission since the TBC4 ligand is known to exhibit broad features in the region of 350-600 nm.[98] However, based on literature precedence,[98,142] the peaks between 470 and 495 nm were also assigned to transitions within the M_J manifolds of the $^4F_{9/2} \rightarrow {}^4H_{15/2}$ transition of the Dy(III) ions

observed arising from partial energy transfer from the *p-tert*-butylcalix[4]arene macrocycles to the lanthanide ions upon excitation at 319 nm, Figure 2.27.

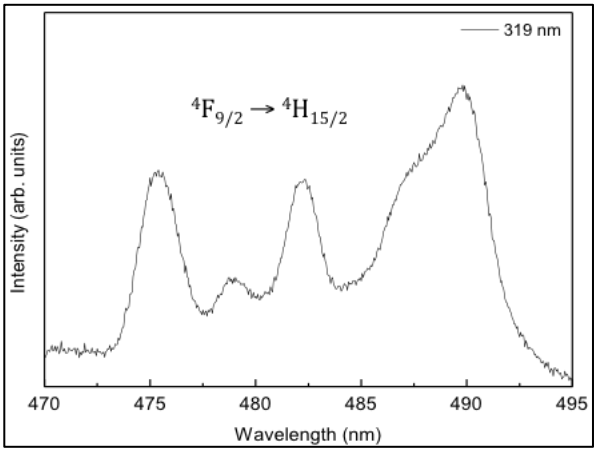

Figure 2.27 Part of the high-resolution solid state emission spectrum of $Dy_6[TBC4]_2$ (**2.3**) at 12 K showing the $^4F_{9/2}$ to $^4H_{15/2}$ transition based on excitation at 319 nm.

Solid-state luminescence studies on the Tb_6 cluster **2.4** were carried out at both 300 and 12 K, after excitation at 280 and 320 nm. Under UV excitation the Tb_6 cluster revealed the typical Tb(III) green emission, Figure 2.28.[98]

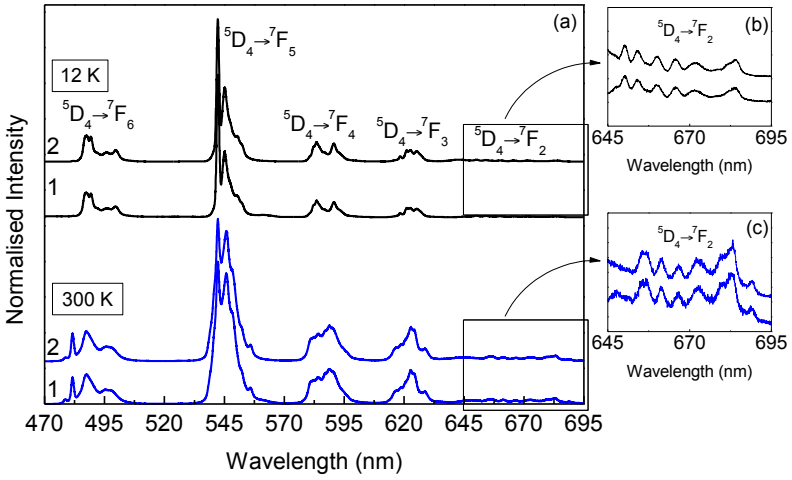

Figure 2.28 Emission spectra of Tb_6 cluster **2.4** acquired at 12 and 300 K and upon excitation at (1) 280 nm (black line) and (2) 320 nm (blue line). (b,c) Magnification (×20) of the $^5D_4 \rightarrow {}^7F_2$ transition.

The emission spectra, namely, energy, number of Stark components and full-width-at-half-maximum (fwhm) are independent of the excitation wavelength, suggesting that the Tb(III) ions occupy a single average local environment. Apart from a decrease in the fwhm, the spectra acquired at low-temperature resemble that measured at 300 K. The excitation spectrum of the Tb_6 cluster, Figure 2.28 displays a series of low-intensity sharp Tb(III) lines, ascribed to the intra-4f^8 transitions between the $^7F_6$ and $^5G_{4\text{-}6}$, $^5L_{9,10}$, $^5D_{2\text{-}4}$ levels, superimposed on a broad band in the range 240-340 nm with two components at 277 nm and 320 nm, ascribed to the ligands excited states. Apart from changes in the relative intensity of these broad components, no relevant changes are detected as the temperature is lowered from room temperature down to 12 K. We note that the ligand-related components dominate the spectra, pointing out an efficient TBC4-to-Tb(III) energy transfer.

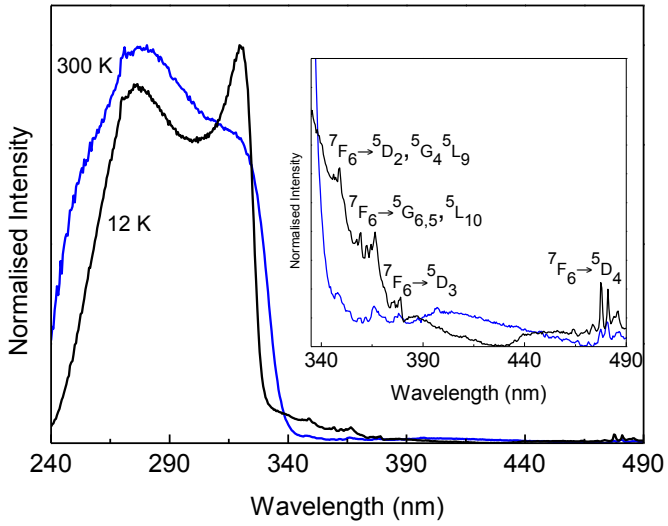

Figure 2.29 Excitation spectra of Tb_6 cluster **2.4** acquired at 12 K and 300 K and monitored at 542 nm. The inset shows a magnification (×50) of the intra-4f^8 transitions.

The photoluminescence properties were quantified by the measurement of the $^5D_4$ lifetime value. Thus, the emission decay curves were monitored around the $^5D_4 \rightarrow {}^7F_5$ transition under the ligand-excitation (280 nm) as function of the temperature, Figure 2.30. Both curves revealed a single exponential behavior yielding lifetime values of $(0.09 \pm 0.01) \times 10^{-6}$ s (300 K) and $(1.60 \pm 0.01) \times 10^{-6}$ s (12 K). The large increase in the value found at 12 K compared with that found at 300 K, suggests the presence of an efficient thermally activated non-radiative mechanism.

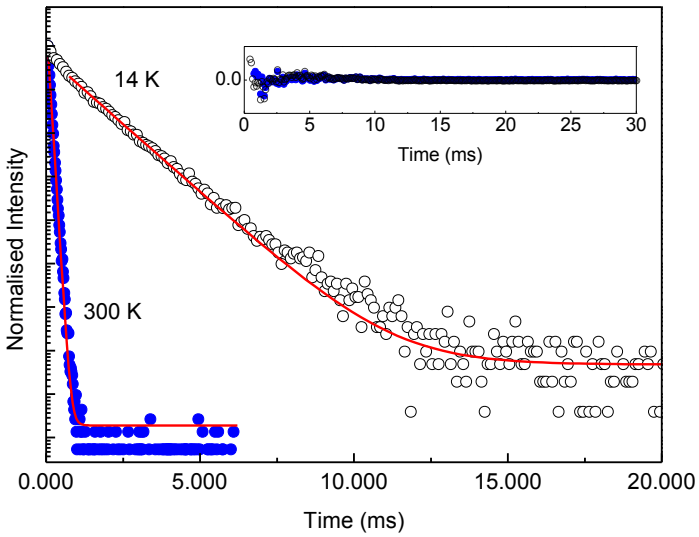

Figure 2.30 Emission decay curves of the Tb_6 cluster **2.4** acquired at 12 K and 300 K, monitored at 542 nm and excited at 280 nm. The solid line corresponds to the data best fit ($r > 0.99$) to a single exponential function. The inset shows the fit residual plots.

The emission features were further quantified by the measurement of the absolute emission quantum yield (ϕ) as function of the excitation wavelength. After excitation into the ligands excited states (250-320 nm), ϕ values (0.06 ± 0.01) were measured. For excitation directly into the intra-$4f^8$ levels (366 nm), ϕ lies below the detection experimental limit (0.01), Table 2.9.

Table 2.9 The absolute emission quantum yields (ϕ) for **2.4** measured at different excitation wavelengths (λ_{exc}, nm)

λ_{exc}	ϕ
250	0.05
280	0.06
320	0.04
366	< 0.01

In contrast to the Dy_6 cluster, the emission spectrum of **2.4** at 12 and 300 K shows sharp intra 4*f* transitions, indicating that the calix[4]arene ligand is more efficient at transferring energy to Tb(III) rather than to Dy(III) ions. This is due to the fact that the luminescence intensity of the Dy(III) ion is lower than that of the Tb(III) since the probability of non-radiative deactivation of the excited states of the Tb(III) ions is considerably higher.[140,143]

CHAPTER 3 – RESULTS AND DISCUSSION

PROJECT 2- The synthesis and coordination chemistry of R/S α-methyl-2-pyridinemethanol with Ni(II) and Co(II): towards the discovery of dual-property SMMs

3.1 Preface

One of the major areas of research interest in the Pilkington group is the development of synthetic routes for the discovery of dual property molecule-based materials where magnetism is combined together with a second physical property such as chirality, conductivity, and/or photoluminescence.[122] In recent years this strategy has afforded a number of interesting compounds that include, chiral spin crossover complexes,[76,144] magnetic conductors[145] and photoluminescent single molecule magnets (SMMs).[136,137,142,146] Extending this approach, as part of collaboration with the Stamatatos group at Brock, we have recently targeted the synthesis of small chiral polydentate organic ligands as precursors to chiral polynuclear transition metal and/or lanthanide clusters. Our long term objectives are to combine the synthetic organic chemistry and X-ray crystallography skillset of the Pilkington group with the cluster chemistry and magnetism expertise of the Stamatatos group, working towards the discovery of chiral polynuclear clusters that include high spin molecules and ultimately new SMMs. Working towards these objectives, the synthesis and coordination chemistry of both enantiomers of the chiral ligand, *R*/*S* α-methyl-2-pyridinemethanol *R*-or *S*-(mpmH), **L3.1** were targeted during the course of this study.

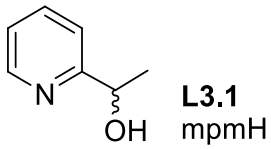

L3.1
mpmH

Figure 3.1 The molecular structure of the chiral chelating/bridging R/S α-methyl-2-pyridinemethanol ligand (mpmH), **L3.1**.

A comprehensive search of the chemical literature revealed that this chiral ligand has not been actively pursued to-date in the field of molecular magnetism with just two examples of magnetic frameworks/networks[147,148], a chiral copper(II) cubane[126] and no reports of any chiral SMMs. Nevertheless, it belongs to a family of pyridine-based alkoxide ligands that are well known in cluster chemistry with N- and O-donor atoms that are capable of both bridging paramagnetic metal centers and promoting strong magnetic exchange interactions.[121] Given these findings, the objectives of this project are: (i) the synthesis of polynuclear Dy(III), Ni(II) and Co(II) complexes of **L3.1**; (ii) the growth of single crystals for structural elucidation by X-ray diffraction; (iii) full characterization of the resulting coordination complexes in both solution and the solid-state; (iv) determination of the chirality of the complexes and (v) magnetic susceptibility studies to elucidate the magnetic properties.

3.2 Ligand Synthesis and Characterization

The racemic analogue of the ligand has been known since 1996 and the chiral derivatives were first prepared by Noyori *et al*. in that same year.[149] Following the literature procedure shown in Scheme 3.1,[150] *R*- and *S*-mpmH, were synthesized from 2-acetylpyridine, employing the commercially available chiral diamine-based

Ru(II) catalysts, RuCl[(*R,R*)-TsDPEN](η^6-arene) and RuCl[(*S,S*)-TsDPEN](η^6-arene) respectively, where TsDPEN = *N*-(*p*-toluenesulfonyl)-1,2-diphenyl ethylenediamine),[150] which are responsible for the asymmetric transfer hydrogenation of 2-acetylpyridine, with formic acid (HCOOH) as the hydrogen source.[151] Employing this strategy, a suspension formed by adding the chiral Ru(II) catalyst to a 1:4.3:2.5 mixture of 2-acetylpyridine/HCOOH/Et_3N afforded both enantiomers of the ligand as oils in 63% yield.

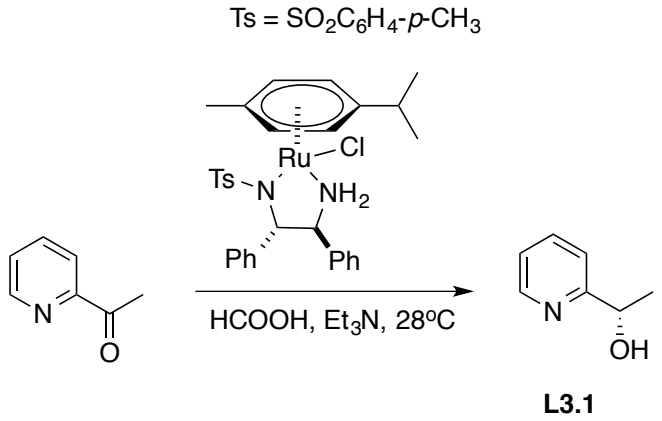

L3.1

Scheme 3.1 Synthetic route for the preparation of both enantiomers of **L3.1**.[150]

The ^{1}H and ^{13}C NMR spectra of *R*-and *S*-mpmH were consistent with the literature.[150] In addition, their optical rotation values $[\alpha]_D^{25.3}$ were determined to be $\pm$19.8 (*c* 0.1, $CHCl_3$), also in good agreement with the chemical literature.[150] The opposite chirality of the two enantiomers was further confirmed by circular dichroism (CD) spectroscopy. In this respect, the *R*-enantiomer displays a positive Cotton effect at λ_{max} = 270 nm, whereas the *S*-enantiomer shows the opposite Cotton effect at the same wavelength, Figure 3.2.

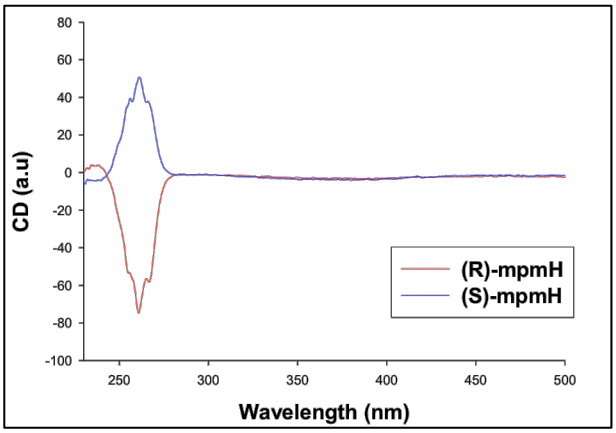

Figure 3.2 CD spectra of 10^{-5} M solutions of *R*- (red) and *S*-mpmH (blue) in DCM at room temperature.

3.3 Coordination Chemistry of L3.1

3.3.1 Rational vs. Serendipitous Self-Assembly

In recent years coordination chemists have made significant advances in applying rational design strategies for the syntheses of large complex molecules. This approach has been widely pursued by the groups of Fujita[152–155] and Stang,[156–158] affording many interesting structural topologies that include nanometer sized clusters.[159–161,162] It is also widely recognized by synthetic chemists within the molecular magnetism community that the lack of control in coordination chemistry can also be successfully exploited as a complementary approach for targeting the synthesis of large polynuclear clusters. This second approach, coined as "serendipitous self-assembly" involves the reaction of simple metal salts or preformed small clusters with polydentate ligands under a range of conditions.[163] At the heart of this approach is the mismatch between the number and type of coordination sites available on a single metal cation and the donor site supplied by

the ligand, which serves to encourage bridging between metal centers facilitating cluster formation. In this context the degree of bridging can be controlled via the adjustment of the pH of the reaction mixture, as well as by the careful choice of the metal-to-ligand ratio. Furthermore, the organic ligand serves to cap the assembling polynuclear cluster, isolating them in the solid state, a prerequisite for SMM properties. Although referred to as serendipitous, this does not mean that this approach is void of chemical design; to the contrary, the choice of ligand, metal ions and reaction conditions such as pH, solvent and temperature must all be systematically optimized, targeting the successful growth of single crystals suitable for X-ray diffraction, which in reality demands hundreds of trial reactions. In this respect there is overlap between rational design and serendipitous approaches for the syntheses of polynuclear clusters and moreover, in recent years the structural and magnetic properties of several families of single molecule magnets have been subsequently tuned by applying rational design methodologies.[6,18,22,24,28,76,84,164–167] The current challenges in the field are the following: (i) the development of new synthetic routes to polynuclear clusters that facilitate ferromagnetic interactions between paramagnetic centers, affording high spin ground states; (ii) to increase the magnetic anisotropy of the clusters to develop single molecule magnets with larger energy barriers and suppressed quantum tunneling; and (iii) the discovery of dual property SMMs where slow relaxation of magnetization is combined together with a second property such as photoluminescence and/or chirality.

3.3.2 Dy(III) Complexes of L3.1

As discussed in Chapter 1, the electronic properties of Dy(III) make it an attractive choice of metal ion for the synthesis of SMMs. To date, the vast majority of polymetallic Ln(III)-complexes with interesting physical properties have been prepared employing serendipitous rather than rational design strategies. Following this path we proposed to react chiral ligand **L3.1** together with a range of Dy(III) salts. The general reaction scheme employed is shown in Scheme 3.2, where X^- = Cl^-, ClO_4^-, NO_3^-, and OAc^-; base = Et_3N and NaOMe; and solvent = EtOH, MeOH, DMF, DCM, DMF/MeCN (3:10), DMF/MeOH (3:10), DMF/acetone (3:10), and DMF/DCM (3:10).

$$DyX_3 + mpmH + base + solvent \rightarrow ?$$

Scheme 3.2 Reaction scheme followed for the synthesis of Dy(III) complexes of **L3.1**.

Following this strategy hundreds of trial reactions were employed, systematically varying the DyX_3:mpmH:base ratios, as well as the solvent(s) and temperature of the reaction, searching for optimal conditions which afford single crystals of the resulting products for characterization by X-ray diffraction. Unfortunately, these reactions all gave precipitates that proved difficult to characterize. The most promising compound was isolated from the reaction of $Dy(ClO_4)_3 \cdot 6H_2O$, *R*-mpmH, and Et_3N in a 2:1:1 molar ratio, in 20 mL of a 3:1 v/v ratio of DMF/MeOH solvent. The coordination complex was isolated as a white dendritic solid after the slow diffusion of Et_2O into the reaction mixture at room temperature. The complex was

preliminary characterized by IR spectroscopy. The OH str in the free ligand at ν = 3356 cm^{-1} is now absent from the IR spectrum of the complex, supporting coordination of the Dy(III) ions through the deprotonated alkoxide O^- functionality of the ligand. In addition, several bands at ν = 1606, 1570, 1479, 1366, and 1074 cm^{-1} in the complex are consistent with the presence of C=C, and C=N str's from the pyridyl rings of the mpm^- ligand, which provides evidence for the presence of the chiral ligand in the complex. Unfortunately, despite our best efforts we were unable to grow suitable single crystals of this complex for characterization by X-ray diffraction.

Given these problems we modified our research objectives and turned our attention towards the synthesis of metal complexes of *3d* transition metal ions. As previously discussed, the choice of *3d*-metal ion is of significance since it will dictate the overall magnetic properties of the complex, for example, whether or not it possesses a spin ground state (S) and significant anisotropy (D). The first choice of metal ion for this project was Ni(II) which has an [Ar]$3d^8$ electronic configuration with two unpaired electrons and a ground state spin value of S = 1 (except square-planar geometries, where S = 0). A review of the chemical literature reveals a number of examples of Ni(II) complexes with zero field splitting parameters $|D|$ > 10 cm^{-1}.[129] Furthermore, in recent years, many tetra-nickel(II) Ni_4O_4 cubane metal clusters are known to give ferromagnetically coupled Ni(II) ions that to give rise to an S = 4 ground state, several of which display SMM behaviour.[168]

3.3.3 Ni(II) Complexes of L3.1

Targeting the preparation of chiral, polynuculear Ni(II) clusters our strategy involved reaction of Ni(II) salts together with *R*- or *S*-mpmH in the presence of pivalic acid. Pivalic acid was chosen as an auxiliary ligand since it has been established previously in the Stamatatos group that incorporation of flexible carboxylate groups together with small organic ligands can serve to aggregate Ni(II) ions into cluster motifs, facilitating the isolation of single crystals suitable for X-ray crystallography.[162] In the absence of any suitable Ni(II) pivalate starting materials our strategy involved the direct addition of pivalic acid together with two equivalents of base which serves to deprotonate both the pivalic acid and mpmH ligands in solution. Hundreds of trial reactions were initially employed varying the metal salt, stoichiometries, solvents, base and temperature of the reactions, Scheme 3.3.

$$NiX_2{\cdot}6H_2O + mpmH + pivH + 2Et_3N \rightarrow \quad ?$$

Scheme 3.3 General reaction scheme followed for the synthesis of Ni(II) complexes of *R*- and *S*-**L3.1**. Where X = Cl^-, and ClO_4^-, solvents = DCM, EtOH, MeCN, Me_2CO, $MeNO_2$, MeOH, DMF, DCM:MeOH (15:2), DMF:MeOH (1:1), MeCN:MeOH (15:2), MeCN:EtOH (15:2).

Fortunately in this case, the one-pot reaction of $Ni(ClO_4)_2{\cdot}6H_2O$, *R*- or *S*-mpmH, pivalic acid (pivH), and Et_3N in a 1:1:1:2 molar ratio in MeCN afforded, after slow evaporation of the solvent at 0°C after one day, green crystals of the chiral tetranuclear complex *R*- or *S*-$[Ni_4(O_2CCMe_3)_4(mpm)_4]{\cdot}H_2O$ (**3.1**) in 39% yield. The molecular structures of both enantiomers of the complex were fully characterized

by CHN elemental analysis, IR, UV-Vis spectroscopy, MALDI/TOF mass spectrometry and single crystal X-ray diffraction, Table 3.1.

Table 3.1 Summary of analytical and spectroscopic data for the Ni_4 complex **3.1**.

Complex		%C	%H	%N	MS (*m/z*)	λ_{max} (nm) (ε / L·mol^{-1}·cm^{-1})
3.1	Found	50.45	6.00	4.92	1049	233 (39700)
Ni_4	Calcd	50.31	6.16	4.89	$[M\text{-}C(CH_3)_3]^+$ (100%)	262 (466000)

For both enantiomers, the elemental analysis data was an acceptable fit ($\pm$0.4%) for the molecular formula (confirmed by X-ray diffraction, see later) $Ni_4(O_2CCMe_3)_4(mpm)_4]\cdot H_2O$ (**3.1**). The IR spectrum of the complex is compared with that of the free mpmH ligand in Figure 3.3.

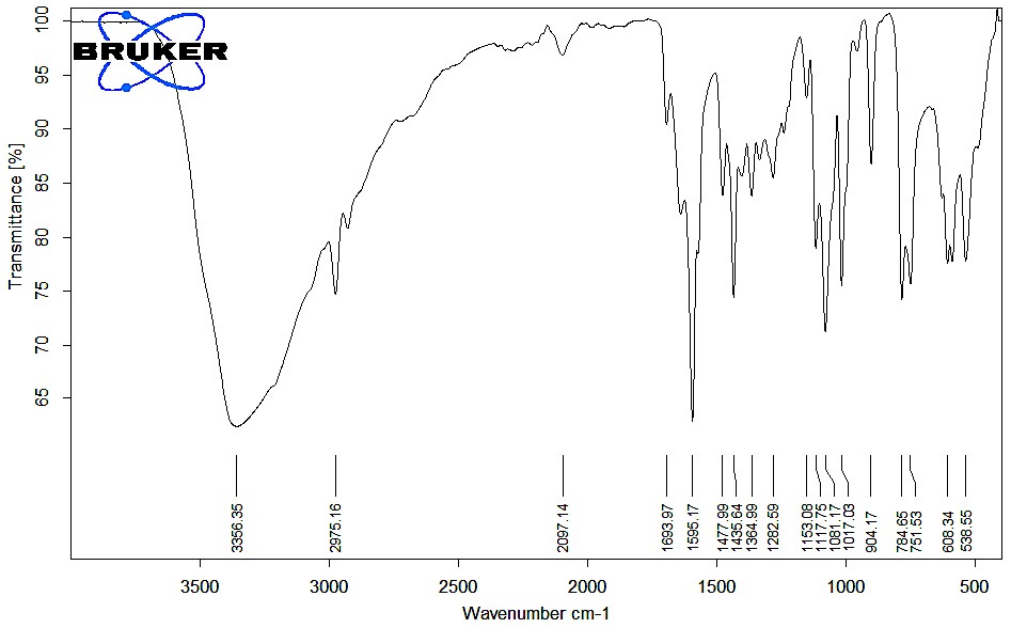

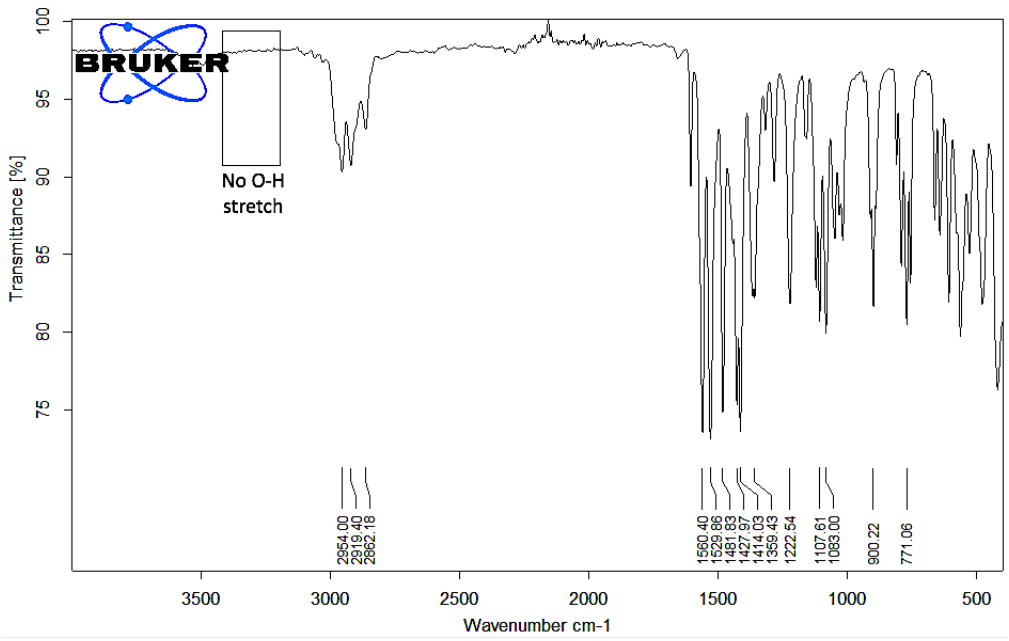

Figure 3.3 IR spectra of ligand *R*-**L3.1** (top) and *R*-$[Ni_4(O_2CCMe_3)_4(mpm)_4]\cdot H_2O$ (**3.1**) (bottom).

In this case the broad O-H str observed at ν = 3356 cm^{-1} in the ligand, Figure 3.3 (top) is now absent from the complex, supporting coordination of the Ni(II) ions through the alkoxide O^- atoms of the mpm^- ligand. Also, several bands at ν = 1606, 1560, 1481, 1370, and 1283 cm^{-1} in the complex are assigned to the C=C, and C=N str's of the pyridyl rings of the mpm^- ligand. Interestingly, a C=O str at 1606 cm^{-1} is also observed in the IR spectrum of the complex, consistent with the presence of the auxiliary pivalate ligands. The electronic absorption spectra of *R*- and *S*-mpmH possess absorption maxima at λ = 207 and 255 nm, which correspond to $\pi \rightarrow \pi^*$ transitions of the pyridine rings of the ligand, Figure 3.4. The UV-Vis spectrum of both enantiomers of complex **3.1** when compared to the free ligand displays two red shifted absorption bands. The first band is red shifted by 26 nm to λ = 233 nm and

the second band at lower energy is just slightly red shifted by 7 nm in the complex to λ =262 nm, Figure 3.4.

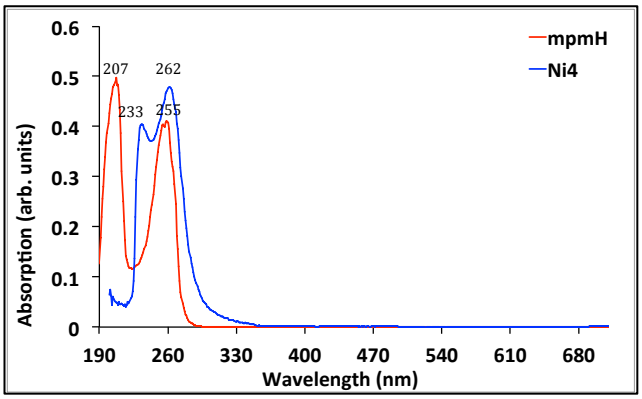

Figure 3.4. Room temperature UV-Vis spectra of a 10^{-5} M MeCN solution of uncomplexed ligand (*R*-**L3.1**), (red line) and the *R*-Ni_4 complex **3.1** (blue line).

The chirality of both enantiomers of **3.1** was confirmed by CD spectroscopy. *R*-**3.1** exhibits negative Cotton effects at λ_{max} = 330 and 280 nm and a positive dichroic signal centered at λ_{max} = 295 nm, while as expected, *S*-**3.1** shows Cotton effects of the opposite sign at the same wavelengths, confirming that the chirality of the ligands has been transferred to their respective coordination complexes, Figure 3.5.

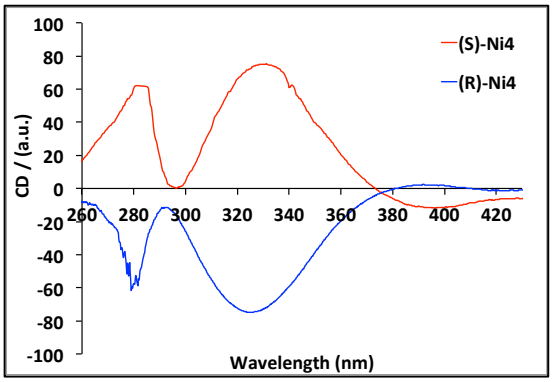

Figure 3.5 CD spectra of 10^{-5} M solutions of *R*-Ni_4 complex (**3.1**) in DCM at room temperature.

The redox properties of the *R*-Ni_4 cluster were investigated by cyclic voltammetry at room temperature. Complex **3.1** exhibits an irreversible oxidation at +1.2 V and an irreversible reduction at -1.5 V, Figure 3.6.

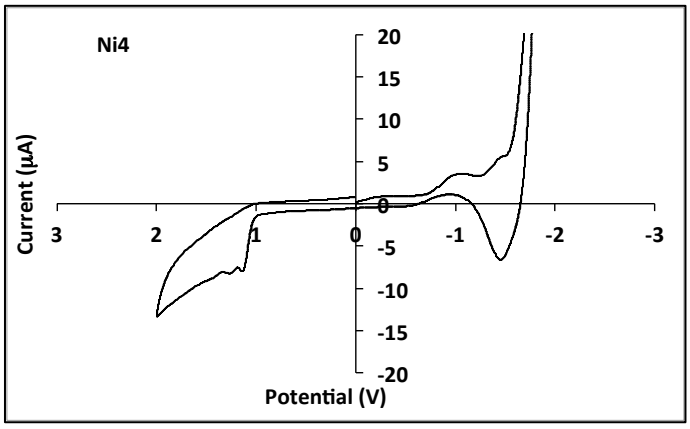

Figure 3.6 Cyclic voltammogram at 100 mV s^{-1} for a 1 mM solution of *R*-**3.1** in MeCN containing 0.1 M $NBu^n_4PF_6$ as the supporting electrolyte.

Comparing our results with related studies on related Ni(II) cubanes, we assign the former peak to the oxidation of Ni(II) → Ni(III) and the latter to the subsequent reduction of Ni(III) → Ni(II).[169]

Structural Studies

The molecular structure of *R*-**3.1** was elucidated by single crystal X-ray diffraction studies and is shown in Figure 3.7. The complex is neutral; hence no counterions are present in the crystal lattice.

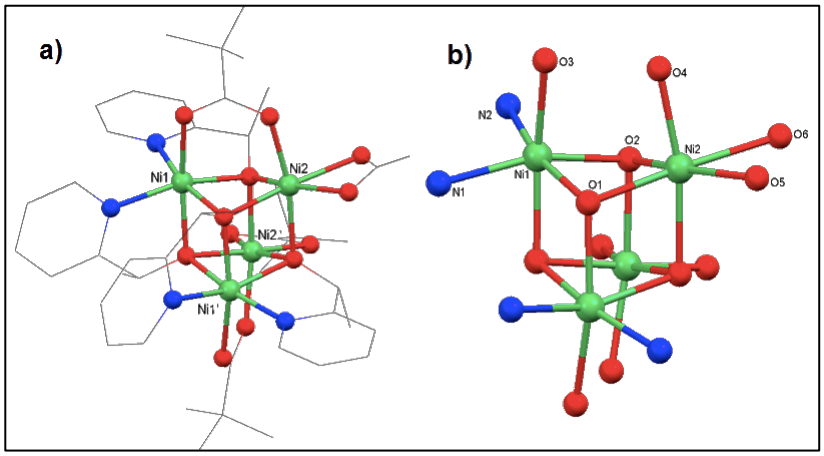

Figure 3.7 a) Molecular structure of *R*-[$Ni_4(O_2CCMe_3)_4(mpm)_4$] (**3.1**), hydrogen atoms are omitted for clarity; b) structure of the magnetic core of the cluster with the crystallographically independent atoms labelled. Colour code: Ni(II) green, O red, N blue, and C grey.

The complex crystallizes in the monoclinic chiral space group C*2*, with half of a crystallographically unique cluster within the asymmetric unit. The complex comprises of a Ni_4O_4 cubane-like core in which the vertices of the cubane are occupied by four Ni(II) centers, Ni1, Ni2 and Ni1' and Ni2', as well as four μ_3-bridging oxygen atoms (O1 and O2 and their symmetry equivalent atoms), Figure 3.7b. In this respect, a two-fold rotation axis passes through the center of the cubane. The deprotonated chiral mpm^- ligand occupies the four apexes of the cubane core. The Ni1 ion is coordinated by three triply bridging μ_3-O atoms, one oxygen atom of a pivalate auxiliary ligand and two pyridyl N atoms of *R*-**L3.1** ligands. The second Ni2 center is linked to three μ_3-O atoms and three oxygen atoms of two pivalate ligands. Interestingly, the pivalate anions bind in two different modes namely, $\eta^1{:}\eta^1{:}\mu$ and bidentate chelating, and the deprotonated chiral mpm^- ligand bridges three Ni(II) ions at the corners of the cubane in a $\eta^1{:}\eta^3{:}\mu_3$ manner, as

shown in Scheme 3.4. Selected interatomic distances and angles for the *R*-Ni4 cluster **3.1** are presented in Table 3.2. It should be noted that the C_2 symmetry of the cubane gives rise to four independent Ni···Ni distances and eight Ni-O-Ni angles which are further summarized in Table 3.4 and are an important considerations for the derivation of a suitable model for the *dc* susceptibility data, *vide infra*.

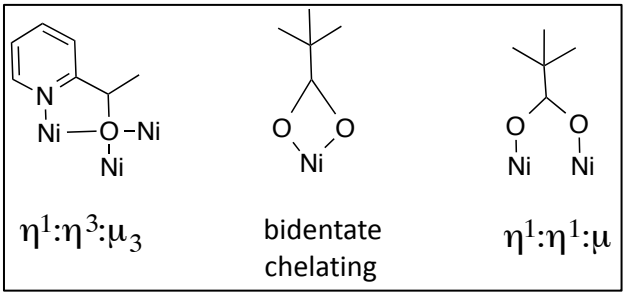

Scheme 3.4 Bridging modes observed for the mpm^- and piv^- ligands in **3.1**.

Table 3.2 Selected interatomic distances (Å) and angles (°) for *R*-Ni_4 (**3.1**).

Bond Distances (Å)		**Bond Distances (Å)**	
Ni1—Ni1	3.200 (2)	Ni1—O1[a]	2.106 (4)
Ni1—Ni2	2.8984 (14)	Ni2—O4	2.032 (6)
Ni1-Ni2[a]	3.161(2)	Ni2—O1[a]	2.063 (8)
Ni2-Ni2[a]	3.249(1)	Ni2—O2	2.083 (4)
Ni1—O1	2.056 (6)	Ni2—O6	2.105 (7)
Ni1—O2	2.061 (8)	Ni2—O2[a]	2.106 (5)
Ni1—O3	2.062 (6)	Ni2—O5	2.152 (5)
Ni1—N2	2.072 (6)	Ni1—N1	2.048 (6)
Bond Angles (°)		**Bond Angles (°)**	
N1—Ni1—O1	79.6 (3)	O4—Ni2—O2	97.4 (2)
N1—Ni1—O2	158.2 (3)	O1[i]—Ni2—O2	88.3 (2)
O1—Ni1—O2	81.1 (3)	O4—Ni2—O6	89.5 (3)
O1—Ni1—O2	81.1 (3)	O1[i]—Ni2—O6	169.6 (2)
N1—Ni1—O3	100.0 (4)	O2—Ni2—O6	102.1 (3)
O1—Ni1—O3	167.1 (2)	O4—Ni2—O2[a]	168.8 (3)
N1—Ni1—Ni2	143.98 (17)	O1[i]—Ni2—O2[a]	79.9 (3)
O1—Ni1—Ni2	90.68 (19)	O2—Ni2—O2[a]	78.24 (19)
O2—Ni1—Ni2	45.94 (12)	O6—Ni2—O2[a]	101.5 (3)

O3—Ni1—Ni2	82.1 (2)	O4—Ni2—O5	89.0 (2)
N2—Ni1—Ni2	122.5 (2)	O1^{a}—Ni2—O5	107.4 (2)
O1^{a}—Ni1—Ni2	45.4 (2)	O2—Ni2—O5	163.1 (3)
O4—Ni2—O1^{a}	89.7 (3)	O6—Ni2—O5	62.2 (2)
		O2^{a}—Ni2—O5	98.1 (2)

Symmetry code: (a) = −x+1, *y*, −*z*+1.

Both crystallographically independent Ni(II) ions have distorted octahedral coordination geometries that were further analyzed by CSMs,[127] Figure 3.8.

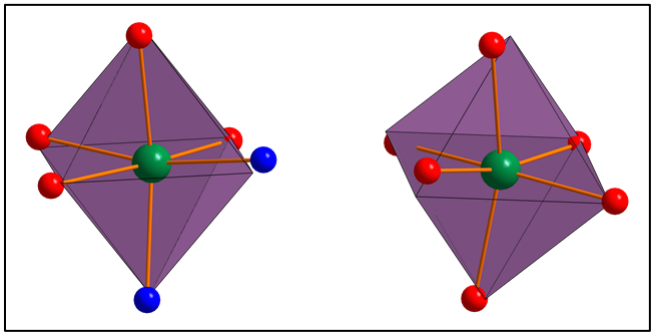

Figure 3.8 Coordination spheres of Ni1, and Ni2. Colour code: Ni green, O red, N blue, and purple idealized polyhedra.

In this respect, the deviation from ideal O_h symmetry is illustrated by CSMs of 1.75 for Ni1 (left) and 2.74 for Ni2 (right), Table 3.3.

Table 3.3 Continuous shape measures (CSMs) for the 6-coordinate Ni(II) coordination polyhedra in **3.1**. The values in red indicate the closest polyhedra for the two independent Ni(II) centers.[127]

Polyhedron	Ni1	Ni2
HP-6	32.48	28.54
PPY-6	22.07	23.19
OC-6	**1.75**	**2.74**
TPR-6	9.71	13.32
JPPY-6	26.04	26.83

It should be noted that after refining the crystal structure, the Flack parameter for the *R*-enantiomer is 0.123(10), which is close to zero indicating that the correct enantiomer was refined. However, the deviation from zero was likely due to the presence of a minor trace of the *S*-enantiomer with inverted configuration.

Examining the crystal packing of the cluster revealed that the *tert*-butyl groups of the carboxylate auxiliary ligands serve to isolate the clusters in the solid state, with the shortest intermolecular Ni···Ni distances of 8.234 Å between Ni1 and Ni2 ions of adjacent layers, Figure 3.9.

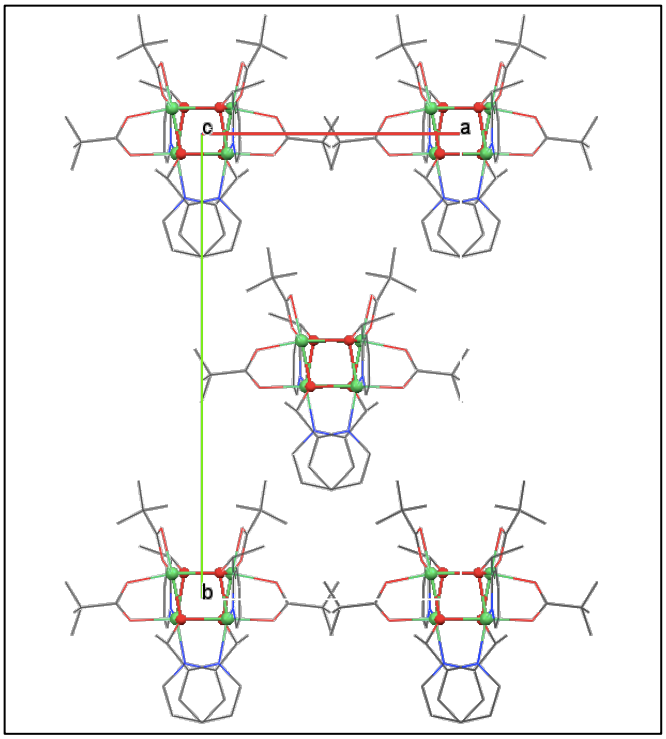

Figure 3.9 Crystal packing of *R*-[$Ni_4(O_2CCMe_3)_4(mpm)_4$]·H_2O (**3.1**). View down the *c*-axis of the unit cell. Hydrogen atoms are omitted for clarity.

The crystal packing generates voids in the structure which are occupied by water molecules but, since they were disordered, they were removed from the crystallographic model using the SQUEEZE command in PLATON.[126] The estimated

electron density from the SQUEEZE process suggests there is at least one water molecule associated with the formula unit of the cluster, consistent with the elemental analysis data.

Ni_4 tetranuclear clusters with cubane topologies are not new to the field of coordination chemistry, being first reported by Andrew and Blake in the late 1960's.[170] The discovery of single molecule magnetism in these complexes over recent years[171–173] has led to a revival in their preparation and study, with particular interest focused on the correlation between magnetic anisotropy and the relaxation of the magnetization at low temperature. As a consequence, the origin of the magnetic exchange interactions in these compounds was now well understood and closely correlated to the Ni-O-Ni angle within the cubane core.[174] For example, a novel chiral tetranuclear Ni(II) cubane-like complex was synthesized from a Schiff-base ligand prepared from *L*-valine. This cluster displayed predominantly ferromagnetic interactions,[165] although no *ac* studies have been reported to date.

Magnetic Studies

Variable temperature *dc* magnetic susceptibility studies were carried out on single crystals of *R*-**3.1** in the temperature range 5 – 300 K under an applied field of 0.1 T. The χT *vs.* T plot is shown in Figure 3.9. Above 100 K, the χT value of 4.7 $cm^3 \cdot K \cdot mol^{-1}$ is in good agreement with the theoretical value of 4.84 $cm^3 \cdot K \cdot mol^{-1}$ for four non-interacting Ni(II) ions ($^3F_4$, S = 1, g = 2.2). As the temperature is lowered, the value of χT slowly decreases until below 50 K it drops sharply to reach a

minimum value of 0.6 $cm^3 \cdot K \cdot mol^{-1}$ at 6 K. The shape of the plot indicates predominantly antiferromagnetic interactions.

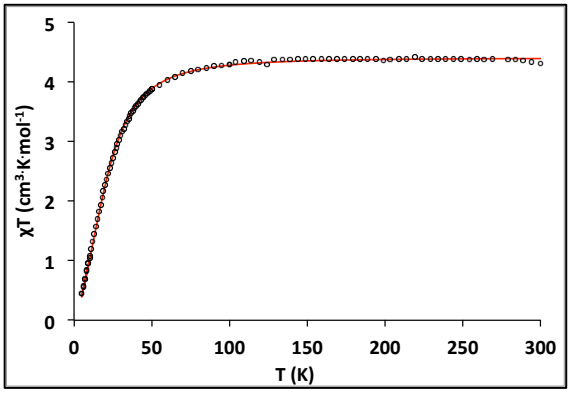

Figure 3.10 Plot of χT *vs.* T for *R*-$[Ni_4(O_2CCMe_3)_4(mpm)_4] \cdot H_2O$ (**3.1**) in a field of 0.1 T from 5 – 300 K. The solid black line represents the best fit of the data to a three-*J* model.

A fit of $1/\chi$ *vs.* T to the Curie-Weiss law gives a Curie constant of 5.2 $cm^3 \cdot K \cdot mol^{-1}$ and a Weiss constant, θ of -16.5 K, Figure 3.11.

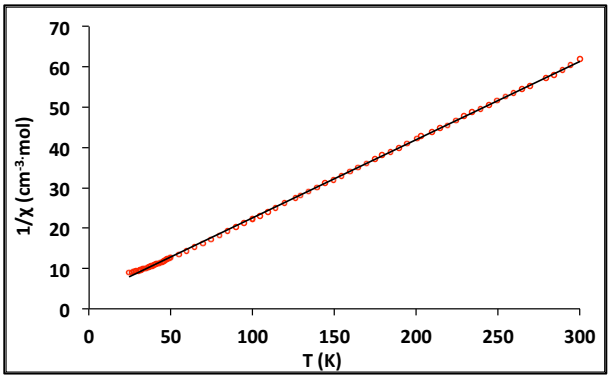

Figure 3.11 Plot $1/\chi$ *vs.* T for *R*-$[Ni_4(O_2CCMe_3)_4(mpm)_4] \cdot H_2O$ (**3.1**). The black line is the best fit to the Curie-Weiss equation.

In order to fully interpret the nature of the magnetic exchange interactions within the cluster the *dc* susceptibility data was initially modelled using a perfect

tetrahedral, or one-*J* model, assuming a single Ni(II)···Ni(II) magnetic exchange interaction according to the spin Hamiltonian shown in equation 3.1.

$$\hat{H} = -J(\hat{S}_1\hat{S}_2 + \hat{S}_1\hat{S}_3 + \hat{S}_1\hat{S}_4 + \hat{S}_2\hat{S}_3 + \hat{S}_2\hat{S}_4 + \hat{S}_3\hat{S}_4) \qquad \textbf{(Eqn 3.1)}$$

Unfortunately, in this case the one-*J* model did not reproduce the experimental data satisfactorily. We therefore carefully reconsidered the Ni···Ni bond lengths and Ni-O-Ni bond angles in the magnetic core of the complex and modified our strategy to employ a lower symmetry, third model that more accurately accounts for the crystallographic symmetry of the cubane, Figure 3.12. Although the cubane has four unique crystallographic faces, given that the Ni-O-Ni angles for the Ni1···Ni1' and Ni2···Ni2' faces are very similar, we assigned both sets of angles to the same J_2 value.

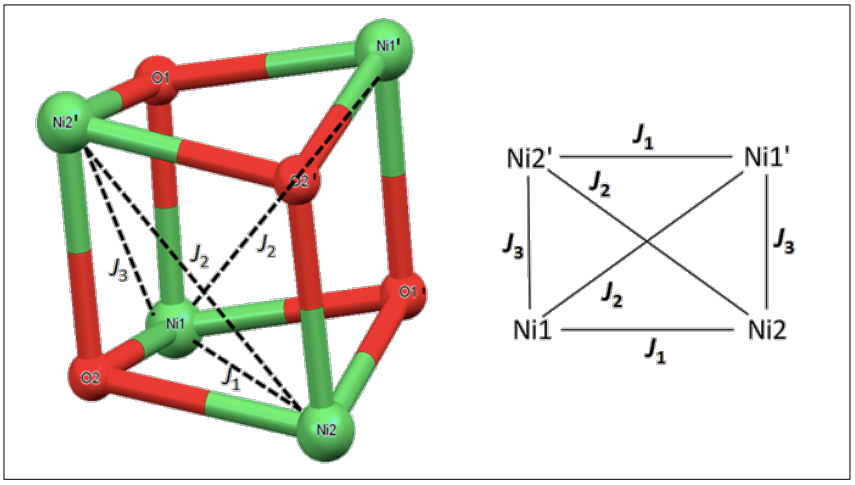

Figure 3.12 Left, the four crystallographically unique faces of the Ni_4 cubane **3.1** with assigned *J* values; right, simplified representation of the *J* coupling scheme employed for the elucidation of the magnetic exchange interactions.

Table 3.4 Summary of crystallographic bond lengths and angles considered for the assignment of the *J* values in the 3*J* model for the Ni_4 cubane **3.1**.

Ni···Ni interactions	Distances (Å)	<Ni-O Ni	(°)	*J* values	Mean <Ni-O-Ni (°)
Ni1···Ni2	2.898	88.77	88.11	J_1	88.44
Ni1'···Ni2'	2.898	88.77	88.11		
Ni1···Ni1'	3.200	100.51	100.51	J_2	101.12
Ni2···N2'	3.249	101.72	101.72		
Ni1···Ni2'	3.161	98.69	100.24	J_3	99.47
Ni1'···Ni2	3.161	98.69	100.24		

On the basis of Figure 3.12 the applied Heisenberg spin Hamiltonian derived for a three-*J* model is expressed as:

$$\widehat{H} = -J_1\left(\hat{S}_1\hat{S}_2 + \hat{S}_3\hat{S}_4\right) - J_2\left(\hat{S}_1\hat{S}_3 + \hat{S}_2\hat{S}_4\right) - J_3\left(\hat{S}_1\hat{S}_4 + \hat{S}_2\hat{S}_3\right) \qquad \textbf{(Eqn 3.2)}$$

The PHI program[175] was used to fit the experimental *dc* magnetic susceptibility data (red line in Figure 3.10), affording best fit parameters: g = 2.1, J_1 = +6.4 cm^{-1}, J_2 = -4.9 cm^{-1}, and J_3 = +1.1 cm^{-1}. For the pure 3*J* isotropic model, excellent fitting results without the need to include a *D* parameter. Furthermore, the magnetic exchange parameters J_1, J_2, and J_3 were in satisfactory agreement with the presence of ferromagnetic and antiferromagnetic interactions which correlate well with the structural topology of the cluster. Based on literature precedence,[13,171–173,174,176,177] we conclude that for this system the Ni(II) e_g electrons couple ferromagnetically through the oxygen *p* orbitals for Ni-O-Ni angles less than 99° and the positive coupling constant value increases as the Ni-O-Ni angle decreases. In contrast, the Ni(II) e_g electrons couple antiferromagnetically through the oxygen *p* orbitals for Ni-O-Ni angles larger than 99° and the absolute value increases as the angle increases. It should be noted that the angle of 99.47° lies right on the ferro/antiferromagnetic

border and thus is the weakest interaction. To summarize, in this chiral Ni_4 complex, the magnetic exchange interactions within the cubane are weak, resulting from a superposition of both ferro- and antiferromagnetic Ni-O-Ni exchange pathways. We thus expect that spin ground state of this cluster to be close to S_T= 0, consistent with the observations of Murray *et al.* for related systems.[178] As expected the *S*-enantiomer is isostructural crystallizing in the same unit cell with identical magnetic susceptibility data. Finally, variable temperature ac susceptibility studies performed on **3.1** showed no out of phase signals in the χ'' *vs* T plots suggesting that this complex is not an SMM.

3.3.4 Co(II/III) Complexes of L3.1

Following our studies with Ni(II) we proposed to extemd the project and investigate the coordination chemistry of the *R*- and *S*-enantiomers of **L3.1** together with Co(II). In an octahedral field, Co(II) ions have a $^4T_{1g}$ ground state and therefore we would expect magnetic behavior consistent with an S = 3/2 ground state, with strong orbital contributions due to the unquenched orbital contribution. In this context, first order spin orbit coupling splits the $^4T_{1g}$ ground state into a set of three levels (J = 5/2, J = 3/2 and J = 1/2). Interpretation of the magnetic susceptibility data for polynuclear complexes of octahedral Co(II) centers can be challenging due to thermal depopulation of the J states upon cooling. As a result the magnetic moment of octahedral Co(II) ions are temperature dependent and strongly deviate from Curie behavior. However, at low temperature, the only level populated was the lowest lying Kramers doublet. In the low temperature regime it is possible to

describe the low temperature behavior of a Co(II) center using an effective spin S'=1/2. However the first order orbital angular momentum was manifested in a strongly anisotropic g-value.[164] Given the potential of Co(II) to afford very large magnetic anisotropies, we therefore targeted the synthesis and study of chiral polynuclear Co(II) complexes. Furthermore, implementing chirality into Co(II) single molecule magnets is currently at the forefront of the field of molecular magnetism where examples of chiral polynuclear Co(II) clusters are still scarce, with the majority of research in this area still focused on studying mixed valence Mn(II)/Mn(III) systems.[81,82,166,179–181] Recently, Podjangy and co-workers were successful in transferring chirality from a chiral hydroxyethylpyridine ligand to a heterometallic cyanide bridged $Co^{II}_9W^{V}_6$ complex which displays SMM properties.[182] Instead of employing cyanide linkers, our strategy involved the use bridging oxygen and nitrogen atoms from the deprotonated chiral mpmH ligand, Scheme 3.5.

$$CoX_2{\cdot}nH_2O + mpmH + Et_3N + solvent \rightarrow ?$$

Scheme 3.5 General reaction scheme for the synthesis of Co complexes of **L3.1**. Where X = ClO_4^- or NO_2^- and the solvent = MeCN, MeOH, Me_2CO, $MeNO_2$, DCM:MeCN (10:5), MeCN:MeOH (15:3), MeCN:THF (10:5).

Following this strategy, reaction of 2 equivalents of *R*-mpmH **L3.1** together with 1 equivalent of $Co(ClO_4)_2{\cdot}6H_2O$ and 2 equivalents of Et_3N in MeCN afforded the linear trinuclear mixed valence complex *R*-$[Co_3(mpm)_6]{\cdot}(ClO_4)_2$ (**3.2**), as red/brown single crystals, in 23% yield after the slow evaporation of the solvent at room temperature. Modifying these reactions conditions, reaction of three equivalents of $Co(NO_3)_2{\cdot}6H_2O$ with 2 equivalents of *R*-mpmH **L3.1** in MeOH in the presence of 1

equivalent of Et_3N gave, after slow evaporation of the reaction mixture, a few dark brown single crystals of the tetranuclear complex *R*-[$Co(II)_2Co(III)_2(NO_3)_2(\mu$-$mpm)_4(ONO_2)_2$], (**3.3**). For the first reaction, the perchlorate salt was chosen because perchlorate is a non-coordinating anion and is most likely to be present as a counter anion within the crystal lattice serving, if needed, to balance the overall charge of the resulting complex.[183] For the second reaction, perchlorate was exchanged for nitrate since the nitrate anion can serve to both balance the charge of the resulting complex and act as a terminal or bridging ligand, thus affording a different structural topology.

The molecular structures of both complexes were fully characterized by elemental analyses, IR and UV-Vis spectroscopy, ESI mass spectrometry and single crystal X-ray diffraction, Table 3.5. The elemental analysis data for **3.2** was consistent with the molecular formula $[Co_3(mpm)_6]\cdot(ClO_4)_2$ and the data for **3.3** was consistent with a tetranuclear cluster of formula $[Co(II)_2Co(III)_2(NO_3)_2(\mu$-$mpm)_4(ONO_2)_2]$.

Table 3.5 Summary of analytical and spectroscopic data for complexes *R*-**3.2** and *R*-**3.3**.

Complex		%C	%H	%N	MS (*m/z*)	λ_{max} (nm) (ε / L·mol^{-1}·cm^{-1})
3.2	Found	45.77	4.46	7.77	1132	230 (348900)
Co_3	Calcd	45.65	4.40	7.87	$[M+H]^+$ (100%)	
3.3	Found	34.84	3.87	10.65	972	204 (150800)
Co_4	Calcd	34.87	3.84	10.67	$[M-NO_3]^+$ (100%)	

The IR spectra for both complexes when compared to the free ligand reveal no broad O-H str, consistent with its deprotonation in the coordination complexes. The

appearance of several bands in the IR spectrum for complex **3.2** at ν = 1605, 1569, 1479, 1366, and 1283 cm^{-1}, corresponding to C=C, and C-N str's of the pyridyl group of the mpm^- ligand; whereas the peaks corresponding to the same stretches (C=C and C=N) of the pyridyl group of mpm^- ligand were found at ν = 1608, 1570, 1460, 1371, and 1280 cm^{-1} in complex **3.3.** The UV-Vis spectra of the two complexes in MeCN were very similar and blue shifted with respect to the corresponding absorption observed for the free ligand, with each complex absorbing strongly at λ_{max} = 230 and 204 nm respectively, Figure 3.12. The chirality of both enantiomers of complexes **3.2** and **3.3** was confirmed by CD spectroscopy. In this respect *R*-enantiomer of the Co_3 complex, **3.2** exhibited positive Cotton effects at λ_{max} = 510 and 400 nm and a negative dichroic signal centered at λ_{max} = 450 nm, while as expected, the *S*-enantiomer showed Cotton effects of the opposite sign at the same wavelengths.

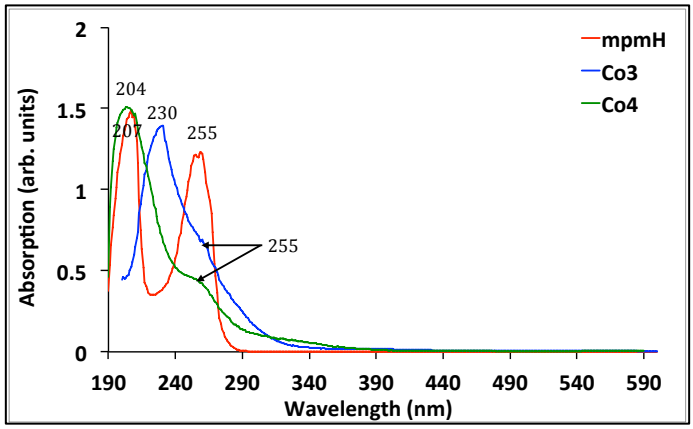

Figure 3.13 UV-Vis spectra of a 10^{-5} M MeCN solution of ligand (**L3.1**) and complexes *R*-**3.2** and *R*-**3.3** at room temperature.

Following the same rationale, the *R*-enantiomer of the Co_4 complex **3.3,** exhibited positive Cotton effects at λ_{max} = 320 nm and a negative dichroic signal centered at

λ_{max} = 450 nm, while as expected, the *S*-enantiomer showed Cotton effects of the opposite sign at the same wavelengths, Figure 3.13.

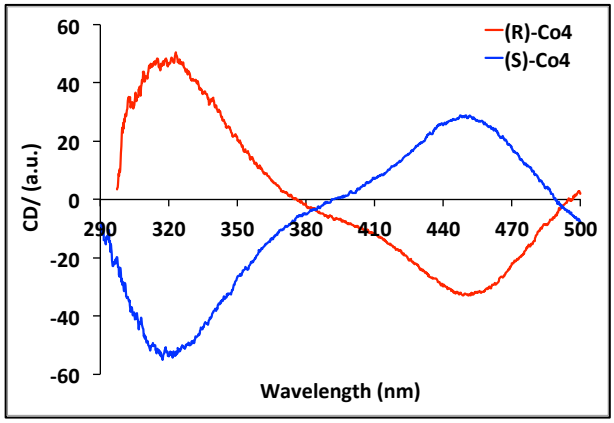

Figure 3.14 CD spectra of 10^{-5} M solutions of *R*- and *S*-Co_4 (**3.3**) in DCM at room temperature.

The redox properties of both clusters were investigated by cyclic voltammetry. The two complexes **3.2** and **3.3** displayed irreversible oxidative responses at +2.0 V, Figure 3.14. This irreversible signal could be attributed to the $Co^{II} \rightarrow Co^{III}$ oxidation as outlined in Equation 3.3, but is most likely due to the breakdown of the solvent/supporting electrolyte.[184,185]

$$[Co^{III}\text{-}Co^{II}\text{-}Co^{III}] \rightarrow [Co^{III}\text{-}Co^{II}\text{-}Co^{III}]^{+} + e^{-} \qquad \textbf{(Eqn 3.3)}$$

A quasi-reversible reductive couple at ~ -1.3 V is assigned to $Co^{III} \rightarrow Co^{II}$ reduction, Equation 3.4.[185]

$$[Co^{III}\text{-}Co^{II}\text{-}Co^{III}] + 2e^{-} \rightarrow [Co^{III}\text{-}Co^{II}\text{-}Co^{III}]^{2-} \qquad \textbf{(Eqn 3.4)}$$

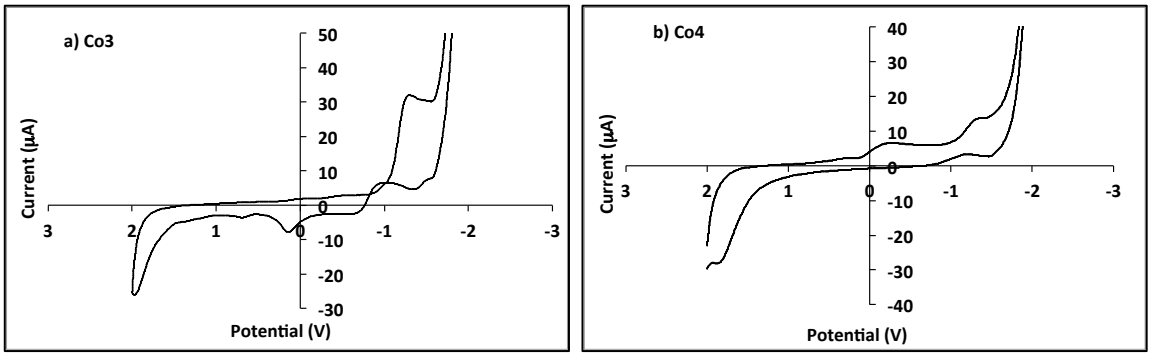

Figure 3.15 Cyclic voltammograms at 100 mV s^{-1} for a 1 mM solution of (a) *R*-**3.2** and (left) and (b) *R*-**3.3** (right) in MeCN containing 0.1 M $NBu^n_4PF_6$ as the supporting electrolyte.

All of the redox signals remain unchanged under different scan rates (100 – 500 mV s^{-1}) at room temperature. These oxidative and reductive signals are consistent with literature reports on related mixed valence Co trimers.[184,185] For example, the mixed valence Co(III)-Co(II)-Co(III) complex **3.4**, reported by Wang *et al.* displays a quasi-reversible Co(III) → Co(II) reduction in the CV spectrum at -1.46 V and an irreversible Co(II) → Co(III) oxidation at +0.99 V, Figure 3.15 (right).[185]

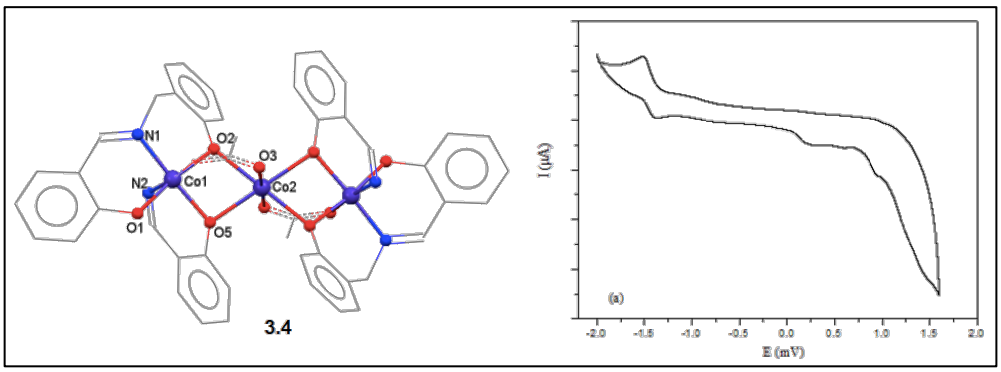

Figure 3.16 Left, Molecular structure of the mixed valence Co(III)-Co(II)-Co(III) cluster **3.4**, (H-atoms and counter ions are omitted for clarity); Right CV spectrum of **3.4** taken in DMF with 0.2 mol·L^{-1} Bu_4NClO_4 electrolyte at a scan rate of 0.1 V·s^{-1}. Reproduced with permission from Ref. 184.

Structural Studies

The molecular structures of the *R*-enantiomers of both Co(II) complexes have been elucidated by X-ray diffraction. Complex **3.2** crystallizes in the trigonal space group *R*32 with a third of the molecule being crystallographically unique, Figure 3.16.

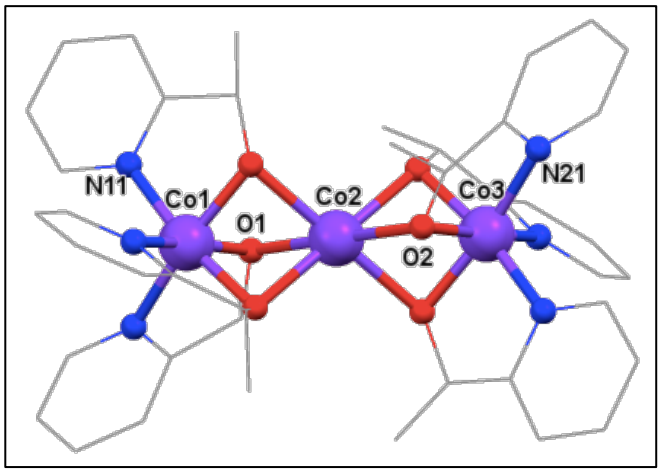

Figure 3.17 Molecular structure of the linear trimer *R*-$[Co_3(mpm)_6]\cdot(ClO_4)_2$ **(3.2).** Hydrogen atoms and ClO_4^- counterions are omitted for clarity. Colour code: Co purple, O red, N blue, and C grey.

The complex comprises three Co ions arranged in a linear fashion, with a Co1-Co2-Co3 angle of 180° and Co1···Co2 and Co2···Co3 intramolecular distances of 2.670 and 2.673 Å.[184,186] Based on charge considerations, we assign the peripheral two cobalt ions to a +3 and the central Co(II) ion to a +2 oxidation state, affording a linear mixed valence Co(III)-Co(II)-Co(III) trimer. This assignment is further supported by the Co-O bond lengths which are *ca* 0.22 Å longer for Co2 compared to their Co1 and Co3 counterparts, consistent with the lower oxidation state, Table 3.6. In the magnetic core of the molecule, the three Co ions are linked via alkoxide bridges from

the mpm^- ligand. All three metal centers are located on a crystallographic 3-fold axis as shown in Figure 3.18.

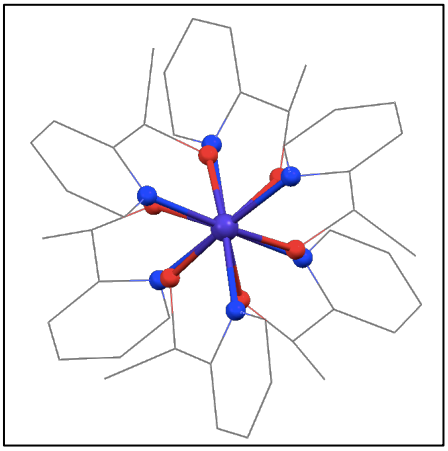

Figure 3.18 View down the crystallographic 3-fold axis for the Co_3 complex *R*-**3.2**.

The central Co(II) ion is bridged by six μ_2-oxygen atoms from six mpm^- ligands, two of which are crystallographically unique (O1 and O2) and the other four, generated by symmetry. The apical Co(III) ions are capped by coordination to N atoms from three mpm^- ligands. The M-O-M bridging angles range from 83.82 to 83.99°, consistent with the presence of non-colinear Co^{III}-O-Co^{II} fragments. The mpm^- ligand bridges in a $\eta^1{:}\eta^2{:}\mu$ mode as shown in Scheme 3.6.

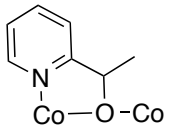

$\eta^1{:}\eta^2{:}\mu$

Scheme 3.6 The coordination mode for the mpm^- bridging ligand in the Co_3 complex **3.2**.

All three Co ions have distorted octahedral geometries that were analyzed by continuous shape measures,[127] Figure 3.19.

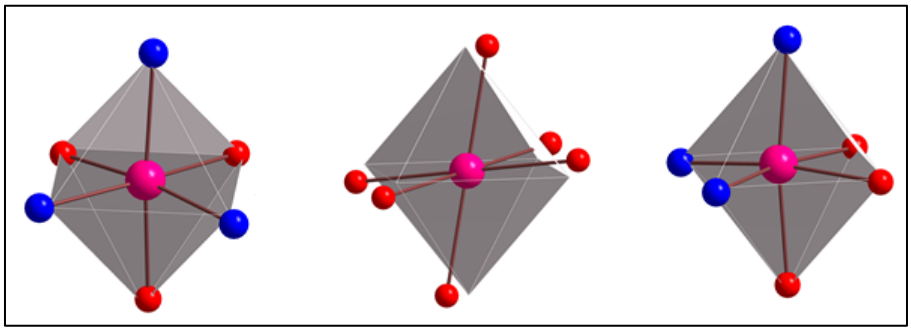

Figure 3.19 Coordination spheres of (from the left to right): Co1 – Co3. Colour code: Co pink/purple, O red, N blue, and grey - idealized polyhedra.

Table 3.6 Continuous shape measures (CSMs)[127] for the Co(II)/Co(III) coordination polyhedra in the Ni_3 cluster **3.2**. The values in red indicate the closest match for both complexes.

Polyhedron	Co1	Co2	Co3
HP-6	32.04	29.44	31.63
PPY-6	28.43	29.39	29.15
OC-6	**0.45**	**3.11**	**0.41**
TPR-6	15.01	14.10	15.89
JPPY-6	32.28	32.09	32.50

The discrepancies from ideal O_h symmetry in **3.2** indicated that the Co1 and Co3 ions in the trinuclear core exhibited an almost perfect octahedral environment, while the Co2 center was more distorted, Table 3.7

Table 3.7 Selected interatomic distances (Å) and angles (°) for the *R*-Co_3 cluster **3.2**.

Bond Distances (Å)		Bond distances (Å)	
Co1—O1[a]	1.887 (3)	Co2—O2[a]	2.104 (3)
Co1—O1	1.887 (3)	Co2—O2[b]	2.104 (3)
Co1—O1[b]	1.887 (3)	Co2—Co3	2.6733 (12)
Co1—N11[a]	1.925 (3)	Co3—O2	1.885 (3)
Co1—N11[b]	1.925 (3)	Co3—O2[a]	1.885 (3)
Co1—N11	1.925 (3)	Co3—O2[b]	1.885 (3)
Co1—Co2	2.6696 (10)	Co3—N21	1.918 (4)

Co2—O1[a]	2.102 (3)	Co3—N21[a]	1.918 (4)
Co2—O1	2.102 (3)	Co3—N21[b]	1.918 (4)
Co2—O2	2.104 (3)		
Bond Angles (°)		**Bond Angles (°)**	
O1[a]—Co1—O1	85.36 (12)	O1—Co2—O2[a]	179.69 (13)
O1[a]—Co1—O1[a]	85.36 (12)	O1[b]—Co2—O2[a]	104.95 (11)
O1—Co1—O1[a]	85.36 (12)	O2—Co2—O2[a]	74.78 (13)
O1[a]—Co1—N11[a]	85.61 (13)	O1[a]—Co2—O2[b]	179.70 (13)
O1—Co1—N11[a]	91.54 (14)	O1—Co2—O2[b]	104.95 (11)
O1[b]—Co1—N11[a]	170.66 (13)	O1[b]—Co2—O2[b]	105.30 (11)
O1[a]—Co1—N11[b]	91.54 (14)	O2—Co2—O2[b]	74.78 (13)
O1—Co1—N11[b]	170.66 (13)	O2[a]—Co2—O2[b]	74.77 (13)
O1[b]—Co1—N11[b]	85.61 (13)	O1[a]—Co2—Co1	44.65 (7)
N11[a]—Co1—N11[b]	97.01 (13)	O1—Co2—Co1	44.65 (7)
O1[a]—Co1—N11	170.66 (13)	O1[b]—Co2—Co1	44.65 (7)
O1—Co1—N11	85.61 (13)	O2—Co2—Co1	135.48 (8)
O1[b]—Co1—N11	91.54 (13)	O2[a]—Co2—Co1	135.48 (8)
N11[a]—Co1—N11	97.01 (13)	O2[b]—Co2—Co1	135.48 (8)
N11[b]—Co1—N11	97.01 (13)	O1[a]—Co2—Co3	135.35 (7)
O1[a]—Co1—Co2	51.52 (8)	O1—Co2—Co3	135.35 (7)
O1—Co1—Co2	51.52 (8)	O1[b]—Co2—Co3	135.35 (7)
O1[b]—Co1—Co2	51.52 (8)	O2—Co2—Co3	44.52 (8)
N11[a]—Co1—Co2	120.13 (10)	O2[a]—Co2—Co3	44.52 (8)
N11[b]—Co1—Co2	120.13 (10)	O2[b]—Co2—Co3	44.52 (8)
N11—Co1—Co2	120.13 (10)	Co1—Co2—Co3	180.0
O1[a]—Co2—O1	74.98 (11)	O2—Co3—O2[a]	85.33 (13)
O1[a]—Co2—O1[b]	74.98 (11)	O2—Co3—O2[b]	85.33 (13)
O1—Co2—O1[b]	74.98 (11)	O2[a]—Co3—O2[b]	85.33 (13)
O1[a]—Co2—O2	104.95 (11)	O2—Co3—N21	86.16 (17)
O1—Co2—O2	105.30 (11)	O2[a]—Co3—N21	170.71 (16)
O1[b]—Co2—O2	179.70 (15)	O2[b]—Co3—N21	90.27 (17)
O1[a]—Co2—O2[a]	105.30 (11)	O2—Co3—N21[a]	90.27 (16)

Symmetry code(s): (a) $-y+1, x-y, z$; (b) $-x+y+1, -x+1, z$.

Examination of the crystal packing of **3.2** showed that the channels in the structure were occupied by the perchlorate counter ions, Figure 3.20. The closest

intermolecular Co···Co distances are 7.789 Å, demonstrating that the Co_3 clusters are well isolated in the solid state.

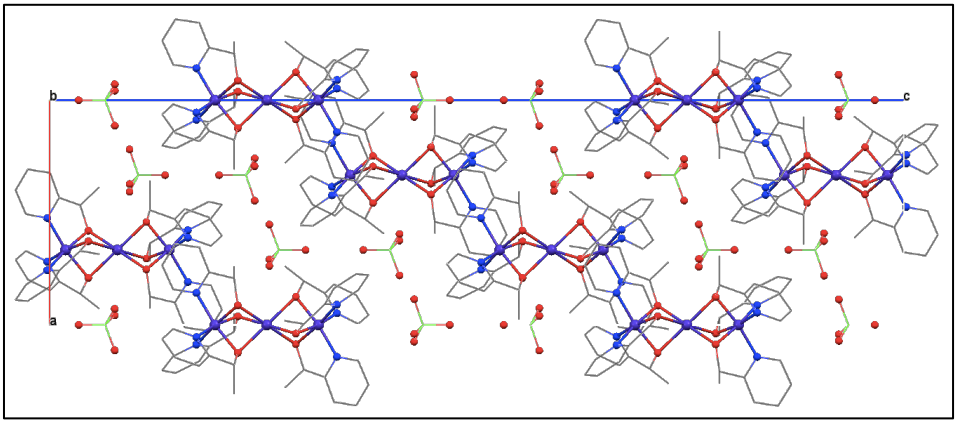

Figure 3.20 Crystal packing of *R*-Co_3 cluster **3.2**. View down the *b*-axis of the unit cell. H-atoms are omitted for clarity. Colour code: Co purple, O red, N blue, Cl green, and C grey.

The Flack parameter in the crystal structure of the *R*-enantiomer is -0.011(8) which is close to 0, consistent with the expected chirality of the complex. Linear Co_3 mixed valence trimers are commonly found in the field of molecular magnetism, which are known since Werner reported a series of such complexes obtained by partial oxidation of the mixtures of Co(II) salts and ethylenediamine.[184] Many of these compounds have been discovered with Schiff-base ligands and are well studied.[184–189] Similar complexes with chiral ligands are scarce;[190,191] to the best of our knowledge, this is the first example of a chiral mixed valence Co_3 complex prepared from a pyridyl-based alkoxide ligand.

Complex **3.3** crystallizes in the chiral space group $P2_12_12_1$ with one crystallographically unique molecule in the asymmetric unit. Analysis of the molecular structure reveals the complex comprises of a tetranuclear mixed valence

cluster of stoichiometry *R*-[Co(II)$_2$Co(III)$_2$(NO$_3$)$_2$(μ-mpm)$_4$(ONO$_2$)$_2$]. (**3.3**) whose structural topology is reminiscent of a defective double cubane, in which two interfaces are occupied by Co(III) ions (Co1 and Co2) and two corners are occupied by Co(II) ions (Co3 and Co4) ions. The two cubanes share one face and each misses one vertex, Figure 3.21.

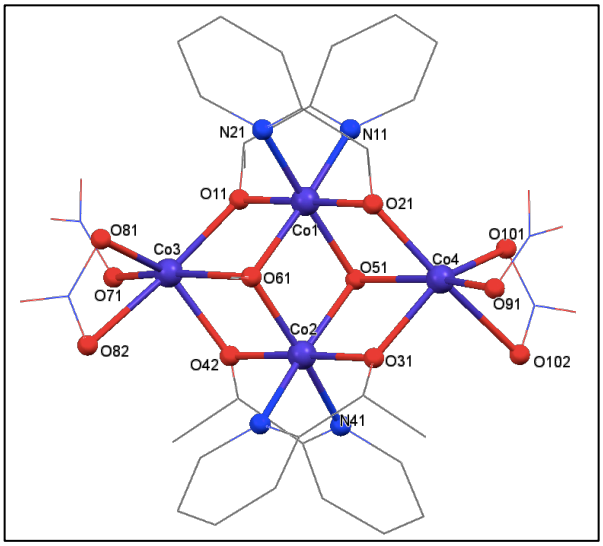

Figure 3.21 Molecular structure of the Co$_4$ cluster *R*-[Co(II)$_2$Co(III)$_2$(NO$_3$)$_2$(μ-mpm)$_4$(ONO$_2$)$_2$] (**3.3**)**.** Hydrogen atoms are omitted for clarity. Colour code: Co purple, O red, N blue and C grey.

The Co1 and Co2 ions are both bridged by two μ$_3$-methoxide-oxygen atoms (O51 and O61) and two bidentate mpm$^-$ anions. Each of the extreme corner Co(II) ions. Co3 and Co4 are coordinated to two nitrate molecules and two oxygen atoms from the chiral mpm$^-$ anions. The mpm$^-$ ligands coordinate in a η^1:η^1:μ manner as previously observed for complex **3.2** and the nitrate ions chelate in a bidentate manner, Scheme 3.7.

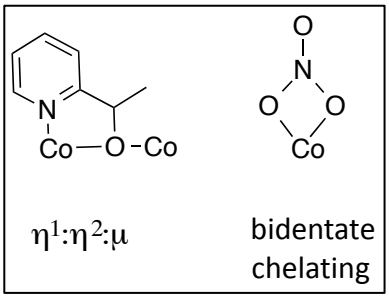

Scheme 3.7 The coordination mode for the mpm⁻ and nitrate bridging ligands in the Co_4 complex *R*-**3.3**.

All four Co ions have distorted octahedral geometries, which were analyzed further by CSMs,[127] Figure 3.21.

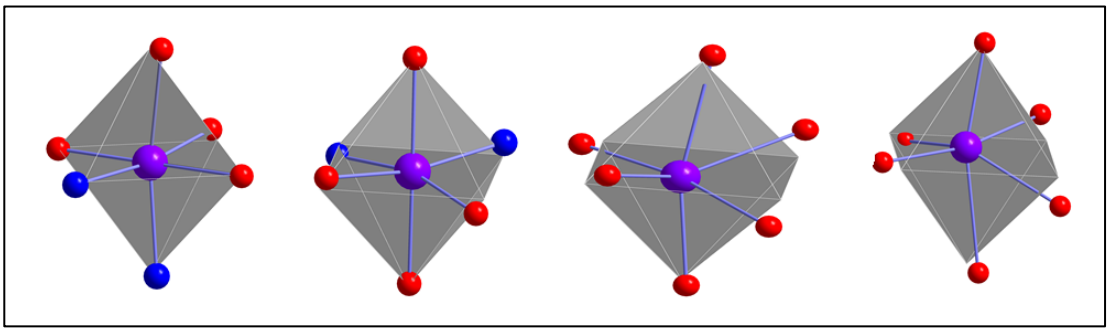

Figure 3.22 Coordination spheres of (from the left to right): Co1 – Co4. Colour code: Co pink/purple, O red, N blue, and grey idealized polyhedra.

Table 3.8 Continuous shape measures (CSMs)[127] for the Co(II) and Co(III) polyhedra in the Co_4 cluster, **3.3**. The values in red indicate the closest polyhedron according to the CSMs.

Polyhedron	Co1	Co2	Co3	Co4
HP-6	30.93	31.57	28.36	27.33
PPY-6	25.49	23.73	16.87	16.69
OC-6	**0.70**	**1.08**	**5.06**	**5.30**
TPR-6	13.53	12.55	9.77	9.99
JPPY-6	29.19	27.43	19.59	19.25

The discrepancies from ideal O_h symmetry in **3.3** are apparent in the CSMs, Table 3.8. These studies indicated that the Co1 and Co2 ions in the tetranuclear unit exhibit an almost perfect octahedral geometry, while the Co3 and Co4 centers are more distorted with M-O distances ranging from 1.973 to 2.374 Å, that are ca. 0.12 Å longer than their Co1 and Co2 counterparts, consistent with the mixed $Co(II)_2$-$Co(III)_2$ valence nature of the complex. Selected bond distances and angles for **3.3** are presented in Table 3.9.

Table 3.9 Selected interatomic distances (Å) and angles (°) for *R*-Co_4 (**3.3**).

Bond Distances (Å)		**Bond Distances (Å)**	
Co1—O11	1.863 (9)	Co3—O11	1.986 (9)
Co1—O21	1.882 (10)	Co3—O42	1.994 (9)
Co1—N11	1.900 (12)	Co3—O71	2.049 (12)
Co1—N21	1.906 (12)	Co3—O81	2.108 (11)
Co1—O61	1.923 (9)	Co3—O82	2.276 (13)
Co1—O51	1.936 (9)	Co3—O61	2.362 (8)
Co1—Co2	2.947 (2)	Co4—O21	1.973 (11)
Co2—O42	1.880 (9)	Co4—O31	2.008 (10)
Co2—N41	1.889 (12)	Co4—O91	2.058 (13)
Co2—O31	1.889 (9)	Co4—O101	2.129 (16)
Co2—N31	1.917 (12)	Co4—O102	2.359 (18)
Co2—O51	1.926 (9)	Co4—O51	2.375 (8)
Bond Angles (°)		**Bond Angles (°)**	
O11—Co1—O21	179.2 (5)	O51—Co2—O61	80.4 (4)
O11—Co1—N11	85.0 (4)	O42—Co2—Co1	91.5 (3)
O21—Co1—N11	95.0 (5)	N41—Co2—Co1	135.3 (4)
O11—Co1—N21	95.3 (5)	O31—Co2—Co1	90.8 (3)
O21—Co1—N21	85.5 (5)	N31—Co2—Co1	134.1 (4)
N11—Co1—N21	87.3 (5)	O51—Co2—Co1	40.4 (3)
O11—Co1—O61	85.7 (4)	O61—Co2—Co1	40.0 (3)
O21—Co1—O61	94.3 (4)	O11—Co3—O42	98.1 (4)
N11—Co1—O61	170.3 (5)	O11—Co3—O71	103.6 (5)
N21—Co1—O61	96.1 (4)	O42—Co3—O71	99.2 (5)
O11—Co1—O51	93.7 (4)	O11—Co3—O81	109.1 (4)

O21—Co1—O51	85.5 (4)	O42—Co3—O81	134.5 (4)
N11—Co1—O51	97.7 (4)	O71—Co3—O81	108.5 (5)
N21—Co1—O51	170.0 (5)	O11—Co3—O82	165.4 (5)
O61—Co1—O51	80.3 (4)	O42—Co3—O82	88.1 (4)
O11—Co1—Co2	90.2 (3)	O71—Co3—O82	88.3 (6)
O21—Co1—Co2	89.3 (3)	O81—Co3—O82	58.3 (5)
N11—Co1—Co2	137.2 (4)	O11—Co3—O61	72.0 (3)
N21—Co1—Co2	135.5 (4)	O42—Co3—O61	70.9 (3)
O61—Co1—Co2	40.2 (3)	O71—Co3—O61	168.0 (5)
O51—Co1—Co2	40.1 (3)	O81—Co3—O61	83.4 (4)
O42—Co2—N41	83.8 (5)	O82—Co3—O61	97.9 (5)
O42—Co2—O31	177.6 (4)	O21—Co4—O31	95.6 (4)
N41—Co2—O31	95.0 (5)	O21—Co4—O91	102.8 (6)
O42—Co2—N31	94.9 (4)	O31—Co4—O91	96.8 (5)
N41—Co2—N31	90.6 (5)	O21—Co4—O101	110.1 (5)
O42—Co2—N31	94.9 (4)	O31—Co4—O101	134.5 (5)
O42—Co2—N31	94.9 (4)	O91—Co4—O101	112.3 (6)
O42—Co2—O51	97.8 (4)	O21—Co4—O102	164.1 (6)
N41—Co2—O51	96.1 (4)	O31—Co4—O102	90.9 (5)
O31—Co2—O51	84.4 (4)	O91—Co4—O102	90.8 (7)
N31—Co2—O51	166.2 (4)	O101—Co4—O102	56.1 (6)
O42—Co2—O61	83.9 (4)	O21—Co4—O51	72.5 (4)
N41—Co2—O61	166.6 (5)	O31—Co4—O51	71.0 (3)
O31—Co2—O61	97.5 (4)	O91—Co4—O51	166.0 (5)

Close examination of the crystal packing of **3.3** reveals the clusters are organized into layers. The shortest intermolecular Co···Co distances are 8.194 Å between the Co1 and Co4 centers of nearest neighbours, Figure 3.23. The Flack parameter determined from the crystal structure refinement of the *R*-enantiomer is -0.011(8) which is close to 0, consistent with an enantiopure complex with correctly assigned chirality. The unit cell parameters for the corresponding *S*-enantiomer were also determined revealing the two complexes are isostructural.

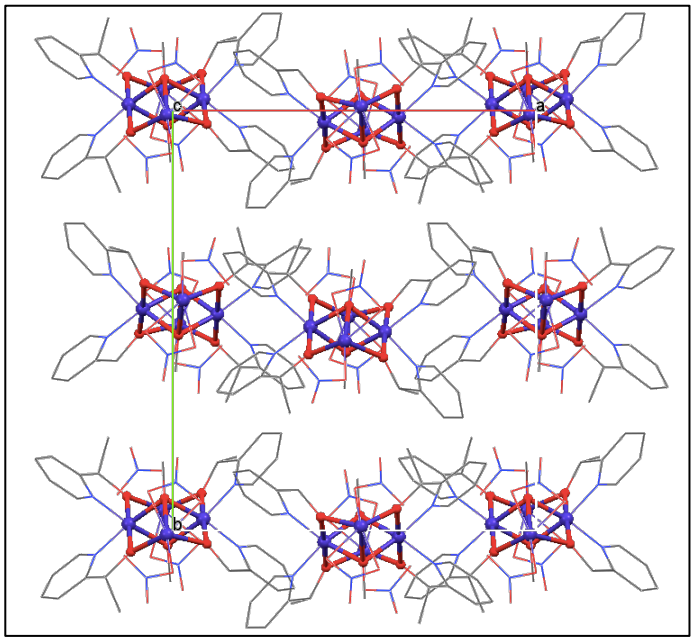

Figure 3.23 Crystal packing of *R*-Co_4 cluster **3.3**. View down the *c*-axis of the unit cell. H-atoms are omitted for clarity. Colour code: Co purple, O red, N blue, Cl green, and C grey.

Over the last decade a number of mixed-valence Co(II/III) complexes containing hydroxyl, alkoxy, oxo, and/or carboxylate bridging ligands with defective double cubane structural topologies have been reported in the chemical literature.[183,192–194] Such studies have provided valuable insight into the synthetic strategies adopted for the preparation of mixed valence polynuclear cobalt compounds with interesting magnetic properties.[183,192–200] For example, a discrete mixed valence Co(II/III) defective cubane assembled from diethanolamine, 2,2'-bipyridine and 1,10-phenanthroline ligands has been reported previously by Powell *et al*.[199] Although our complex adopts a similar structural topology, it is to the best of our knowledge the first example of a chiral Co_4 mixed valence polynuclear complex with a defective cubane topology.

Magnetic Studies

Variable temperature *dc* magnetic susceptibility studies were carried out on freshly prepared, single crystals of the *R*-Co_3 cluster **3.2** in the temperature range 2 – 300 K under an applied field of 0.1 T. Fundamentally, the only unpaired electrons will be on the high spin Co(II) ions ($e_g^2\, t_{2g}^5$, S = 3/2) since the Co(III) ions are low-spin (t_{2g}^6, S = 0) and thus, from a magnetism perspective, the complex is mononuclear.[194] The χT *vs.* T plot for **3.2** is shown in Figure 3.24.

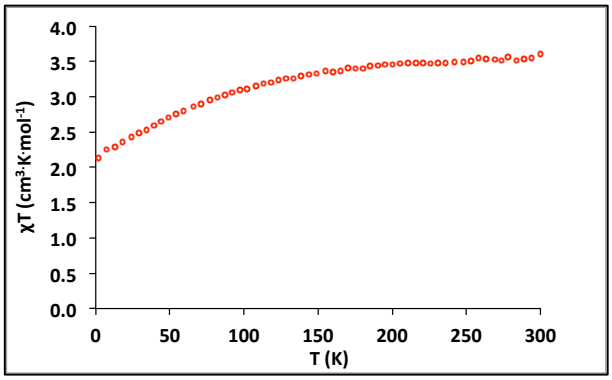

Figure 3.24 χT *vs.* T for *R*-Co_3 (**3.2**) in a field of 0.1 T from 2 – 300 K.

The value of χT above 100 K is 3.48 $cm^3 \cdot K \cdot mol^{-1}$, in good agreement with the expected value of 3.75 $cm^3 \cdot K \cdot mol^{-1}$ for non-interacting Co(II) ions (calculated g = 2.0). Upon cooling, the value of χT gradually decreases, dropping gradually to a minimum value of 2.06 $cm^3 \cdot K \cdot mol^{-1}$ at 3 K. The *dc* magnetic susceptibility data was fitted to the Curie-Weiss equation, which afforded a Curie constant C of 3.82 $cm^3 \cdot K \cdot mol^{-1}$ and a Weiss constant θ of -21.5 K, Figure 3.25.

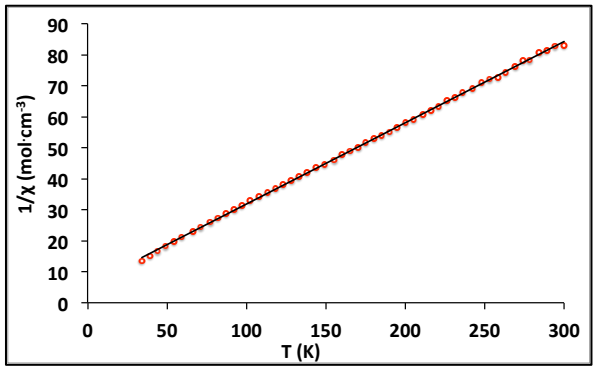

Figure 3.25 $1/\chi$ *vs.* T for *R*-Co_3 (**3.2**). The black line is the best fit to the Curie-Weiss equation.

Variable temperature *dc* magnetic susceptibility studies were also carried out on freshly prepared single crystals of **3.3** in the temperature range 2 – 300 K under an applied field of 0.1 T. The room temperature χT value of 6.25 $cm^3 \cdot K \cdot mol^{-1}$ is within the range of expected values (6.76 $cm^3 \cdot K \cdot mol^{-1}$, calculated g = 2.68) for two non-interacting Co(II) ions with negligible spin-orbit coupling, Figure 3.26.[194] Below 50 K, χT gradually decreases, dropping to a minimum value of 4.68 $cm^3 \cdot K \cdot mol^{-1}$ at 25 K.

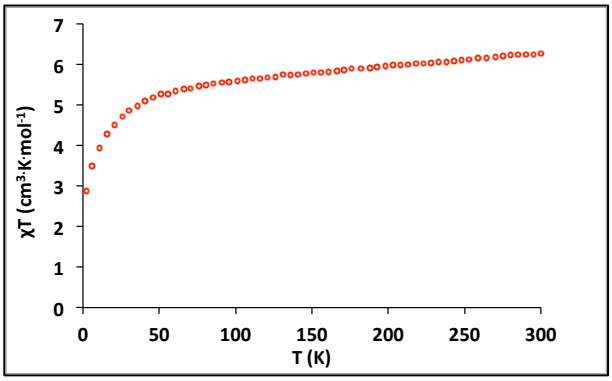

Figure 3.26 χT *vs.* T for **3.3** in a field of 0.1 T from 2 – 300 K.

The *dc* magnetic susceptibity data were fitted to the Curie-Weiss equation which afforded a Curie constant of 6.43 $cm^3 \cdot K \cdot mol^{-1}$ and a Weiss constant θ of -13.5 K, Figure 3.27.

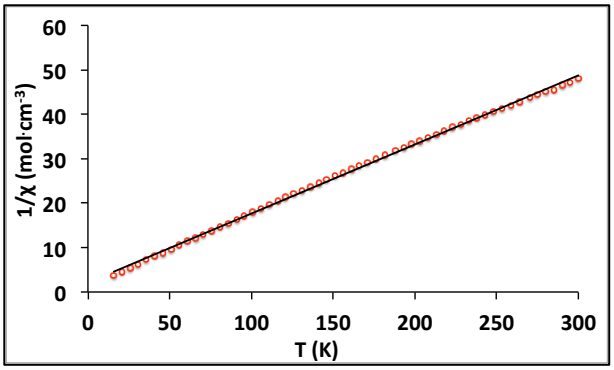

Figure 3.27 $1/\chi$ *vs.* T for *R*-Co_4 (**3.3**). The black line is the best fit to the Curie-Weiss equation.

The downward curve in the χT upon cooling most likely reflects a mixture of the presence of spin orbit coupling and significant single ion anisotropy. In this context, single ion anisotropy will be most prevalent in the low temperature regime, below 50 K, and exchange coupling interactions will dominate at higher temperatures.

For this complex the magnetic susceptibility data supported the presence of a mixed valence complex displaying predominant antiferromagnetic interactions. Furthermore, the complex does not show any out of phase *ac* magnetic susceptibility signals down to 5 K in zero field, suggesting that this is not an SMM, Figure 3.28.

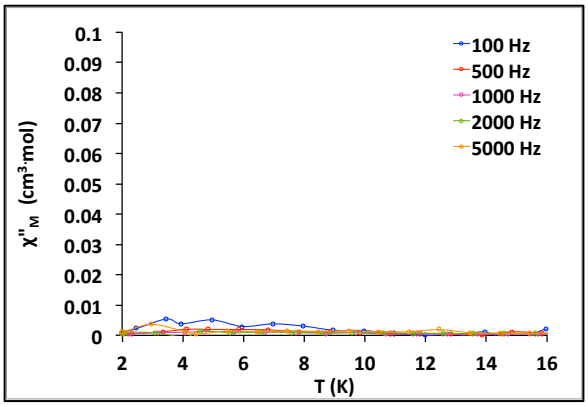

Figure 3.28 χ_M'' *vs.* temperature for the cluster **3.3** in a zero field.

CHAPTER 4 – CONCLUSIONS

To conclude two complementary strategies have been adopted for the self-assembly of polynuclear clusters. In Project 1, following a rational self-assembly approach, two hexanuclear Ln_6 complexes capped by *p-tert*-butylcalix[4]arene macrocycles have been successfully prepared and characterized. Conditions for the growth of single crystals of two Dy(III) and Tb(III) clusters have been established and their molecular structures fully elucidated by X-ray crystallography. Despite having very similar unit cell parameters, X-ray diffraction studies revealed that the coordination geometries of the lanthanide ions in the two compounds were subtly different which had important consequences for their magnetic properties. Our studies showed that for large polynuclear clusters, it is not always advisable to use the unit cell parameters alone to draw conclusions regarding their molecular structures and in particular, the coordination geometries of their metal centers. Magnetic susceptibility studies revealed that the $Dy_6[TBC4]_2$ cluster **2.3** displayed SMM properties with effective energy barriers of 48 K in the high temperature regime (9 – 18 K), and 13 and 10 K in the low temperature regime (3-8 K). Solid-state photoluminescence measurements revealed the cluster displays luminescence properties at low temperature, but the absorption bands are broad due to ligand based fluorescence overlapping with the *f-f* transitions. Although the Tb(III) derivative crystallized in a very similar unit cell affording a hexanuclear cluster core of Tb_6 ions, the coordination geometry of the apical Tb(III) ions were subtly different, with the apical Tb ion having lost a water molecule. To our surprise, *ac* magnetic susceptibility studies on this cluster revealed that it also displays SMM

properties. The *ac* susceptibility data afforded larger energy barriers of 80 and 63 K telling us that either the quantum tunneling of magnetization was less efficient in this system and/or the first excited states are better isolated. Solid state luminescence measurements at both 300 and 12 K revealed that upon excitation, the complex displayed the green luminescence characteristic for Tb(III) ions. Interestingly, the broad luminescence of the TBC4 ligand is now quenched, revealing five sharp bands corresponding to intra-4f^6 transitions.

Given the conflicting magnetic reports in the chemical literature concerning the magnetic properties of this family of clusters, future studies should involve the preparation of these complexes by hydrothermal synthesis. Detailed magnetostructural investigations would then permit detailed studies s to how subtle changes to the coordination geometries of the Dy(III) ions in the cluster affect the relaxation dynamics of the system. In addition it is also possible to increase the size of the macrocyclic cavity of the calixarene macrocyle and prepare for example calix[5], [6], or [7]arenes that may afford other new cluster motifs that would be structurally and magnetically interesting. While synthetic methodologies to these larger macrocycles are available, their synthesis can involve many steps and may be far from facile when compared to the commercially available calix[4]arene macrocycles. One could also synthetically modify the functionality on the upper and/or lower rims of the calixarene macrocycles. In addition it would also be interesting to employ other classes of oxophilic macrocycles for the preparation of polynuclear Ln-SMMs. In this respect the cucurbituril family[201] of macrocycles shown in Figure 2.30 might also be worth pursuing in the future.

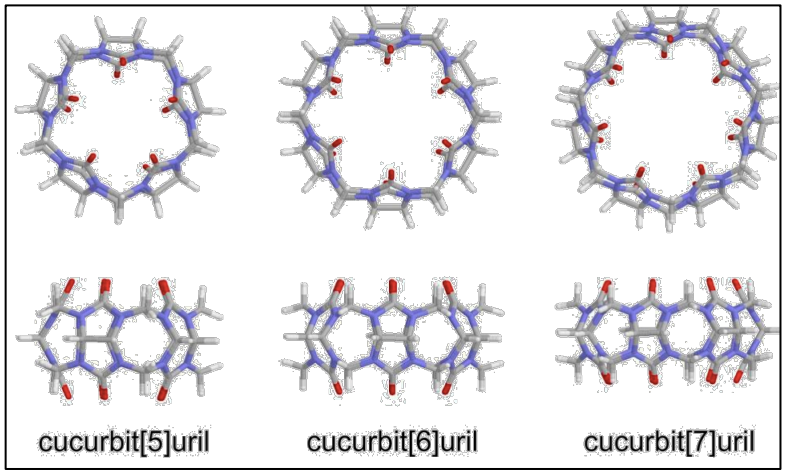

Figure 4.1 Molecular structures of selected members of the cucurbituril family of macrocycles.[202]

In project 2, employing a serendipitous strategy, the chirality of the α-methyl-2-pyridinemethanol ligand ***R/S*-L3.1** was successfully transferred to three polynuclear complexes **3.1, 3.2** and **3.3**. In this respect, reaction of **L3.1** with Ni(II) afforded a Ni_4 cluster with a cubane topology that is well known in Ni(II) chemistry. In contrast reaction with Co(II) afforded two mixed-valence complexes; a linear Co_3 trimer and a Co_4 tetramer with a defective double cubane structure. Our studies show that for all three complexes, both enantiomers of the ligand behaved in the same way, affording the same coordination complexes with inverted configurations at the chiral centers. Magnetostructural studies on all three complexes revealed that the dominant magnetic exchange interactions were antiferromagnetic which renders them unsuitable for the development of single molecule magnets. Complex **3.3** represented the first example of a chiral mixed valence Co_4 cluster with a defective double cubane topology. Since these complexes crystallize in chiral space groups, future studies will involve determining whether or not they display

ferroelectric properties. Unfortunately, within the time constraints of this project we were not able to find suitable conditions for the growth of single crystals of Dy(III) complexes, so more studies are needed to pursue the coordination chemistry of this ligand together with other Ln(III) ions. Nevertheless, these preliminary studies demonstrated that chiral pyridine-based alkoxide ligands are a very promising class of ligands for the synthesis of polynuclear clusters. Further work is also needed to adjust the reaction conditions e.g. pH, choice of secondary building block, metal salt, solvent system, stoichiometries, to target the crystallization of higher nuclearity systems. In addition, coordination chemistry studies of this ligand together with Mn and Fe, as well as targeting synthetic strategies for the discovery of heteronuclear *4f-3d* complexes are all research goals that could be actively pursued in the near future.

CHAPTER 5 – EXPERIMENTAL

5.1 General Information

All reagents were purchased from Sigma-Aldrich, Alfa Aesar, or Strem Chemicals and used without further purification. Anhydrous solvents were obtained from a Puresolve PS MD-4 solvent purification system.

5.2 Instrumentation

Circular dichroism spectroscopy (CD): Spectra were collected on a Jasco J-600 spectrometer at room temperature and the data was processed, using J7STDANL software.

Elemental analysis: CHN measurements were performed by Atlantic Microlab Inc**.**

Electrochemical studies: Electrochemical studies were performed under nitrogen using a BASi EC-epsilon Autoanalyzer and a standard three-electrode assembly (glassy carbon working, Pt wire auxiliary, and $Ag/AgNO_3$ reference) with 0.1 M $NBu^n_4PF_6$ as supporting electrolyte. Quoted potentials are versus the ferrocene/ferrocenium couple, used as an internal standard. The scan rates for cyclic voltammetry were 100 mV/s. Distilled solvents were employed and the concentrations of the complexes were approximately 1 mM.

Infrared spectroscopy: Infrared spectra were recorded as solids or oils between 4000 – 400 cm^{-1} on a Bruker Alpha FT-IR spectrometer.

Magnetic susceptibility measurements: *Dc* measurements were performed on single crystals using a Quantum Design SQUID magnetometer MPMS. Temperature scans were performed at applied fields between 0.1 - 0.2 T, from 2 – 300 K. Field scans were performed over the range -5 to 5 T, at temperatures between 3 - 5 K. *Ac* measurements were carried out on single crystals using a Quantum Design PPMS, in an oscillating field of 3.5 Oe over multiples frequencies between 25 and 1500 MHz. Static fields ranging from 0 to 0.5 T were applied, from 2 – 15 K. The samples were corrected for the sample diamagnetism and sample holder.

Mass spectrometry: The Electrospray Ionization (ESI) measurements were recorded on a Carlo Erba/Kratos EC/ms acquisition system and processed at a SPARC workstation. Samples were introduced through a direct inlet system, with *tris*(perflouroheptyl-*S*-triazine) as the internal standard. The Time-of-Flight mass spectrometry (TOF-MS) measurements were carried out on a micromass LCT – Electrospray Ionization Time-of-Flight mass spectrometer. All samples were prepared in a solution of acetonitrile with 0.1% trifluoroacetic acid (TFA). ESI measurements were performed in the presence of 0.1% TFA to ensure sufficient amount of ions reach the detector.

NMR spectroscopy: ^{1}H and ^{13}C NMR spectra were recorded at 400 and 75 MHz, respectively, on a Bruker Advance AV 400 Digital NMR spectrometer in deuterated solvents. Data was analyzed using the Bruker TOPSPIN 2.1 PL6 software.

Luminescence measurements: Luminescence spectra were recorded at 300 K and at 12 K with a modular double grating excitation spectrofluorimeter with a TRIAX

320 emission monochromator (Fluorolog-3, Horiba Scientific) coupled to a R928 Hamamatsu photomultiplier, using a front face acquisition mode. The excitation source was a 450 W Xe arc lamp. The emission spectra were corrected for detection and optical spectral response of the spectrofluorimeter and the excitation spectra were corrected for the spectral distribution of the lamp intensity using a photodiode reference detector. The room temperature time-resolved emission spectra and emission decay curves (10^{-6} – 10^{-9} s) were recorded on a Fluorolog TCSPC spectrofluorimeter (Horiba Scientific) coupled to a TBX-04 photomultiplier tube module (950 V), 200 ns time-to-amplitude converter and 70 ns delay. The excitation source was a Horiba-Jobin-Yvon pulsed diode (NanoLED-390, peak at 390 nm, 1.2 ns pulse duration, 1 MHz repetition rate and 150 ns synchronization delay). The emission decay curves (10^{-6} – 10^{-2} s) were recorded at room temperature with a Fluorolog TCSPC spectrofluorometer (Horiba Scientific) coupled to a TBX-04 photomultiplier tube module (950 V), 50 μs delay. The exciting source was a Horiba Scientific pulsed diode light source (SpectraLED-355, peak at 356 nm).

Optical rotation: Optical activity was measured with a Rudolph Autopol IV Polarimeter. The measurements were carried out in a quartz vessel (ℓ = 100 mm) and with D line of sodium lamp (589 nm). Given is the specific activity which was calculated with the following formula

$$[\alpha]_{\lambda}^{T} = \frac{\alpha}{\ell(dm) \cdot c(g/ml)}$$

[α] = specific rotation in degrees; T = temperature in °C; λ = wavelength in nm; α = rotation degree value; ℓ = cell length in dm.

UV-visible spectroscopy: UV-Vis spectra were recorded at room temperature on a Beckman Coulter DU 720 General-Purpose UV-Vis spectrophotometer.

X-ray diffraction: Single crystals suitable for X-ray diffraction were mounted on a cryoloop with paratone oil and examined on a Bruker APEX-II CCD diffractometer equipped with a CCD area detector and an Oxford Cryoflex low temperature device. Data were measured at 150(2) and 173(2) K with Mo-Kα radiation (λ = 0.71073 Å) using the APEX-II software.[124] Cell refinement and data-reduction were carried out by SAINT.[203] An absorption correction was performed by the multi-scan method implemented in SADABS. The structures were solved by direct methods (SHELXS-97).[204] and refined using SHELXL-2013 in the Bruker SHELXTL suite and Olex2.[205] A summary of the experimental crystallographic data for all five complexes can be found in the in Tables 4.1 and 4.2 at the end of this chapter.

5.3 Synthesis of Organic Ligands

5.3.1Synthesis of L2.2 (TBC4)[206]

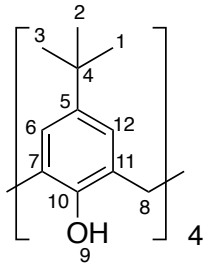

A mixture of *p-tert*-butylphenol (100 g, 0.66 mol), 37 % formaldehyde (62 mL, 0.83 mol), and NaOH (1.2 g, 0.03 mol) in water (3 mL) was placed in a 3-L, three-necked, round-bottom-flask equipped with a mechanical stirrer. The contents

of the open flask were allowed to stir in air for 15 min at RT, and then heated for 2 h at 120˚C. The reaction mixture, which was clear and colourless at the beginning, became light yellow after 30 min, a somewhat deeper yellow after 2 hrs, and eventually changed to a thick slurry as the water evaporated, finally turning to a deep brown-yellow very viscous mass. During this period, there was considerable frothing, and the reaction mixture filled most of the flask before it shrunk back to the original volume. The reaction was allowed to sit and cool to RT. To this reaction mixture, warm diphenyl ether (800 mL) was added to dissolve the residue and the contents were stirred at RT for at least 1 hr. The reaction mixture was then stirred and heated at 120˚C under nitrogen during which time the colour of the solution changed from yellow to light brown. The reaction mixture was then stirred and refluxed at 150˚C under a gentle flow of nitrogen for 4 hrs. The reaction mixture was cooled to RT and the product was precipitated by the addition of ethyl acetate (1.5 L). The resulting mixture was stirred for 30 min and allowed to stand for 1 hr. The solid was filtered by vacuum filtration and washed with ethyl acetate (2 x 100 mL), acetic acid (1 x 200 mL), distilled water (2 x 100 mL), and acetone (2 x 50 mL). The crude product was then recrystallized from hot toluene (1.8 L) and concentrated to 0.9 L. On cooling, the desired product, **L2.2** was isolated as a while solid. Yield = 61.05 g, 0.094 mol, 49 %.

M.p.:	342 – 344°C (Lit. 344 – 346°C)[206]
TOF-MS:	m/z = 647 $[M-H]^+$ (4%).
^{1}H NMR ($CDCl_3$, 400 MHz) δ (ppm):	9.71 (4H, s, O-H9), 7.33 (8H, s, H6 and H12), 4.47 (4H, d, J = 13.3 Hz, $H8_2$), 3.60

	(4H, d, *J* = 14.2 Hz, $H8_2$), 1.33 (36H, s, H1, H2, H3).
^{13}C NMR ($CDCl_3$, 75 MHz) δ (ppm):	146.6 (C10), 144.71 (C5), 128.71 (C11), 125.52 (C6, C12), 34.01 (C4), 32.23 (C8), 31.47 (C1, C2, C3).
IR (cm^{-1}):	3148, 2954, 2864, 1599, 1452, 1391, 1362, 1307, 1285, 1262, 1200, 1123, 1102, 816, 781, 741, 698, 591.
UV-Vis (MeCN, nm (ε/L·mol^{-1}·cm^{-1})):	λ_{max} = 208 (ε = 256800), 279 (ε = 42900), 287 (ε = 37900).

5.3.2 Synthesis of *R*-L3.1 (*R*-mpmH)[150]

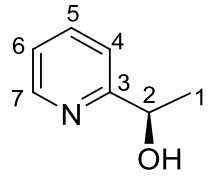

Formic acid (8.12 mL, 50 mmol) and Et_3N (17.41 mL, 125 mmol) were cooled to 0˚C under a nitrogen atmosphere. After stirring for 10 min, 2-acetylpyridine (5.6 mL, 50 mmol) and (*R,R*)-RuTsDPEN (0.033 g, 0.05 mmol) was added into the clear reaction mixture. The reaction was then stirred at 28˚C for 6 hrs or until the evolution of any gas ceased. The mixture at this point turned from yellow to green. To this solution was added a second portion of (*R,R*)-RuTsDPEN catalyst (0.033 g, 0.05 mmol). The resulting green solution was stirred at room temperature overnight; after which time it turned a yellow/orange colour. The reaction was then stopped and the mixture was extracted three times with Et_2O (3 x 60 mL) and the ether layers were

combined and washed with distilled water (40 mL). The combined organic extracts were dried over Na_2SO_4 and filtered. The solvent was evaporated under reduced pressure to afford the desired alcohol, *R*-**L3.1** as a clear, off-white coloured oil (3.84 g, 0.031 mol, 63 % yield). $[\alpha]_D^{25.3}$+19.8 (*c* 0.1, $CHCl_3$).[150,207,208]

M.p.:	53-54°C
^{1}H NMR ($CDCl_3$, 400 MHz) δ (ppm):	8.53 (1H, d, *J* = 4.72 Hz, H7), 7.68 (1H, td, *J* = 7.79, 6.39 Hz, H5), 7.29 (1H, d, *J* = 7.94 Hz, H4), 7.19 (1H, dd, *J* = 5.29, 5.14 Hz, H6), 4.89 (1H, q, *J* = 6.57 Hz, H2), 4.10 (1H, s, OH), 1.50 (3H, d, *J* = 6.59 Hz, H1).
^{13}C NMR ($CDCl_3$, 75 MHz) δ (ppm):	162.9 (C3), 147.9 (C7), 137.1 (C5), 122.3 (C4), 119.9 (C6), 68.8 (C2).
IR (cm^{-1}):	3356, 2975, 1595, 1477, 1364, 1282, 1081, 1017, 904, 784, 751, 608, 538.
UV-Vis (MeCN, nm, (ε/L·mol^{-1}·cm^{-1})):	λ_{max} = 207 (ε = 298300), 255 (ε = 239700).

5.3.3 Synthesis of *S*-L3.1 (*S*-mpmH)[150]

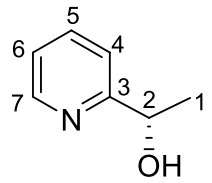

Following the same procedure as above, the *S*-enantiomer (*S*-mpmH) was also prepared using (*S,S*)-RuTsDPEN as the catalyst, which had identical spectral

properties to the *R*-**L3.1** enantiomer (3.84 g, 0.031 mol, 63 % yield). $[\alpha]_D^{25.3}$-19.8 (*c* 0.1, $CHCl_3$).[150,207,208]

5.4 Synthesis of Coordination Complexes

5.4.1 Synthesis of $[Dy_6(TBC_4)_2(DMF)_4(HCO_2)_2(HCO_3)_2(\mu_4O)_2(OH)_2(H_2O)_4]\cdot 7MeCN\cdot 7MeOH$ (2.3)

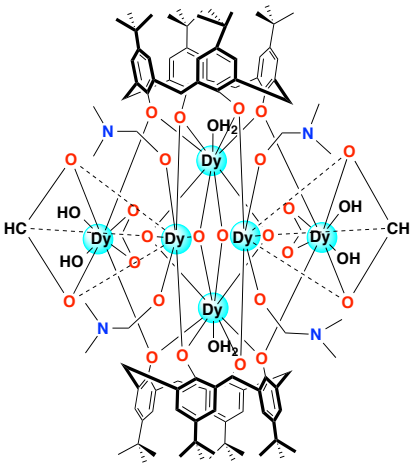

$Dy(ClO_4)_3\cdot 6H_2O$ (0.10 mL, 0.32 mmol) and 18-crown-6 (0.085 g, 0.32 mmol) were dissolved in a 3:1 ratio of MeCN:MeOH (1.2 mL). The mixture was stirred at 61˚C for 2.5 hrs followed by the addition of a solution of TBC4 (0.070 g, 0.11 mmol) in a 1:1 mixture of DMF/MeOH (20 mL). The reaction mixture was then stirred and heated at 61˚C for an additional 5 min before Et_3N (1.2 mL) was added. The mixture was then stirred under the same conditions for a further 5 hrs, resulting in the presence of a pale yellow solution that was allowed to cool to RT and filtered. Colourless block shaped crystals of complex **2.3** were grown via the slow evaporation of the reaction mixture at RT after 2 days. Yield = 78 mg, 0.023 mmol, 92 %.

TOF-MS: m/z = 2341 $[M\text{-}TBC4+H_2O]^+$ (75%).

IR (cm^{-1}): 3594, 3520, 2949, 2902, 2861, 1673, 1656, 1539, 1464, 1199, 1057.

CHN: Found C: 44.42, H: 5.13, N: 4.44%; Calcd. for $C_{104}H_{146}N_4O_{28}Dy_6$ – C: 44.33; H: 5.80; N: 4.55%.

UV-Vis (MeCN, nm, (ε/L·mol^{-1}·cm^{-1})): λ_{max} = 209 (ε = 318000), 279 (ε = 44600), 287 (ε = 41400).

5.4.2 Synthesis of $[Tb_6(TBC4)_2(DMF)_4(HCO_2)_2(HCO_3)_2(\mu_4\text{-}O)_2(OH)_2(H_2O)_2]\cdot 10MeCN\cdot H_2O\cdot 3MeOH$ (2.4)

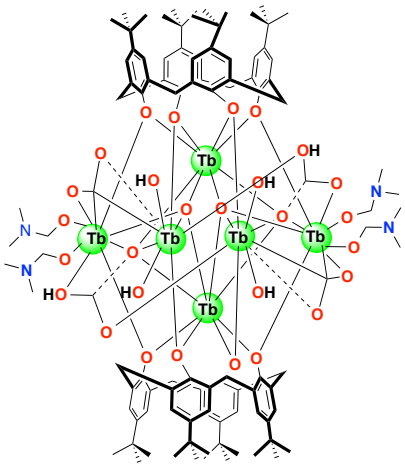

Following the previous procedure, colorless single crystals **2.4** were obtained from the reaction of $Tb(ClO_4)_3\cdot 6H_2O$, 18-crown-6, and TBC4 after slow evaporation of the reaction mixture at room temperature after a few days. Yield = 82 mg, 0.024 mmol, 94 %.

ESI-MS: *m/z* = 2976 $[M\text{-}(OH)_2\text{-}H_2O+H]^+$ (25%)

IR (cm^{-1}): 3431, 2948, 1650, 1553, 1455, 1356, 1292, 1100, 906, 803, 482.

CHN: Found C: 44.01, H: 6.15, N: 6.00%; Calcd. for $C_{104}H_{142}N_4O_{26}Tb_6$ – C: 43.98; H: 5.81; N: 5.65%.

UV-Vis (MeCN, nm, (ε/L·mol^{-1}·cm^{-1})): λ_{max} = 212 (ε = 350400), 297 (ε = 39800), 305 (ε = 34800).

5.4.3 Synthesis of *R*- and *S*-[$Ni_4(O_2CCMe_3)_4(mpm)_4$] (3.1)

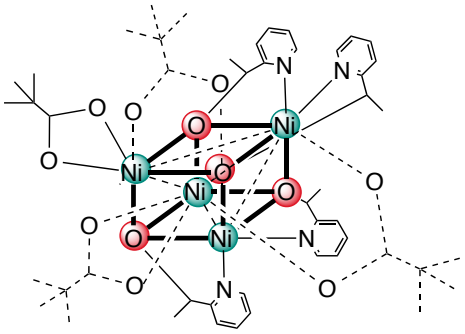

The *R*- or the *S*-enantiomer of **L3** (0.079 g, 0.6 mmol) was dissolved in MeCN (20 mL). To this solution was added Et_3N (0.167 mL, 1.2 mmol), pivalic acid (0.069 mL, 0.6 mmol), and $Ni(ClO_4)_2{\cdot}6H_2O$ (0.22 g, 0.6 mmol), respectively. The reaction mixture was then stirred at RT for 20 min. Green crystalline blocks of **3.1** were obtained via the slow evaporation of the reaction mixture at 0˚C after 1 day. Yield = 28 mg, 0.026 mmol, 39 %.

MALDI/TOF-MS: *m/z* = 1049 $[M\text{-}C(CH_3)_3]^+$ (100%).

IR (cm^{-1}): 2953, 2919, 2860, 1606, 1560, 1530, 1481, 1412, 1358, 1283, 1223, 1082, 900, 771, 662, 564, 478, 426.

CHN:	Found C: 50.45, H: 6.00, N: 4.92%; Calcd. for $C_{44}H_{70}N_4Ni_4O_{13}$ – C: 50.31; H: 6.16; N: 4.89%.
UV-Vis (DCM, nm, (ε/L·mol^{-1}·cm^{-1})):	λ_{max} = 233 (ε =39700), λ = 262 (ε = 466000).

5.4.4 Synthesis of *R*- and *S*-$[Co_3(mpm)_6]\cdot(ClO_4)_2$ (3.2)

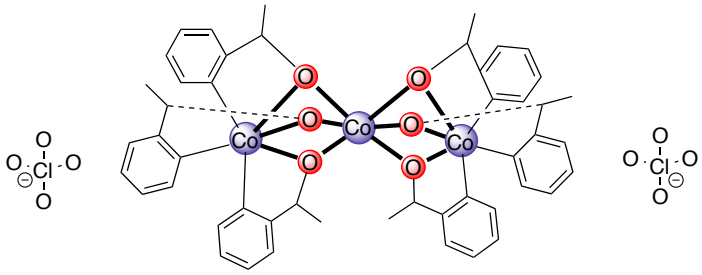

The R- or S-enantiomer of **L3** (0.079 g, 0.6 mmol) was dissolved in MeCN (20 mL). To this solution was added Et_3N (0.084 mL, 0.6 mmol), and $Co(ClO_4)_2\cdot 6H_2O$ (0.11 g, 0.3 mmol), respectively. The reaction mixture was then stirred at RT for 20 min. Both enantiomers of complex **3.2** were obtained as red/brown crystalline blocks via the slow evaporation of the reaction mixture at RT after 1 day. Yield = 26 mg, 0.023 mmol, 23 %.

FAB-MS:	*m/z* = 1132 $[M+H]^+$ (100%).
IR (cm^{-1}):	3074, 2975, 2781, 1605, 1569, 1479, 1442, 1366, 1322, 1282, 1222, 1161, 1074, 1016, 913, 790, 763, 662, 619, 576, 495, 459.

CHN:	Found C: 45.77, H: 4.46, N: 7.77%; Calcd. for $C_{42}H_{48}Cl_2N_6Co_3O_{14}$ – C: 45.65; H: 4.40; N: 7.87%.
UV-Vis (DMF, nm, (ε/L·mol^{-1}·cm^{-1})):	λ_{max} = 230 (ε =348900).

5.4.5 Synthesis of *S*- and *R*-[Co(II)$_2$Co(III)$_2$(NO$_3$)$_2$(μ-mpm)$_4$(ONO$_2$)$_2$] (3.3)

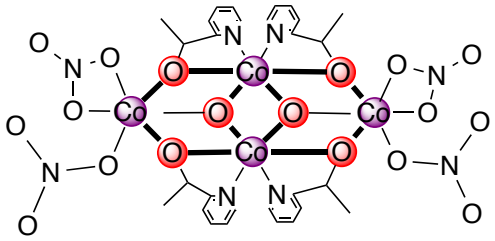

R- and *S*-enantiomers of **L3** (0.47 g, 0.36 mmol) was dissolved in MeOH (20 mL). To this solution was added Et_3N (0.084 mL, 0.6 mmol), and $Co(NO_3)_2{\cdot}6H_2O$ (1.57 g, 0.5 mmol), respectively. The reaction mixture was then stirred at RT for 20 min. Dark brown single crystals of both enantiomers of **3.3** grew as blocks via the diffusion of a (1:1) solution of Et_2O and hexane into the reaction mixture at RT after 3 weeks. Yield = 14 mg, 0.014 mmol, 4 %.

ESI-MS:	*m/z* = 972 $[M\text{-}NO_3]^+$ (100%)
IR (cm^{-1}):	3092, 2980, 2937, 2293, 2100, 1608, 1570, 1460, 1371, 1280, 1220, 1162, 1098, 1054, 1016, 920, 810, 799, 676, 746, 694, 663, 593, 549, 524, 477, 419.

CHN: Found C: 34.84, H: 3.87, N: 10.65%; Calcd. for $C_{30}H_{38}N_8Co_4O_{18}$ – C: 34.87; H: 3.84; N: 10.67%.

UV-Vis (MeCN, nm, (ε/L·mol^{-1}·cm^{-1})): λ_{max} = 204 (ε =150800).

Table 5.1 Summary of crystallographic data for $Ln_6[TBC4]_2$ complexes **2.3** and **2.4**.

	2.3	**2.4**
Chemical formula	$C_{125}H_{195}Dy_6N_{11}O_{35}$	$C_{127}H_{200}Tb_6N_{14}O_{37}$
M_r	3386.98	3468.61
Crystal system, space group	Monoclinic, $C2/m$	Monoclinic, $C2/m$
Temperature (K)	150	173
a, b, c (Å)	22.957 (3), 28.023 (5), 15.2098 (18)	23.484 (3), 28.178 (4), 15.647 (2)
β (°)	128.736 (4)	129.968 (4)
V (Å^3)	7632.6 (19)	7935.4(3)
Z	4	4
ρ_{calc} (mg/mm^3)	1.291	1.225
Radiation type	Mo $K\alpha$	Mo $K\alpha$
μ (mm^{-1})	2.691	2.988
F (000)	2912	2896
Crystal size (mm)	0.4 × 0.12 × 0.5	0.38 × 0.10 × 0.06
No. of measured, independent and observed [$I > 2\sigma(I)$] reflections	8010, 4185, 3454	24636, 5086, 5065
R_{int}	0.030	0.0500
$(\sin\theta/\lambda)_{max}$ (Å^{-1})	0.617	0.594
$R[F^2 > 2\sigma(F^2)]$, $wR(F^2)$, S	0.090, 0.260, 1.79	0.105, 0.246, 0.93
No. of reflections	4185	5086
No. of parameters	340	298
No. of restraints	31	203
H-atom treatment	H-atom parameters constrained	H-atom parameters constrained

Table 5.2 Summary of crystallographic data for complexes **3.1**, **3.2**, and **3.3**.

	3.1	**3.2**	**3.2**
Chemical formula	$C_{44}H_{70}N_4Ni_4O_{13}$	$C_{42}H_{48}Cl_2Co_3N_6O_{14}$	$C_{30}H_{38}Co_4N_8O_{18}$
M_r	1127.90	1108.55	1034.40
Crystal system, space group	Monoclinic, *C*2	Trigonal, *R*32	Orthorhombic, $P2_12_12_1$
Temperature (K)	173	173	173
a, *b*, *c* (Å)	12.548 (3), 20.583 (6), 12.063 (3)	13.3781 (7), 13.3781(7), 44.098 (2)	14.3290 (7), 16.5539 (8), 17.8987 (9)
α, β, γ (°)	90, 114.276 (10), 90	90, 90, 120	90, 90, 90
V (Å^3)	2840.1 (13)	6835.0 (8)	4245.6 (4)
Z	2	6	4
ρ_{calc} (mg/mm^3)	1.291	1.616	1.618
Radiation type	Mo *K*α	Mo *K*α	Mo *K*α
μ (mm^{-1})	1.36	1.27	1.62
F (000)	1184	3414	2104
Crystal size (mm)	0.2 × 0.15 × 0.05	0.40 × 0.31 × 0.27	0.10 × 0.10 × 0.04
No. of measured, independent and observed [$I > 2\sigma(I)$] reflections	20232, 4437, 4202	21852, 3506, 2964	50579, 8326, 6294
R_{int}	0.040	0.035	0.053
$(\sin\theta/\lambda)_{max}$ (Å^{-1})	0.595	0.650	0.617
$R[F^2 > 2\sigma(F^2)]$, $wR(F^2)$, *S*	0.050, 0.118, 1.09	0.038, 0.091, 1.04	0.076, 0.243, 1.19
No. of reflections	4437	3506	8326
No. of parameters	256	204	547
No. of restraints	1	0	0
H-atom treatment	H-atom parameters constrained	H-atom parameters constrained	H-atom parameters constrained

REFERENCES

(1) Yakhmi, J. V. *Bull. Mater. Sci.* **2009**, *32* (3), 217.

(2) Stefanita, C.-G. *Magnetism*; Springer-Verlag: Berlin Heidelberg, 2012.

(3) Train, C.; Gruselle, M.; Verdaguer, M. *Chem. Soc. Rev.* **2011**, *40* (6), 3297.

(4) Enoki, T.; Miyazaki, A. *Chem. Rev.* **2004**, *104* (11), 5449.

(5) Miller, J. S. *In Crystal Engineering: From Molecules and Crystals to Materials*; Springer, Ed.; 1999.

(6) Miller, J. S.; Gatteschi, D. *Chem. Soc. Rev.* **2011**, *40* (6), 3065.

(7) Yakhmi, J. V. *Bull. Mater. Sci.* **2009**, *32* (3), 217.

(8) Callister, W.; Rethwisch, D. *Materials Science and Engineering: An Introduction*, 7th ed.; John Wiley and sons, Inc., 2007; Vol. 94.

(9) Miller, J. S.; Epstein, A. J. *Mrs. Bull.* **2000**, 21.

(10) Bruce, D.W., OHare, D., Walton, R. I. *Molecular Materials*; John Wiley and sons, Ltd., 2010.

(11) Jeong, U.; Teng, X.; Wang, Y.; Yang, H.; Xia, Y. *Adv. Mater.* **2007**, *19* (1), 33.

(12) Orchard, A. F. *Magnetochemistry*; Oxford Chemistry Primers, Oxford University Press: Oxford, 2003; Vol. 75.

(13) Kahn, O. *Molecular Magnetism*; VCH: Weinheim, Germany, 1993.

(14) Miller, J. S.; Epstein, A. J. *Angew. Chem. Int. Ed. Engl.* **1994**, *33*, 385.

(15) Habib, F. PhD Thesis: Investigating and Enhancing Spin Reversal Barriers in Dinuclear 4f Single-Molecule Magnets and the Ultimate Shift to Mononuclear 3d Complexes, University of Ottawa, 2015.

(16) Housecroft, C.; Sharpe, A. G. *Inorganic Chemistry*, 4th ed.; Pearson, 2012.

(17) Woodruff, D. N.; Winpenny, R. E. P.; Layfield, R. A. *Chem. Rev.* **2013**, *113* (7), 5110.

(18) Bagai, R.; Christou, G. *Chem. Soc. Rev.* **2009**, *38* (4), 1011.

(19) Christou, G.; Gatteschi, D.; Hendrickson, D. N.; Sessoli, R. *Mrs. Bull.* **2000**, No. November, 66.

(20) Sorace, L.; Benelli, C.; Gatteschi, D. *Chem. Soc. Rev.* **2011**, *40* (6), 3092.

(21) Feltham, H. L. C.; Brooker, S. *Coord. Chem. Rev.* **2014**, *276*, 1.

(22) Neese, F.; Pantazis, D. *Faraday Discuss.* **2011**, *148*, 229.

(23) Rawson, J. *Magnetism of Clusters: Lectures*; University of Windsor: Windsor, Canada, 2009.

(24) Christou, G. *Polyhedron* **2005**, *24* (16-17), 2065.

(25) Christou, G. *J. Am. Chem. Soc* **1993**, *115* (6), 1804.

(26) Miyasaka, H.; Clérac, R.; Wernsdorfer, W.; Lecren, L.; Bonhomme, C.; Sugiura, K.; Yamashita, M. *Angew. Chemie Int. Ed.* **2004**, *43* (21), 2801.

(27) Andres, H.; Basler, R.; Güdel, H.-U.; Aromí, G.; Christou, G.; Büttner, H.; Rufflé, B. *J. Am. Chem. Soc.* **2000**, *122* (50), 12469.

(28) Milios, C. J.; Vinslava, A.; Wernsdorfer, W.; Moggach, S.; Parsons, S.; Perlepes, S. P.; Christou, G.; Brechin, E. K. *J. Am. Chem. Soc.* **2007**, *129* (10), 2754.

(29) Brechin, E. K.; Soler, M.; Davidson, J.; Hendrickson, D. N.; Parsons, S.; Christou, G. *Chem. Commun.* **2002**, *7* (19), 2252.

(30) Rumberger, E. M.; Zakharov, L. N.; Rheingold, A. L.; Hendrickson, D. N. *Inorg. Chem.* **2004**, *43* (21), 6531.

(31) Murugesu, M.; Wernsdorfer, W.; Abboud, K.; Christou, G. *Angew. Chemie Int. Ed.* **2005**, *44* (6), 892.

(32) Murugesu, M.; Raftery, J.; Wernsdorfer, W.; Christou, G.; Brechin, E. K. *Inorg. Chem.* **2004**, *43* (14), 4203.

(33) Jones, L. F.; Rajaraman, G.; Brockman, J.; Murugesu, M.; Sanudo, E. C.; Raftery, J.; Teat, S. J.; Wernsdorfer, W.; Christou, G.; Brechin, E. K.; Collison, D. *Chem. - A Eur. J.* **2004**,

10 (20), 5180.

(34) Soler, M.; Rumberger, E.; Folting, K.; Hendrickson, D. N.; Christou, G. *Polyhedron* **2001**, *20* (11-14), 1365.

(35) Tasiopoulos, A. J.; Vinslava, A.; Wernsdorfer, W.; Abboud, K. a.; Christou, G. *Angew. Chemie Int. Ed.* **2004**, *43* (16), 2117.

(36) Ako, A. M.; Hewitt, I. J.; Mereacre, V.; Clérac, R.; Wernsdorfer, W.; Anson, C. E.; Powell, A. K. *Angew. Chemie Int. Ed.* **2006**, *45* (30), 4926.

(37) Fang, M.; Zhao, H.; Prosvirin, A. V.; Pinkowicz, D.; Zhao, B.; Cheng, P.; Wernsdorfer, W.; Brechin, E. K.; Dunbar, K. R. *Dalt. Trans.* **2013**, *42* (41), 14693.

(38) Rinehart, J. D.; Long, J. R. *Chem. Sci.* **2011**, *2* (11), 2078.

(39) Ishikawa, N.; Sugita, M.; Ishikawa, T.; Koshihara, S.; Kaizu, Y. *J. Am. Chem. Soc.* **2003**, *125* (29), 8694.

(40) Mazarakioti, E. C.; Poole, K. M.; Cunha-Silva, L.; Christou, G.; Stamatatos, T. C. *Dalt. Trans.* **2014**, *43* (30), 11456.

(41) Rinehart, J. D.; Fang, M.; Evans, W. J.; Long, J. R. *J. Am. Chem. Soc.* **2011**, *133* (36), 14236.

(42) Quahab, L. *Multifunctional Molecular Materials*; Pan Stanford Publishing, 2013: Singapore, 2012.

(43) Provent, C., Williams, A. F. *The Chirality of Polynuclear Transition Metal Complexes*, Sauvage, J.; John Wiley and sons, Ltd., 1999.

(44) Lin, S.-Y.; Wang, C.; Zhao, L.; Wu, J.; Tang, J. *Dalt. Trans.* **2015**, *44* (1), 223.

(45) Train, C.; Gheorghe, R.; Krstic, V.; Chamoreau, L.-M.; Ovanesyan, N. S.; Rikken, G. L. J. a; Gruselle, M.; Verdaguer, M. *Nat. Mater.* **2008**, *7* (9), 729.

(46) Ramesh, R.; Spaldin, N. *Nat. Mater.* **2007**, *6* (1), 21.

(47) Li, X.-L.; Chen, C.-L.; Gao, Y.-L.; Liu, C.-M.; Feng, X.-L.; Gui, Y.-H.; Fang, S.-M. *Chem. - A*

Eur. J. **2012**, *18* (46), 14632.

(48) Crassous, J. *Chem. Soc. Rev.* **2009**, *38* (3), 830.

(49) Chirality_with_hands https://en.wikipedia.org/wiki/Chirality_(chemistry).

(50) Decurtins, S.; Schmalle, H. W.; Schneuwly, P.; Oswald, H. R. *Inorg. Chem.* **1993**, *32* (Ii), 1888.

(51) Ok, K. M.; Chi, E. O.; Halasyamani, P. S. *Chem. Soc. Rev.* **2006**, *35* (8), 710.

(52) Haertling, G. H. *J. Am. Ceram. Soc.* **1999**, *82* (4), 797.

(53) Barron, L. D. *Nat. Mater.* **2008**, *7* (9), 691.

(54) Curie, P. *J.Phys.Theor.Appl.* **1894**, *3* (1), 395.

(55) Kimura, T.; Goto, T.; Shintani, H.; Ishizaka, K.; Arima, T.; Tokura, Y. *Nature* **2003**, *426* (6962), 55.

(56) Martin, L. W.; Ramesh, R. *Nature* **2006**, *442*, 759.

(57) Ascher, E. *J. Appl. Phys.* **1966**, *37* (3), 1404.

(58) Hill, N. A. *J. Phys. Chem. B* **2000**, *104* (29), 6694.

(59) Ohkoshi, S. I.; Tokoro, H.; Matsuda, T.; Takahashi, H.; Irie, H.; Hashimoto, K. *Angew. Chemie - Int. Ed.* **2007**, *46* (18), 3238.

(60) Kundys, B.; Lappas, A.; Viret, M.; Kapustianyk, V.; Rudyk, V.; Semak, S.; Simon, C.; Bakaimi, I. *Phys. Rev. B* **2010**, *81* (22), 224434.

(61) de Jongh, L. J. *J. Appl. Phys.* **1969**, *40* (3), 1363.

(62) Andrés, R.; Gruselle, M.; Malézieux, B.; Verdaguer, M.; Vaissermann, J. *Inorg. Chem.* **1999**, *38* (21), 4637.

(63) Andrés, R.; Gruselle, M.; Malézieux, B.; Verdaguer, M.; Vaissermann, J. *Inorg. Chem.* **1999**, *38* (21), 4637.

(64) Gruselle, M.; Andres, R.; Malezieux, B.; Brissard, M.; Train, C.; Verdaguer, M. *Chirality* **2001**, *13* (10), 712.

(65) Rikken, G. L.; Raupach, E. *Nature* **2000**, *405* (6789), 932.

(66) Rikken, G. L. J. A.; Raupach, E. *Nature* **1997**, *4*, 493.

(67) Ferlay, S.; Mallah, T.; Ouahès, R.; Veillet, P.; Verdaguer, M. *Nature* **1995**, *378* (6558), 701.

(68) Verdaguer, M.; Bleuzen, a.; Marvaud, V.; Vaissermann, J.; Seuleiman, M.; Desplanches, C.; Scuiller, a.; Train, C.; Garde, R.; Gelly, G.; Lomenech, C.; Rosenman, I.; Veillet, P.; Cartier, C.; Villain, F. *Coord. Chem. Rev.* **1999**, *190-192*, 1023.

(69) Holmes, S. M.; Holmes, S. M.; Girolami, G. S.; Girolami, G. S. *J. Am. Chem. Soc.* **1999**, *121* (23), 5593.

(70) Andrés, R.; Brissard, M.; Gruselle, M.; Train, C.; Vaissermann, J.; Malézieux, B.; Jamet, J.; Verdaguer, M. *Inorg. Chem.* **2001**, *40* (18), 4633.

(71) Clement, R.; Decurtins, S.; Gruselle, M.; Train, C. *Monatshefte fur Chemier Chemie / Chem. Mon.* **2003**, *134* (2), 117.

(72) Gruselle, M.; Andres, R.; Malezieux, B.; Brissard, M.; Train, C.; Verdaguer, M. *Chirality* **2001**, *714* (March), 712.

(73) Coronado, E.; Gala, J. R.; Gomez-Garcia, C.J., Martinez-Agudo, J. M. *Inorg. Chem.* **2001**, *40* (13), 113.

(74) Gruselle, M.; Train, C.; Boubekeur, K.; Gredin, P.; Ovanesyan, N. *Coord. Chem. Rev.* **2006**, *250* (19-20), 2491.

(75) Clemente-León, M.; Coronado, E.; López-Jordà, M.; Desplanches, C.; Asthana, S.; Wang, H.; Létard, J.-F. *Chem. Sci.* **2011**, *2* (6), 1121.

(76) Mossin, S.; Tran, B. L.; Adhikari, D.; Pink, M.; Heinemann, F. W.; Sutter, J. J.; Szilagyi, R. K.; Meyer, K.; Mindiola, D. J. *J. Am. Chem. Soc.* **2012**, *134* (33), 13651.

(77) Inoue, K.; Kikuchi, K.; Ohba, M.; Okawa, H. *Angew. Chemie - Int. Ed.* **2003**, *42* (39), 4810.

(78) Caneschi, A.; Gatteschi, D. *Inorg. Chem.* **1991**, No. 7, 3936.

(79) Domingo, N.; Gerbier, P.; Gómez, J.; Ruiz-Molina, D.; Amabilino, D. B.; Tejada, J.; Veciana, J. *Polyhedron* **2003**, *22* (14-17), 2355.

(80) Gerbier, P.; Domingo, N.; Gomez-Segura, J.; Ruiz-Molina, D.; Amabilino, D. B.; Tejada, J.; Williamson, B. E.; Veciana, J. *J. Mater. Chem.* **2004**, *14* (15), 2455.

(81) Liu, C. M.; Xiong, R. G.; Zhang, D. Q.; Zhu, D. Ben. *J. Am. Chem. Soc.* **2010**, *132*, 4044.

(82) Inglis, R.; White, F.; Piligkos, S.; Wernsdorfer, W.; Brechin, E. K.; Papaefstathiou, G. S. *Chem. Commun. (Camb).* **2011**, *47* (11), 3090.

(83) Zaleski, C. M.; Depperman, E. C.; Kampf, J. W.; Kirk, M. L.; Pecoraro, V. L. *Inorg. Chem.* **2006**, *45* (25), 10022.

(84) Wen, H.-R.; Liu, S.-J.; Xie, X.-R.; Bao, J.; Liu, C.-M.; Chen, J.-L. *Inorganica Chim. Acta* **2015**, *435*, 274.

(85) Guo, P.-H.; Liu, J.-L.; Jia, J.-H.; Wang, J.; Guo, F.-S.; Chen, Y.-C.; Lin, W.-Q.; Leng, J.-D.; Bao, D.-H.; Zhang, X.-D.; Luo, J.-H.; Tong, M.-L. *Chem. - A Eur. J.* **2013**, *19* (27), 8769.

(86) Scott, J. F. *Nat. Mater.* **2007**, *6* (April), 256.

(87) Long, J.; Rouquette, J.; Thibaud, J.-M.; Ferreira, R. A. S.; Carlos, L. D.; Donnadieu, B.; Vieru, V.; Chibotaru, L. F.; Konczewicz, L.; Haines, J.; Guari, Y.; Larionova, J. *Angew. Chemie Int. Ed.* **2015**, *54* (7), 2236.

(88) Homden, D. M.; Redshaw, C. *Chem. Rev.* **2008**, *108* (12), 5086.

(89) Aronica, C.; Chastanet, G.; Zueva, E.; Borshch, S.; Clemente-Juan, J. M.; Luneau, D. *J. Am. Chem. Soc.* **2008**, *130* (7), 2365.

(90) Gutsche, C.; Dietrich, B. *Calixarenes Revisited*; Stoddart, J. F., Ed.; The Royal Society of Chemistry, Turpin Distribution Services Ltd.: UK, 1998.

(91) Ikeda, A.; Shinkai, S. *Chem. Rev.* **1997**, *97* (5), 1713.

(92) Taylor, S. M.; McIntosh, R. D.; Piligkos, S.; Dalgarno, S. J.; Brechin, E. K. *Chem. Commun.*

2012, *48*, 11190.

(93) Karotsis, G.; Teat, S. J.; Wernsdorfer, W.; Piligkos, S.; Dalgarno, S. J.; Brechin, E. K. *Angew. Chemie Int. Ed.* **2009**, *48* (44), 8285.

(94) Taylor, S. M.; Frost, J. M.; McLellan, R.; McIntosh, R. D.; Brechin, E. K.; Dalgarno, S. J. *CrystEngComm* **2014**, *16* (35), 8098.

(95) Taylor, S. M.; Karotsis, G.; McIntosh, R. D.; Kennedy, S.; Teat, S. J.; Beavers, C. M.; Wernsdorfer, W.; Piligkos, S.; Dalgarno, S. J.; Brechin, E. K. *Chemistry* **2011**, *17* (27), 7521.

(96) Karotsis, G.; Teat, S. J.; Wernsdorfer, W.; Piligkos, S.; Dalgarno, S. J.; Brechin, E. K. *Angew. Chemie Int. Ed.* **2009**, *48* (44), 8285.

(97) Sanz, S.; McIntosh, R. D.; Beavers, C. M.; Teat, S. J.; Evangelisti, M.; Brechin, E. K.; Dalgarno, S. J. *Chem. Commun.* **2012**, *48*, 1449.

(98) Bi, Y.; Xu, G.; Liao, W.; Du, S.; Deng, R.; Wang, B. *Sci. China Chem.* **2012**, *55* (6), 967.

(99) Sanz, S.; Ferreira, K.; McIntosh, R. D.; Dalgarno, S. J.; Brechin, E. K. *Chem. Commun.* **2011**, *47*, 9042.

(100) Karotsis, G.; Evangelisti, M.; Dalgarno, S. J.; Brechin, E. K. *Angew. Chemie - Int. Ed.* **2009**, *48* (52), 9928.

(101) Karotsis, G.; Kennedy, S.; Teat, S. J.; Beavers, C. M.; Fowler, D. a.; Morales, J. J.; Evangelisti, M.; Dalgarno, S. J.; Brechin, E. K. *J. Am. Chem. Soc.* **2010**, *132* (37), 12983.

(102) Karotsis, G.; Kennedy, S.; Dalgarno, S. J.; Brechin, E. K. *Chem. Commun. (Camb).* **2010**, *46* (22), 3884.

(103) Taylor, S. M.; McIntosh, R. D.; Beavers, C. M.; Teat, S. J.; Piligkos, S.; Dalgarno, S. J.; Brechin, E. K. *Chem. Commun.* **2011**, *47* (5), 1440.

(104) Tan, H.; Du, S.; Bi, Y.; Liao, W. *Chem. Commun. (Camb).* **2013**, *49* (74), 8211.

(105) Liu, M.; Liao, W. **2012**, *14* (18), 5727.

(106) Liu, M.; Liao, W.; Hu, C.; Du, S.; Zhang, H. *Angew. Chemie Int. Ed.* **2011**, n/a.

(107) Su, K.; Jiang, F.; Qian, J.; Wu, M.; Gai, Y.; Pan, J.; Yuan, D.; Hong, M. *Inorg. Chem.* **2014**, *53* (1), 18.

(108) Xiong, K.; Jiang, F.; Gai, Y.; Yuan, D.; Chen, L.; Wu, M.; Su, K.; Hong, M. *Chem. Sci.* **2012**, *3* (c), 2321.

(109) Palacios, M. A.; McLellan, R.; Beavers, C. M.; Teat, S. J.; Weihe, H.; Piligkos, S.; Dalgarno, S. J.; Brechin, E. K. *Chem. - A Eur. J.* **2015**, *21* (31), 11212.

(110) Gao, F.; Cui, L.; Song, Y.; Li, Y.; Zuo, J. *Inorg. Chem.* **2014**, *53*, 562.

(111) McLellan, R.; Kennedy, K. M.; Denis, M.; McIntosh, R. D.; Brechin, E. K.; Dalgarno, S. J. *Polyhedron* **2013**, *64*, 388.

(112) Taylor, S. M.; Sanz, S.; McIntosh, R. D.; Beavers, C. M.; Teat, S. J.; Brechin, E. K.; Dalgarno, S. J. *Chem. - A Eur. J.* **2012**, *18* (50), 16014.

(113) McLellan, R.; Taylor, S. M.; McIntosh, R. D.; Brechin, E. K.; Dalgarno, S. J. *Dalt. Trans.* **2013**, *42* (19), 6697.

(114) Alexopoulou, K. I.; Raptopoulou, C. P.; Psycharis, V.; Terzis, A.; Tangoulis, V.; Stamatatos, T. C.; Perlepes, S. P. *Aust. J. Chem.* **2012**, *65* (12), 1608.

(115) Champness, N. R. *Dalt. Trans.* **2011**, *40* (40), 10311.

(116) Hameury, S.; Kayser, L.; Pattacini, R.; Rogez, G.; Wernsdorfer, W.; Braunstein, P. *Dalt. Trans.* **2013**, *42* (14), 5013.

(117) Zhang, W.-H.; Sulaiman, N. B.; Tio, P. X. S.; Hor, T. S. A. *CrystEngComm* **2011**, *13* (8), 2915.

(118) Stamatatos, T. C.; Poole, K. M.; Abboud, K.; Wernsdorfer, W.; O'Brien, T. A.; Christou, G. *Inorg. Chem.* **2008**, *47* (11), 5006.

(119) Stamatatos, T. C.; Abboud, K.; Wernsdorfer, W.; Christou, G. *Angew. Chemie Int. Ed.* **2006**, *45* (25), 4134.

(120) Zhang, J.; Teo, P.; Pattacini, R.; Kermagoret, A.; Welter, R.; Rogez, G.; Hor, T. S. A.; Braunstein, P. *Angew. Chemie Int. Ed.* **2010**, *49* (26), 4443.

(121) Alexandropoulos, D. I.; Mukherjee, S.; Papatriantafyllopoulou, C.; Raptopoulou, C. P.; Psycharis, V.; Bekiari, V.; Christou, G.; Stamatatos, T. C. *Inorg. Chem.* **2011**, *50* (22), 11276.

(122) Gavey, E. L.; Al Hareri, M.; Regier, J.; Carlos, L. D.; Ferreira, R. a. S.; Razavi, F. S.; Rawson, J. M.; Pilkington, M. *J. Mater. Chem. C* **2015**, *3* (29), 7738.

(123) Blagg, R. J.; Muryn, C. A.; McInnes, E. J. L.; Tuna, F.; Winpenny, R. E. P. *Angew. Chemie - Int. Ed.* **2011**, *50* (29), 6530.

(124) *APEX-II*; Bruker AXS: Madison, Wisconsin, USA, 2007.

(125) Gutsche, C. D. *Calixarenes*; Royal Society of Chemistry: Cambridge, 2008; Vol. 34.

(126) Spek, A. L. *Acta Crystallogr. Sect. C Struct. Chem.* **2015**, *71*, 9.

(127) Zabrodsky, H.; Peleg, S.; Avnir, D. *J. Am. Chem. Soc.* **1992**, *114* (20), 7843.

(128) Seitz, M.; Oliver, A. G.; Raymond, K. N. *J. Am. Chem. Soc.* **2007**, *129* (36), 11153.

(129) AlDamen, M.; Cardona-Serra, S.; Clemente-Juan, J. M.; Coronado, E.; Gaita-Ariño, A.; Martí-Gastaldo, C.; Luis, F.; Montero, O. *Inorg. Chem.* **2009**, *48* (8), 3467.

(130) Tang, J.; Zhang, P. *Lanthanide Single-Molecule Magnets*; Springer, 2015.

(131) Frost, J. M.; Harriman, K. L. M.; Murugesu, M. *Chem. Sci.* **2016**, *7*, 2470.

(132) Ganivet, C. R.; Ballesteros, B.; De La Torre, G.; Clemente-Juan, J. M.; Coronado, E.; Torres, T. *Chem. - A Eur. J.* **2013**, *19* (4), 1457.

(133) Sanz, S.; McIntosh, R. D.; Beavers, C. M.; Teat, S. J.; Evangelisti, M.; Brechin, E. K.; Dalgarno, S. J. *Chem. Commun.* **2012**, *48* (10), 1449.

(134) Bünzli, J.-C. G.; Eliseeva, S. V. *Chem. Sci.* **2013**, *4* (5), 1939.

(135) Huang, W.; Wu, D.; Zhou, P.; Yan, W.; Guo, D.; Duan, C.; Meng, Q. *Cryst. Growth Des.* **2009**, *9* (3), 1361.

(136) Qiao, Y.; Lin, Y.; Zhang, S.; Huang, J. *Chem. - A Eur. J.* **2011**, *17* (18), 5180.

(137) Li, X.-L.; Chen, C.-L.; Xiao, H.-P.; Wang, A.-L.; Liu, C.-M.; Zheng, X.; Gao, L.-J.; Yang, X.-G.; Fang, S.-M. *Dalt. Trans.* **2013**, *42* (43), 15317.

(138) Gavey, E. L. PhD Thesis: Novel Magnetic Materials Based on Macrocyclic Ligands: Towards High Relaxivity Contrast Agents and Mononuclear Single-Molecule-Magnets, Brock University, 2015.

(139) Armelao, L.; Quici, S.; Barigelletti, F.; Accorsi, G.; Bottaro, G.; Cavazzini, M.; Tondello, E. *Coord. Chem. Rev.* **2010**, *254* (5-6), 487.

(140) Bünzli, J.-C. G.; Piguet, C. *Chem. Soc. Rev.* **2005**, *34* (12), 1048.

(141) Steffen, C.; Thomas, K.; Huniar, U.; Hellweg, A.; Rubner, O.; Schroer, A. *J. Comput. Chem.* **2010**, *31* (16), 2967.

(142) Bünzli, J. C. G. *Chem. Rev.* **2010**, *110* (5), 2729.

(143) Gusev, A. N.; Hasegawa, M.; Shimizu, T.; Fukawa, T.; Sakurai, S.; Nishchymenko, G. A.; Shul'gin, V. F.; Meshkova, S. B.; Linert, W. *Inorganica Chim. Acta* **2013**, *406*, 279.

(144) Bao, X.; Leng, J. D.; Meng, Z. S.; Lin, Z.; Tong, M. L.; Nihei, M.; Oshio, H. *Chem. - A Eur. J.* **2010**, *16* (21), 6169.

(145) Coronado, E.; Day, P. *Chem. Rev.* **2004**, *104* (11), 5419.

(146) Xu, S.; Liu, M.; Han, H.-L.; Li, Z.-F.; Jin, Q.-H.; Hou, J.; Su, W.; Chen, Y.-Y.; Yao, J.-Y. *Polyhedron* **2014**, *85*, 69.

(147) Gu, Z.-G.; Zhou, X.-H.; Jin, Y.-B.; Xiong, R.-G.; Zuo, J.-L.; You, X.-Z. *Inorg. Chem.* **2007**, *46* (14), 5462.

(148) Chorazy, S.; Podgajny, R.; Nitek, W.; Fic, T.; Görlich, E.; Rams, M.; Sieklucka, B. *Chem. Commun.* **2013**, *49* (60), 6731.

(149) Fujii, A.; Hashiguchi, S. *J. Am. Chem. Soc.* **1996**, *2* (Ii), 2521.

(150) Koike, T.; Murata, K.; Ikariya, T. *Tetrahedron Lett.* **2000**, *2* (24), 3833.

(151) Noyori, R.; Hashiguchi, S. *Acc. Chem. Res.* **1997**, *30* (2), 97.

(152) Sato, S.; Iida, J.; Suzuki, K.; Kawano, M.; Ozeki, T.; Fujita, M. **2016**, *313* (5791), 1273.

(153) Yoshizawa, M.; Tamura, M.; Fujita, M. *Science (80-.).* **2006**, *312* (5771), 251.

(154) Fujita, M. *Chem. Soc. Rev.* **1997**, *27*, 417.

(155) Fujita, M.; Umemoto, K.; Yoshizawa, M.; Fujita, N.; Kusukawa, T.; Biradha, K. *Chem. Commun.* **2001**, No. 6, 509.

(156) Yuan, Q. H.; Wan, L. J.; Jude, H.; Stang, P. J. *J. Am. Chem. Soc.* **2005**, *127* (46), 16279.

(157) Russell Seidel, S.; Stang, P. J. **2002**, *35* (11), 972.

(158) Leininger, S.; Olenyuk, B.; Stang, P. J. *Chem. Rev. (Washington, D. C.)* **2000**, *100* (3), 853.

(159) Scott, R. T. W.; Parsons, S.; Murugesu, M.; Wernsdorfer, W.; Christou, G.; Brechin, E. K. *Angew. Chemie - Int. Ed.* **2005**, *44* (40), 6540.

(160) Manoli, M.; Inglis, R.; Manos, M. J.; Nastopoulos, V.; Wernsdorfer, W.; Brechin, E. K.; Tasiopoulos, A. J. *Angew. Chemie Int. Ed.* **2011**, *50* (19), 4441.

(161) Whitehead, G. F. S.; Moro, F.; Timco, G. A.; Wernsdorfer, W.; Teat, S. J.; Winpenny, R. E. P. *Angew. Chemie Int. Ed.* **2013**, *52* (38), 9932.

(162) Athanasopoulou, A. MSc Thesis: Polynuclear Ni(II) Complexes with Schiff Bases as Bridging Ligands: A Molecular Approach to Nanoscience, Brock University, 2015.

(163) Winpenny, R. E. P. *J. Chem. Soc. Dalt. Trans.* **2001**, *6* (1), 1.

(164) Murrie, M. *Chem. Soc. Rev.* **2010**, *39* (6), 1986.

(165) Liang, Q.; Huang, R.; Chen, X.; Li, Z.; Zhang, X.; Sun, B. *Inorg. Chem. Commun.* **2010**, *13* (10), 1134.

(166) Bradley, J. M.; Thomson, A. J.; Inglis, R.; Milios, C. J.; Brechin, E. K.; Piligkos, S. *Dalt. Trans.* **2010**, *39* (41), 9904.

(167) Yoshihara, D.; Karasawa, S.; Koga, N. *J. Am. Chem. Soc.* **2008**, *130* (32), 10460.

(168) Hendrickson, D. N.; Yang, E. C.; Isidro, R. M.; Kirman, C.; Lawrence, J.; Edwards, R. S.; Hill, S.; Yamaguchi, A.; Ishimoto, H.; Wernsdorfer, W.; Ramsey, C.; Dalal, N.; Olmstead, M. M. *Polyhedron* **2005**, *24* (16-17), 2280.

(169) Shit, S.; Nandy, M.; Rosair, G.; Gómez-García, C. J.; Borras Almenar, J. J.; Mitra, S. *Polyhedron* **2013**, *61*, 73.

(170) Andrew, J. E.; Blake, A. B. *J. Chem. Soc. A* **1969**, 1456.

(171) Cadiou, C.; Murrie, M.; Paulsen, C.; Villar, V.; Wernsdorfer, W.; Winpenny, R. E. P. *Chem. Commun.* **2001**, No. 24, 2666.

(172) Andres, H.; Basler, R.; Blake, A. J.; Cadiou, C.; Chaboussant, G.; Grant, C. M.; Güdel, H.-U.; Murrie, M.; Parsons, S.; Paulsen, C.; Semadini, F.; Villar, V.; Wernsdorfer, W.; Winpenny, R. E. P. *Chem. - A Eur. J.* **2002**, *8* (21), 4867.

(173) Ochsenbein, S. T.; Murrie, M.; Rusanov, E.; Stoeckli-Evans, H.; Sekine, C.; Güdel, H. U. *Inorg. Chem.* **2002**, *41* (20), 5133.

(174) Moragues-Cánovas, M.; Helliwell, M.; Ricard, L.; Rivière, É.; Wernsdorfer, W.; Brechin, E.; Mallah, T. *Eur. J. Inorg. Chem.* **2004**, No. 11, 2219.

(175) Chilton, N. F.; Anderson, R. P.; Turner, L. D.; Soncini, A.; Murray, K. S. *J. Comput. Chem.* **2013**, *34* (13), 1164.

(176) Halcrow, M. A.; Sun, J.; Huffman, J. C.; Christou, G. *Inorg. Chem.* **1995**, *34* (16), 4167.

(177) Aromí, G.; Batsanov, A. S.; Christian, P.; Helliwell, M.; Roubeau, O.; Timco, G. A.; Winpenny, R. E. P. *Dalt. Trans.* **2003**, No. 23, 4466.

(178) Hudson, T. a; Berry, K. J.; Moubaraki, B.; Murray, K. S.; Robson, R.; Road, W. *Society* **2006**, *45* (9), 3549.

(179) Novitchi, G.; Pilet, G.; Luneau, D. *Comptes Rendus Chim.* **2012**, *15* (10), 937.

(180) Zhang, L.; Clérac, R.; Heijboer, P.; Schmitt, W. *Angew. Chemie - Int. Ed.* **2012**, *51* (12), 3007.

(181) Domingo, N.; Gerbier, P.; Gomez, J.; Ruiz-Molina, D.; Amabilino, D. B.; Tejada, J.; Veciana, J. *Polyhedron* **2003**, *22* (14-17), 2355.

(182) Chorazy, S.; Reczyński, M.; Podgajny, R.; Nogaś, W.; Buda, S.; Rams, M.; Nitek, W.; Nowicka, B.; Mlynarski, J.; Ohkoshi, S.; Sieklucka, B. *Cryst. Growth Des.* **2015**, *15* (8), 3573.

(183) Tandon, S. S.; Bunge, S. D.; Rakosi, R.; Xu, Z.; Thompson, L. K. *Dalt. Trans.* **2009**, No. 33, 6536.

(184) Chattopadhyay, S.; Bocelli, G.; Musatti, A.; Ghosh, A. *Inorg. Chem. Commun.* **2006**, *9* (10), 1053.

(185) Yang, C.; Wang, Q.-L.; Tang, G.-T.; Wang, C.; Yan, S.-P.; Liao, D.-Z. *J. Coord. Chem.* **2010**, *63* (3), 505.

(186) Khalaji, A. D.; Triki, S. *Russ. J. Coord. Chem.* **2011**, *37* (9), 664.

(187) Mahmudov, K. T.; Kopylovich, M. N.; Guedes da Silva, M. F. C.; Mahmudova, G. S.; Sutradhar, M.; Pombeiro, A. J. L. *Polyhedron* **2013**, *60*, 78.

(188) Mechi, L.; Siega, P.; Dreos, R.; Zangrando, E.; Randaccio, L. *Eur. J. Inorg. Chem.* **2009**, *2009* (18), 2629.

(189) Pradeep, C. P.; Zacharias, P. S.; Das, S. K. *Eur. J. Inorg. Chem.* **2007**, *2007* (34), 5377.

(190) Pradeep, C. P.; Zacharias, P. S.; Das, S. K. *Eur. J. Inorg. Chem.* **2007**, No. 34, 5377.

(191) Stamatatos, T. C.; Boudalis, A. K.; Pringouri, K. V.; Raptopoulou, C. P.; Terzis, A.; Wolowska, J.; McInnes, E. J. L.; Perlepes, S. P. *Eur. J. Inorg. Chem.* **2007**, *2007* (32), 5098.

(192) Alley, K. G.; Bircher, R.; Waldmann, O.; Ochsenbein, S. T.; Gudel, H. U.; Moubaraki, B.; Murray, K. S.; Fernandez-Alonso, F.; Abrahams, B. F.; Boskovic, C. *Inorg. Chem.* **2006**, *45* (22), 8950.

(193) Abedin, T. S. M.; Thompson, L. K.; Miller, D. O. *Chem. Commun.* **2005**, *2* (44), 5512.

(194) Stamatatos, T. C.; Dionyssopoulou, S.; Efthymiou, G.; Kyritsis, P.; Raptopoulou, C. P.; Terzis, A.; Vicente, R.; Escuer, A.; Perlepes, S. P. *Inorg. Chem.* **2005**, *44* (10), 3374.

(195) Mondal, P.; Singh, R.; Hens, A.; Cano, J.; Colacio, E.; Rajak, K. K. *Polyhedron* **2013**, *65*, 60.

(196) Wang, C.; Gao, E.; He, Z.; Yan, C. *Chem. Commun.* **2004**, *911* (6), 720.

(197) Zhang, S. Y.; Xu, B.; Zheng, L.; Chen, W.; Li, Y.; Li, W. *Inorganica Chim. Acta* **2011**, *367* (1), 44.

(198) Chen, Z.; Li, W.; Kang, B.; Wu, B.-M.; Mak, T.; Cai, Y.-B. *J Coord Chem* **1998**, *44*, 33.

(199) Siddiqi, Z. A.; Siddique, A.; Shahid, M.; Khalid, M.; Sharma, P. K.; Ahmad, M.; Kumar, S.; Lan, Y.; Powell, A. K. *Dalt. Trans.* **2013**, *42* (26), 9513.

(200) Banerjee, S.; Nandy, M.; Sen, S.; Mandal, S.; Rosair, G. M.; Slawin, A. M. Z.; Gómez García, C. J.; Clemente-Juan, J. M.; Zangrando, E.; Guidolin, N.; Mitra, S. *Dalt. Trans.* **2011**, *40* (8), 1652.

(201) Lagona, J.; Mukhopadhyay, P.; Chakrabarti, S.; Isaacs, L. *Angew. Chemie Int. Ed.* **2005**, *44* (31), 4844.

(202) Cucurbiturils https://en.wikipedia.org/wiki/Cucurbituril.

(203) *SAINT*; Bruker AXS: Madison, Wisconsin, USA, 2000.

(204) Sheldrick, G. M. *Acta Crystallogr. Sect. A Found. Crystallogr.* **2008**, *64* (1), 112.

(205) Ridout, J.; Probert, M. R. *CrystEngComm* **2014**, *16* (32), 7397.

(206) Gutsche, C. D.; Iqbal, M.; Stewart, D. *J. Org. Chem.* **1986**, *51* (5), 742.

(207) Itoh, T.; Matsushita, Y.; Abe, Y.; Han, S. H.; Wada, S.; Hayase, S.; Kawatsura, M.; Takai, S.; Morimoto, M.; Hirose, Y. *Chem. - A Eur. J.* **2006**, *12* (36), 9228.

(208) Busto, E.; Gotor-Fernández, V.; Gotor, V. *Tetrahedron Asymmetry* **2005**, *16* (20), 3427.